Recognition, Distortion And Allosteric Control During Purine Catalysis

A Thesis

Submitted in partial fulfillment of the requirements

of the degree of

Doctor of Philosophy

by

Vishakha Karnawat

20133290

Indian Institute of Science Education and Research

Pune - 411 008

2015

Certificate

Certified that the work incorporated in the thesis entitled "Recognition, Distortion and Allosteric Control during Purine Catalysis" submitted by Vishakha Karnawat was carried out by the candidate under my supervision. The work presented here or any part of it has not been included in any other thesis submitted previously for the award of any degree or diploma from any other University or Institution.

Dr. Mrinalini Puranik
Thesis Supervisor,
Indian Institute of Science Education
and Research,
Pune, Maharashtra

Declaration

I declare that this written submission represents my ideas in my own words and where others' ideas have been included, I have adequately cited and referenced the original sources. I also declare that I have adhered to all principles of academic honesty and integrity and have not misrepresented or fabricated or falsified any idea/data/fact/source in my submission. I understand that violation of the above will be cause for disciplinary action by the Institute and can also evoke penal action from the sources which have thus not been properly cited or from whom proper permission has not been taken when needed.

Vishakha Karnawat

Date: Roll No. 20133290

I learnt from him that:

"There is an invisible strength within us; when it recognizes two opposing objects of desire, it grows stronger".

Rumi

To my father

Acknowledgements

I have been fortunate to have met a few people who have been a constant source of inspiration during this endeavor, it is my pleasure to have now this opportunity to extend my sincere gratitude to them.

I would like to express my deep gratitude to my PhD advisor Dr. Mrinalini Puranik for her constant guidance, support and encouragement during the course of this thesis work. I have learnt a great deal from her enthusiasm for quality research and talent for seeing the bigger picture. Her exemplary attitude towards science and useful critical discussion not only helped me to develop an understanding of the subject but also imbibed in me the qualities of an excellent experimentalist.

I would like to extend my sincere thanks to Prof. Hemalatha Balaram for helping me at various steps of PhD. Her wisdom, ability to explain the things clearly and useful discussion enabled the successful completion of this PhD thesis. Though too short, I enjoyed the time spent in her lab where I learnt to acquire a different perspective of the field.

I am greatly thankful to Prof. Jayant Udgaonkar, Dr. Harinath Chakrapani and Dr. Gayathri Pananghat for their sound advices and useful suggestions during the course of this PhD.

I thank my lab seniors, Spriha Gogia and Namrata Jayanth, for teaching me almost everything necessary for performing a successful experiment.

I consider myself privileged to have shared the lab with two incredible physicists, Erix and Sayan. I thank them for their help related to almost everything in and outside the lab during all these years. In particular, I thank Erix for his advices to keep moving on even in difficult and stressful situations. Sayan deserves a special thank for his tremendous help in technical matters and for all the relentless discussion which keeps the lab cheerful. I have spent the most enjoyable period of my PhD years in his company.

I thank all the past and present lab members, specially, Anusuya, Nirmala, Hemanth, Panda, Sudeb, Yashwant, Anil, Shahila and Arya for making the lab such a lively place to work in. Though my PhD years did not overlap much with theirs, I will always cherish the tremendously wonderful time I spent with them.

I would like to thank all the short-term and long-term visitors, in particular, Amitha Shreesh and Snehal Supekar, who have helped me in purification of various enzymes. A special thank is due to Prashant Badgujar for helping me with PfADSS purification.

I wish to thank the director, Prof. K. N. Ganesh, for allowing the transfer of my PhD registration. I would like to thank all the administrative and academic staff at IISER Pune and at NCBS, Bangalore for dealing with many issues related to PhD registration transfer.

I would also like to thank the members in Dr. Hema's lab at JNCASR: Sonia, Sanjeev, Prasoona, Jyothi and Sourav for help in various issues.

I must acknowledge all the friends I have made during these years at NCBS/IISc/JNCASR, Bangalore and at IISER, Pune.

I have been incredibly fortunate to have Ravi as a 'friend for life'. From him, I learnt that 'Pain is inevitable but suffering is optional' (though the phrase is by Haruki Murakami). He has been the source of mental toughness I have achieved during these years.

Finally, I gratefully thank the most important people in my life, my family, for providing me with every possible means to achieve knowledge. I thank them for coping with the distance during all these years.

Contents

List of Abbreviations

6-pI: 6-phosphoryl inosine

6-pIMP: 6-phosphoryl IMP

9DAG: 9-deazaguanine

9DAH: 9-deazahypoxanthine

ADSS: Adenylosuccinate synthetase

AMP: Adenosine monophosphate

B3LYP: Becke, three-parameter, Lee-Yang-Parr

BBO: Barium borate

Be: bending vibration

Bre: breathing vibration

DFT: Density Functional Theory

E. coli: *Escherichia coli*

E•S: Enzyme•Substrate complex

EcADSS: *E. coli* ADSS

FPLC: Fast Protein Liquid Chromatography

FTIR: Fourier Transform Infrared

GDP: Guanosine-5′-diphosphate

GMP: Guanosine-5′-monophosphate

GS: Ground-state

GTP: Guanosine-5′-triphosphate

Gua: Guanine

H→D: Hydrogen to Deuterium

HDA: Hadacidin

HEPES: (4-(2-hydroxyethyl)-1-piperazineethanesulfonic acid)

HGPRT: Hypoxanthine Guanine Phosphoribosyltransferase

hHGPRT: human HGPRT

HPLC: High Performance Liquid Chromatography

HPP: 4-hydroxypyrazolo[3, 4]pyrimidine

Hx: Hypoxanthine

Im: imidazole ring

ImmGP: Immucillin GP

ImmHP: Immucillin HP

IMP: Inosine-5′-monophosphate

ITP: Inosine-5′-triphosphate

LBO: Lithium Borate

LtHGPRT: *Leshmenia tarentoale* HGPRT

MES: 2-(N-morpholino) ethane sulfonic acid

MjADSS: *Methanocaldococcus jannaschii* ADSS

mm: mouse muscle

Nd-YLF: Neodymium-doped yttrium lithium fluoride

PED: Potential Energy Distribution

PEI: Polyethylene imine

PfADSS: *Plasmodium falciparum* ADSS

PfHGPRT: *Plasmodium falciparum* HGPRT

PhADSS: *Pyrococcus horikoshii* ADSS

Pi: Inorganic Phosphate

PMSF: Phenylmethylsulfonyl fluoride

PPi: Inorganic Pyrophosphate

PRPP: α-D-5-phosphoribosyl-1-pyrophosphate

Prr: pyrrole ring

Py: pyrimidine ring

QM: Quantum Mechanical

ref: reference

RP-HPLC: Reverse Phase-HPLC

sA: succinyl Adenosine

sAMP: succinyl-AMP

Sci: scissoring vibration

Str: stretching vibration

TfHGPRT: *Tritrichomonas foetus* HGPRT

TgHGPRT: *Toxoplasma gondii* HGPRT

Ti-S: Titanium Sapphire

TS: Transition-state

UVRR: Ultraviolet Resonance Raman Spectroscopy

UTP: Uracil-5′-triphosphate

wt: wild type

Xan: Xanthine

XMP: Xanthosine-5′-monophosphate

XTP: Xanthosine-5′-triphosphate

Synopsis

Introduction

Enormous progress has been made in the understanding of the mechanistic origin of catalysis and specificity of enzymes. Structural information on enzyme-ligand complexes has played an indispensable role in deciphering the strategies employed by enzymes during catalysis. 'Lock and Key' hypothesis provides the analogy of lock with the enzyme and key with the substrate. This was followed by 'induced fit' model which suggested that enzymes are flexible and that binding of substrate induces conformational change in enzyme and pre-organization of the active-site [1, 2]. The active-site is complementary to the transition-state of the reaction and not necessarily to the substrates, asserted the transition-state theory [3]. This is the most widely accepted theory, transition-state stabilization (TSS). There is a large amount of evidence to suggest that enzymes also employ ground-state destabilization (GSD) during catalysis [4-12]. The energy of the enzyme•substrate complex (E•S) is increased by the distortion or strain caused due to non-covalent interactions at the active-site of the enzyme. Further, it may also happen that at the active-site, the charges of the substrate molecule are placed next to similar charges of amino-acid residues. This is the basis of electrostatic destabilization. Such structural distortions in enzyme-bound substrate (as compared to that of free substrate) are quite small: in the range of 0.1-1 Å [13-16]. The conventional biophysical techniques like X-ray and NMR are not suitable for obtaining structural information at this precision. Thus, I have employed a vibrational technique, ultraviolet resonance Raman spectroscopy (UVRR), to experimentally observe such distortions in enzyme bound ligands. Vibrational spectroscopy is a very sensitive technique which can measure structural changes in enzyme bound ligands, on the order of a bond-length [7, 15, 17-22]. Vibrational spectral band positions are directly proportional to the force constant of a bond between the atoms undergoing vibrations. Thus,

distortion in a substrate molecule which results in a small change in bond strength can manifest itself as an altered vibrational shift. In particular, vibrational Raman spectroscopy with ultraviolet light and in resonant conditions, UVRR, is the experimental method of choice for studying enzyme-nucleobase complexes because of the high Raman cross-section of nucleobases at UV wavelengths. In addition, different cross-sections of enzymes and nucleobases allow selective enhancement of the nucleobase substrate vibrations with minimum interference from protein vibrations.

Motivation

In my work, I have studied enzyme•ligand complexes of purine salvage pathway. This pathway of nucleotide synthesis involves recycling of nucleobases and nucleosides which are generated from nucleic-acid breakdown. Another major pathway of nucleotide synthesis is the *de novo* pathway which begins with metabolic precursors such as aspartate, ribose-5'-monophosphate, CO_2 and NH_3 [23, 24]. Whereas humans can utilize both the pathways, parasitic protozoa like *Plasmodium, Tritrichomonas, Leshmania* and *Trypanosoma* lack *de novo* pathway and depend solely on salvaging nucleotides from their hosts [25-28]. The ability of these parasites to develop resistance against existing drugs has led to the need of identification of new drug targets inside parasites. In this regard, the enzymes of the purine salvage pathways are regarded as potential therapeutic targets against such parasites [25-28]. In this work, I have studied enzyme•ligand complexes of two enzymes from this pathway: hypoxanthine guanine phosphoribosyltransferase (HGPRT) and adenylosuccinate synthetase (ADSS).

Results and Discussion

HGPRT: an essential enzyme of purine salvage pathway

HGPRT catalyzes Mg^{2+} dependent phosphoribosylation of nucleobases (hypoxanthine or guanine) to their corresponding mononucleotides. The reaction proceeds in a sequential and ordered fashion where α-D-5-phosphoribosyl-1-pyrophophate (PRPP) binds first followed by the binding of

the nucleobase [29]. As compared to its human counterpart, *Plasmodium falciparum* (Pf) HGPRT shows expanded substrate specificity and can catalyze xanthine also in addition to guanine and hypoxanthine [30]. Since human (h) and Pf enzymes share 80% sequence similarity at the active-site [31], the expanded substrate specificity of PfHGPRT remains an unresolved question. To capture a ternary complex in the forward reaction of HGPRT, I have used two purines analogues, 9-deazaguanine (9DAG) and 9-deazahypoxanthine (9DAH), which are structural mimic of guanine and hypoxanthine, respectively. These analogues possess a carbon atom at 9^{th} position of nucleobase in place of nitrogen, which renders them incapable of nucleophilic attack on C1' of sugar moiety of PRPP.

9-deazapurines exist in the neutral form at physiological pH

Enzymes are known to perturb protonation-state of ligands and thus, I started with characterization of the solution structure of 9-deaza analogues before moving on to the enzyme•ligand complexes. This was done using UVRR, at an excitation wavelength of 260 nm, coupled with density functional theory (DFT). A Comparison between experimental and theoretically predicted data (structures and protonation-states) shows that both 9DAG and 9DAH exist in neutral form with the proton at N1 and N7 position, at physiological pH. At pH 1.5, protonation in both the molecules occurs at N3 position of pyrimidine ring. Further, at pH 12.5, the N1 of pyrimidine ring is the site of deprotonation whereas the proton at N7 remains intact even at pH 12.5. These results are different from those obtained in case of hypoxanthine where, the first deprotonation occurs at N7 position of imidazole ring. To further substantiate the data, isotopic labeling of the enzyme•ligand complexes in experimental and computational simulations was also done. Such labeling and the resultant isotope induced shifts are helpful in assigning the Raman band positions with normal modes. A comparison between the experimentally and computationally obtained isotope induced shifts in wavenumbers provides a reliable method to assign the observed band positions with the calculated normal modes.

Hydrogen bonding network and stacking interactions provide greater rigidity to hHGPRT

Having identified the solution structure of 9-deazapurines, I studied the complexes of these ligands with the two HGPRTs using UVRR at an excitation wavelength of 260 nm. In an intriguing manner, I found that the magnitude of Raman shifts and the loss in Raman cross-section in the observed UVRR spectrum of these enzyme•ligand complexes show distortion in the bound ligands towards the transition-state of HGPRT catalyzed reaction. Magnitude of Raman shifts shows that the hydrogen bonding network at the active-site of hHGPRT is more rigid as compared to PfHGPRT. Loss in Raman cross-section of 9-deazapurines bound to both the HGPRTs is attributed to the stacking interaction between the Phe residue and the nucleobase at the active-site. Further, this loss in intensity was found out to be greater in hHGPRT than PfHGPRT suggesting a closer stacking interaction in the former than in the latter. UVRR experiments of 9DAH bound to HGPRTs show comparatively less compact active-site interactions with 9DAH than with 9DAG. In conclusion, with the effective use of substrate analogues, I have shown that the enzyme-induced distortions in ligands, indistinguishable in other biophysical techniques, are integral to catalysis and stabilize pre-transition state of HGPRT catalyzed reaction. My results establish that stacking interactions between purine substrates and the Phe residue at the active-site provide more rigid active-site to hHGPRT as compared to *Pf*HGPRT.

ADSS: an enzyme essential for purine nucleotide synthesis

Adenylosuccinate synthetase (ADSS) is a regulatory enzyme which binds to many ligands and employs allostery for its functioning. In order to elucidate the effect of allostery on enzyme-induced distortion, I have investigated two homologues of ADSS, one from a thermophile *Methanocaldococcus jannaschii* (Mj) and a second from a mesophile *P. falciparum*. Though catalyzing identical reactions, these homologues follow different kinetic cycles resulting from discrete allosteric mechanisms [32, 33]. The enzyme commits the conversion of inosine-5'-monophosphate (IMP) to

succinyl adenosine-5'-monophosphate (sAMP) in the nucleotide synthesis pathway. In my PhD work, I have determined the solution structure of various ligands including substrates, intermediates and products of ADSS. Subsequently, I furthered my studies to the complexes of these ligands with both the homologues of ADSS.

Solution structure of sAMP and 6-pIMP

Ligands of the forward reaction complexes include IMP, GTP and L-Aspartate. Previous vibrational studies have established the structures of IMP and GTP in solution at different pH values [34-36]. sAMP, a product of ADSS catalyzed reaction, has not been studied and hence, in my thesis, I deciphered its structure in solution. This was done using UVRR at an excitation wavelength of 260 nm. A comparison between experimental data with theoretically predicted structure, in addition to isotope labeling of enzyme•ligand complexes, establishes that, at neutral pH, sAMP exists as a neutral amino species with a proton at exocyclic N6 position of pyrimidine ring. Reverse phase HPLC profile shows the presence of two isomers of sAMP in solution. Further, I studied 6-pIMP complexed with ADSS; the free form of 6-pIMP is highly unstable in solution form and has not been studied so far. Based on the exhaustive comparison between experimental and computed data, the structure of 6-pIMP was established.

6-pIMP is stabilized by ligation of L-Aspartate pocket in MjADSS

Having identified the solution structures, I moved on to study the complexes of these ligands with MjADSS. My results show that although IMP bound to MjADSS is distorted towards its deprotonated form, it remains bound as neutral species until GTP is present. GTP in the ADSS catalyzed reaction provides γ-phosphate to the IMP and does not undergo any chemical transformation at the nucleobase moiety. UVRR data of GTP•MjADSS show that the nucleotide is held strongly at the active-site and confirm that the nucleobase is intact at the active-site. When IMP and GTP are added together to MjADSS, not only do the downshifts in IMP bands suggest greater distortion but the appearance of new bands in IMP•GTP•MjADSS which are

attributed to 6-pIMP shows that the formation of this intermediate is already initiated even in the absence of the ligation of L-Aspartate pocket. In the next step, upon addition of HDA to the ternary complex, it is observed that the marker bands of IMP completely disappear. Complete change in the spectral pattern of IMP•GTP•HDA•MjADSS suggests complete transformation of IMP to 6-pIMP in presence of HDA. A comparison of the UVRR spectra of above mentioned ternary and quinternary complexes shows that although 6-pIMP is formed in the ternary complex, it is not stabilized at the active-site and thus falls off from the active-site and forms IMP again. However, upon ligation of L-Aspartate pocket by either HDA or L-Aspartate, local conformational re-organization leads to the stabilization of 6-pIMP at the active-site for indefinite period of time. The direct implication of this finding lies in the identification of potential drug candidates against ADSS. The present data suggest that a mimic of 6-pIMP alone cannot act as a potential therapeutic agent but it should be provided along with a mimic of L-Aspartate.

MjADSS catalyzes reverse reaction under in vitro conditions

Having identified the transitions in the IMP molecule at different catalytic steps in MjADSS, I characterized the distortions in product molecules at the active-site of MjADSS. While the order of binding of these ligands to ADSS is known in the reverse direction, the conformational changes driven by their individual binding are elusive. Not only does the UVRR capture distortion in sAMP which is attributed to hydrogen bonding interactions at N6—H position but the wavenumber shifts in sAMP•MjADSS suggest that sAMP alone is sufficient to drive conformation re-organization of the dynamic loops in the MjADSS active-site. Distortion in the guanine moiety of GDP is essentially same as that in GTP and GMP-PNP which suggests unaltered active-site interactions in the moiety in GDP•MjADSS, GTP•MjADSS and GMP-PNP•MjADSS complexes. Enhanced magnitude of shifts in the marker bands of sAMP and GDP in sAMP•GDP•MjADSS suggests that both the ligands bind synergistically to ADSS. Addition of phosphate to sAMP•GDP•MjADSS results in the occurrence of reverse reaction under in vitro conditions at the active-site of ADSS.

PfADSS employs different mechanistic to catalyze the identical reaction

PfADSS is a potential chemotherapeutic target against malaria which employs a unique kinetic mechanism. In an ordered manner, IMP binds first to the apoenzyme and then only can the GTP bind, followed by the binding of L-Aspartate. The release of the products is also ordered where, phosphate leaves the active-site first followed by the release of GDP and then sAMP leaves the active-site. An only crystal structure of PfADSS is available in the fully ligated form which means that the conformational changes brought about by the binding of individual ligand are elusive. In my PhD work, I have determined the enzyme-induced distortions in PfADSS•ligand complexes and the same is compared with those observed in MjADSS•ligand complexes. This was done using UVRR at an excitation wavelength of 260 nm.

Absence of substantial shifts in the wavenumber of IMP•PfADSS spectrum shows that IMP alone is not sufficient to completely organize the active-site of PfADSS. A comparison between the UVRR spectrum of IMP•PfADSS with that of IMP•MjADSS shows that IMP is activated differently in the two homologues. Whereas kinetic results suggest that GTP binds only to IMP•PfADSS, UVRR results sample a population of PfADSS which is capable of binding to GTP even in the absence of IMP. Addition of GTP to the IMP•PfADSS complex further distorts the structure of IMP which is evident from the increase in the magnitude of shifts in IMP•GTP•PfADSS with respect to the IMP•PfADSS complex. Unlike in case of MjADSS, the ternary complex of PfADSS does not show any signature of 6-pIMP while in the quinternary complex, complete transformation of IMP to 6-pIMP is observed. In the absence of any stabilization at the active-site of PfADSS in the ternary complex, 6-pIMP falls off and gets converted into IMP. IMP is again catalyzed to 6-pIMP; the process continues till GTP lasts. Since PfADSS is fully active at room temperature, thus during the time period of UVRR experiment, GTP has already been exhausted. This results in the signature of only IMP in ternary complex. However, upon ligation of the L-Aspartate pocket, I found that in PfADSS also, local conformational changes stabilize 6-pIMP at the active-site for indefinite period of time. In the reverse reaction of

PfADSS, I found that sAMP alone is sufficient to organize the active-site conformation. Active-site interactions and conformation organization in GDP•PfADSS resemble that of GTP•PfADSS. In ternary product complex of PfADSS, sAMP•GDP•PfADSS, no synergism in the binding of sAMP and GDP was observed which means that the release of the products is less controlled in PfADSS as compared to that in MjADSS. Likewise MjADSS, reverse reaction is also observed in fully ligated product complex of PfADSS, which is further corroborated by the RP-HPLC data.

Significance

The work done in this thesis reveals new insights into the extent of ligand distortion during enzyme catalysis. In addition to this, the work also captures extremely subtle local conformational dynamics at the active-site which are integral to catalysis and lowers the activation energy barrier. My work adds significantly to understanding the differential substrate specificity of human and Pf HGPRTs. Using highly sensitive resonance Raman spectroscopy, I found that the hydrogen bonding network and stacking interactions are more rigid at the active-site of hHGPRT. The work also establishes the importance of using vibrational technique to capture the enzyme-induced distortions which typically lie at sub-angstrom level and are indistinguishable in other biophysical techniques.

In case of ADSS, I found that the two homologues of the same enzyme catalyzing same reaction employ different mechanistics. The work done in this thesis not only quantifies different distortions at each step of a complex kinetic mechanism but also shows how allostery regulates these distortions. My work highlights the importance of using UVRR to study the complexes of enzyme with intermediates and distorted species which are transient and cannot be captured separately in solution-state. In the absence of availability of crystal structures at each kinetic step of ADSS, the results obtained from the present study provide insights about the conformational re-organization driven by the binding of each individual ligand. The work shows that UVRR holds a

lot of promise in studying enzymes which follow complex kinetics and bind to many substrates.

"And what can life be worth if the first rehearsal for life is life itself?"

Milan Kundera

I

Introduction

1.1 Structural and functional aspects of enzymes

Enzymes lie at the heart of all biochemical processes and facilitate enormous rate acceleration with extraordinary specificity. Conversion of substrates to products in biochemical processes depends on the mechanism of action of the underlying enzymes. Most of these enzymes are highly specific to their substrates and the reactions they catalyze. This extraordinary specificity of enzymes provides them with the remarkable prowess to lower the activation barrier selectively. This results in rate enhancements in the range of 7 to 15 orders of magnitude faster than their uncatalyzed counterparts [23].

In a catalytic process, substrate molecules react to form products and in doing so pass through a highly distorted state called transition-state (TS). Figure 1.1 shows changes in the free energy of proton transfer from a water molecule to a chloride ion and is plotted against the progress of the reaction (reaction coordinate). The starting point of the reaction (either forward or reverse) is called the ground state (GS). The highest energy species on this plot is termed as the transition-state. Intermediates, on the other hand, occur in the multi-step reactions of metabolic pathways. These intermediates are transient species with relatively longer life-times (10^{-13} to 10^{-3} s) and are subsequently consumed to generate the final products. In order for the reaction to proceed, the ground state must overcome a free energy barrier, termed as

the activation energy ($\Delta G^{\dagger}$) and reach the transition state. Smaller the value of $\Delta G^{\dagger}$, faster will be the rate of the reaction.

1.1.1 Hammond's Postulate

A clear structure-reactivity relationship between the TS and the intermediate is established by Hammond's postulate, which states that the structure of an unstable intermediate along the reaction coordinate resembles the structure of the TS [37]. This hypothesis provides a useful way of predicting the structure of highly unstable TS which can otherwise he a technically challenging task.

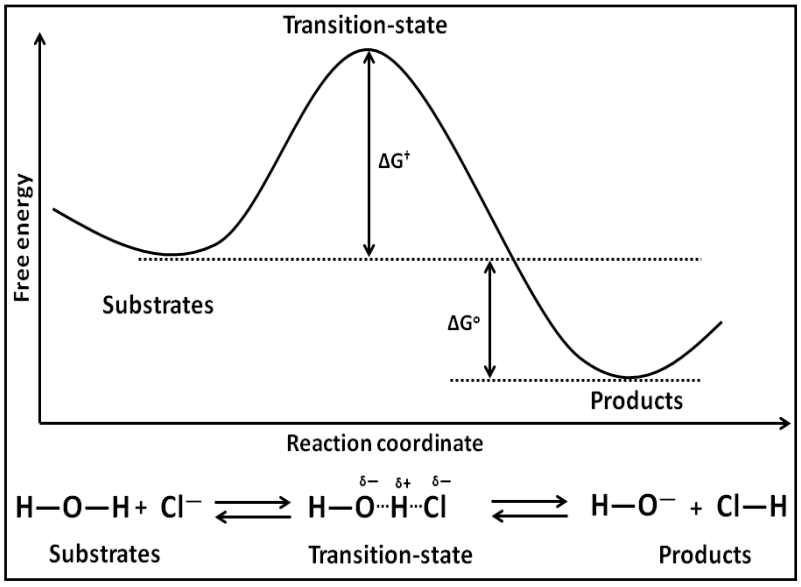

Figure 1.1: Hypothetical free energy profile depicting the transfer of proton from water molecule to the chloride ion. The partially formed bond between a water molecule and chloride ion represents the transition-state. $\Delta G^{\dagger}$ is the free energy of activation and $\Delta G°$ is the difference in the free energy between the substrates and products.

1.2 Strategies employed by enzymes during catalysis

Several strategies for barrier reduction and consequent rate acceleration have been proposed and observed [1, 2, 38-40]. In the following, I shall discuss these strategies one after the other.

1.2.1 Transition-state stabilization

Linus Pauling first proposed his seminal hypothesis that enzymes lower the activation energy barrier by binding the TS more tightly than the GS and in doing so they stabilize the TS of the reaction [3]. This is the most widely accepted proposal to explain the general mechanism of enzyme function and is

known as transition-state stabilization (TSS). This proposal suggests that the enzyme orients the substrates with respect to one-another in a reactive conformation. Complementarity in polarity, electrostatic charges and geometry between the enzyme active-site and TS renders the non-covalent interactions between them to be more favourable and thereby stabilizes the TS. This implies that the active-site geometry is not complementary to the GS structure of substrate but rather, it is complementary to the substrate molecule in a distorted geometry, such as the geometry expected to be formed in the TS.

Enzyme•substrate (E•S) is the Michaelis complex which is stabilized due to the formation of non-covalent interactions between the enzyme and substrate. It is important to note that equally stabilizing both E•S and E•$X^{\dagger}$ (enzyme•TS) would not result in rate enhancement because the activation energy barrier would remain the same as that of their uncatalyzed counterpart (Figure 1.2). However, a pre-requisite for enzyme catalysis is differential stabilization of TS with respect to GS. Introducing complementary amino-acid residues at the active-site of enzyme which can form interactions with this species can selectively stabilize the TS with respect to GS.

1.2.2 Intrinsic binding energy

Formation of weak non-covalent interactions between the substrate molecule and the active-site residues of an enzyme is accompanied by the release of free energy. Such energy provides stabilization to the E•S complex and is termed as the intrinsic binding energy (ΔG_b). Weak non-covalent interactions like hydrogen bond, hydrophobic, ionic and van der Waals interactions account for the binding enthalpy. This favourable enthalpy is the result of substrate binding to the enzyme active-site and compensates the entropy loss due to the formation of the E•S complex.

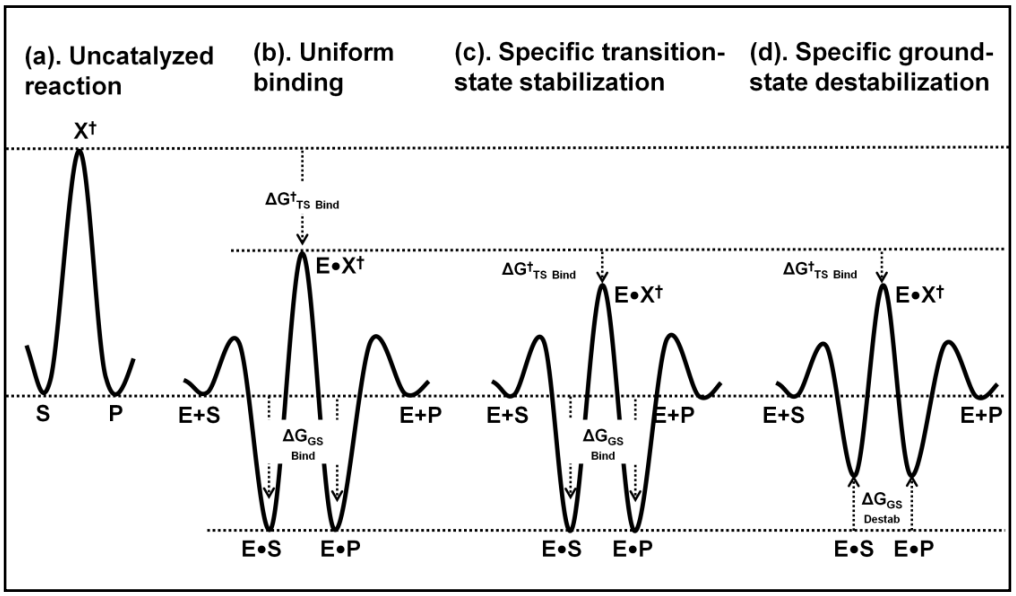

Figure 1.2: Hypothetical free energy profiles illustrating the role of transition-state stabilization and ground-state destabilization in enzyme catalysis. Hypothetical free energy profile illustrating (a) an uncatalyzed reaction, (b) equal stabilization of ground-state and transition-state, (c) preferential stabilization of transition-state over ground-state, and (d) preferential destabilization of ground-state in addition to stabilization of transition-state. Abbreviations; E: enzyme, S: substrate, P: product, X†: transition-state, $\Delta G_{TS\ Bind}$ is the change in free energy arising from the specific interaction with the transition-state, $\Delta G_{GS\ Bind}$ is the intrinsic binding energy, $\Delta G_{GS\ Destab}$ is the change in the free energy resulting from destabilization of ground-state. ***Adapted from Andrews et al., Plos Biology, 11, 2013 ref. [6].***

1.2.3 Ground-state destabilization

Another strategy employed by enzymes during catalysis is ground-state destabilization (GSD). As illustrated in Figure 1.2 (d), E•S complex is destabilized with respect to Figure 1.2 (b,c). The energy of E•S complex is raised by the distortion caused due to non-covalent interactions formed at the active-site of enzyme. This may also happen due to the entropy loss at the active-site, desolvation of substrate molecules and electrostatic effects. Jencks first proposed that combining substrate molecules at the active-site of an enzyme results in the loss of translational, rotational and vibrational degrees of freedom. This phenomenon raises the rate of the enzyme-catalysed reaction by a factor of 10^8 [24].

A charged substrate is solvated by water molecules and is thus stabilized in solution. When such substrate is moved from solution to the enzyme active-

site, its water of solvation is replaced by weak non-covalent interactions at the active-site. This raises the energy of charged substrate molecules resulting in a more reactive species.

Further, it may also happen that at the active-site, the charge of the substrate molecule is placed next to a similarly charged residue of the active-site. This leads to the repulsion between the two and is the basis for electrostatic destabilization. Orotidine-5'-monophosphate (OMP) decarboxylase employs a similar strategy to catalyze the formation of uridine-5'-monophosphate from OMP. This contributes to a rate enhancement which is 17 orders of magnitude faster when compared with the uncatalyzed reaction [41].

1.2.4 Formation of near attack conformers (NAC)

NACs are the ground-state structures of the E•S complex which resemble the transition-state in terms of orientation of the substrate molecule and the active-site residues. The relative contribution of each to the overall free energy and catalysis is dependent on the specific system being examined. Several studies by Bruice and co-workers have demonstrated the presence of NAC [39, 42-48]. Other studies using computer simulations by Warshel and co-workers emphasize the crucial role of electrostatic interactions to catalysis [49-53]. Such interactions formed between the substrate and active-site residues lead to pre-organization of the active-site which in turn stabilizes the TS.

1.2.5 Role of protein dynamics in enzyme catalysis

Accumulating data implicates the role of protein dynamics in substrate binding, product release and fast chemical conversion. Based on the time-scales of each of the various motions, protein dynamics can be divided into:

- Rotation of medium-sized side chains in the protein interior (micro-milli second).
- Hinge bending at the domain interfaces (100 pico sec- 10 nano sec).

- Bond vibrations (10-100 femto sec).

These motions have been shown to play a role in catalysis by either pre-organizing the active-site or by promoting vibrations which lead to chemical barrier crossing [54, 55].

In general, enzyme catalysis is a combined effect of all the above mentioned phenomena. Further, comprehending these effects is fundamentally important to deduce the catalytic mechanism and also to design effective analogues against enzymes. In my thesis, I have deduced the extent of ground-state distortion in enzyme•ligand complexes. I have also captured the extremely subtle local conformational dynamics in enzymes upon binding to ligands.

1.3 Understanding the kinetic mechanism of enzyme catalyzed reactions

Most of the enzyme catalyzed reactions involve two or more substrates. Such reactions result in the transfer of an atom or a group from one substrate molecule to another and occur at the active-site of the enzyme. Consider a hypothetical reaction in which an enzyme E reacts with two substrates, A and B and generates two products, P and Q. In such a mechanism, the order of substrate binding is regulated in the following manner [23]:

Sequential: Here, both the substrate molecules are bound to the active-site which results in the formation of a ternary complex (EAB). This further leads to the formation and release of product, but the fomation of EAB can take place in two ways:

Random: either of the substrate molecules can bind first, followed by the binding of the next substrate, example: adenylosuccinate synthetase (Scheme 1).

Scheme 1

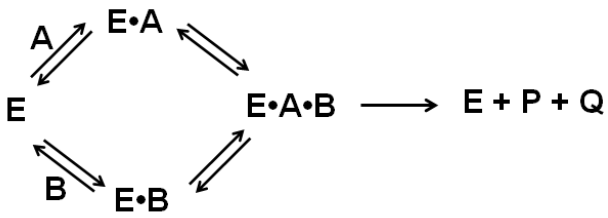

Ordered: Substrate 'A' must bind the enzyme first and then only can the substrate 'B' bind, example: hypoxanthine guanine phosphoribosyltransferase (Scheme 2).

Scheme 2

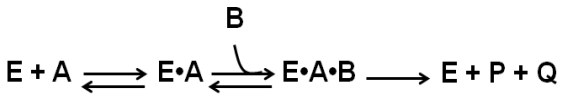

Ping-pong: In another possibility, substrate A reacts with enzyme and covalently modifies it (E′). In the next step, modified 'A' leaves the active-site followed by the binding of 'B' to the modified enzyme. The major difference between sequential and ping-pong mechanism is that there is no formation of ternary complex in the ping-pong mechanism (Scheme 3).

Scheme 3

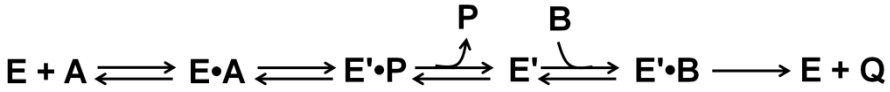

1.4 Purine salvage pathway

Nucleotide synthesis takes place by two pathways viz. *de novo* and salvage pathways. *De novo* pathway, which begins with metabolic precursors aspartate, ribose-5'-monophosphate, CO_2 and NH_3, takes place in almost all organisms. On the other hand, only few organisms can exploit the salvage pathway for the formation of nucleotides. Here, nucleobases and nucleosides which are generated from nucleic-acid breakdown are recycled to nucleotides. Humans can utilize both pathways, but parasitic protozoa like *Plasmodium*,

Tritrichomonas, *Leshmania* and *Trypanosoma* lack the *de novo* pathway and depend solely on salvaging the nucleobases and nucleosides from their hosts [28].

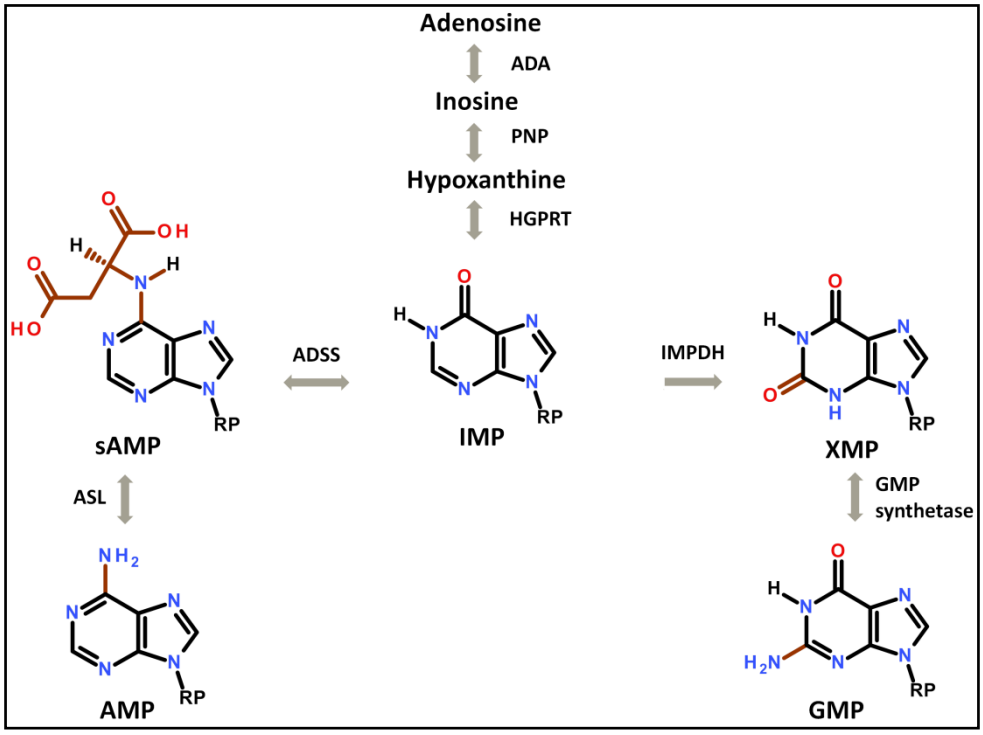

Figure 1.3: Schematic illustration of purine salvage pathway. Abbreviations; ADA: adenosine deaminase, PNP: purine nucleoside phosphorylase, HGPRT: hypoxanthine guanine phosphoribosyltransferase, ADSS: adenylosuccinate synthetase, IMP: inosine-5'-monophosphate, IMPDH: IMP dehydrogenase, ASL: adenylosuccinate lyase, AMP: adenosine-5'-monophosphate, sAMP: succinyl AMP, XMP: xanthosine-5'-monophosphate, GMP: guanosine-5'-monophosphate. RP: ribose-5'-monophosphate

The ability of parasites to develop resistance against existing drugs has led to the need for identification of new drug targets. The enzymes of purine salvage pathways are potential therapeutic targets against such parasites. In this regard, purine nucleoside phosphorylase (PNP) has been studied in great detail by Schramm and co-workers [56-61]. However, other enzymes of the pathway such as adenosine deaminase, hypoxanthine guanine phosphoribosyltransferase (HGPRT) and adenylosuccinate synthetase (ADSS) have been less explored (Figure 1.3). Further, targeting a single enzyme in this pathway may not prove useful as mutations can provide parasites with the

ability to develop resistance against existing drugs. The activities of the enzymes present in these parasites suggest that a combination of inhibitors may be required to effectively inhibit their growth. Simultaneously, targeting two different enzymes of the pathway, HGPRT and ADSS, would improve our ability to combat these parasites. In this regard, developemt of inhibitors depends on the availability of structural information on the active-site interactions of E•S complexes. During the work presented in this thesis, I have investigated the enzyme•ligand complexes of HGPRT and ADSS and thus in the following sections, the structure, function and dynamics of these two enzymes are discussed.

1.5 HGPRT: a multi-substrate binding enzyme

HGPRT (EC 2.4.2.8) catalyzes the formation of 6-oxopurine mononucleotides by transferring the phosphoribosyl moiety to N9 position of a purine nucleobase (hypoxanthine or guanine) (Figure 1.4). It is a Mg^{2+} dependent reversible reaction in which the phosphoribosyl moiety is donated by α-D-5-phosphoribosyl-1-pyrophophate (PRPP). The ratio of Mg^{2+} to PRPP is known to influence the rate of catalysis [62]. The reaction proceeds in a sequential and ordered fashion where, PRPP binds first followed by the binding of the nucleobase. This leads to the formation of a transient ternary complex where the rapid phosphoribosyl transfer reaction takes place. After catalysis, nucleotide leaves the active-site first followed by the release of PPi [29].

HGPRT has been characterized in various organisms including human, several bacteria, protozoa parasites, and HeLa cells [63] [Figure 1.5]. In humans, HGPRT exists as a soluble cytoplasmic enzyme in all cells, but in low levels. However, significantly higher levels are detected in nervous tissue, erythrocytes, platelets and bone marrow tissue [64-67]. HPRT, the gene responsible for the expression of HGPRT, is 44 kilo base pairs long and has been mapped onto the X-chromosome in humans [68]. Apart from its potential to act as a chemo-therapeutic target against protozoan parasites, HGPRT has

been exploited in many other *in vitro* techniques. A medium containing hypoxanthine, aminopterin and thymidine called HAT medium exclusively selects $HPRT^+$ cells from the culture. In this medium, hypoxanthine acts as purine source and is thus a substrate for HPRT, aminopterin acts as an inhibitor for dihydrofolate reductase and thymidine serves as a substrate for thymidine kinase. Development of this medium revolutionized the field of hybridoma fusion and somatic cell hybrid techniques [69, 70].

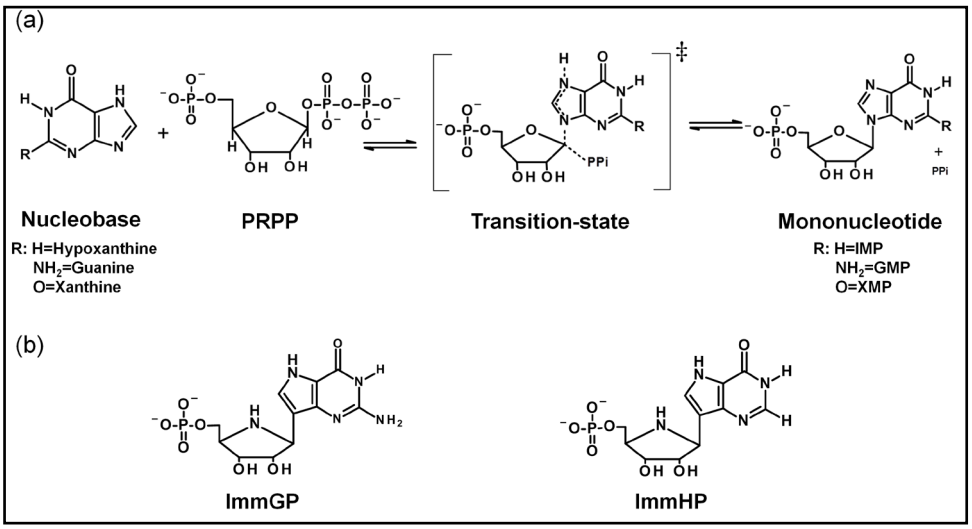

Figure 1.4: Reaction scheme of HGPRT and chemical structures of TS analogues. (a) Schematic representation of reaction catalyzed by HGPRT. Glycosidic bond formation between N9 of nucleobase and C1' of PRPP leads to the formation of product at the active-site of HGPRT. (b) ImmGP and ImmHP are TS analogues of HGPRT.

HGPRT is one of the 10 phosphoribosyltransferases (PRTases) that are essential for the biosynthesis of nucleotides, purine, pyrimidine and pyridine as well as the aromatic amino-acids like histidine and tryptophan [63]. These PRTases are highly specific for a nitrogen nucleophile and PRPP. Thus, a sequence of 12 amino-acid residues present in these PRTases common to PRPP synthetases is regarded as the PRPP binding motif [71-73]. During my PhD, I have worked on two HGPRT homologues viz. human and *P. falciparum* and thus I will discuss these enzymes in detail in the following section.

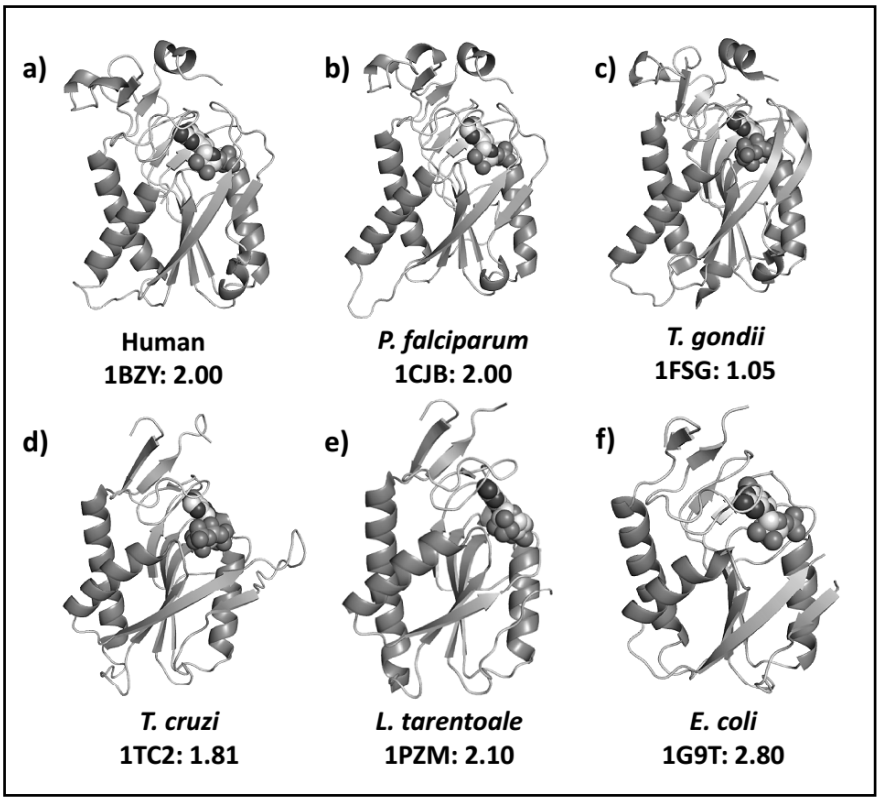

Figure 1.5: Structures of HGPRT from different organisms. PDB accession codes with resolution (Å) are mentioned.

1.5.1 Structure of human HGPRT monomer

HGPRT exists as tetramer in solution under physiological conditions. However, depending on the ionic strength and pH, a mixture of dimer and tetramer can also exist. Figure 1.6 (a) shows the structure of a tetramer of HGPRT in complex with a transition-state analogue (1S)-1-(9-deazaguanin-9-yl)-1,4-dideoxy-1,4-imino-D-ribitol 5-phosphate (ImmucillinGP or ImmGP). Each monomer unit of hHGPRT consists of 217 amino-acids and has a molecular weight of 24470 Da [72]. X-ray crystallography reveals that a single subunit of HGPRT is made up of 10 β strands and 6 α helices [74]. The entire structure is divided into a larger core and a smaller hood domain. Further, the core domain is divided into a larger sub-domain containing 5 parallel twisted β sheets flanked by 2 α helices on either side. The smaller core sub-domain is oriented perpendicular to the larger one. Here, 2 anti-parallel strands corresponding toresidues 100-117 constitute the catalytic-loop or flexible-loop (Figure 1.6 (b)). This loop undergoes a conformational change of 25 Å to

cover substrates and thereby sequester the transition-state during catalysis. The hood domain is made up of a 4 stranded anti-parallel β sheet and forms a minor part of the monomeric structure.

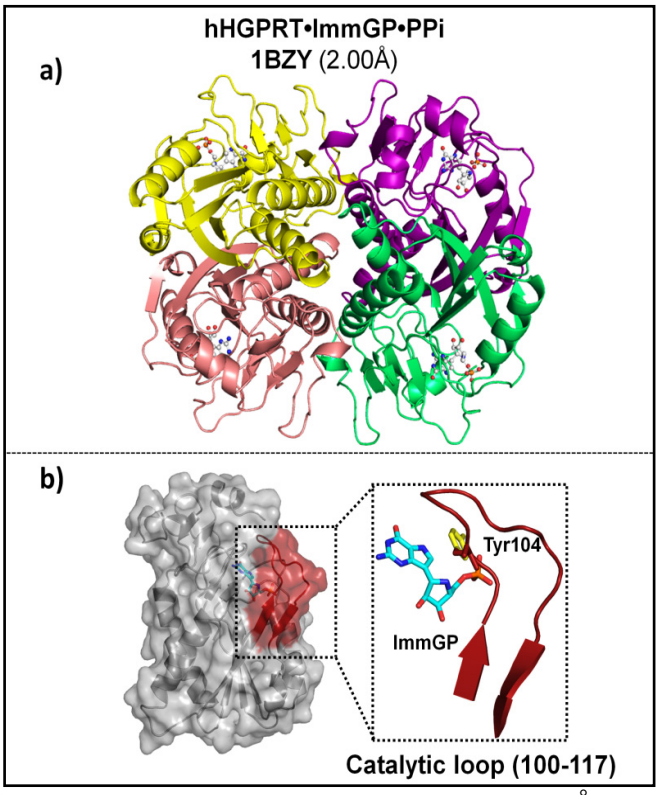

Figure 1.6: Crystal structure of hHGPRT (1BZY: 2.0 Å) complexed with transition-state analogue, ImmGP. (a) tetramer of hHGPRT, (b) surface view of HGPRT monomer unit. Inset shows the catalytic loop (residues 100-117) sequestering the active-site of the enzyme.

1.5.2 Comparison between human and Pf enzymes

PfHGPRT differs from hHGPRT as it possesses 230 amino-acid residues (*Mr* 26229 Da) (Figure 1.7 and Figure 1.8) [75]. Biochemical studies have shown that PfHGPRT can bind to PRPP in the absence of Mg^{2+}, hHGPRT recognizes the PRPP-Mg^{2+} complex only [75]. Further, kinetic assays suggest that the two enzymes also differ in their catalytic efficiency (Table 1.1). A major difference between human and Pf enzymes lies in their substrate specificity. Although active-sites of human and Pf enzymes show 80% sequence similarity, PfHGPRT exhibits larger substrate promiscuity. In addition to hypoxanthine and guanine, it can also catalyze xanthine to xanthosine-5'-monophosphate (XMP, and is hence termed as HGXPRT).

Interestingly, it has been reported that unlike hHGPRT, *Pf*HGPRT can catalyze several other nucleobases such as allopurinol, 6-thioxanthine, 6-chloroguanine, 8-azahypoxanthine and 8-azaguanine, under *in vitro* conditions [30]. Structural and computational studies suggest that the difference in the specificity is due to the greater flexibility in the base binding region of PfHGPRT [9, 31, 76-84].

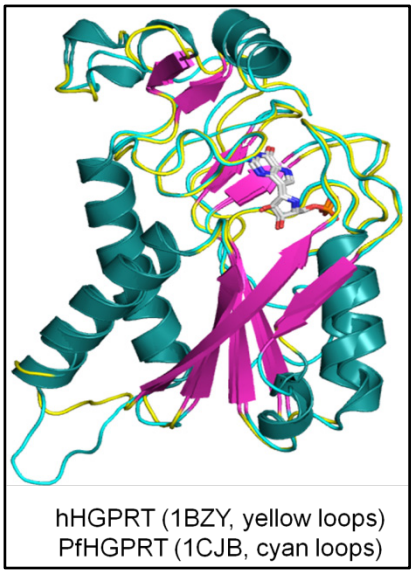

Figure 1.7: The overlay of crystal structures from human and Pf HGPRTs.

Table 1.1: Comparison of kinetic constants of HGPRT from human, *Plasmodium falciparum*, *Trypanosoma cruzi* and *Leshmania donovanii*.

Enzyme	Hypoxanthine		Guanine		Xanthine	
	k_{cat} (s^{-1})	K_m (μM)	k_{cat} (s^{-1})	K_m (μM)	k_{cat} (s^{-1})	K_m (μM)
human[a]	7.1	1.4	25.5	4.5	0.007	-
P. falciparum[b]	1.13	<1.0	1.2	<1	2.9	261
T. cruzi[c]	22.9	8.6	32.2	12.4	-	-
L. donovanii[d]	5.7	6.4	12.1	10	-	-

[a]values are taken from ref. [29]. [b]values are taken from ref. [31]. [c]values are taken from ref. [85]. [d]values are taken from ref. [86].

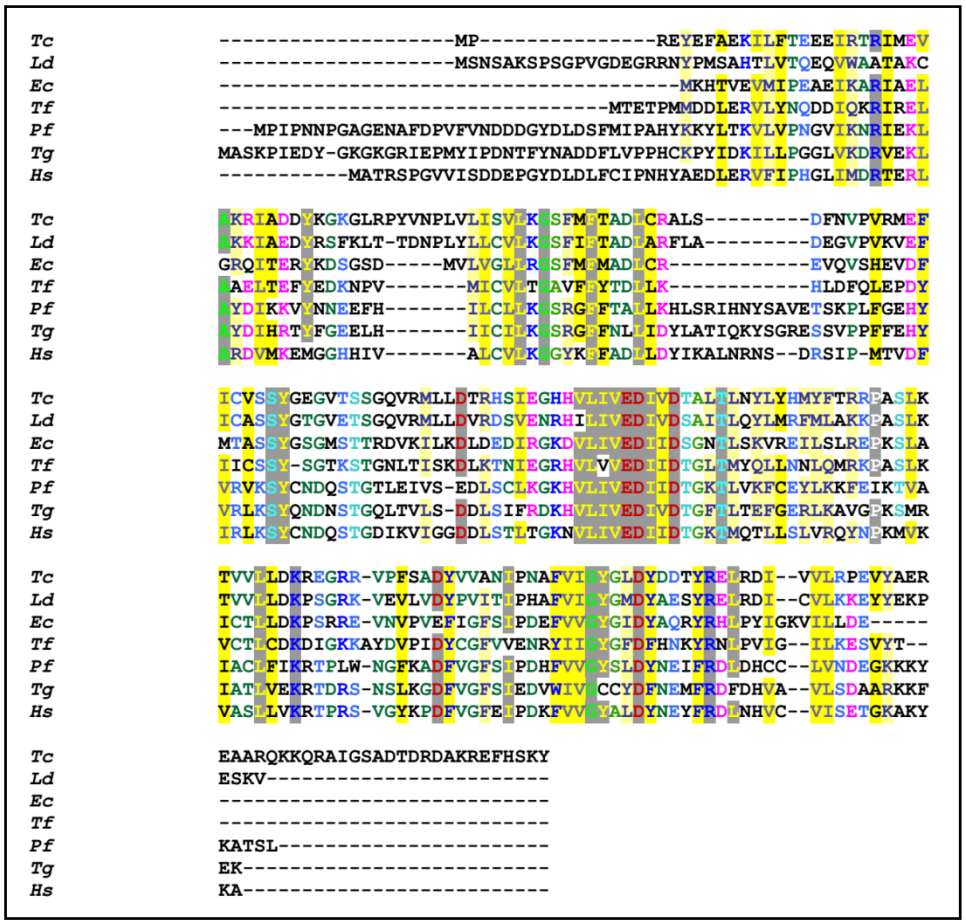

Figure 1.8: Multiple sequence alignment of HGPRT homologues from *Trypanosoma cruzi* (*Tc*), *Leshmania donovanii* (*Ld*), *E. coli* (*Ec*), *Tritrichomonas foetus* (*Tf*), *Plasmodium falciparum* (*Pf*), *Toxoplasma gondii* (*Tg*) and human (*Hs*). Conserved residues are shaded in grey. The alignment was carried out using ClustalW and coloured by using the software CHROMA [87]. Amino-acids that are conserved across all sequences are highlighted in grey, while the amino-acids highlighted in yellow are conserved only across a few sequences.

1.5.3 Weak non-covalent interactions at the active-site of HGPRT

Extensive structural studies on hHGPRT carried out using a non-reactive hypoxanthine analogue [7-hydroxy [4,3-d] pyrazolo] (HPP), and a transition-state analogue like ImmGP to product complexes predict that weak non-covalent interactions may be the driving force for the phosphoribosyltransferase reaction. Structure of hHGPRT co-crystallized with ImmGP shows that the TS analogue binds between the β sheets of core and hood domains[88]. Exocyclic O6 of guanine moiety forms a hydrogen bond with back-bone amide of Val187 and side-chain of Lys165 (Figure 1.9 (a)). Exocyclic —NH_2 interacts with the back-bone amide of Asp193 and the side-

chain of Val185. N1—H interacts with the side-chain carbonyl of Val187. Further, Phe186 is found to stack over the nucleobase in all HGPRT complexes. The closeness between residue Asp137 and N7 of the nucleobase suggests the role of Asp 137 as the catalytic residue. Mutational studies prove the role of Asp137 as a catalytic base and catalytic acid in the forward and reverse reactions, respectively [89]. Apart from the interactions which are mentioned in the TS complex, hHGPRT•HPP structure predicts interactions that result from the difference in electronic distribution in HPP due to the presence of Nitrogen at the 8th position [9]. These interactions vary at a critical N7 and C6=O position. Here, Lys165 forms a hydrogen bond with N7 of HPP instead of C6=O, and Asp137 interacts with N8 instead of N7 (Figure 1.9 (b)).

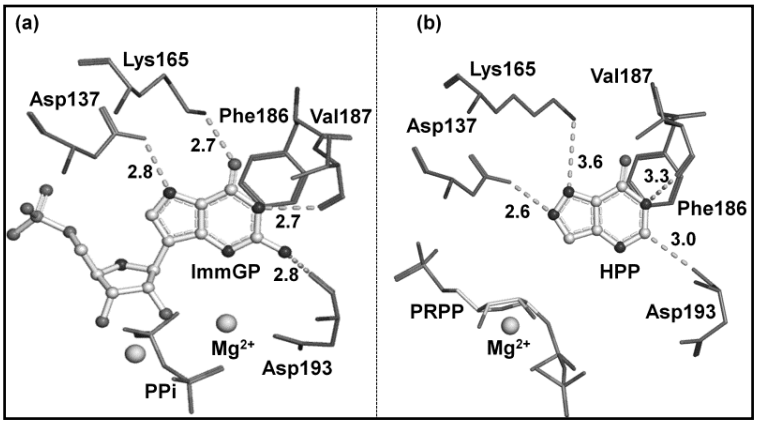

Figure 1.9: Hydrogen bonding network of hHGPRT. Active-site interactions of hHGPRT with (a) a TS analogue, ImmGP (PDB ID: 1BZY) and (b) a substrate analogue, HPP (PDB ID: 1D6N).

Residues 100-117 constitute the catalytic-loop which closes onto the active-site and sequesters it from bulk solvent. Stopped-flow fluorescence experiments with Y74W mutant of *Tritrichomonas foetus* HGXPRT reported conformational changes in the flexible loop during HGPRT catalyzed reaction [81]. However, in hHGPRT•GMP complex, the catalytic-loop is disordered and oriented away from the active-site. Interestingly, a similar disordered loop is also reported in different PRTases bound to product complexes, which may be an essential step to facilitate the easy release of product from the active-site [90].

A detailed knowledge of the active-site interactions in human and *Pf* HGPRTs is a pre-requisite for designing potent drug molecules against this

enzyme. Subsequent structural studies on PfHGPRT reveal that the hydrogen bonding network is identical in the two homologues in terms of amino-acid residues [31, 91]. Two different structures of PfHGPRT, co-crystallized with (1S)-1-(9-deazahypoxanthin-9-yl)-1,4-dideoxy-1,4-imino-D-ribitol 5-phosphate (ImmucillinHP or ImmHP) and S-SerMe-ImmH phosphonate, respectively, resemble the TS of PRTase reaction [91]. Another structure with Hx and PPi does not lie on the catalytic path and resembles the dead-end complex (HGPRT•Hx•PPi) of the reaction (3OZF) (Figure 1.10). Further, structural studies show marked variations in B-factors (temperature-factors, indicates dynamic nature of an atom or group of atoms) among the two homologues. While average protein and ligand B-factor ($Å^2$) in PfHGPRT (1CJB: 2 Å) is 30.6 and 24.2, respectively, it is 16.9 and 12.9, respectively in hHGPRT (1BZY: 2 Å). Larger B-factors in PfHGPRT suggests that is has greater flexibility than hHGPRT [31].

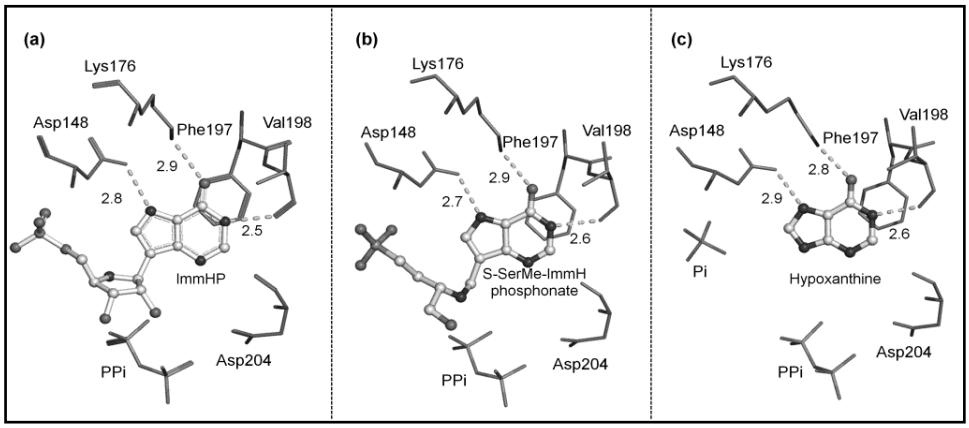

Figure 1.10: Active-site organization of PfHGPRT with (a) TS analogue ImmHP (1CJB), (b) derivative of TS analogue, S-SerMe-ImmH phosphonate (3OZF), and (c) Hx (3OZF).

Further, the enzymes of purine salvage pathway have been proposed as potential therapeutic targets for a very long time [92]. But, lack of proper structural differentiation between human and Pf enzymes has prevented the exploitation of HGPRT as a drug target against the malaria parasite.

1.6 ADSS: an enzyme common to the *de novo* and salvage pathways

Adenylosuccinate synthetase (ADSS, EC 6.3.4.4) catalyzes the Mg^{2+} dependent condensation of a molecule of IMP with L-Aspartate to form

succinyl adenosine-5′-monophosphate (sAMP), in a reaction coupled with the hydrolysis of guanosine-5'-triphosphate (GTP) to guanosine-5'-diphosphate (GDP) (Figure 1.11). The catalytic mechanism of ADSS is a two step process [93] (Figure 1.12); the first step is a phosphoryl transfer reaction where, Asp43 (mouse muscle ADSS numbering is used unless otherwise specified) acts as a catalytic base and abstracts a proton from N1—H of IMP leading to the formation of 6-oxy anionic IMP. His71, on the other hand, provides a proton from its ND1 position to the leaving β-phosphate group of GDP. The γ-phosphate group of GTP is transferred to the 6-oxo position of IMP resulting in the formation of an intermediate 6-phosphoryl IMP (6-pIMP). This involves the first TS of the reaction. The second step is the phosphoryl displacement reaction where, the nucleophilic displacement of 6-phosphoryl group by L-Aspartate takes place to form sAMP. In this step, Asp43 and His71 both act as catalytic acids. His71, donates a proton from NE2 position to the 6-phosphoryl group, leading to its expulsion. At the same time, Asp43 returns a proton to the N1 position of the nucleotide which likely results in the resonance stabilization of C6 carbonium ion. This leads to the nucleophilic attack of L-Aspartate at the C6 position thereby leading to the formation of sAMP. In this catalytic mechanism, Mg^{2+} coordinates with α and β phosphoryl group of GDP, oxygen atom of 6-phosphoryl group, L-Aspartate and Gly70. Thus Mg^{2+} ion helps the assemble the reactants to facilitate the final catalytic step [94].

The kinetic mechanisms of ADSS from most organisms has been found to be rapid equilibrium random and ordered where, IMP and GTP bind randomly to the enzyme and L-Aspartate binds to the preformed ternary complex (ADSS•IMP•GTP) [33]. Release of the product follows a similar pattern where Pi leaves the active-site first followed by the random release of sAMP and GDP. So far, the only homologue of ADSS which shows ordered binding mechanism is *Plasmodium falciparum* adenylosuccinate synthetase (PfADSS) [33]. A crystal structure of PfADSS reports the conformational dynamics resulting from the binding of one ligand which in turn reorganizes the binding-site for the other and thus leads to the ordered binding mechanism [95]

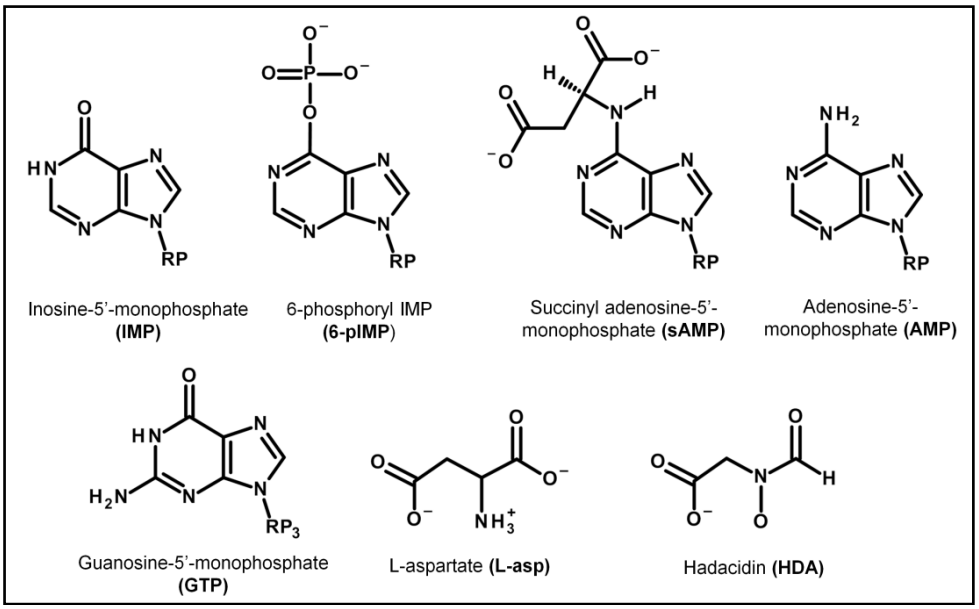

Figure 1.11: Chemical structures of the ligands of ADSS.

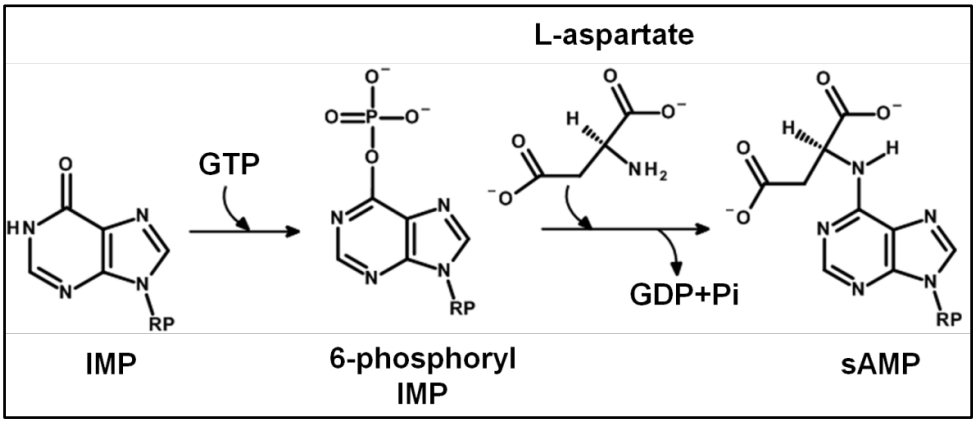

Figure 1.12: Reaction scheme of ADSS. RP: ribose-5′-monophosphate.

ADSS is part of purine nucleotide cycle in case of vertebrates while in all other organisms, it is a part of the *de novo* synthesis. Because of its importance in the biosynthesis of AMP, the enzyme is known to present in all forms of life except in red blood cells. This synthetase has been isolated from various organisms such as *E. coli*, *Saccharomyces cerevisiae*, *Arabidopsis thaliana*, *Plasmodium falciparum*, *Leshmania donovanii*, mouse and human. Crystal structures have been determined for a few of them (Figure 1.13). Vertebrates are reported to have two forms of ADSS: basic (pI 8.9) and acidic (pI 5.9) [96]. The basic form is mostly confined to the cells of muscles and takes part in both the *de novo* and the salvage pathway, whereas the acidic form is part of the *de novo* pathway only [97, 98]. The two forms of ADSS in

mouse have 75% amino acid sequence similarity. These forms also differ with respect to the action of inhibitors like AMP and fructose-1,6-biphosphate (FBP). AMP inhibits the acidic form to a larger extent than the basic form and vice-versa for FBP [99].

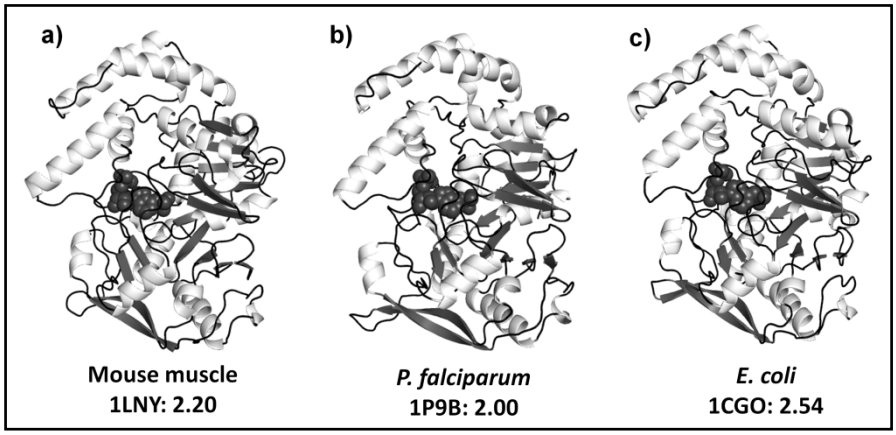

Figure 1.13: Structures of ADSS. a) mouse muscle, b) *P. falciparum* and, c) *E.coli*. PDB accession codes and resolution (Å) are also mentioned.

ADSS commits IMP to the first step of AMP formation and thereby maintains the ratio of AMP to GMP in a cell. Because of its critical role in the nucleotide synthesis pathway, ADSS has been regarded as an important drug target against leukemia [96]. Further, the enzyme has been exploited as a target for various antibiotics and herbicides [100].

1.6.1 Catalytically important residues in ADSS

Preponderance of biochemical data suggests that ADSS can tolerate a few modifications at the ribose moiety of IMP. The fact that both 2′-deoxy-IMP and β-D-arabinosyl IMP are the substrates of ADSS shows that the 2' position of IMP does not govern its substrate specificity. Further, binding of IMP to the active-site leads to ligand induced dimerization of ADSS. Assembly of the complete active-site involves hydrogen bonding between the 5′ phosphate group of IMP and Arg of a symmetry related subunit. Thus, a complete active-site in ADSS involves the contribution from two subunits. The mutation of Arg143 to either Leu or Lys increases the K_m of IMP but does not affect k_{cat} [101]. Gln227 interacts with N7 and O6 of IMP. Mutation of Gln227 to glutamate or methionine does not affect the K_m of IMP but decreases the k_{cat} by a factor of 10^{-3} and 10^{-2}, respectively [102]. Asp13 acts as

a catalytic base and abstracts a proton from N1 position of IMP, and its mutation to Ala results in complete inactivation of the enzyme [103]. His41 and Mg^{2+} interact with the γ and β-phosphate of GTP and increase electrophilicity of the leaving γ-phosphate group. Mutation of His41 to Asn results in a k_{cat} which is approximately 1% of the wild-type enzyme [103].

Interestingly, nucleotides other than GTP have been reported to act as substrates in ADSS catalyzed reactions. For instance, the yeast homologue can utilize ATP, 2′-dGTP and dd-GTP as an analogue of GTP [104]. Similarly, EcADSS can exploit ITP, XTP and UTP in the place of GTP [105]. Apart from Mg^{2+} the other metal cations which are known to occupy the binding site are Ba^{2+}, Ca^{2+}, Mn^{2+}, and Ca^{2+} [106]. ADSS is reported to utilize hydroxylamine as a substrate in place of L-Aspartate as well [93].

Hadacidin (HDA: N-formyl N-hydroxylamine) is a potent competitive inhibitor of L-Aspartate with a K_i value of 10^{-6} M [107, 108]. Electron density map in several crystal structures suggests that HDA occupies the site of L-Aspartate. The carboxylate group of HDA is equivalent to the β-carboxylate group of L-Aspartate and hydrogen bonds with the backbone amide of Arg303 and OG1 of Thr301. Also, the N-formyl group of HDA corresponds to one oxygen atom of an α-carboxylate group and coordinates with Mg^{2+}, whereas the N-hydroxyl group corresponds to the other oxygen atom of the α-carboxylate group and interacts with Arg305 and Asp13. Further, there is no equivalent group to the α-amino of L-Aspartate in HDA. In L-Aspartate, there is an unfavourable steric hindrance between the α-amino group and base of IMP which is not possible in HDA. In addition to this, N-hydroxyl group of HDA forms a stable hydrogen bond with Asp13 which is the crucial reason for the potent inhibition by this analogue [93, 109, 110].

1.6.2 Mechanistic details of ADSS catalysis

Detailed pre-steady-state and steady-state kinetic measurements have led to the origin of a mechanistic proposal for ADSS catalysis. Lieberman (1956) first proposed the formation of 6-pIMP as an intermediate in the catalytic mechanism of ADSS [111]. He investigated the reaction mechanism with the

help of 6[^{18}O] IMP and reported the formation of [^{18}O] labeled Pi (Table 1.3). In 1962, Miller and Buchanan proposed a concerted mechanism where simultaneous attack of L-Aspartate at C6 position of IMP and release of oxyanion to gamma-phosphate of GTP was proposed [112]. This mechanism was proposed to involve simultaneous bond-breaking and bond-making steps. Later in 1975, Markham and Reed proposed, on the basis of pre-steady state and steady state kinetic experiments, that L-Aspartate adds onto the C6 position of IMP which leads to the formation of a tetrahedral intermediate [113]. Subsequently, C6-oxyanion is phosphorylated by GTP. These proposals were subsequently investigated using variety of methods. Bass et al. using the technique of positional isotope exchange reported scrambling between ^{18}O at β, γ- bridging position of GTP and the non-bridging position of a β-phosphate only in presence of IMP and ADSS [114]. Such exchange is possible only when the γ-phosphate of GTP dissociates from it for a time interval which is long enough for the rotational isomerisation to occur at the β-phosphate group. Further, the fact that the exchange occurs only when IMP is present in reaction mixture suggests that 6-pIMP forms as an intermediate in the catalytic pathway of ADSS which is in support of Lieberman's proposal. Most importantly, this experiment excludes the other two proposed mechanisms [112, 113].

Table 1.2: Major proposals explaining the mechanistic details of ADSS catalyzed reaction.

Scientist (year)	**Lieberman (1956)**	**Miller and Buchanan (1962)**	**Markham and Reed (1975)**
Technique	Use of 6[^{18}O] IMP	Aresenolysis and phosphorolysis in reverse reaction	Pre-steady state and steady-state kinetics
6-pIMP Intermediate	Yes	No	No
Mechanism	Sequential	Concerted	Concerted

In my PhD work, I have compared the structure and function of ADSS from thermophilic archaea, *Methanocaldococcus jannaschii* (Mj) and a mesophilic protozoan parasite *Plasmodium falciparum* (Pf). As a consequence, the following discussion focuses mainly on MjADSS and PfADSS.

1.6.3 Structure of ADSS monomer

Amino-acid sequences from thermophilic archea *M. jannaschii* and *Pyrococcus horikoshii* show 68% sequence identity [32]. X-ray crystal structure of the latter has been solved recently (PDB: 2D7U and PH0438) (Figure 1.14). Due tot the absence of the structure of *M. jannaschii* ADSS, structure of *P. horikoshii* plays an important role in establishing the structure-function relationship in MjADSS.

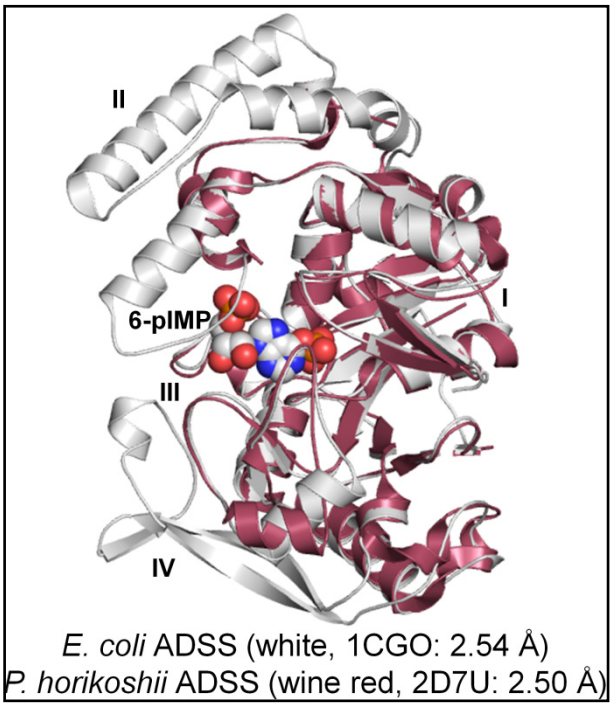

Figure 1.14: Overlay of crystal structures of *E. coli* ADSS ligated to 6-pIMP and apo form of *P. horikoshii* ADSS.

Each monomer of ADSS is divided into four sub-domains termed as I, II, III and IV. While the majority of the residues from sub-domain I, III and IV form the ligand binding site, residues from sub-domain II and α11 to α13 (do not belong to any sub-domain) contribute to the subunit interface. Further, each monomer of MjADSS is 345 amino-acid long (*Mr* 37855 Da) against an average length of 430-457 amino-acids. Apart from MjADSS, this truncated form has been reported in 22 other homologues [32]. Multiple sequence alignment in Figure 1.15 shows two major deletions in the amino-acid sequence of MjADSS. These deletions map to the middle region and C-terminus of the protein i.e. sub-domains II and IV, respectively. While the deleted segments are part of sub-domains involved in ligand binding and

subunit interface, the residues within these deleted segments do not contribute to either of these [32].

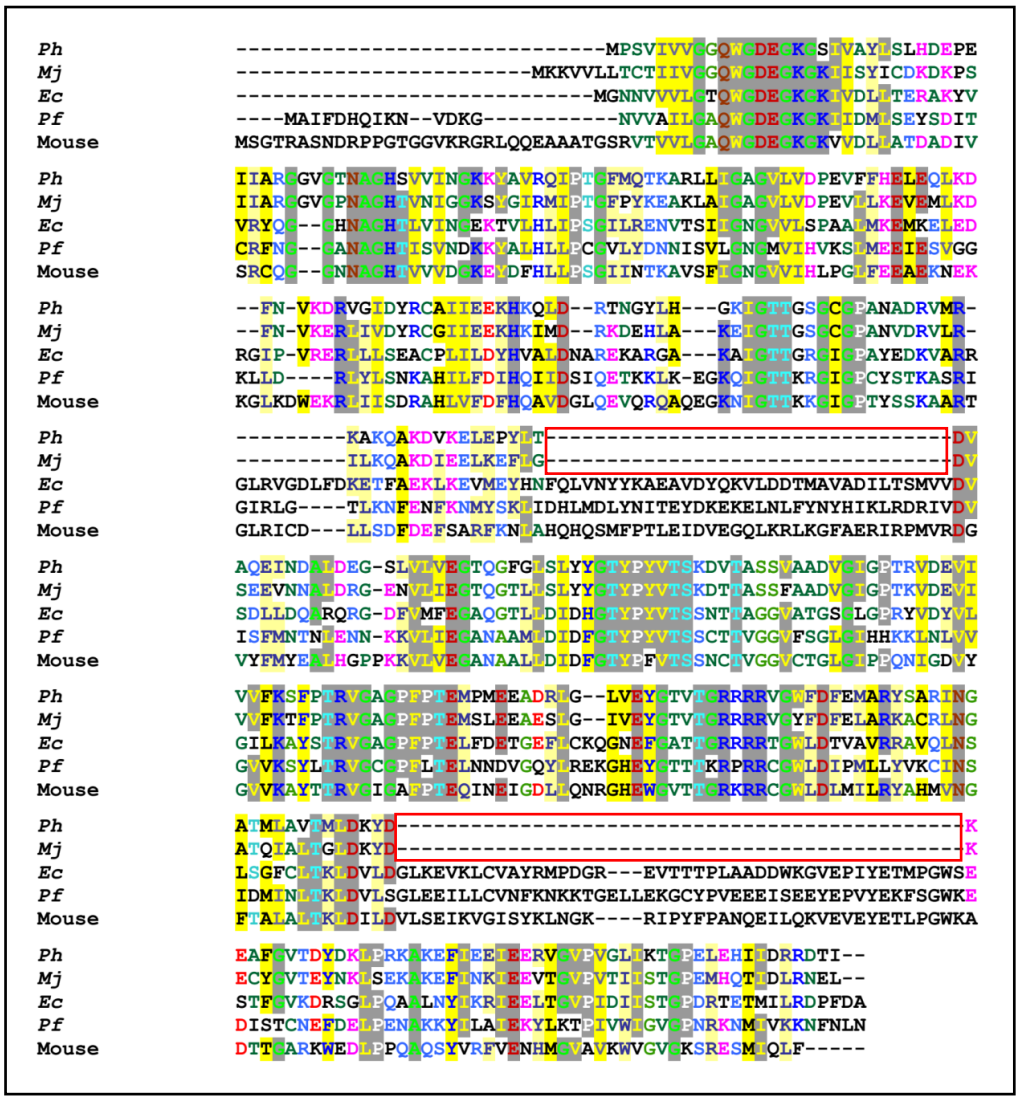

Figure 1.15: Multiple sequence alignment of ADSS homologues from *Pyrococcus horikoshii (Ph)*, *Methanocaldococcus jannaschii (Mj)*, *E. coli (Ec)*, *Plasmodium falciparum (Pf)* and mouse muscle. Deletions in thermophilic ADSS from *Ph* and *Mj* are marked with red box. The alignment was carried out using ClustalW and coloured by using the software CHROMA [87]. Amino-acids that are conserved across all sequences are highlighted in grey, while the amino-acids highlighted in yellow are conserved only across a few sequences.

MjADSS is a thermophilic enzyme which shows continuous increase in activity till 85°C [115]. Interestingly, at 25°C, not only does the enzyme show binding to all substrates but it also leads to the formation of product at a low catalytic-rate (Table 1.3). k_{cat} of the enzyme at 70°C and 25°C is 4.2 s^{-1} and 0.45 s^{-1}, respectively. Kinetic studies on MjADSS revealed that the activation

energy (E_a) is 16.1 kcal/mol in the temperature range from 20 to 40°C and is 7.6 kcal/mol between 40 to 85°C [115]. The study also suggested that the rate of formation of the intermediate, 6-pIMP, in MjADSS catalyzed reaction is same at 70°C and 25°C. Pre-steady state kinetic measurements suggest that the movement of dynamic loops is hindered at ambient temperature which in turn prevents the release of products from the active-site [115]. This study establishes that the release of product is the slowest step in MjADSS catalyzed reaction at ambient temperature. Pre-incubating the enzyme at temperatures varying from 65 to 90°C followed by measurement of activity and structural stability suggested that MjADSS is not a hyperthermophile under *in vitro* conditions [115].

Table 1.3: Comparison of kinetic constants of ADSS from *M. jannaschii*, *P. falciparum*, *E. coli*, mouse (basic and acidic).

	k_{cat} (s^{-1})	K_m (μM)		
Enzyme		IMP	GTP	aspartate
M. jannaschii[a]	4.2±0.1	75.5±4.6	42.6±2.8	1079±74
P. falciparum[b]	1.1±0.03	23±4	18.4±2.0	1800±50
E. coli[c]	1.0±0.05	30±0	26.2±2.3	230 ±40
Mouse (basic)[d]	5.4±0.4	45±7	12±2	140±20
Mouse (acidic)[d]	4.2±0.4	12± 2	15± 2	950±50

[a]values are taken from ref. [32]. [b]values are taken from ref. [33]. [c]values are taken from ref. [101]. [d]values are taken from ref. [98].

Gel filtration profiles show that MjADSS exists as a mixture of dimerand tetramer in solution. Addition of salt results in the shift of the equilibrium towards the dimer [115]. All other homologues of ADSS are known to exist as an equilibrium mixture of monomer and dimer in solution, for example, *E. coli* [109, 114], mammalian [116] and yeast ADSS [117]. The enhanced stability at the dimer interface was previously elucidated by comparing the residues at the interface with mouse muscle, *E. coli* and *P. falciparum* ADSS. This revealed a considerable increase in the number of salt bridges, hydrophobic and cation-pi interactions. Previously, thermostability of

other proteins has been attributed to higher oligomeric states, reduced surface-area, larger number of disulphide bonds in addition to the above mentioned interactions [118-122].

Since the crystal structure of MjADSS is not available, I have used the structural information from mouse muscle and *E. coli* ADSS to elucidate the structure-function relationship in MjADSS. Over-all sequence similarity between MjADSS and mouse muscle is 36% and between MjADSS and EcADSS is 48%.

1.6.4 ADSS employs extensive conformational dynamics

Extensive structural studies of ADSS complexes that mimic various steps of the catalytic cycle in mouse muscle (mm) and *E. coli* (Ec) are available [96, 99, 107, 109, 110]. These studies suggest that unligated ADSS is disordered while IMP alone is capable of organizing the active-site [123]. By the effective use of HDA along with IMP and GTP, the fully ligated conformation of ADSS was achieved [109]. The dynamic loops which organize upon ligand binding in mmADSS have been designated as Pre-switch loop (65-69), Switch loop (70-83), IMP loop (152-165), Val loop (304-310), GTP loop (448-452) and Asp loop (330-336) (Figure 1.16). A conformational change of 25 Å has been reported during ADSS catalysis. The largest displacement, of 9 Å, is observed in the Switch loop of both mmADSS and EcADSS. Conformational change in loop 299-304 is driven by the binding of L-Aspartate or HDA [106]. However, a study with analogues of GTP shows that the enzyme does not undergo any conformational change in response to the binding of guanine nucleotide and, IMP and/or Mg^{2+} is required for the recognition of pyrophosphate group of GTP [110]. A complete active-site of IMP requires two subunits as Arg177 from one subunit anchors IMP of the symmetry related subunit by forming a hydrogen bond with the 5′-phosphoryl group of IMP.

1.6.5 PfADSS: a unique enzyme among its homologues

P. falciparum, a protozoan parasite, depends solely on purine salvage pathway for its nucleotide requirements. This makes the enzymes of the purine salvage pathway essential for the survival of the parasite. Inhibition of these enzymes results in death of the parasite which is why these enzymes have been regarded as potential therapeutic targets [95]. While a few enzymes of the salvage pathway such as purine nucleoside phosphorylase and HGPRT from *P. falciparum* have been well characterized, structural information on enzyme like ADSS are scant.

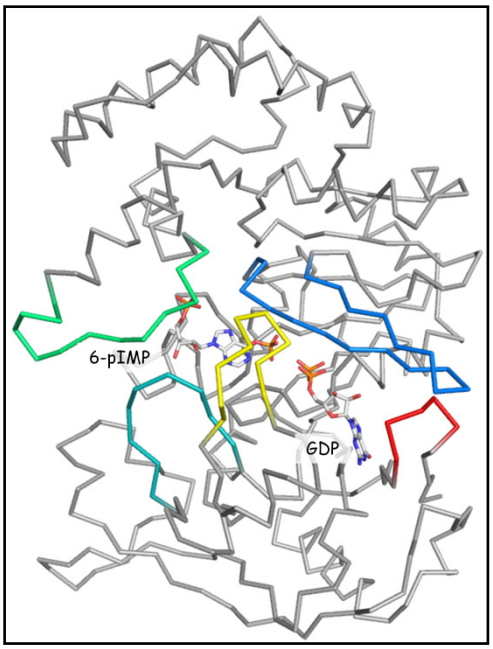

Figure 1.16: Structure of *P. falciparum* ADSS (1P9B: 2.00 Å) ligated to 6-pIMP and GDP. The active-site loops are shown in different loops (Switch loop: 49-66 (blue), IMP loop (green): 131-143, Asp loop: 305-309 (yellow), GTP loop: 427-431 (red), Val loop: 279-287 (cyan)). *Adapted from Mehrotra et al., Biochimica et Biophysica Acta, 1804, 2010 ref. [124].*

PfADSS is made up of 440 amino-acidswith a subunit molecular mass of 50000 Da [95] (Figure 1.16). Gel filtration profiles suggest that PfADSS exists as homodimer in solution [124]. Complete organization of the active-site involves contributions from both subunits. Interestingly, differential allosterism in PfADSS as compared to other homologues is evident in the form of the unique kinetic mechanism of this parasitic enzyme [33]. While ADSS from all other organisms shows a random kinetic mechanism, PfADSS, thus far, is the only homologue which shows an ordered sequential

mechanism. IMP binds first to the enzyme followed by the binding of GTP. L-Aspartate then binds to the ternary complex, PfADSS•IMP•GTP. Further, K_m values of PfADSS for IMP and GTP are 22.8 and 18.4 μM, respectively whereas the K_m value for L-Aspartate is 1.8 mM. While these equilibrium binding constants are comparable to other homologues [33], the turnover number of the parasitic enzyme is very low ($1.1 \pm 0.03\ s^{-1}$) making it one of the least efficient enzymes described in literature [96] (Table 1.3).

Almost 70% of the genome of *P. falciparum* consists of (A+T). This percentage is significantly higher than the (A+T) content in the genome of any other organism [125]. This suggests that the enzyme ADSS is strictly regulated to maintain AMP/GMP ratio in cell. The lower content of (G+C) in *P. falciparum* depicts the need to strictly regulate the non-productive hydrolysis of GTP which in turn manifests in the ordered binding mechanism of ADSS. This implicates a differential ligand-mediated allosteric effect between *Pf*ADSS and homologues from other organisms.

The only crystal structure of a fully ligated (6-pIMP, GDP, HDA and Mg^{2+}) PfADSS predicts non-covalent interactions among dynamic loops which may result in the ordered binding pattern of the enzyme [95]. Similar to EcADSS and mmADSS, the entire structure of PfADSS is divided into six loops. The largest conformational change, of 9 Å, has been reported in the switch loop comprising of residues from 53-66 (PfADSS numbering). Interestingly, overlaying the structure of PfADSS with an equivalent structure of EcADSS and mmADSS suggests that the switch-loop has a different orientation from the latter two. NZ of Lys62, which lies at the end of the loop, hydrogen bonds with the ribose hydroxyl of GDP. Also, Ser57 and Asp60 interact with Asn429 in the GTP loop. This implies that the IMP binding results in the formation of interactions between the residues in the switch-loop and GTP, which in turn facilitate the ordered binding of GTP. Such interactions are not observed in the homologues exhibiting random kinetic mechanism. Furthermore, GDP interacts with OG of Thr307 in Asp loop which in turn hydrogen bonds with O of HDA. This suggests possible interactions which are unique to PfADSS and hence can be implicated in the

ordered substrate binding mechanism. Further, the catalytically important residues (Asp26 and His54) and their interactions with nucleotides in PfADSS are similar to those observed in other homologues.

The importance of residues Asn429, Lys62 and Thr307 in ligand binding, ligand affinity and pre-organization of the active-site for catalysis has been demonstrated by site-directed mutagenesis studies [124]. While Asn429Val mutation does not lead to a significant change in K_m values of GTP, the K_m values of IMP and Asp increases by 3 and 2 fold, respectively. Further, a 5 fold drop in k_{cat} is also observed for the mutant. Lys62Leu mutation increases the K_m values for GTP and L-Aspartate whereas k_{cat} and K_m for IMP remain unchanged. While the mutation of Thr307 to Val does not perturb k_{cat} and K_m for IMP and GTP, it increases the K_m for L-Aspartate suggesting the role of Thr307 in stabilizing the binding of L-Aspartate/HDA at the active-site [124]. Further, Arg155 of the symmetry related subunit stabilizes IMP at the active-site by interacting with its 5′-phosphate group. In addition to the diminished substrate affinity, Arg155Lys, Arg155Leu and Arg155Ala mutations show a drastic loss in activity [124].

1.7 Biophysical tools employed to study the E•S complex

High resolution structural information of the E•S complex is a pre-requisite for understanding weak non-covalent interactions which are fundamental to rationalize the underlying mechanism of substrate specificity and rate-enhancement in enzymatic catalysis. X-ray crystallography and NMR are by far, the most commonly used techniques for the purpose. However, fluorescence spectroscopy and mass spectrometry coupled to H/D exchange play significant roles in interpreting the dynamical aspects of enzymes.

1.7.1 X-ray Crystallography

X-ray crystallography reveals the ensemble averaged three dimensional structure of a protein by determining distances between atoms in angstroms. Wavelength of x-rays used for the purpose is in the range of 0.5-1.5 Å which is long enough to measure inter-atomic distances. However, it is important to

note that the electron density map is the primary information obtained from X-ray diffraction and its subsequent interpretation yields atomic coordinates. Application of x-ray crystallography forprotein structure determination has revolutionized structural biology. There are about 99,642 crystal structures deposited in protein data bank (PDB), nearly 89,344 of which are determined by the x-ray diffraction method *(http://www.rcsb.org/pdb/statistics/holdings.do)*.

Crystal structures of protein are indispensable in their ability to predict protein-protein and protein-ligand interactions. In case of enzymes, high resolution crystal structures at various steps of the kinetic cycle have helped to deduce their catalytic mechanisms. Structures of enzymes with their ligand bound to the active-site predict interactions between the two, the knowledge of which is useful to develop the potent drug molecules against the target enzymes.

Although unparallelled in protein structure determination, crystal structures have some limitations such as the requirement of highly pure homogenous protein that should be capable of forming crystals. Few proteins, because of their intrinsically disordered regions, cannot form crystals. Crystallizing proteins is therefore a rather difficult, trial-and-error method which requires exhaustive optimization of buffer, solvent, pH and temperature. Most importantly, crystallization selects one of the several conformations of the protein which is present in solution and thus is not suitable to obtain information regarding conformational heterogeneity. That the conformation selected during crystallization is actually an active enzyme has been demonstrated by adding an effector ligand to ‘phosphorylase a’ which cracks upon interacting with ligand and anneals again in a different conformation [126]. Predicting conformational mobility upon ligand binding in proteins requires crystallization of protein in the presence and absence of ligand molecules which is a laborious and iterative task.

Further, the process of refinement which is done to optimize the agreement of the structure with the electron density map includes manual

correction which may result in a degree of subjectivity (different people produce slightly different results). One of the parameters that is manually optimized during refinement is the B-factor ($Å^2$), also called as the displacement parameter or the temperature factor which represents the mobility of individual atoms. Atoms in a well-ordered structure generally have lower B-factors and those with maximum static disorder exhibit higher B-factors. It is important to mention here that B-factors should be considered with caution. For instance, the crystal structure of 5ER1 complexed with leucinol shows B-factors of <1 whereas B-factors for individual atoms even for a high resolution structure are never <5 [127].

Furthermore, while most crystal structures are of good resolution and can accurately capture the active-site organization and the orientation of amino-acid residues and ligands, typical structures are incapable of predicting enzyme-induced distortions which lie in the range of 0.1-1 Å, and obtaining crystals that diffract at such a high resolution is difficult.

1.7.2 NMR spectroscopy

Nuclear magnetic resonance (NMR) spectroscopy is a powerful biophysical tool that is not only capable of predicting the three dimensional structure of protein but can also determine the time-scale of conformational transitions within the protein ensemble. Chemical shifts in NMR render the technique with a unique property to monitor individual atoms and their respective environment. Slight conformational and structural changes are manifested as changes in line-shape and intensity of peaks in NMR spectra. Isotope labeling (^{15}N, ^{13}C and ^{1}H) of amino-acid residues lining the active-site allows determination of conformational transitions upon encountering the ligand.

NMR is advantageous relative to X-ray diffraction because of its capability to determine high resolution solution structures of proteins that do not crystallize due to the presence of intrinsically disordered regions. By contrast, NMR monitors conformational transitions which fall in the time-scale of picoseconds to seconds. Nonetheless, the information obtained from

NMR is complementary to X-ray diffraction studies. With the development of multidimensional NMR techniques, it is now possible to obtain good quality NMR spectra of a protein at concentrations as low as 10 μmol/L [128]. Furthermore, changes in the chemical environment of a ligand upon binding to a protein can be monitored in the form of perturbations in chemical shifts. NMR has also been employed in identifyingintermolecular interactions in enzyme-substrate complexes and determination of pKa of a specific Lys residue at the active-site of an enzyme [129].

Although highly advantageous relative to the X-ray diffraction method, NMR also has a few limitations. When resonance in the protein is observed, a molecular size greater than 30 kDa results in peak broadening due to substantial resonance overlap [130]. A protein which undergoes oligomerization or aggregation gives unreliable NMR spectra because of the change in the inherent molecular tumbling in the solution-state [130]. In order to obtain unambiguous spectral identity, assignment of all resonances is the first and most time consuming step which guides the spectroscopist from the spectra to the structure. Another disadvantage of NMR spectroscopy is the requirement of isotope labeling of either protein or ligand. Over-expressing an isotopically labeled protein in *E. coli* is an expensive task. Further, the capability of NMR to detect the binding affinity of ligand towards protein does exclude detection of non-specific binding between the two [131, 132].

1.7.3 Vibrational Spectroscopy

Coupling the three dimensional structure with the functional and dynamical aspects of a protein is the ultimate goal of structural biology. Accumulating evidence in enzyme catalysis shows that a small change, of 0.01 Å, in bond length results in large change in reactivity [13-16]. Obtaining such precision is beyond the resolution of routine biophysical techniques like X-ray diffraction and NMR [20, 133, 134]. Vibrational spectroscopy is a powerful technique which probes molecular vibrations and can thus quantitate such small changes in bond lengths. Also, weak interactions like hydrogen bonding, hydrophobic and van der Waals interactions are difficult to observe in X-ray

crystal structures, and the alternative technique - NMR is restricted by the size of the protein. However, vibrational spectroscopy with its ability to report on the electronic structure of a ligand can show the presence of such interactions between ligand and active-site residues of an enzyme. E•S complexes at various steps of catalysis can therefore be probed comprehensively [7, 19, 21, 22, 56, 133, 135-137].

Vibrational spectroscopy offers several other advantages, for instance, this technique can be employed to samples in both solid [138] and liquid [18] states, which allows for its application to large protein molecules that do not crystallize. Most importantly, reactivity at the various steps of catalysis and dynamics of the protein can be probed by combining the technique with a time-resolved [139, 140] domain, which is experimentally challenging in the case of X-ray diffraction.

The following section outlines the basics of vibrational spectroscopy, in particular, ultraviolet resonance Raman spectroscopy (UVRR) followed by application of this technique to understand the structure-function relationship of E•S complexes. Vibrational spectroscopy consists of two main techniques, infra-red (IR) and Raman, which are based on different physical phenomena. IR absorption spectroscopy will be discussed only briefly. When a photon that interacts with a molecule has energy corresponding to the energy of a molecular vibration, the molecule is promoted to higher vibrational energy level. This process is termed as IR absorption which is detected by measuring the loss in energy of the incident radiation. Since the wavenumber ($\tilde{\nu}$) is proportional to the energy ($E=hc\tilde{\nu}$), the IR vibrational spectrum is plotted with wavenumber on the x-axis against (%) transmittance on the y-axis. Fundamental vibrations in a molecule have absorption frequencies in the mid-infrared region (4000 to 400 cm^{-1}) and hence the technique is called infra-red spectroscopy.

In Raman spectroscopy, a photon that interacts with a molecule is scattered with energy slightly higher or lower than the incident photon. The difference in the energy between the incident and scattered radiation yields

information about the vibrational transitions in the molecule. Since the underlying principle of IR and Raman is to probe molecular vibrations, the same is discussed here in detail.

Normal modes of vibration

A concerted independent motion of a group of atoms in a molecule about their equilibrium position is called a normal mode. Classically, normal modes are treated as simple harmonic oscillations which result in vibrational transitions. A molecule having 'n' number of atoms has 3n independent degrees of freedom which also include the three translational degrees of freedom along x, y and z coordinates and the three rotational degrees of freedom about the three principle axes of molecule. Thus, a non linear molecule has 3n-6 normal modes of vibration. Since, the rotation about the molecular axis is not possible, a linear molecule has 3n-5 normal modes. Further, it should be noted that each vibrational transition corresponds to a unique normal mode of a molecule and is observed in the form of a band in a vibrational spectrum. A triatomic molecule such as H_2O will have three normal modes of vibration which includes a symmetric stretch, an anti-symmetric stretch and a bending or deformation mode. The frequency of each normal mode is referred to as the fundamental frequency of that normal mode and is intrinsic to a functional group in a molecule. It is because of this reason that the vibrational spectrum of a molecule is considered as its fingerprint.

Selection rules in IR and Raman spectra

Vibrational spectra of IR and Raman have different origins which are explained by basic selection rules according to which a vibration in a molecule is IR-active if it results in a change in dipole moment of the molecule whereas a vibration is Raman active if it changes the polarizability of the electron cloud in a molecule. Thus, a symmetric vibration in a molecule results in maximum Raman scattering and minimum IR absorption and vice-versa for an anti-symmetric vibration. Further, a vibration arising from an ionic bond is strong in IR and that arising from a covalent bond is stronger in Raman. It should be noticed that because of these selection rules, all the vibrations in a molecule

cannot be IR as well as Raman active. Therefore, IR and Raman spectra of a molecule provide complementary information which is of great importance in the field of analytical chemistry.

Factors influencing vibrational spectra

According to Hooke's law, atoms in a diatomic molecule behave like rigid spheres and the nature of the bond connecting these atoms is similar to an elastic spring. Therefore, the relation between the frequency of vibration, mass of atoms undergoing vibration and bond strength is given by equation (1.1)

$$\nu = \frac{1}{2\pi}\sqrt{\frac{K}{\mu}} \quad \text{..... (1.1)}$$

Where, ν is vibrational frequency which is conventionally referred in wavenumber units ($\tilde{\nu}$, cm^{-1}; relation between vibration frequency and wavenumber is as follows: $\nu = c\tilde{\nu}$), K is the force constant of the bond between atoms A and B and μ is the reduced mass of atoms which is given by equation (1.2)

$$\mu = \frac{M_a M_b}{M_a + M_b} \quad \text{..... (1.2)}$$

From equation (1.1), it is clear that the heavier the atoms, the lower will be the frequency. The force constant is the measure of bond strength and thus, stronger the bond is, the higher the frequency of vibration will be. Equation (1.1) also allows estimation of energies ($E = h\nu$) of a specific bond involved in the vibration.

Due to the dependency of vibrational frequency on the mass of atoms, isotope exchange with heavier atoms viz. ^{2}H, ^{15}N and ^{14}C is routinely employed for the purpose of assigning modes in an observed vibrational spectrum. Bands in a vibrational spectrum of a molecule comprising of heavier atoms generally shows a downshift as compared to that with lighter atoms. For

instance, in the UVRR spectrum of guanosine-5'-monophosphate (GMP), acquired at an excitation wavelength of 260 nm in H_2O buffer (Tris-HCl, pH 7), a band at 1603 cm^{-1} is assigned to the pyrimidine ring stretch coupled to NH_2 scissoring vibrations (sci). Deuterium isotope labeling of GMP results in the conversion of —NH_2 to —ND_2 which in turn downshifts the band from 1603 cm^{-1} to 1572 cm^{-1}. The downshift of the band upon H→D labeling confirms the involvement of —NH_2 sci the band at 1603 cm^{-1}. Such an approach to assigning bands is unambiguous in attributing the involvement of a particular atom to a specific vibrational frequency. Isotope exchange effect in vibrational spectroscopy is a powerful method in assigning tautomerism and protonation-state to small molecules like nucleobases and nucleotides.

Formation of weak non-covalent interactions, e.g. hydrogen bonding and electrostatic interactions, with the atoms undergoing vibrations, tends to reduce the bond strength in a molecule and thus decreases the frequency of vibration. This provides vibrational spectroscopy with a remarkable potential to detect subtle non-covalent interactions formed upon binding of a substrate to the active-site of an enzyme. Furthermore, wavenumbers in a vibrational spectrum are also influenced by the electrostatic environment around the molecule. This has been useful in several occasions where the change in the pKa of ligand upon binding to the active-site of an enzyme has been determined using vibrational spectroscopy. Also, sequential change in the environment of an amino-acid residue from hydrophilic to hydrophobic has been traced using Raman spectroscopy.

Application of IR spectroscopy in Biology

IR has been used to determine the change in molecular structure of a ligand upon encountering the active-site of a protein. In one of the pioneering studies, picosecond time-resolved IR spectroscopy has been used to investigate the structure of Fe-carbonyl complexed with myoglobin and haemoglobin [141]. IR has also been employed in studying the conformational dynamics of bacteriorhodopsin, asthe protein passes through various intermediate stages [142]. In a completely different approach, IR has been

used in tracing the activity of an enzyme Ca^{2+}-ATPase by monitoring the hydrolysis of ATP. In this study, change in substrate concentration was followed by monitoring the absorption of α and β PO_2^- group of ATP, and the formation of product was traced by monitoring the β phosphate group of ADP. The important advantage of this application is that the progress of reaction directly quantifies the concentration of product formation and no further activity assay was required [143]. Using IR coupled to Raman spectroscopy, bond order and bond length of P—O in phosphoric acid has been determined to an accuracy of 0.04 and 0.004 Å, respectively [22]. This study has been followed by several other studies which involved elucidation of distortion of phosphate group at the active-site of purine nucleoside phosphorylase reaction [56]. In a completely different approach, IR coupled to Raman and *ab initio* calculations have been employed to the TS analogue complex of HGPRT•ImmHP•Mg^{2+}PPi to characterize the electrostatic interactions between ligand and the enzyme [144]. With the advent of 2D-IR correlation spectroscopy (COSY) and three IR pulse stimulated echo spectroscopy (THIRSTY), it has been convenient to probe Amide I region of small peptides and proteins in the region 1550-1700 cm^{-1} [145]. IR holds a lot of promise in its ability to determine the distribution of population in protein samples against NMR which gives an ensemble averaged signal [145].

The Raman Effect

Although the concept of inelastic scattering was first predicted by Adolf Smekal in 1923, it was observed experimentally for the first time by Prof. Sir Chandrashekara Venkata Raman and his graduate student Kariamanickam Srinivasa Krishnan in Calcutta, India in February, 1928. The phenomenon was termed as the Raman effect by German scientists who were able to reproduce this process of inelastic scattering, and as a consequence Sir C. V. Raman was awarded the Nobel Prize in Physics in 1928 [146].

Raman spectroscopy involves inelastic scattering of photons upon irradiating a molecule with the light of a certain frequency. The irradiation distorts the electron cloud around the nuclei and forms a transient state called a

'virtual-state'. The scattered photons may have energy (E=hv_o) either higher or lower than the incident photons. When the energy of the scattered photons is lower than the energy of incident photons, the process is called as Stokes scattering (ΔE=hv_o- hv), where, v is the vibrational frequency of molecule undergoing the energy transition. However, if the energy of the scattered photons is higher than that of incident photons, the process is termed as anti-Stokes scattering (ΔE=hv_o+ hv) (Figure 1.17). The Stokes and anti-Stokes scattering take place when the molecules undergoing transitions are in their ground vibrational state and excited vibrational state, respectively. Difference in the energy of incident and scattered photons corresponds to the quantum of vibrational transition.

Further, it may also happen that the scattered photons are scattered with energy exactly equal to the incident photons, and this phenomenon is termed as Rayleigh scattering. In fact, Rayleigh scattering is a dominant process and does not lead to any vibrational transitions. The probability of occurrence of Raman scattering is 1 in 10^7 photons which implies that the Raman scattering is inherently a weak process.

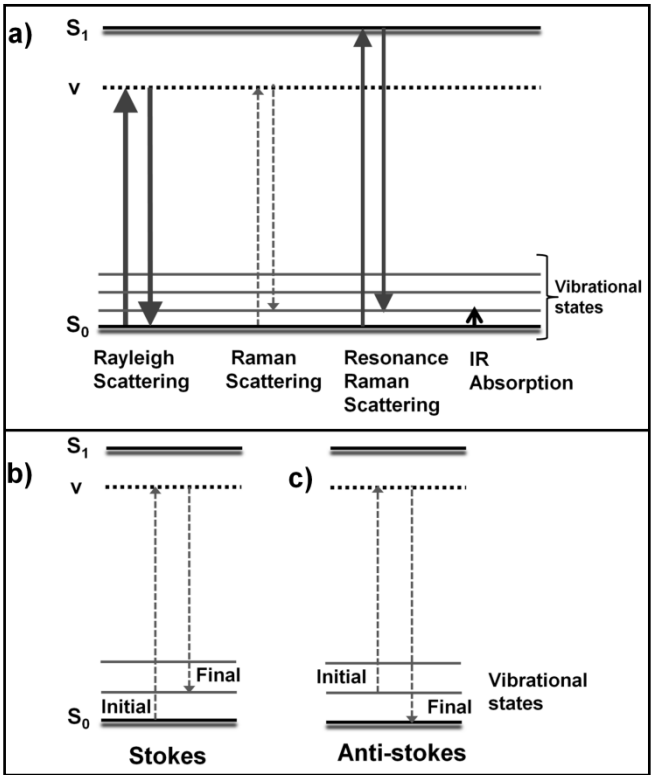

Figure 1.17: Energy transitions in a molecule upon interacting with light radiations. S_0, S_1 and v are ground electronic state, excited electronic state and virtual-state, respectively.

Maxwell-Boltzmann Distribution Law

Majority of the molecules at room temperature remain present in the ground vibrational state and thus the intensity of the Stokes lines is higher than the anti-Stokes line. The ratio of population of molecules (P) in the excited vibrational state (v=1) to the ground vibrational state (v=0) is given by the Maxwell-Boltzmann distribution law which is presented in equation (1.3).

$$\frac{P_{v=1}}{P_{v=0}} = e^{-\Delta E/kT} \quad \text{..... (1.3)}$$

Where, ΔE is the energy difference between two vibrational states, k is Boltzmann's constant (equal to 1.38 x 10^{-23} Joules $Kelvin^{-1}$) and T is the absolute temperature.

As the temperature increases, population of molecules in excited vibrational state increases and thus intensity of anti-Stokes lines increases.

Raman Spectra

Similar to the IR absorption spectrum, the Raman spectrum is also plotted in terms of wavenumbers. However, unlike IR where the absolute wavenumbers are plotted, the Stokes and anti-Stokes wavenumber in Raman spectrum is relative to the incident wavenumber. The absolute wavenumber which corresponds to Rayleigh scattering is assigned as zero and the difference between the Rayleigh and Raman lines is termed as Raman shifts. Thus, a Raman spectrum is plotted with the Raman shift on the x-axis and the Raman intensity on the y-axis. As Stokes lines are more intense than anti-Stokes lines, the former are depicted in a typical Raman spectrum. However, anti-Stokes lines can also be acquired by moving the grating position of the spectrophotometer. Differential Raman cross-section is another physical quantity which provides information on the electronic environment around the molecule. It is typically measured in $barns.str^{-1}$ (1 barn = 10^{-24} $cm^2.mol^{-1}$). A

cross-section greater than 60 barns.str^{-1} is considered as a strong resonance Raman cross-section [17].

Resonance Raman Scattering

Though Raman spectroscopy finds wide application in determining the molecular structure, the weak Raman cross-section of molecules, in particular of those which are not aromatic, renders this technique to be less applicable than IR. This limitation of Raman scattering can be circumvented by choosing an excitation wavelength which matches with the electronic transition. This is called as resonance Raman (RR) scattering which leads to an enhancement of Raman intensities in the observed spectral pattern by a factor of 10^5-10^7 as compared to normal Raman intensities. Further, if the wavelength of excitation lies in the ultraviolet region (190-380 nm) of the electromagnetic radiation, then the technique is called as ultraviolet resonance Raman spectroscopy (UVRR) (Figure 1.18). UVRR has a great utility in determining the molecular structure of biological samples in their physiological states. UVRR simplifies the spectrum, for the wavelength of excitation is chosen so as to obtain the resonance enhancement of only the chromophoric group.

UVRR is highly sensitive to slight perturbations in the electronic environment of the ligand and thus it serves as an appropriate technique to study distortions in the ligand upon binding to the enzyme. A Raman spectrum can probe subtle changes in the molecular geometry of a substrate which may occur upon interacting with the enzymes through non-covalent interactions. It can also report on the conformation, protonation-state and structure of nucleotide molecules at the active-sites of enzymes.

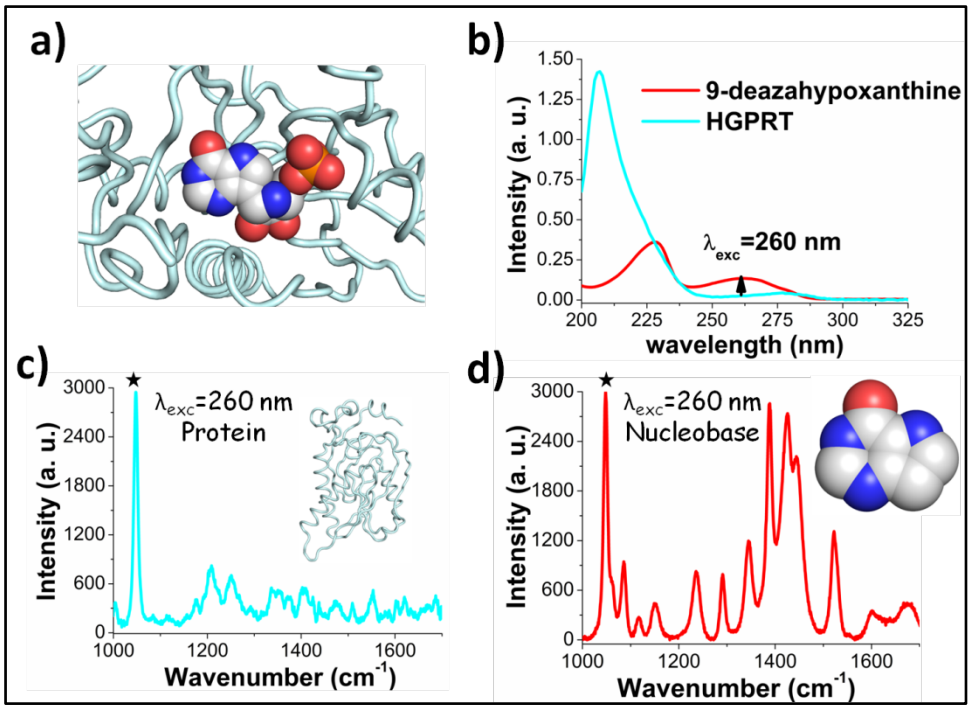

Figure 1.18: Illustration of resonance Raman enhancement of the chromophoric group at the active-site of enzyme. (a) Crystal structure of hHGPRT complexed with ImmHP, (b) absorption spectrum of HGPRT (blue) and 9-deazahypoxanthine (red) in Tris-HCl buffer, pH, 7.0, (c) Raman spectrum of hHGPRT, and (d) resonance Raman spectrum of 9-deazahypoxanthine; acquired at 260 nm excitation wavelength in Tris-HCl buffer, pH, 7.0.

Application of Raman and resonance Raman spectroscopy in Biology

Although crystallographers have guided enzymologists towards the elucidation of structure and development of drugs, alternative techniques which can transform the understanding of the structure functionrelationship at atomic resolution are required. In this respect, Raman spectroscopy holds a lot of promise in the field of structural biology. However, the use of this technique was limited by the unavailability of lasers and poor sensitivity of spectrophotometers and detectors [147]. The advent of the state-of-the-art instrumentation in Raman spectroscopy which includes tunable Nd-YAG based laser sources and detectors such as charged coupled device (CCD) has facilitated the effective use of this technique in the field of biological macromolecules [17, 148]. The increased sensitivity of the instrument can be judged by the use of sample volume which is practically 20 µL having 100-300 µM of protein concentration [19]. Highly dispersive grating and adjustable slit width and slit height of the spectrophotometer allow studies with high

resolution and precision. Development of new user friendly softwares has impeded the problems with data analysis [149]. The ability of the technique to detect the energy difference between the two energy levels in the ground electronic state allows probing of vibrational modes of a molecule which in turn yields information on the molecular conformation and electron distribution as a function of bond strength and molecular environment.

Callender and co-workers have employed normal Raman spectroscopy to study protein-ligand interactions [21]. In order to obtain the information about the molecular structure of the enzyme-bound ligand, the Raman spectrum of the enzyme was subtracted from the spectrum of enzyme•ligand complex. This process is termed as Raman difference spectroscopy [18, 150]. Alternatively, an atom within a bond of interest can be labeled with a stable isotope (^{2}H, ^{13}C, ^{15}N, ^{18}O) which results in the shift in the wavenumber associated with this bond vibration. Subtracting the spectrum of unlabeled protein from the labeled one yields a difference spectrum from only the modes involving the labeled atoms [18].

Reduction in the activation free-energy (ΔG) along the reaction co-ordinate leads to the enhancement of the rate of an enzyme catalyzed reaction. Information related to the components of free energy i.e. enthalpy and entropy can be deduced from a Raman spectrum of the Michaelis complex. The magnitude of downshift in a Raman band is directly proportional to the interaction energy or heat of formation of a hydrogen bond (ΔH). Inhomogeneous broadening of the Raman bands provides information on the accessible ground states of the ligand at the active-site of the enzyme. This is an entropic effect where reduction in band-width suggests reduction in the number of conformations available to the substrate i.e. loss of entropy (ΔS). Furthermore, binding of substrate to the enzyme modifies the electronic distribution on the molecule which in turn changes the force constants of the bonds between the atoms in the molecule. Thus, a Raman spectrum directly measures distortion in the substrate upon binding to the enzyme and provides information on the mechanism of enzyme-catalyzed reactions.

Information on the ground-state structure of a ligand bound to the active-site of an enzyme can also be obtained. A difficult task is to capture the TS of an enzyme-catalyzed reaction which is a very short-lived species. The fact that an enzyme binds with greater affinity to the TS implies that subtle distortions captured using the Raman technique in GS structure can be extrapolated to approximate the TS of a reaction. The pre-transition-state of adenosine deaminase with a TS analogue was captured to characterize hydrogen bonding interactions between the analogue and the active-site residues [136]. Similarly, the protonationstate of dihydrofolate bound to dihydrofolate reductase was also determined [135].

Specific amino-acid residues in a protein like tryptophan, tyrosine and phenylalanine, and chromophoric groups which are involved in specific intermolecular interactions can be probed by resonance Raman spectroscopy [36]. Comparatively localized vibrations which include C=O, C=C stretch and ring-breathing mode of 5-methyl thienylacrylic acid (MTA) have been analyzed to probe the active-site of a protease [7, 20, 137, 151] using RR spectroscopy. RR spectroscopy has proven to be of great utility in obtaining key information regarding the chromophoric groups in heme binding proteins [152-154]. Further, a wealth of such information could be obtained in the case of metalloproteins using RR spectroscopy [155]. Examination of α, β-unsaturated acyl serine and cystiene proteases using resonance Raman spectroscopy at the excitation wavelength of 350 nm has been reported as one of the pioneering works by Carey and co-workers [19, 20, 156-158]. Flavoproteins which are difficult to study because of their photosensitivity and intrinsic fluorescence have now been probed using Raman spectroscopy [150]. Changes in the chemistry of cofactors have been reported in case of chlorophyll, vitamin B12 and carotenes in plant tissues [159, 160].

Earlier, peptide backbone conformation and protein folding has been probed using wavenumber shifts and amide band intensities [17]. Deep ultraviolet resonance Raman spectroscopy at the excitation wavelength of 206.5 and 195 nm has been used to quantitate secondary structure in proteins [161]. Using 12 proteins of varied secondary structure composition, basis

spectra were established for α-helix, β-sheet and disordered structures [161]. Extensive RR studies on nucleobases have been done which pave the way for further elucidation of the conformational transitions in DNA and other nucleic acids [17, 162-165].

Comparison of IR and Raman

IR absorption has certain disadvantages over Raman spectroscopy. Water absorbs strongly in IR and thus makes it difficult to study biological samples in their solution-state which is a physiological condition and is certainly the most informative state. On the other hand, Raman scattering from water molecules is very weak and thus it can be easily employed to study proteins which are susceptible to dehydration. The vibrational spectrum obtained from IR absorption spectroscopy involves signal from all the functional groups in the sample. This makes the spectrum complicated to analyse and assign vibrational modes to each band. However, Raman has an advantage of selectively enhancing the vibrations from a chromophoric group by choosing the appropriate excitation wavelength.

1.7.4 Computational Calculations

Computational chemistry employs theoretical simulations to solve chemical problems. Studies using this approach are aimed at understanding the chemical structure of molecules including wave-functions of atoms, energies and other properties such as vibrational and NMR spectra. This allows one to examine reaction mechanisms, intermediates and transient species which are difficult to capture in an experimental method. Computational chemistry approach can be divided into the following broad areas:

Molecular mechanics employ the laws of classical physics to predict the structure and chemical properties of a molecule. The method does not take into consideration the explicit treatment of electrons and hence cannot address the problems in a system where electronic effects dominate e.g. study of bond breaking and bond formation in a chemical reaction. The calculations incorporate the interactions only between the various atomic nuclei. Molecular

mechanics uses different force fields (mathematical parameters to describe the potential energy surface) for different molecular systems. The method takes less computational time and can be applied to a larger molecular system like proteins.

Electronic structure methods use laws of quantum mechanics in place of classical physics, and treats electrons by solving the Schrödinger equation. Hydrogen is the only atom for which the quantum equations have been solved. For all other chemical systems, it provides the basis of approximations and assumptions in order to decipher the electronic structure and energy of the system. These methods can further be classified into three categories:

Semi-empirical methods use input parameters from experimental data which simplifies the computation. The method incorporates many approximations to solve the Schrödinger equation and relies on the accuracy of experimental parameters. Semi-empirical method is advantageous in taking less computational time and is applicable to systems of moderate size (10^2 atoms).

Ab-initio ('from the beginning') methods such as Hatree-Fock (HF) and Møller Plesset (MP2) use first principles of quantum mechanics (hence the name *ab-initio*) to determine the structure and chemical properties of molecules. Unlike molecular mechanics and semi-empirical methods, *ab-initio* methods do not use experimental parameters in their calculations. Structures of molecules in ground-state, excited-state, ionic and radical forms can be calculated. These calculations are highly demanding in terms of computational power and are relatively slower.

Density functional theory (DFT) is similar to *ab-initio* methods except that it takes into account the effects of electron correlation on atoms. The method was developed by Hohenberg and Kohn in 1964 for which they were awarded the Nobel Prize [166]. According to Hohenberg-Kohn theorem, electron density can be used to study all molecular properties (hence the name

DFT). The method is applicable to smaller systems and is more efficient than *ab-initio* methods.

Quantum mechanics/molecular mechanics (QM/MM) is a hybrid approach to simulate a larger molecular system. It combines the accuracy of the quantum mechanical method and the speed of molecular mechanics approach. It is this method which brought Warshel, Levitt and Karplus the Nobel Prize of 2014 in Chemistry. QM/MM approach is used for complex systems like proteins where the reaction centre, which is electronically important, is treated with QM approach which reliably predicts the breaking and formation of bonds. Surrounding atoms are treated with the MM force field which allows calculations on large number of atoms in short period of time. This method provides very useful information on the dynamics of an enzyme.

Use of computational methods in enzymology

X-crystallography being the most common method to study enzyme-substrate complex typically cannot provide the coordinates of hydrogen atoms. Such hydrogen atoms are placed in computational methods. Also, a single crystal structure of an enzyme bound to a ligand can be modified to obtain a complex with a substrate analogue or the transition-state of the reaction. QM/MM approach has been used to trace reaction trajectories in enzyme-substrate complexes by calculating free energies [44, 45, 83, 84, 167, 168].

A catalytic loop in inosine-adenosine-guanosine nucleoside Hydrolase displays very high B-factors and is found missing in the crystal structures. Computational simulations aided in positioning of this loop at the active-site [44]. MD simulations established that OMP decarboxylase complexed with substrate and intermediates displayed a change in conformation of the catalytic loop from unstructured to an ordered β-hairpin [44]. Further, despite X-ray and NMR studies on self catalytic hammerhead ribozyme, reactive conformations and role of Mg^{2+} ions were unknown. In-line attack conformation of self cleavage of hammerhead RNA has been traced using MD simulations. The rate limiting step was determined to be breaking up of intermediates to form

products. The dynamics of Mg^{2+} assisted self cleavage in the catalytic RNA has been investigated using DFT [44]. Also, protonation-states and pKa of titratable groups such as Lys-NH_3^+, Asp-COOH, Glu-COOH and His-ImH^+ at the active-site of an enzyme have been determined using hybrid QM/MM dielectric calculations and quantum chemistry with dielectric continuum [44].

Quantitative determinination of free energy profiles is essential for understanding the enzymatic reaction and the corresponding reaction in solution. Although QM/MM has been used to understand the chemical processes in enzymatic reactions, it has not been possible to apply QM/MM to obtain complete insights into quantitative studies. This is because calculating the potential energy surface, a pre-requisite for quantitative evaluation, requires *ab initio* electronic structure calculations which are too expensive to calculate free energy surfaces. Also, such QM/MM approach does not incorporate entropic effects and thus for a wide-ranging analysis of a system, a hybrid QM/MM along with a classical molecular dynamic approach is required [169] . Further, MD simulations are also limited by their general neglect of zero point energy and tunnelling effect [169].

Previously, DFT has been employed to predict vibrational wavenumbers. A modest agreement between the experimental and theoretical wavenumbers has been observed in several cases [170-173]. In my PhD work, I have used DFT calculations to predict structure of small molecules and to assign normal modes of vibrations to these molecules. In case of HGPRT, I have also determined the structure of 9-deazapurines along with the conserved hydrogen bonding network. This was followed by the Raman wavenumber calculations on these complexes.

1.8 Overview of the thesis

In my PhD work, I have studied the enzyme•ligand complexes of HGPRT and ADSS, using resonance Raman spectroscopy at an excitation wavelength of 260 nm. Comparative analysis was made based on the studies done on two homologues of each enzyme (HGPRT: human and *P. falciparum*; ADSS: *M. jannaschii* and *P. falciparum*). Excitation wavelength of 260 nm

allowed selective resonance enhancement of the ligand bound to the active-site of these enzymes and thus no interference was observed from the enzymes (Figure 1.18). I have also established the chemical identity (protonation-state and tautomers) of the ligands of these enzymes in solution-state. For this, I have employed the technique of UVRR and DFT calculations in combination with isotopic labeling.

"But in space light is light and doesn't know where it came from."

Richard Feynman

2

Methodology

2.1 Human HGPRT

2.1.1 Bacterial strains, plasmids, media and growth conditions

Plasmid (pET23d) containing the human HGPRT (hHGPRT) gene was obtained from Dr. Hemalatha Balaram's lab at Jawaharlal Nehru Centre for Advanced Scientific Research (JNCASR), Bangalore [174]. This was transformed into *E. coli* strain BL21 (DE3) cells. Glycerol stocks of transformed BL21 (DE3) cells, containing 20% glycerol, were stored at -80°C and used subsequently for protein purification. An overnight culture of the transformed cells in Luria Bertani (LB) medium containing 0.1 mg/ml ampicillin (Sigma Aldrich Co.) was used to inoculate 500 to 1000 ml Terrific Broth (TB) containing 0.1 mg/ml ampicillin for protein purification. Bacterial culture was grown at 37°C till the OD reached 0.6 (absorption at 600 nm). At this time point, protein production was induced by adding 1 mM IPTG (Isopropyl β-D-1-thiogalactopyranoside, Sigma-Aldrich Co.). After an induction period of 20 hrs at 20°C, the cells were harvested by centrifugation at 6000 rpm for 10 min at 4°C. These cells were stored at -80°C till the over-expression was ensured.

2.1.2 Expression and purification of hHGPRT

Over-expression of the protein was checked by taking out an aliquot of 1 mL culture from each flask, which was further lysed to run on an SDS-PAGE stained with Coomassie Brilliant Blue R250 (Sigma-Aldrich Co.). Pelleted

down cells from over-expressing flasks were used for subsequent protein purification steps.

Protocol for protein purification was taken from Subbayya and co-workers [174]. The harvested cells were resuspended in lysis buffer (50 mM Tris-HCl pH 7.4, 10% glycerol, 2 mM $MgCl_2$, 0.1 mM PMSF (phenylmethanesulfonylfluoride, Sigma-Aldrich Co.), 1 mM DTT (dithiotreitol, Sigma Co.)) and lysed using ultrasonic homogenizer (sonicator). The lysed cells were centrifuged at 16000 rpm for 20 min at 4°C. Supernatant was collected in a fresh tube and was treated with 0.1% PEI (polyethyleneimine, Sigma-Aldrich Co.). The resultant solution was further centrifuged for 20 min at 16000 rpm at 4°C. The supernatant was subjected to 40% ammonium sulphate fractionation at 4°C with continuous stirring. After 3 hrs, the solution was again centrifuged at 16000 rpm for 20 min at 4°C. The supernatant was subjected to 70% ammonium sulphate treatment stirring overnight at 4°C. The resultant solution was centrifuged at 16000 for 20 min at 4°C. In this step, the pellet contains the protein and thus was subjected to hydrophobic ion exchange chromatography using an FPLC system (ÄKTA Explorer, GE Healthcare). The pellet was resuspended in Buffer A (20 mM Tris-HCl pH 8.0, 12 mM $MgCl_2$, 0.1 mM EDTA (ethylene diamine tetraacetic acid, Sigma-Aldrich Co.), 1.2 M ammonium sulphate, 10% glycerol and 1 mM DTT). The resuspended protein was loaded onto a Phenyl Sepharose column (GE Healthcare) and the protein was eluted from the column by giving a linear gradient of 0 to 100% Buffer B (20 mM Tris-HCl pH 8.0, 12 mM $MgCl_2$, 0.1 mM EDTA, 10% glycerol and 1 mM DTT).

Fractions were collected by monitoring the increase in UV absorbance at 280 nm. An aliquot from each fraction was run on SDS-PAGE to check the presence of protein. The fractions containing hHGPRT were pooled together and the resulting solution was subjected to 80% ammonium sulphate precipitation for overnight at 4°C. In the next step, the solution was centrifuged at 16000 rpm for 20 min at 4°C. The pellet containing hHGPRT was subjected to anion exchange chromatography on an FPLC system. The pellet was resuspended in Buffer A (20 mM Tris-HCl pH 7.4, 10% glycerol

and 1 mM DTT) and desalted on a G-25 (Sigma-Aldrich Co.) column. The presence of protein in the eluted fractions was confirmed by Bradford's test. The fractions tested positive were pooled together and loaded onto a Q-Sepharose column (GE healthcare). Protein was eluted from the column using a linear gradient of 0 to 100% Buffer B (20 mM Tris-HCl pH 7.4, 10% glycerol, 1M NaCl and 1 mM DTT). 5-6 mL fractions were collected. An aliquot of 50 µL was taken out from each fraction and was run on an SDS-PAGE. At this step, pure protein was obtained but if the protein was still impure, the Q-Sepharose chromatography was repeated and the buffer pH was increased to 8.0. The resultant pure protein was concentrated and desalted using a Sephacryl 200 (GE healthcare) column on an FPLC system. The protein was eluted in a buffer containing 20 mM Tris-HCl pH 6.9, 10% glycerol and 1 mM DTT. Finally, the protein was concentrated using Amicon filters (Millipore, 10 kDa cut-off) and stored at -20°C in small aliquots.

2.2 PfHGPRT

2.2.1 Bacterial strains, plasmids, media and growth conditions

E. coli strain Sφ609 transformed with expression vector pTrc99A containing the PfHGPRT gene was obtained from Dr. Hemalatha Balaram's lab [175]. Glycerol stocks were made out of this inoculum and stored at -80°C for subsequent protein preparation. After this, an overnight grown culture at 37°C was prepared by inoculating the glycerol stock in 200 mL LB medium containing 0.1 mg/mL ampicillin. This culture was used to inoculate 500 mL of TB containing 0.1 mg/mL ampicillin. Cells were allowed to grow at 37°C until the OD at 600 nm reached to 0.6. After this the culture was induced with 1 mM IPTG for 24 hrs at 20°C. Post culturing, the cells were harvested by centrifuging at 6000 rpm for 10 min at 4°C and stored at -80°C.

2.2.2 Expression and purification of PfHGPRT

Expression of PfHGPRT was ensured by running an aliquot of bacterial culture on an SDS-PAGE. The cells over-expressing PfHGPRT were lysed, treated with PEI and were subjected to 40% and 70% ammonium sulphate fractionation (according to the protocol mentioned for the human homologue).

The resultant pellet was subjected to an anion exchange chromatography using the Q-Sepharose column. The pellet was resuspended in Buffer A (20 mM Tris-HCl pH 8.9, 10% glycerol and 1 mM DTT) and was loaded onto G-25 column to desalt the protein. Different fractions containing PfHGPRT were pooled together and loaded onto the Q-Sepharose anion exchange column connected to an FPLC system. A linear gradient of 0 to 100% Buffer B (20 mM Tris-HCl pH 8.9, 10% glycerol, 1 M NaCl and 1 mM DTT) was used to elute protein from the column. Fractions containing protein were pooled and subjected to 80% ammonium sulphate precipitation followed by a step of centrifugation as described for the human enzyme. Pellet obtained from the previous step was desalted using G-25 column using Buffer A (20 mM Tris-HCl pH 6.9, 10% glycerol and 1 mM DTT) and was subjected to cation exchange chromatography using an FPLC system.

Desalted protein fractions were pooled together and loaded onto a CM sepharose column (GE Healthcare). Fractions eluted using a linear gradient of 0 to 100% Buffer B (20 mM Tris-HCl pH 6.9, 10% glycerol, 1M NaCl and 1 mM DTT) was tested for the presence of pure protein using SDS-PAGE. In the last step, the purified protein was desalted on a Sephacryl 200 column connected to an FPLC system using a buffer composition of 20 mM potassium phosphate pH 7.0, 20% glycerol and 2 mM DTT. The purified protein was concentrated and stored at -20°C.

2.3 Enzymatic activity assay of hHGPRT and PfHGPRT

Enzyme from each batch of purification was subjected to an activity assay as described previously [174, 176]. hHGPRT and PfHGPRT were activated by different methods before conducting an activity assay or Raman experiment. In case of hHGPRT, the concentration of DTT in the enzyme solution was raised from 1 mM to 5 mM and the resultant solution was incubated overnight at 4°C. PfHGPRT required addition of 60 μM IMP along with an increase in DTT concentration to 5 mM, three hours prior to the activity assay. Activity of the enzymes was measured on a UV-visible spectrophotometer by detecting an increase in absorbance at a particular

wavelength due to product formation. A reaction mixture containing 100 mM Tris-HCl pH 7.4, 12 mM $MgCl_2$, 1 mM PRPP and 100 µM of hypoxanthine or guanine or 200 µM of xanthine (in case of PfHGPRT) was prepared. Upon addition of the enzyme (0.1 to 0.2 µg of hHGPRT and 1 to 2 µg of PfHGPRT), an increase in absorbance was monitored at 245 nm, 257.5 nm and 255 nm for formation of IMP, GMP and XMP, respectively. The Δε values used for calculating the specific activity and turn-over number are as follows: 1900 M^{-1} cm^{-1} for hypoxanthine→IMP, 5900 M^{-1} cm^{-1} for guanine→GMP and 3794 M^{-1} cm^{-1} for xanthine→XMP.

2.4 MjADSS

2.4.1 Bacterial strains, plasmids, media and growth conditions

Plasmid (pET23d) containing the 'gene insert' for MjADSS was obtained from the lab of Dr. Hemalatha Balaram at JNCASR, Bangalore [32]. This was transformed into *E. coli* strain BL21 (DE3). Colonies over-expressing the protein was inoculated into 200 mL LB medium containing 0.1 mg/mL ampicillin. The culture was grown overnight at 37°C. Glycerol stocks were made from this culture and stored at -80°C for subsequent protein preparation.

Large scale purification of MjADSS was done as described previously [32]. A glycerol stock was inoculated into 200 mL LB medium containing 0.1 mg/mL ampicillin; the culture was grown at 37°C for 12-14 hrs. The LB culture was used to inoculate larger volume (500 mL) of TB medium containing 0.1 mg/mL ampicillin. This culture was allowed to grow for 10 hrs at 37°C and was harvested by centrifuging at 6000 rpm for 10 min at 4°C. Thee harvested cells were stored at -80°C.

2.4.2 Expression and purification of MjADSS

Expression of MjADSS was ensured by running an aliquot of lysed bacterial culture on an SDS-PAGE. The cells over-expressing MjADSS were resuspended in lysis buffer containing 50 mM Tris-HCl pH 7.4, 10% glycerol, 300 mM NaCl, 0.2 mM PMSF and 2 mM DTT, sonicated and treated with

0.01% PEI, as described above for HGPRT. The supernatant obtained in this step was subjected to a heat treatment at 65°C for 25 minutes. This denatures all the protein from *E. coli* but MjADSS being thermophilic enzyme remains in the native state. Post heat treatment, the solution was subjected to centrifugation at 16000 rpm for 20 min at 4°C. The supernatant from this step was subjected to 40% ammonium sulphate precipitation at 4°C for 2-3 hrs with continuous stirring. The resultant solution was centrifuged at 16000 rpm for 20 min at 4°C. In the supernatant, the concentration of ammonium sulphate was raised to 75% at 4°C. This step was performed slowly over a period of 45 min by adding small quantities of ammonium sulphate to the solution with continuous stirring. The solution was kept at 4°C for overnight. The resultant solution was centrifuged at 16000 rpm for 20 min at 4°C. Pellet obtained in this step was subjected to an anion exchange chromatography.

The pellet was resuspended in Buffer A (20 mM Tris-HCl pH 6.9, 10% glycerol, 2 mM DTT and 0.1 mM PMSF) and desalted using G-25 gel filtration column before loading onto the Q-Sepharose anion exchange column connected to an FPLC system. The protein was eluted using a linear gradient of 0 to 100% Buffer B (20 mM Tris-HCl pH 6.9, 10% glycerol, 1 M NaCl, 2mM DTT and 0.1 mM PMSF). Fractions, each of 5-6 mL, were collected and an aliquot from each fraction was taken out in order to check the purity of the protein on an SDS-PAGE. The fractions containing MjADSS were pooled together and kept for 80% ammonium sulphate precipitation overnight at 4°C with continuous stirring. The resultant solution was centrifuged at 16000 rpm for 20 min at 4°C. The pellet was resuspended in the buffer and a maximum of 2 mL was loaded onto Sephacryl 200 column connected to an FPLC system. Buffer used for this purpose is as follows: 20 mM Tris-HCl pH 7.4, 10% glycerol, 1mM EDTA, 2mM DTT and 0.1 mM PMSF.Fractions were collected by monitoring an increase in UV absorbance at 280 nm. An aliquot from the collected fractions were run on an SDS-PAGE to confirm the purity of the protein. The fractions showing the pure protein were pooled together and concentrated using centrifugal filter units (Millipore, Amicons; 10 kDa). The final concentrated protein was stored at -20°C.

2.4.3 **Enzymatic activity assay of MjADSS**

Activity assay of MjADSS was conducted as described previously [32]. The assay was conducted at 70°C using a peltier controlled cell holder fitted to a UV-visible spectrophotometer (Cary). Reaction mixture containing 30 mM MES pH 6.5, 15 mM magnesium acetate, 10 mM L-Aspartate and 500 µM IMP along with 0.65 to 0.85 µg of MjADSS was pre-incubated at 70°C for 30 s before beginning with the kinetic assay. The reaction was initiated by adding 250 µM of GTP. Conversion of IMP to sAMP was detected by monitoring an increase in absorbance at 290 nm for 5 min. The Δε value used for this calculation is 3390 M^{-1} cm^{-1}.

2.5 PfADSS

2.5.1 **Bacterial strains, plasmids, media and growth conditions**

Plasmid, pET23d, containing the gene of PfADSS was obtained from the lab of Dr. Hemalatha Balaram at JNCASR, Bangalore [177]. This was transformed into *E. coli* strain BL21 (DE3). Freshly transformed colonies were inoculated in 200 mL LB medium containing 0.1 mg/mL ampicillin and the culture was grown overnight at 37°C. This culture was made into glycerol stocks (containing 20% glycerol) and stored at -80°C. Subsequently, a glycerol stock was inoculated into 200 mL LB medium containing 0.1 mg/mL ampicillin. This was cultured for 12-14 hrs at 37°C and was subsequently (10 mL) was used to inoculate a TB medium (500 mL). Cells were allowed to grow at 37°C until the OD reached 0.6 at 600 nm. At this time point, the culture was induced using 200 µM IPTG at 20°C and allowed to grow for 10 hrs at the same temperature. Post induction, the culture was harvested by centrifuging at 6000 rpm for 10 min at 4°C. The pellet was stored at -80°C until the over-expression in the cells was ensured.

2.5.2 **Expression and purification of PfADSS**

An aliquot (1 mL) of bacterial culture was taken out before pelleting down the cells. This aliquot was lysed and run on an SDS-PAGE to check the over-expression of the protein in the culture. Pellets from the flasks over-

expressing the protein was resuspended in lysis buffer containing 50 mM Tris-HCl pH 7.4, 10% glycerol, 1 mM DTT and 0.1 µM PMSF [177]. The resuspended pellet was sonicated and treated with 0.2% PEI with a method as described for MjADSS. However, unlike MjADSS, no heat treatment was given to the solution containing PfADSS. Supernatant obtained from the last step was subjected to 40% and 65% ammonium sulphate fractionation. The resultant solution was centrifuged at 16000 rpm for 20 min at 4°C. The pellet obtained from this step was subjected to an anion exchange chromatography.

The pellet was resuspended in Buffer A (20 mM Tris-HCl pH 8, 10% glycerol and 1 mM DTT) and desalted using G-25 column. The desalted fractions of protein were pooled together and loaded onto a Q-sepharose column connected to an FPLC system. The protein was eluted by giving a linear gradient of 0 to 100 % Buffer B (20 mM Tris-HCl pH 8, 10% glycerol, 1 M NaCl and 1 mM DTT). Aliquots from the collected fractions were run on an SDS-PAGE to check the presence of the protein. The fractions containing PfADSS were pooled and concentrated using 80% ammonium sulphate precipitation. The resultant solution was centrifuged at 16000 rpm for 20 min at 4°C. Pellet thus obtained was resuspended in buffer containing 20 mM Tris-HCl pH 6.9, 10% glycerol, 1mM EDTA and 1mM DTT. Maximum of 2 mL of the resuspended pellet was loaded onto the Sephacryl 200 size exclusion column connected to an FPLC system. Protein fractions were collected by monitoring an increase in absorbance at 280 nm. Aliquots from the fractions were run on an SDS-PAGE to confirm the purity of protein. The fractions showing pure bands on the SDS-PAGE were pooled and concentrated using centrifugal filters and stored at -80°C.

2.5.3 **Enzymatic activity assay of PfADSS**

Activity assay of PfADSS was conducted as described previously [33]. The assay was conducted at room temperature on a UV-visible spectrophotometer (Cary). The reaction mixture contained 30 mM sodium phosphate pH 7.5, 5 mM magnesium acetate, 250 µM IMP, 150 µM GTP and 5 mM L-Aspartate. 1-1.5 µg of PfADSS was added to initiate the reaction.

Increase in the concentration of product, sAMP, upon addition of enzyme was monitored by an increase in the absorbance of 290 nm (Δε value for IMP→sAMP is 3390 M^{-1} cm^{-1}).

2.6 Ultraviolet resonance Raman spectroscopy

2.6.1 Laser setup inside cavity

The light of wavelength 260 nm was generated by solid-state, tunable ultra-violet laser (Indigo-S, Coherent, Inc.) capable of producing narrow-linewidth output. Two main components of Indigo-S laser are Evolution-15 pump laser (Evolution cavity) and Ti-sapphire oscillator. Etalon mirrors in Ti:sapphire oscillator acts as wavelength filters resulting in the narrow linewidth of ultraviolet light. The Evolution cavity encompasses a gain medium which is comprised of Nd:YLF laser rod generating radiation of 1054 nm at 1 KHz repetition rate and 40 ns pulse width. This radiation is frequency doubled by a temperature controlled Lithium triborate (LBO) crystal to obtain the output wavelength of 527 nm. This output wavelength is pumped to water-cooled Ti: sapphire oscillator which in turn produces fundamental radiations in infra-red region (780 nm). With the help of highly reflective mirrors, the fundamental output is tuned into a Barium borate (BBO) crystal to generate a frequency doubled (second harmonic) output at 390 nm. Dichroic mirrors and IR mirrors allow mixing of fundamental (780 nm) and second harmonic (390 nm) in another BBO crystal and thereby generating third harmonic light of 260 nm. The three outputs viz. IR at 780 nm, visible at 390 nm and UV at 260 nm were impinged on a Pellin broca prism which disperses the three wavelengths in space and thus allows selecting only one wavelength for the experiments. The UVRR experiments presented in this thesis are carried out at an excitation wavelength of 260 nm. Further, typical power of UV radiation was maintained at 0.6 mW at sample.

2.6.2 Outer optical path of laser

As shown in Figure 2.1, light of 260 nm wavelength was allowed to pass through prisms (P_1 and P_2) and irises (I_1 to I_3) to reach the sample compartment. An iris (I_3) just before the sample compartment was used to

control the laser power. A maximum of 1 mW laser power was maintained at this iris. In the sample compartment, two cylindrical lenses of focal length 200 mm (L_1) and 150 mm (L_2) were used to focus the beam on a prism (P_3) which in turn impinged the beam on the sample in NMR tube (fused silica, Wilmad Labglass). NMR tubes were kept spinning with the help of a motor to prevent degradation of samples due to continuous UV exposure. The light scattered from the sample was collected by 135° back scattered geometry using two spherical lenses having focal length of 50 mm (L_3) and 250 mm (L_4). The collected photons were focused at a slit of monochromator (Jobin-Yvon, 1250M) having a spectral range of 0-15000 Å and consisting of a single diffraction grating with 3600 grooves/mm. The slit width and slit height of the monochromator was maintained at 300 μm and 2 mm, respectively for all experiments. Liquid nitrogen cooled charged coupled device (CCD) camera (Jobin-Yvon) having a pixel density of 1024 x 256 was used to record all spectra. Typical sample volume used for all experiments was 150 μL.

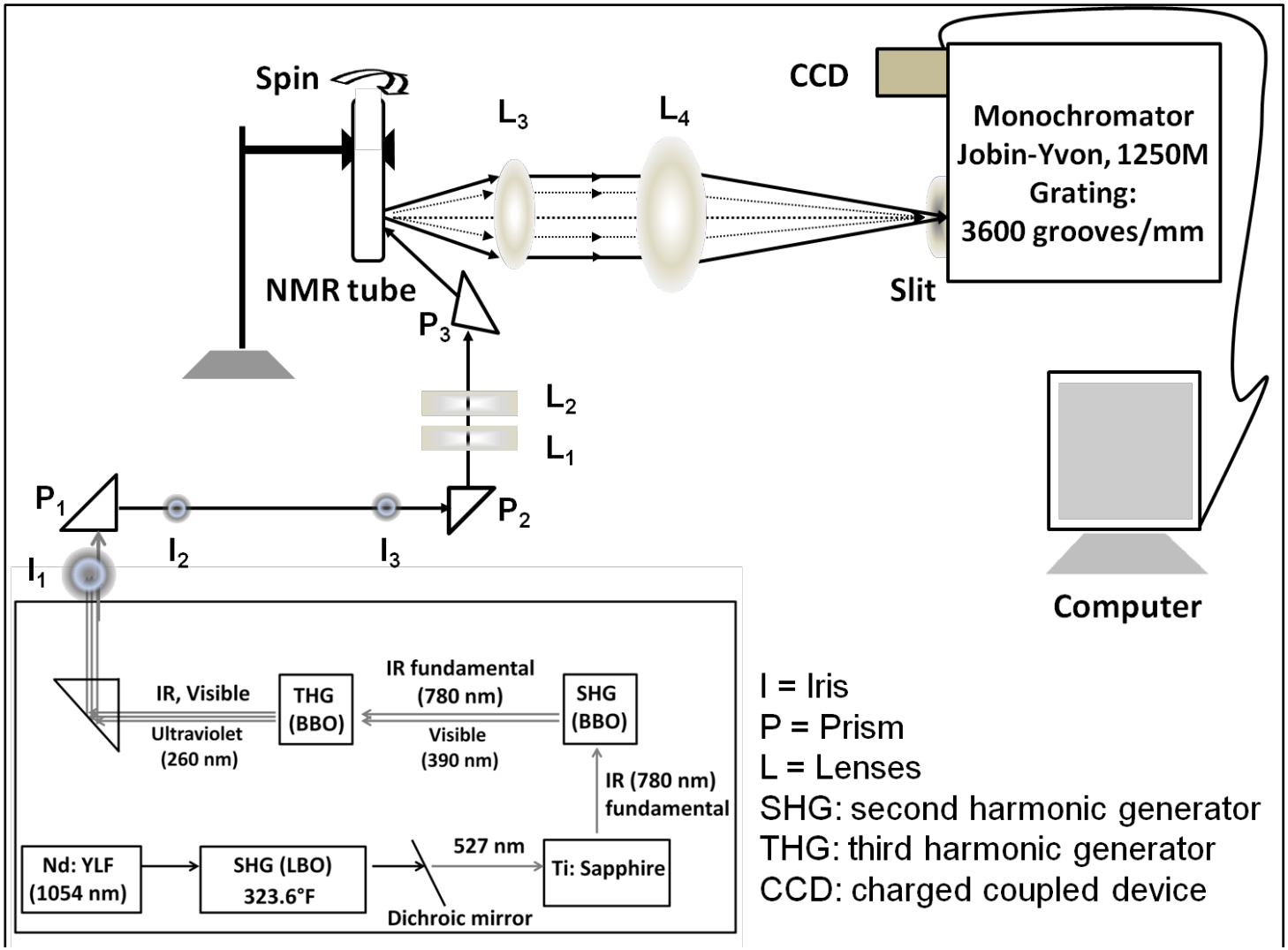

Figure 2.1: Schematic illustration of optical setup for UVRR experiments.

2.6.3 **Calibration of grating position**

The Raman spectra of several standard solvents such as dimethylformamide (Rankem, Analytical reagent), cyclohexane (Rankem, HPLC grade), acetonitrile (Sigma-Aldrich CO., Spectroscopic grade), trichloroethylene (Rankem, Analytical reagent), isopropanol (Rankem, HPLC grade), carbon tetrachloride (Rankem, Analytical reagent), chloroform (Sigma-Aldrich CO., Spectroscopic grade) and indene (Sigma-Aldrich CO., Spectroscopic grade) were recorded for each experiment. Positions of the bands in the Raman spectra of standard solvents in terms of the CCD pixel number were obtained by fitting Lorenzian lineshapes (Equation 2.1) to each band in the spectrum.

$$y = y_0 + \frac{2A}{\pi} \frac{w}{4(x-x_c)^2+w^2} \quad \text{..... (2.1)}$$

Where, y_o is the base line of the band

A is area under the curve

w is full width at half maxima

x_c is the center of the band

Pixel number for each solvent band obtained by using Lorentzian fit was plotted against their respective band positions obtained from literature [178]. A scatter plot between the two was fitted with a linear function which in turn was used to calibrate the Raman band positions on that particular day. Lorentzian fit to the solvent dimethylformamide and calibration curve are illustrated in Figure 2.2 and 2.3, respectively. Goodness of the linear fit was estimated by R^2 value and standard deviations which were typically kept at 0.9999 and <1, respectively.

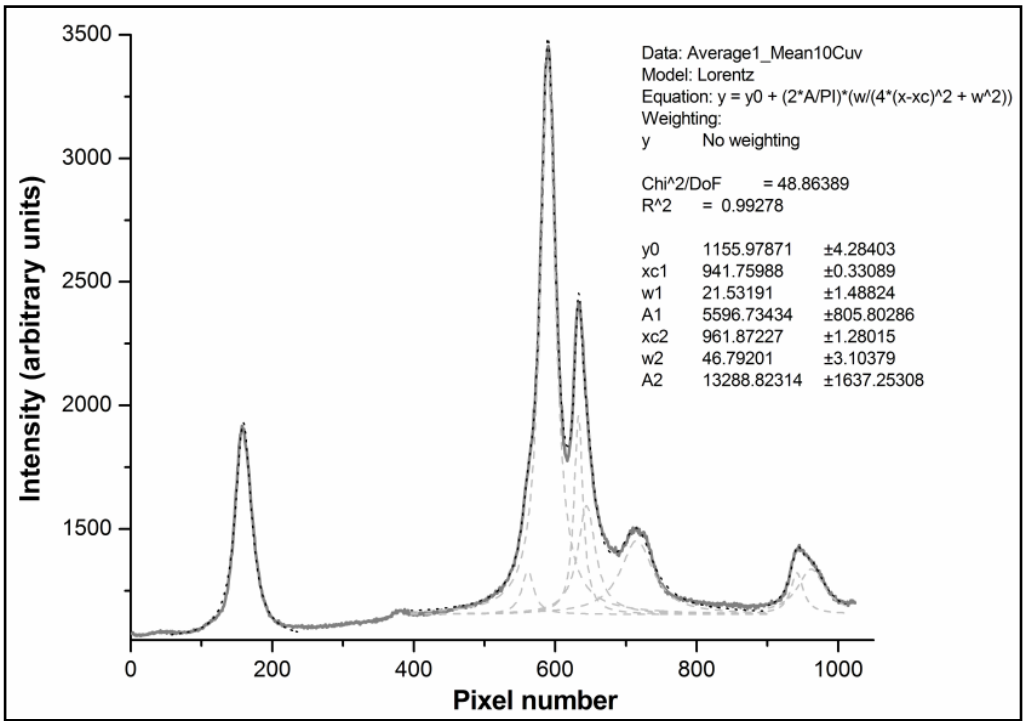

Figure 2.2: Lorentzian fit to the Raman spectrum of a standard solvent, dimethylformamide. Grey line is the Raman spectrum, black small dotted line depicts Lorentzian fit to the spectrum and light grey dashed line represents deconvolve fit to individual fits. Various parameters of Lorentzian fit are also shown in the figure.

Free fitting of the Raman bands was carried out with Voigt, Gaussian and Lorentzian functions. In case of Voigt functions, relative contribution of Lorentzian and Gaussian line-shapes was varied using a least squares algorithm. These fits converge to a final line-shape with most of the contribution from the Lorentzian function. Therefore, I used Lorentzian functions to model line-shapes. In Figure 2.4, I have illustrated the Raman band fitting using Lorentzian and Gaussian line-shapes. Deconvoluted fit to the band shows a better fit with the Lorentzian line-shape as compared to the Gaussian line-shape. As a consequence, I have employed only Lorentzian function for fitting the spectral bands observed for all samples. Figure 2.5 shows a typical fit to the spectrum of 9-deazahypoxanthine using Lorentzian line-shape.

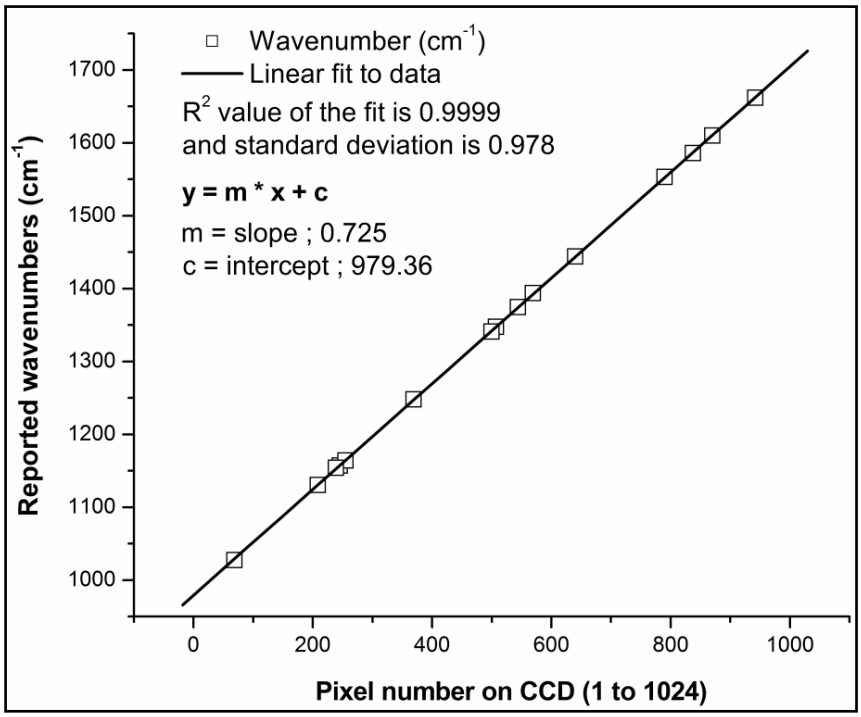

Figure 2.3: A scatter plot between pixel numbers on CCD camera (from 1 to 1024) and reported Raman wavenumbers of standard solvents. Black solid line depicts a linear fit to the plot. The plot was used to calibrate the Raman band wavenumbers on that particular day.

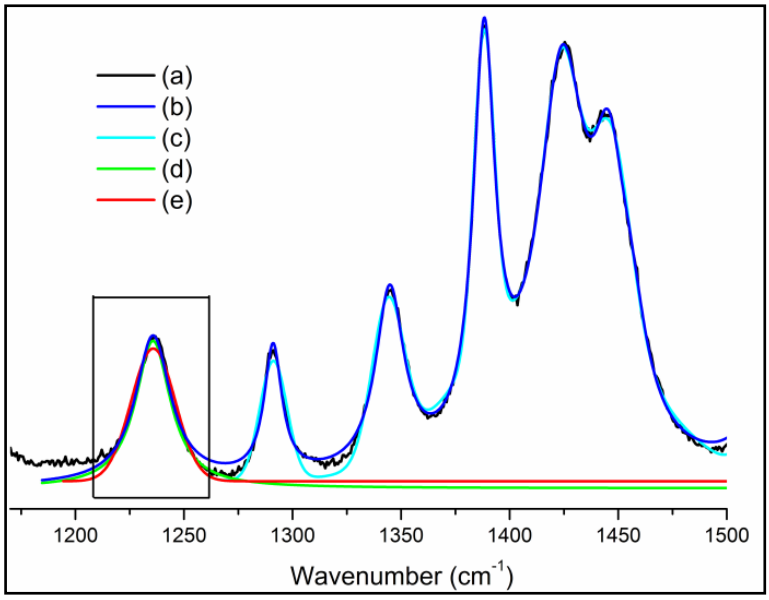

Figure 2.4: Fitted peaks of 9-deazahypoxanthine using Lorentzian and Gaussian line-shapes. (a) is the data plot for 9-deazahypoxanthine, (b) is data fitted using Lorentzian line-shapes, (c) is the fit to whole spectrum, fitted using Gaussian line-shapes. Inset shows deconvolve fits with Lorentzian (d) and Gaussian (e) line-shapes, respectively.

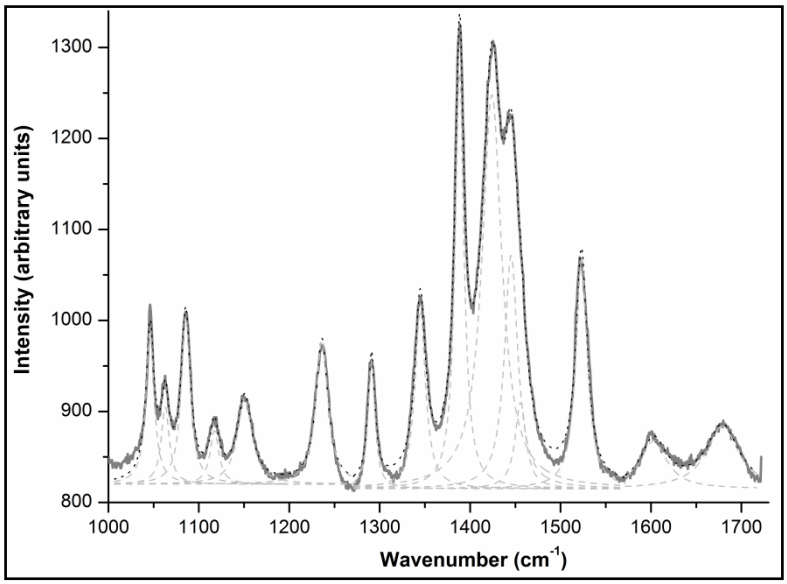

Figure 2.5: Fitted peaks of 9DAH using Lorentzian line-shape.

2.6.4 **Raman sample preparation and deuterium labeling of nucleobase**

Nucleobase analogues, 9-deazaguanine and 9-deazahypoxanthine were a generous gift from Dr. Vern Schramm. Stock solutions (25 mM each) of these nucleobases were prepared in 0.4 N NaOH and the same was stored at -20°C. Inosine-5'-monophosphate, guanosine-5'-triphosphate, guanosine-5'-diphosphate, succinyl adenosine-5'-monophosphate and adenosine-5'-monophosphate were purchased from Sigma-Aldrich Co. The stocks were prepared in Milli-Q water and stored at -20°C. Other ligands like α-d-5-phosphoribosyl pyrophosphate (PRPP), L-Aspartate and cofactors like magnesium chloride and magnesium acetate were purchased from Sigma-Aldrich Co. Hadacidin was procured from Developmental Therapeutic Programme, NIH. 1 M stock of this was prepared in Milli-Q water and stored at -20°C. Sodium nitrate (Sigma-Aldrich Co.) was used as an internal standard in all samples. Typical concentration of nucleobases and nucleotides used in Raman experiments was 500 μM and the concentration of internal standard was maintained at 30 mM.

Labile hydrogens in nucleobases were labeled with deuterium by preparing the stock in D_2O. Subsequent sample preparation was done in D_2O buffers. pD values were adjusted by adding appropriate amount of NaOD and DCl to the D_2O buffers.

2.6.5 **Raman sample preparation and deuterium labeling of enzymes**

For Raman experiments, all the enzymes (hHGPRT, PfHGPRT, MjADSS and PfADSS) were used at a typical concentration of 150 μM. During sample preparation, different substrates were added in the order in which they bind to enzyme during catalysis. hHGPRT and *Plasmodium falciparum* HGPRT were activated before the Raman experiment as described above. hHGPRT samples were prepared in 20 mM Tris-HCl, pH 7.0 and PfHGPRT samples were prepared in 20 mM potassium phosphate, pH 7.0. MjADSS and PfADSS samples were prepared in MES buffer pH 6.5 and HEPES buffer pH 7.0, respectively. For deuterium labeling, the enzyme buffer was exchanged with a D_2O buffer of same concentration and pD, using centrifugal filter units (Millipore-Amicon, 10kDa).

2.6.6 **Data acquisition, processing and analysis**

Each Raman spectrum was acquired at 20000 exposure time with 2 accumulations and 20 cycles (~14 min). For all enzyme samples, 3 such files were recorded, the average of which was used for further processing and analysis. Data acquisition and processing were done on SynerJY (Jobin-Yvon). To obtain the wavenumber of a spectrum, Raman bands were fitted using the Lorentzian line-shape function (Equation 2.1). Area under the curve was used as a measure of intensity analysis. The absence of photodamage was confirmed by comparing the first and last spectra acquired. Raman spectrum of buffer was subtracted from the sample spectrum. The Raman band assignments are done by comparing the isotopic shift (^{15}N, D) in the experimental and calculated Raman spectra. Wavenumber positions in the two cases are not used to assign normal modes to a particular band in a Raman spectrum. In order to obtain the Raman spectrum of enzyme•nucleobase complex, contribution of unbound apoenzyme and unbound ligand was removed from the Raman spectrum of enzyme•nucleobase.

2.7 Quantum mechanical calculations

2.7.1 Structure determination of nucleobases and nucleotides

DFT calculations were carried out on N7H tautomer of hypoxanthine and guanine and their analogues, 9-deazahypoxanthine and 9-deazaguanine using dispersion corrected density functional wB97XD with 6-31G (d, p) basis set as implemented in Gaussian 09. wB97XD functional allows studying of non-covalent dispersive forces and is widely used to study non-covalent complexes [179]. The functional is chosen with the aim to determine the non-covalent complexes of these nucleobases with amino-acid residues of HGPRT (*vide-infra*).

The structures of the ligands (6-phosphoryl IMP and sAMP) of ADSS were energy minimized using the functional B3LYP with 6-31G (d, p) basis set as implemented in Gaussian 09. The monophosphate group of nucleotides was replaced with methyl group while the sugar moiety was retained. Structures of protonated and deprotonated nucleobases were computed by adding or removing a proton from the neutral molecule in the software, GaussView 5.0. Calculations with the heavier isotope (deuterium) were done by replacing the mass of the hydrogen with deuterium in the input file for Gaussian 09. The energy minimized structures were made into input files for subsequent Raman wavenumber calculations. The resultant output was converted into 'form chk file' which in turn was used to do potential energy distribution (PED) analysis using the software VEDA 4.0 (Vibrational energy distribution analysis) [180]. This software provides the contribution of various internal coordinates to a particular normal mode. However, internal coordinates contributing less than 10% to a normal mode was analyzed using Chemcraft 1.6 (http://www.chemcraftprog.com). A typical visualization of a normal mode contribution is illustrated for a molecule 9-deazaguanine in Figure 2.6. Similar normal modes depiction for other molecules has been provided in Appendix (Figure A.1, A.2 and A.3). Agreement between the experimental and computational Raman wavenumbers was obtained by using scaling factors. Computed wavenumbers were scaled with factors ranging

from 0.96 to 1.00 by increasing in step of 0.01, to match the experimental values. The discrepancies between experimentally and computationally observed Raman shifts may arise due to the harmonic approximation employed in quantum mechanical methods.

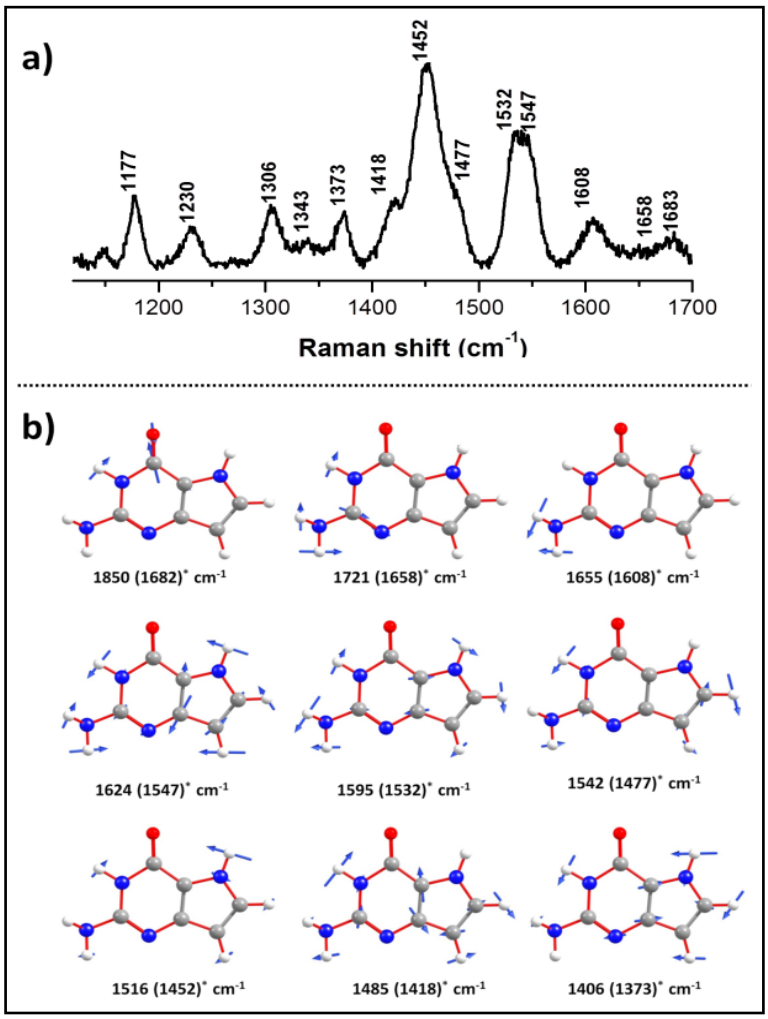

Figure 2.6: Normal mode vectors of neutral 9-deazaguanine as visualized in Chemcraft 1.6. Computationally predicted and experimentally observed wavenumbers (*) are mentioned.

"When the mysteries are very clever they hide in the light."

Jean Giono

3

Solution Structure of 9-deazapurines

3.1 Overview

Analogues of nucleobases hold a lot of promise as inhibitors and drug molecules against enzymes of nucleotide synthesis pathway. In particular, 9-deazapurines have found many applications in elucidating the dynamics and mechanistic details of purine nucleoside phosphorylase (PNP) and hypoxanthine guanine phosphoribosyltransferase (HGPRT) [181-184]. 9-deazaguanine (9DAG) and 9-deazahypoxanthine (9DAH) act as substrate mimics of natural nucleobase guanine and hypoxanthine, respectively. These analogues possess a carbon atom at 9^{th} position of nucleobase in place of nitrogen, which renders them incapable of nucleophilic attack on C1' of sugar moiety of PRPP (Figure 3.1). Since, the salvage pathway is the only nucleotide synthesis pathway in protozoan parasites like *Plasmodium*, *Trypanosoma*, and *Tritrichomonas* etc. and thus, the enzymes of this pathway are vulnerable to such inhibitors [163]. However, in addition to their binding with target enzymes, these inhibitors are also shown to bind the host enzymes. Knowledge of the molecular structure, protonation-state at different pH values and predominant tautomers at physiological conditions is essential for designing the derivatives of deaza analogues that specifically bind to the parasitic enzymes.

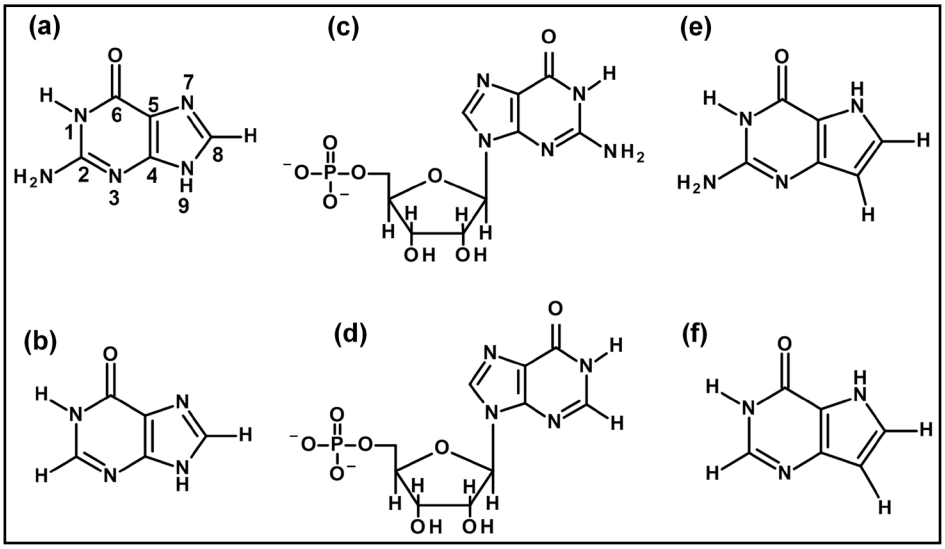

Figure 3.1: Structures of purine nucleobases and nucleotides. Natural nucleobases guanine (a) and hypoxanthine (b) and their corresponding mononucleotides GMP (c) and IMP (d) and the structure mimic 9-deazaguanine (e) and 9-deazahypoxanthine (f), respectively are shown.

3.1.1 9-deazapurines in literature

Previously, in PNP, derivatives of 9DAG have been exploited as multi-substrate analogue inhibitors [185, 186]. Purine analogues have also shed light on the structure of active-site structure and dynamics in PNP [187-190]. 9-deaza inosine derivatives have been identified as good inhibitors of PNP (K_i=1.8 x 10^{-17}) [191, 192]. In case of HGPRT, 9DAG have been used to trap the Michaelis complex of the reaction. Co-crystal structure of HGPRT with these analogues revealed the active-site interactions of the substrate with the enzyme. In case of crystal structure of *Toxoplasma gondii* HGPRT, 9DAG not only captured the distortion in the ligand towards the transition-state of the reaction coordinate but also suggested that the reaction proceeds through SN2 mechanism [80]. Further, crystal structure of *Tritrichomonas foetus* HGPRT along with 9DAG captured the dynamics of the catalytic-loop during catalysis [81]. These motions were further implicated in sequestering the transition-state of phosphoribosyltransferase reaction.

Theoretical methods have previously been employed to elucidate the structure of nucleobases in several studies [34, 35, 170, 171, 193]. Such methods are essential to assign normal modes to the observed vibrational spectra of small molecules. In this regard, use of DFT in place of HF or semi-

empirical methods has shown to provide much better agreement with the experimental data [194]. Other methods, such as MP2, provide good agreement between experimental and theoretical values but are computationally expensive [195, 196].

Using solid and solution NMR chemical shifts, Schramm and co-workers have determined the pKa values of Immucillin HP and Immucillin GP which are corresponding nucleotides of 9DAH and 9DAG, respectively [197]. The pKa values of 1.4 and 10 correspond to the deprotonation at N3 and N1 position, respectively, of the purine ring.

In the work done in this thesis, I have employed the technique of ultraviolet resonance Raman spectroscopy (UVRR) along with density functional theoretical (DFT: wB97XD/6-31G (d, p)) calculation to decipher the solution structure of 9DAG and 9DAH. UVRR is an experimental vibrational technique which is immensely sensitive to a slight substitution or perturbation in the molecular structure of nucleobases. Different protonation-states of nucleobase at different pH values are manifested in the form of characteristic vibrational spectra of these molecules. Moreover, a large enhancement in the Raman cross-section of nucleobases can be achieved by exciting the aromatic ring with the ultraviolet wavelength. These properties render UVRR a powerful and versatile label-free technique to study nucleobases bound to a specific enzyme.

A detailed comparison between the experimentally observed spectra and theoretically predicted structure was used to decipher the predominant structure at different pH values. To further substantialte the data, isotopic labeling of experimental and computational data was also done. Such labeling and the resultant isotope incuced shifts are helpful in assigning the Raman band positions with the computed normal modes.

3.2 Methodology

3.2.1 Sample preparation for absorption and UVRR spectroscopy

Initial samples of 9DAG and 9DAH were the gift from Dr. Vern Schramm. Subsequently, these were purchased from Sigma-Aldrich Co. and used without any further purification. 25 mM stock solution of these nucleobases was prepared in 0.2 N NaOH. Concentration of nucleobases in all UVRR experiments was 500 μM and the sample was prepared in 20 mM Tris-HCl. pH of the sample was adjusted by dissolving appropriate amount of 13 N HCl and 10 N NaOH for the acidic and basic pH, respectively. To prepare the samples in D_2O, NaOD and DCl was used. To ensure complete exchange of labile protons, the samples were kept overnight in deuterated buffers. For absorption spectra, nucleobase solution of 50 μM was prepared in Tris-HCl buffer of suitable pH for neutral, acidic and alkaline solutions.

3.2.2 Computational methods

Quantum chemical calculations were performed on 9DAG and 9DAH to obtain energy minimized structure. Density functional theoretical formalism was employed using wB97XD [198] with a 6-31G (d, p) basis set, as implemented in Gaussian 09 [149]. Raman wavenumber calculations were done on the optimized structure. To calculate the structure of a charged molecule, a proton was added or removed from the neutral molecule using GaussView 5.0 [199]. Following which the structure was optimized. Potential energy distribution calculations were performed using the software VEDA 4.024 (vibrational energy distribution analysis) [180]. Experimentally observed shifts due to isotopic labeling were computed by replacing the mass at the labile hydrogens with the mass of deuterium in the molecules. Normal mode description was inferred by visualizing the vibrational modes in the software Chemcraft 1.6 *(http://www.chemcraftprog.com)*. Diagrams depicting normal mode contributions were generated by Chemcraft 1.6. In molecules where more than one tautomer is possible, all the possible tautomers were optimized and the Raman wavenumber calculations were done. These were further compared with experimentally observed Raman wavenumbers.

3.3 Results and Discussion

Figure 3.2 shows the absorption spectra of 9DAG (a) and 9DAH (b) at different pH values 1.5, 7 and 12.5. An excitation wavelength of 260 nm, in resonance with π-π* allowed transition, was chosen for the UVRR experiments.

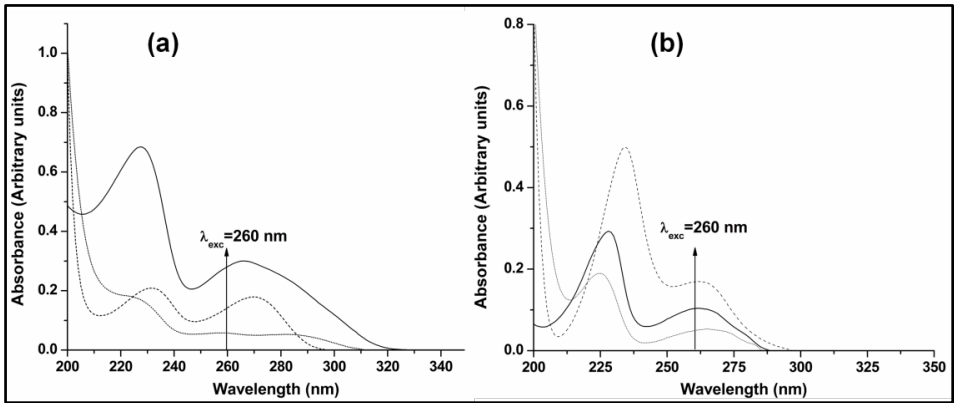

Figure 3.2: UV Absorption spectra of 9-deazapurines (50 µM) at different pH. (a) 9DAG at neutral pH (solid dark line), at pH 1.0 (dashed line), at pH 12 (short dotted line); (b) 9DAH at neutral pH (solid dark line), at pH 1.0 (dashed line), at pH 12 (short dotted line). The arrow depicts the excitation wavelength of 260 nm used for the UVRR spectroscopy experiment.

3.3.1 Neutral, protonated and deprotonated forms of 9DAG

The observed spectra of 9DAG at pH values 1.5, 7 and 12.5 were compared with all the possible computed spectra which includes 9DAG in neutral, cationic form protonated at N3, and anionic form deprotonated either at N1 or N7. The Raman band assignments are done by comparing the isotopic shifts (H→D) in the experimental and calculated Raman spectra. Wavenumber positions in the two cases are not used to assign normal modes to a particular band in a Raman spectrum. Based on the comparison between the experimenatal and theoretical specta, along with the isotope (H→D) induced shift, the spectrum at pH 7 is assigned to the neutral species (Figure 3.3 and Table 3.1). Further, using computational data, particularly in case of 6-oxopurines, it has been shown earlier that the N3 protonated tautomer is of higher energy and hence does not populate at physiological conditions [200]. Becasue of these reasons, the neutral form of 9DAG which bears a proton at N3 position is not considered. The observed Raman spectrum consists of the

entire set of in-plane vibrations of the nucleobase and the vibrations of the non-planer exocyclic —NH_2 moiety.

3.3.2 9DAG exists as neutral form with proton at N1 and N7 positions of purine ring at physiological conditions

Carbonyl Stretch: The band at 1684 cm^{-1} in the UVRR spectrum of 9DAG at pH 7.0 is attributed to carbonyl stretch coupled to N1—H of purine ring. Upon deuteration (H→D labeling), the band shows a downshift of 21 cm^{-1} further corroborating the coupling of carbonyl stretch with N1—H. A downshift of 81 cm^{-1} in deprotonated 9DAG at higher pH indicates the loss of proton at N1 position of purine ring and thus loss of double bond character in the carbonyl (Table 3.2). Absence of any isotope induced shift in carbonyl stretch at higher pH further corroborates that the proton is lost from N1 position and thus N1—H has no contribution in the carbonyl stretch mode. Further, in 9DAGH+, the band at 1715 cm^{-1} is attributed to the carbonyl stretch (Table 3.3). An upshift of 62 cm^{-1} in this mode with respect to the neutral form indicates the greater double bond character resulting from the protonation at N3 position.

Pyrimidine ring distortion: The mode observed at 1658 cm^{-1} in neutral 9DAG is assigned to the pyrimidine ring distortion mode. This band shows a downshift of 62 cm^{-1} upon H→D labeling. DFT calculations predict that the decoupling of —NH_2 scissoring vibrations (sci) from the mode results in the large downshift in this band. Further, only a small magnitude of 2 cm^{-1} isotope induced downshift observed in deprotonated form shows a lesser contribution of —NH_2 sci as compared to that in the neutral species. By contrast, protonation results in the upshift of pyrimidine ring mode suggesting an increase in the double bond character of the pyrimidine ring. Sensitivity of this band to the isotopic labeling suggests the ability of this band to act as a marker band of hydrogen bonding interaction between protein and —NH_2 moiety of nucleobase in 9DAG•enzyme complex.

—NH_2 scissoring mode: The band at 1608 cm^{-1} in 9DAG spectrum arises from —NH_2 sci. Based on the exhaustive comparison between the magnitudes of isotope induced shift in experimental and theoretical data

($\Delta\nu_{HtoD}$ = -397 cm^{-1}), the corresponding band in the deuterated 9DAG spectrum is assigned to 1391 cm^{-1} ($\Delta\nu_{HtoD}$ = -217 cm^{-1}). In deprotonated 9DAG (9DAG-), the corresponding band with slightly different normal mode composition (—NH_2 sci coupled to C4C5N7 bend) is observed at 1540 cm^{-1}. In protonated 9DAG, the mode appears at 1601 cm^{-1} and upon deuteration decouples from —NH_2 to appear at 1584 cm^{-1}.

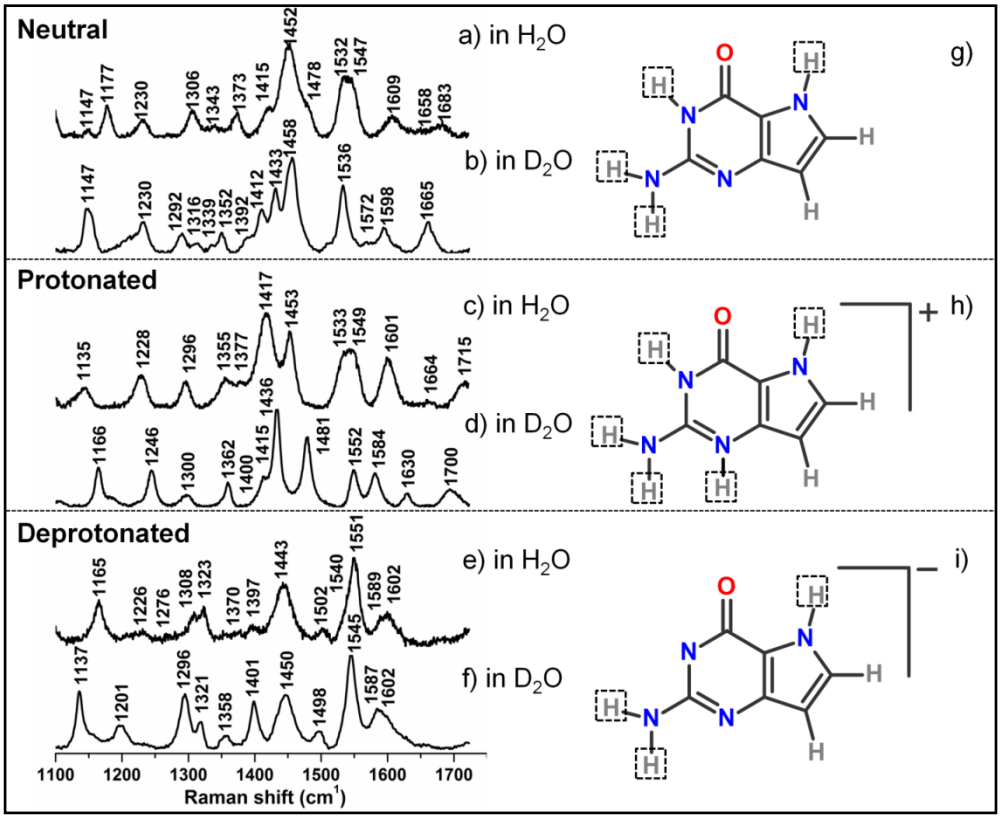

Figure 3.3: Resonance Raman spectra of 9DAG acquired at an excitation wavelength of 260 nm. Concentration of nucleobase in the spectra (a) to (f) was 500 µM and was prepared in 20 mM Tris-HCl. pH of the sample was adjusted by dissolving appropriate amount of 13 N HCl and 10 N NaOH for the pHs acidic (1.5) and basic (12.5), respectively. (g) to (i) are the corresponding chemical structures of 9DAG. Protons marked within dashed boxes are labile and would be replaced by deuterons in D_2O buffer. In order to prepare the samples in D_2O, appropriate amount of NaOD and DCl was added in D_2O.

C—N stretch coupled to C—C stretch: The band at 1547 cm^{-1} in the spectrum of 9DAG at pH 7 is attributed to the stretching vibrations (str) of C4—C5 and C8—C9 coupled to N3—C4. DFT calculations also predict a minor contribution from N7H, N1H str and NH_2 bending vibrations (bend). Further, whereas calculations predict a downshift in this band upon

deuteration, an upshift of 27 cm^{-1} in the observed spectrum implies decoupling of N1H and —NH_2 bend. The disparity in the experimental and theoretical data shows that DFT calculations underestimate the contributions of the bend to this mode. A minor upshift in the band in 9DAGH+ shows the presence of more localized mode resulting from the protonation at N3 of purine ring.

Triene stretch: The most intense band 1452 cm^{-1} in 9DAG spectrum in water at pH 7 is ascribed to the in-plane C4—C5, C5—N7 str and N3—C4—C5 bend. While DFT predicts an isotopic induced downshift of 7 cm^{-1}, the observed value of 20 cm^{-1} indicates the contribution from N1—H str and —NH_2 bend to this mode. Further, deprotonation of 9DAG results in the reorganization of the normal mode composition. This results in an upshift of this band to 1551 cm^{-1}. In 9DAGH+, the band appears at 1453 cm^{-1}. DFT calculations predict that upon deuteration the mode delocalizes to the entire pyrimidine ring and includes a significant contribution from N1—C2 str resulting in an isotopic induced shift of 17 cm^{-1}.

C8—H bending mode: The band at 1532 cm^{-1} in the spectrum of neutral 9DAG is assigned to C8—C9 str and N7C8H bend. Whereas DFT calculations predict a downshift in the mode upon deuteration, an upshift of 3 cm^{-1} in the observed spectrum indicates contribution of N1—H bend to the band in water. Further, upon deprotonation at N1 position, the band downshifts to 1323 cm^{-1} corroborating that the mode is contributed by N1—H bend. In 9DAGH+, the band downshifts to appear at 1417 cm^{-1}.

Pyrrole ring vibrations: The band at 1477 cm^{-1} in the spectrum of 9DAG at pH 7.0 is attributed to pyrrole ring vibrations coupled to N1—H bend. Upon deuteration, the band shows a downshift in experimental (20 cm^{-1}) and theoretically predicted spectra (31 cm^{-1}), suggesting that the band can serve as a marker for hydrogen bonding at N7 position of the purine with the active-site residues of HGPRT.

Purine ring mode: The mode appears at 1373 cm^{-1} in 9DAG at pH 7 and downshifts in experimental as well as DFT predicted spectra. Upon deprotonation at N1 position of purine ring in 9DAG-, an upshift of 70 cm^{-1} is

observed whereas DFT predicts an upshift of 40 cm^{-1}. In protonated 9DAG, an upshift in this mode implies the strengthening of C—C and C—N bond upon protonation at N3 position. Disparities between the shifts in the observed and DFT predicted spectra may arise because of highly delocalized nature of the purine ring mode. The results suggest that DFT is incapable of adequately predicting the shifts in such delocalized mode.

Pyrimidine ring distortion coupled to C4—C5—N7 bend: A moderately intense band at 1417 cm^{-1} in the spectrum of 9DAG at pH 7 is assigned to N1—C2 str and C4—C5—N7 bend. A downshift is observed in the band upon H→D labeling as correctly predicted by DFT. Further, DFT predicts a huge downshift in this band in 9DAG- as well as 9DAGH+ species. Corroborating to these predictions, the corresponding band in deprotonated and protonated spectra do not appear in the range of observation in these experiments.

Table 3.1: Experimental resonance Raman shifts of neutral 9DAG in water and D_2O at pH 7.0 and computed (wB97XD/6-31G (d, p)) vibrational wavenumbers of neutral 9DAG with mode assignments[a]

UVRR in H_2O	DFT	Mode assignments	UVRR in D_2O	DFT	Mode assignments
1682	1850	Str C6O6 (69%)	1661	1843	Str C6O6 (71%) + Be C6N1C2 (12%)
1658	1721	Str C2N3 (50%) + C2N2 (-12%) + Sci $N2H_2$	1596	1693	Str C2N3 (59%)
1608	1655	Sci NH_2 (55%)	1391	1258	Sci ND_2 (32%) + Be N1DC6 (-13%)
1547	1624	Str C4C5(42%)-C8C9 (-16%) + Str N3C4 (-11%) + Be N7H+N1H+NH_2	1574	1616	Str C4C5 (47%) + Str C8C9 (-28%) + Str N3C4 (-15%)
1452	1595	Str C4C5N7(16%) + Be N3C4C5(14%) + Sci NH_2 + Be C9H + C8H + N1H	1432	1588	Be N3C4C5 (18%) + Be C4C5N7 (17%) + Str C2N2 (10%) + StrN1C2N3 (10%)
1532	1542	Be N7C8H (15%) + Str C8C9 (32%)	1535	1530	Str C8C9 (32%) + Be C8HC9 (-15%)
1477	1516	Be N7HC5 (22%) + Str C5N7 (-20%)-N7C8 (-13%) +BeN7C8C9 (-11%)+N1H	1457	1485	Str C5N7 (32%) + Be N7C8C9 (19%) + Str C4C5 (-11%)
1418	1485	Str N1C2 (-10%) + Str C4C5 (29%) + Be C4C5N7 (-11%)	1412	1461	Str N1C2 (31%) + Str C4C5 (-13%) + Str C2N2 (-15%) + be N2D2a
1373	1406	Str N3C4 (29%) + Str C5N7 (-21%) + Str N7C8 (-14%) + Be N1H	1352	1388	Str N3C4 (25%) + Str N7C8 (-22%)
1343	1344	Be N1HC6 (29%)+Str C2N2 (10%)+Rock NH2b			
1306	1329	Be N7C8H (15%) + Str N1C6 (15%) + Be C9HC8 (13%) + Be N1HC6 (-12%) + Str C2N2 (-12%)			
1230	1248	Str N1C6 (-17%) + Be N7HC5 (23%) + Str N7C5 (13%)	1154	1184	Str N1C6 (21%) + Be ND_2 (18%) + Be N7D + Be C9H
1177	1179	Str N7C8 (27%) + Str N1C6 (-10%) + Be N2H2b (14%)	1147	1089	Str C2N2 (15%) + Sci $N2D_2$ (-14%) + Be N1C6=O (-13%) + Be N1DC2 (-10%)

1147	1144	Be N7C8H (28%) + Be N2H2b (-18%) + Str N7C8 (24%) + Str N1C6 (-10%)	1336	1320	Str N1C6 (24%) + Str N7C8 (18%) + Be C8HC9 (-11%)
1120	1114	Be C9HC8 (16%) + Be C5N7H (-15%) + Be C5N7C8 (-13%) + Str N7C8 (11%) + Str C8C9 (10%)	1291	1193	Be C8HC9 (16%) + Be C9HC8 (-14%) + Str C5N7 (-11%) + Be C5N7C8 (10%)
1096	1096	Be C9HC8 (27%) + Be N7C8H (-17%) + Be C2N2H2b (-14%) + Str C8C9 (11%)			
			1235	983	Be C2N2D2a (21%) + Be N1DC2 (18%) + Str C2N3 (11%) + Be N7D + Be C9H

[a]Abbreviations: Str, stretch; Be, bend; Py, pyrimidine; Sci, scissors; Pu, purine.

Table 3.2: Experimental resonance Raman shifts of deprotonated 9DAG in water and D_2O at pH 12.5 and computed (wB97XD/6-31G (d, p)) vibrational wavenumbers of deprotonated 9DAG with mode assignments[a]

UVRR in H_2O	DFT	Mode assignments	UVRR in D_2O	DFT	Mode assignments
1602	1736	Str C6O6 (70%)	1602	1735	Str C6O6 (71%)
1589	1624	Str C2N3 (18%) + Be C4C5N7 (10%) + Be NH_2 (-30%)	1587	1610	Str C2N3 (30%) + Be C4C5N7 (22%)
1540	1618	Be C4C5N7 (20%) + Be NH_2 (35%)	1156	1175	Be C4C9H (10%) + Be ND2 (23%)
1551	1643	Str C8C9 (-14%) + Str C4C5 (34%) + Str N3C4 (-12%)	1548	1638	Str C8C9 (-14%) + Str C4C5 (34%) + Str N3C4 (-16%)
1502	1514	Str C2N3 (11%) + Str C4C5 (14%) + Str N7C8 (-11%) + Be C4C5N7 (-11%)	1498	1505	Str C2N3 (16%) + Str C4C5 (10%) + Str C2N2 (-12%) + Be C4C5N7 (-15%) + Be N1C2N3 (-10%)
1323	1548	Str C8C9 (30%) + Str C2N3 (-10%) + Be C8HC9 (-20%)	1320	1539	Str C8C9 (33%) + Be C8HC9 (-23%) + Be C5N7C8 (12%)
1397	1473	Str C4C5 (-12%) + Str C5N7 (22%) + Be N7HC8 (12%) + Be C8HC9 (13%)	1358	1436	Str N1C2 (12%) + Str N7C8 (19) + Str C5N7 (-16%) + Be C4C9H (10%) + Be N7HC8 (-10%) + Be N7C8C9 (-17%)
1443	1362	Str N3C4 (28%) + Str C5N7 (-18%)	1449	1366	Str N3C4 (-29%) + Str C5N7 (18) + Str N2C2 (10%) + Be C8HC9 (12%)
			1401	1224	Str N1C6 (-10%) + Str N7C8 (23%) + Be C8HC9 (-14%) + Be ND2 (12%)
1308	1312	Str N1C6 (24%) + Str N7C8 (10%)	1296	1311	Str N1C6 (33%) + Str N7C8 (17%)
1165	1244	Str N1C6 (22%) + Be N7HC8 (16%) + Be C2N2H (10%)	1138	947	Be N7HC8 (-17%) + Be C2N2Ha (-22%) + Str N1C6

1226	1208	Str N7C8 (19%) + Be N7HC8 (11%) + Be C2N2Ha (-11%) + Be C2N3C4 (-12%) + Be C5N7C8 (12%)	1200	1169	Be ND2 (-18%) + Be C2N3C4 (-10%) + Be C5N7C8 (13%)

[a]Abbreviations: Str, stretch; Be, bend; Py, pyrimidine; Sci, scissors; Pu, purine.

Table 3.3: Experimental resonance Raman shifts of protonated 9DAG in water and D_2O at pH 1.5 and computed (wB97XD/6-31G (d, p)) vibrational wavenumbers of protonated 9DAG with mode assignments[a]

UVRR in H_2O	DFT	Mode assignments	UVRR in D_2O	DFT	Mode assignments
1715	1912	Str C6O6 (78%) + Str C5C6 (-14%)	1700	1906	Str C6O6 (-79%) + Str C5C6 (14%)
1664	1752	Str C2N3 (-15%) + Str C2N2 (34%) + Be N3HC4 (-10%) + Be NH_2 (11%)	1625	1704	Str C2N3 (-20%) + Str C2N2 (38%) + Be N1C2N3 (-18%)
1601	1696	Str C4C5 (-13%) + Str C2N3 (12%) + Be NH_2 (20%)	1584	1671	Str C4C5 (24%) + Str N1C2 (16%) + Str C2N3 (-14%)
1549	1615	Str C4C5 (21%) + Str N1C2 (-13%) + Str N3C4 (-13%)	1552	1610	Str C4C5 (-17%) + Str N1C2 (-11%) + Str N3C4 (18%)
1453	1591	Str C2N3 (-12%) + Be C4C5N7 (14%) + Be N7C8H (11%)	1436	1564	Str C2N3 (-12%) + Str C8C9 (11%) + Str N1C2 (18%) + Be C8HC9 (-16%)
1417	1510	Str C8C9 (29%) + Str N7C8 (-15%) + Be N7C8H (21%)	1415	1485	Str C8C9 (27%) + Str C5C6 (-11%) + Be C4C5N7 (-12%) + Be C8HC9 (-11%)
1533	1546	Str C5N7 (26%) + Be N7HC8 (22%) + Be N7C8C9 (18%)	1481	1514	Str C5N7 (32%) + Be C8HC9 (26%)
1377	1363	Str C2N2 (16%) + Str C5N7 (-11%) + Be N3HC4 (20%) + Be N1HC2 (-13%) + Be N1HC8 (11%)	1400	1416	Str N7C8 (27%) + Str N3C4 (-14%) + Be C4C9H (15%)
1355	1406	Str N7C8 (-13%) + Be N1HC2 (35%)	1300	1323	Str N7C8 (-17%) + Be ND2 (13%)
1296	1248	Str N7C8 (-15%) + Be N7HC8 (-16%) + Be C5N7C8 (-14%)	1246	1206	Be C8HC9 (10%) + Be C4C9H (18%) + Be C5N7C8 (15%)
1228	1120	Str C8C9 (15%) + Str N7C8 (12%) + Be C2N2Ha (-16%)	1362	1179	Str C8C9 (12%) + Str N7C8 (13%) + Be N3HC4 (-16%) + Be N1DC2 (-16%) + ND2 (-11%)

1142	1116	Str N1C2 (-15%) + Be C8C9H (30%)	1166	1125	Str C2N2 (-10%) + Be C8HC9 (18%) + Be C4C9H (-10%) + Be ND2 (27%)

[a]Abbreviations: Str, stretch; Be, bend; Py, pyrimidine; Sci, scissors; Pu, purine.

3.3.3 Neutral, protonated and deprotonated forms of 9DAH

9DAH, an analogue of Hx, possess carbon in place of nitrogen at 9th position of purine. Therefore, unlike in case of Hx which is known to exist as a mixture of N7H and N9H tautomer, 9DAH exists only in N7H form at pH 7. Although 9DAH, Hx and IMP differ in terms of slight substitution in the purine ring, they have discrete UVRR spectra. In the present work, I have elucidated the solution structure of 9DAH at pH 1.5, 7 and 10.5. UVRR spectra of 9DAH at these pH values were acquired and compared with the computed spectra of 9DAH in neutral, cationic form protonated at N3, and anionic form deprotonated either at N1 or N7. I found that at lower pH 9DAH exists as N3H protonated form and at higher pH, deprotonation occurs at N1 position of the purine ring. I have further compared the UVRR spectrum of 9DAH with that of IMP.

3.3.4 9DAH exists as neutral species with proton at N1 and N7 positions at physiological conditions

Carbonyl stretch: A weak band in the UVRR spectrum of 9DAH at 1681 cm^{-1} is assigned to carbonyl stretch coupled to N1—H (Figure 3.4 and Table 3.4). The band shows an isotope induced (H→D) shift of 15 cm^{-1} indicating the weakening of C=O bond of the purine ring. This observed downshift is similar to the one observed in IMP (17 cm^{-1}) upon H→D labeling. Similar isotope induced downshift implies that the mode is equally sensitive to the perturbations at C6—O and N1—H bonds in 9DAH and IMP. Thus, the carbonyl moiety of 9DAH can very well mimic Hx/IMP in terms of their ability to form non-covalent interactions with active-site residues. In deprotonated 9DAH at pH 12.5 (Table 3.5), the loss of proton at N1 position of purine ring results in the downshift of the band in computed (1732 cm^{-1}) and experimental (1664 cm^{-1}) wavenumbers. Further, absence of any isotope induced shift indicates that at higher pH in 9DAG-, a proton is lost from N1 position of purine ring. In protonated species, the band upshifts to 1730 cm^{-1} with respect to that in the neutral form (Table 3.6). An upshift in the wavenumber of carbonyl implies absence of charge separation and hence stronger C6=O bond.

C2—N3 stretch coupled to bending vibrations: The band at 1602 cm^{-1} in the neutral 9DAH is assigned to C2—N3 str coupled to N1—H, C2—H and N7—H bends. Upon deuteration, downshifts in the computed and experimental wavenumbers indicate the contribution from the labile hydrogens on the purine ring. This band appears at 1598 cm^{-1} in 9DAH-, and further downshifts to 1595 cm^{-1} upon deuterium labeling suggesting a minor contribution from N7—H bends. In 9DAHH+ at pH 1.5, the band upshifts to 1653 cm^{-1}. DFT calculations also predict an upshift of 35 cm^{-1} in the mode in 9DAHH+ as compared to the neutral form.

C—N stretch coupled to C—C stretch: The band at 1523 cm^{-1} is maximally attributed to N3—C4 str. Further, N3 in 9DAH remains deprotonated at pH 7 (neutral species) and at pH 12 (deprotonated species) and thus any isotope induced shift in this band at these pH values indicates the over-all distortion in the purine ring moiety. By contrast, at lower pH, 9DAH is protonated at N3 position and thus show a huge H→D induced downshift of 34 cm^{-1}. Differential intensities of this band in neutral and deprotonated form can report on the perturbations in the protonation-state of 9DAH.

Pyrrole ring mode: The band pertaining to pyrrole ring mode appears at 1424 cm^{-1} and is contributed by C4—C5 str coupled to C5—N7—C8 and N7—C8—C9 bends. This band shows a huge downshift of 91 cm^{-1} upon deuteration. In 9DAH- at pH 12.5, the band does not show any shift with respect to the neutral form suggesting no contribution from N1—H part of purine ring. In 9DAHH+, the mode appears at 1421 cm^{-1} with an additional contribution from N1HC2 bend, as predicted by DFT. A minor downshift in all protonation-states upon H→D labeling suggests minor contribution from N—H str and bends into the ring mode.

Pyrimidine ring mode: An intense band at 1388 cm^{-1} in the spectrum of neutral 9DAH is assigned to pyrimidine ring mode which is contributed by C2HN3 bend, N1HC6 bend and C2—N3, N3—C4 str. H→D labeling of 9DAH results in a downshift of 8 cm^{-1} and intensity loss of this band. In 9DAH- at pH 12.5, the band appears at 1368 cm^{-1} with a weak intensity and

shows a downshift of 1 cm^{-1} upon deuterium labeling. DFT calculations also predict a minor downshift of 3 cm^{-1}. In protonated 9DAH, the band at 1371 cm^{-1} is assigned to this mode. DFT calculations predict that H→D labeling results in large reorganization of the normal mode composition which results in a huge downshift of 270 cm^{-1}. Thus in the experimentally observed spectrum the band corresponding to 1371 cm^{-1} in D_2O downshifts to a wavenumber region below the range of examination in these experiments.

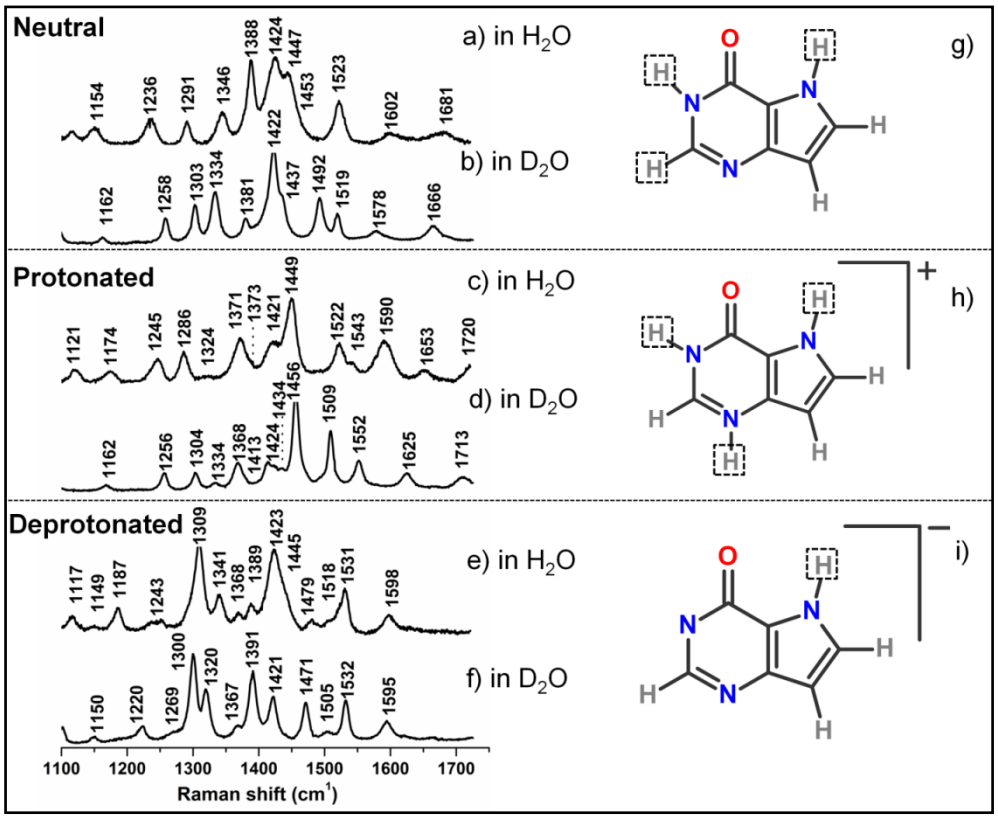

Figure 3.4: Resonance Raman spectra of 9DAH acquired at an excitation wavelength of 260 nm. Concentration of nucleobase in the spectra (a) to (f) was 500 µM and was prepared in 20 mM Tris-HCl. pH of the sample was adjusted by dissolving appropriate amount of 13 N HCl and 10 N NaOH for the pHs acidic (1.5) and basic (12.5), respectively. (g) to (i) are the corresponding chemical structures of 9DAH. Protons marked within dashed boxes are labile and would be replaced by deuterons in D_2O buffer. In order to prepare the samples in D_2O, appropriate amount of NaOD and DCl was added in D_2O.

Purine ring mode: An intense band at 1346 cm^{-1} in the UVRR spectrum of neutral 9DAH is assigned to the purine ring distortion mode having contribution from C2HN3 and N7HC8 bends followed by N3—C4, C5—N7 and N7—C8 str. Upon deuteration, an observed downshift of 44 cm^{-1} in this

band is underestimated in DFT calculations which show a downshift of 29 cm^{-1}. Further, the band appears at 1341 cm^{-1} in the UVRR spectrum of 9DAH- at pH 12.5 and shows a downshift of 21 cm^{-1} upon H→D labeling. This downshift implies the contribution of N7H str to this mode and corroborates that the proton at N7 position remains intact at higher pH and thus N1 is the site of deprotonation. In 9DAHH+, the band at 1373 cm^{-1} is attributed to this mode which further downshifts to 1334 cm^{-1} upon deuteration. DFT calculations predict an upshift in the band from neutral to protonated 9DAH species which arises from the decoupling of N1H bend from the rest of the purine ring mode. Since, the inherent wavenumber of C—N str lies in the region of 1400-1600 cm^{-1} [18, 201] and thus decoupling of N1—H results in the upshift of the C—N str to the higher wavenumber region.

C—H bending mode in pyrrole ring: The band at 1291 cm^{-1} is attributed to the C8HC9 and C8C9H bends along with a minor contribution from N1—C6 str. A downshift of 34 cm^{-1} is observed upon H→D labeling in neutral 9DAH. In 9DAH-, the band appears at 1243 cm^{-1} and downshifts to 1220 cm^{-1} upon deuteration. The isotope induced shift in 9DAH-, where no N1—H proton is present, suggests the reorganization of the normal mode to include contribution from N7—H. DFT calculations also predict different composition of the normal mode in deprotonated and neutral species. The mode reorganizes to include N1—C2—N3, C4—C5—N7 bends in addition to C8HC9 and C8C9H bends. Further, in protonated species (9DAHH+), the band appears at 1286 cm^{-1} and downshifts to 1256 cm^{-1} (-30 cm^{-1}) upon H→D labeling similar to the downshift predicted by DFT calculations (21 cm^{-1}).

N7—H bending mode: The band at 1236 cm^{-1} in the 9DAH spectrum at pH 7.0 is assigned to N7HC8 and C8C9H bends. This band upshifts to 1309 cm^{-1} and 1245 cm^{-1} in deprotonated and protonated 9DAH, respectively. H→D labeling results in the decoupling of N7HC8 and the reorganized mode is comprised of C5—N7—C8 bend in all three species.

Table 3.4: Experimental resonance Raman shifts of neutral 9DAH in water and D_2O at pH 7.0 and computed (wB97XD/6-31G (d, p)) vibrational wavenumbers of neutral 9DAH with mode assignments[a]

UVRR in H_2O	DFT	Mode assignments	UVRR in D_2O	DFT	Mode assignments
1681	1850	Str C6=O (71%) + C6N1C2 (-12%) + N1H	1666	1843	Str C6=O (74%) + Be C6N1C2 (-10%)
1602	1698	Str C2N3 (59%) + Be N1H + C2H + N7H	1578	1690	Str C2N3 (61%) + Be C2H
1523	1604	Str C4C5 (32%) + C8C9 (-16%) + Str N3C4 (-11%)	1492	1595	Str C4C5 (43%) + Str C8C9 (-16%) + StrN3C4 (-16%)
1455	1584	Be C4C5N7 (32%) + Be C5N7C8 (10%)	1439	1568	Be C4C5N7 (30%) + Be C8HC9 (-16%) + Be C5N7C8 (11%) + Be C2H
1447	1526	Str C8C9 (39%) + Be C8HC9 (-13%)	1422	1516	Str C8C9 (42%) + Be C4C5N7 (-15%)
1424	1500	Str C5N7 (17%) + Be N7C8C9 (17%) + Be C5N7C8 (-11%) + Str C4C5 (-10%)	1333	1487	Str C5N7 (31%) + Be N7C8C9 (19%) + Str C4C5 (-14%) + Be C5N7C8 (-12%)
	1464	Be N1HC6 (33%) + Str N1C2 (-20%) + Str C4C5 (11%)			
1388	1443	Be C2HN3 (43%) + Be N1HC6 (12%) + Str N3C4 (-11%) + Str C2N3 (10%)	1380	1439	Be C2HN3 (58%)
			1519	1371	Str N1C2 (40%) + Str N1C6 (-17%) + Be N1HC2 (-13%)
1346	1371	Be C2HN3 (23%) + Str N7C8 (-21%) + Str C5N7 (-12%) + Str N3C4 (12%) + Be N7HC8 (11%)	1302	1342	Str N7C8(35%) + Str N3C4 (-10%) + Be N1H+ C2H

1291	1323	Be C8HC9 (19%) + Str N1C6 (-18%) + Be C8C9H (-11%)	1257	1296	Be C8HC9 (20%)
1236	1251	Be N7HC8 (21%) + Be C8C9H (-12%)	1163	1188	Be C8HC9 (19%) + Be C8C9H (-14%) + Be C5N7C8 (13%)
1151	1153	Str N1C2 (22%) + Str N7C8 (18%) + Be N1HC2 (17%) + Str N1C6 (-12%) + Be C8HC9 (-11%)			
1118	1128	Str N7C8 (24%) + Str N1C2 (-15%) + Be N7HC8 (10%) + Be N1HC2 (-11%)			
1086	1097	Str N1C6 (14%) + Be N7HC8 (13%) + Be C5N7C8 (-13%)	1095	1114	Str N1C6 (28%) + Str N7C8 (-14%) + Be N1C6O (-12%)
1062	1082	Be C9HC8 (49%) + Str C8C9 (17%) + Be C8HC9 (15%)	1064	1083	Be C9HC8 (44%) + Be C8HC9 (17%) + Str C8C9 (16%)

[a]Abbreviations: Str, stretch; Be, bend; Py, pyrimidine; Sci, scissors; Pu, purine.

Table 3.5: Experimental resonance Raman shifts of deprotonated 9DAH in water and D_2O at pH 12.5 and computed (wB97XD/6-31G (d, p)) vibrational wavenumbers of deprotonated 9DAH with mode assignments[a]

UVRR in H_2O	DFT	Mode assignments	UVRR in D_2O	DFT	Mode assignments
1663	1732	Str C6O6 (69%) + Be N1C6C2 (-11%)	1664	1732	Str C6O6 (69%)+ Be C6N1C2 (-10)
1598	1633	Str C2N3 (-13%) + Str C8C9 (-10%) + Str C4C5 (24%) + C2H + N7H	1595	1628	StrC2N3 (-115) + Str C8C9 (-12%) + Str C4C5 (29%)
1518	1605	Str C2N3 (12%) + Str N3C4 (-11%) + Be C4C5N7 (32%)	1505	1601	Str C2N3 (20%) + Str N1C6 (-10%) + Be C4C5N7 (30%)
1531	1469	Str C4C5 (-11%) + Str C5N7 (23%) + Be N7C8C9 (15%) + Be N7HC8 (12%)	1532	1501	Str C4C5 (-24%) + Be C2HN3 (20%) + Be C4C5N7 (14%)
1479	1546	Str C8C9 (37%) + Be C8HC9 (-17%) + Be C2HN3 (13%)	1471	1543	Str C8C9 (39%) + Be C8HC9 (-19%) + Be C2HN3 (105) + Be C5N7C8 (10%)
1424	1513	Str C4C5 (-16%) + Str N7C8 (11%) + Be C2HN3 (20%)	1391	1448	Str N7C8 (-10%) + Str C5N7 (31%) + Be N7C8C9 (13%)
1445	1405	Str N1C2 (35%) + Str N1C6 (-10%) + Be C2HN3 (-17%)	1421	1394	Str N1C2 (38%) + Str N7C8 (11%) + Be C2HN3 (-16%)
1368	1413	Str C2N3 (25%) + Be C2HN3 (33%)	1367	1410	Str C2N3 (26%) + Str N3C4 (-11%) + Be C2HN3 (26%)
1341	1325	Str N1C2 (11%) + Str N3C4 (18%) + Str N7C8 (-17%) + Str N1C6 (-15%) + Str C5N7 (-12%)	1320	1319	Str N3C4 (-18%) + Str N7C8 (22%) + Str N1C6 (13%)

1243	1261	Str C2N3 (-10%) + Be N7HC8 (12%) + Be C8HC9 (25%) + Be C8C9H (-13%) + Be C4C5N7 (11%) + Be N1C2N3 (10%)	1220	1249	Str C2N3 (-11%) + Str N7C8 (-16%) + Be C8HC9 (21%) + Be N1C2N3 (11%)
1309	1208	Str C5N7 (-10%) + Be N7HC8 (18%) + Be C5N7C8 (11%)	1300	1169	Be C8HC9 (15%) + Be C8C9H (-12%) + Be C5N7C8 (14%)

[a]Abbreviations: Str, stretch; Be, bend; Py, pyrimidine; Sci, scissors; Pu, purine.

Table 3.6: Experimental resonance Raman shifts of protonated 9DAH in water and D_2O at pH 1.5 and computed (wB97XD/6-31G (d, p)) vibrational wavenumbers of protonated 9DAH with mode assignments[a]

UVRR in H_2O	DFT	Mode assignments	UVRR in D_2O	DFT	Mode assignments
1730	1917	Str C6=O (77%) + Str C5C6 (-14%)	1713	1911	Str C6=O (80%) + StrC6C5 (-13%)
1658	1733	Str C2N3 (34%) + Str N1C2 (-16%) + Be N1C2H (14%) + Be N1H + C2H + N7H	1625	1719	StrC2N3 (35%) + StrN1C2 (-20%) + Be N1C2H (16%)
1543	1639	Str N1C2 (-19%) + Str N3C4 (18%) + Be N3HC2 (28%)	1509	1610	Str C4C5 (-26%) + Str N3C4 (30%)
1599	1616	Str C2N3 (10%) + Str C8C9 (25%) + Str N3C4 (-10%) + Be N7HC8 (11%)			
1444	1572	Str C4C5 (-13%) + Str C5N7 (23%) + Be N7HC8 (11%) + Be C4C5N7 (-12%)	1456	1587	Str N1C2 (14%) + Str C8C9 (14%) + Str C4C5 (-11%) + Be N1C2H (-10%) + Be C8HC9 (-11%) + Be C4C5N7 (17%)
1421	1528	Str C5N7 (15%) + Be N7C8C9 (19%) + Be N1HC2 (18%)	1424	1531	Str C4C5 (-12%) + Str C5N7 (40%) + Be N7C8C9 (11%)
			1413	1475	StrN7C8 (11%) + Be C8HC9 (15%)
1451	1502	Str C8C9 (28%) + Str N7C8 (-12%) + Be C8HC9 (-17%)	1434	1489	StrC8C9 (-30%) + Be C4C5N7 (17%)
1324	1451	Str C8C9 (-13%)+ Be N1HC2 (-16%) + Be C8C9H (10%) + Be C2H + Be N1H	1304	1413	StrN1C2 (25%) + Be N1C2H (33%) + Be C2H + Be N1D

1371	1330	Be C2N3H (-28%) + Be N1HC2 (11%) + Be N1C2H (35%)		1060	Str N7C8 (12%) + Be C2N3D (23%) + BeN1DC2 (-16%) + Be C6C5N7 (10%)
1373	1395	Str C5N7 (-18%) + Str N7C8 (-20%) + Be N7C8H (18%)	1334	1351	Str N7C8 (40%) + Be N1C2H (20%)
1286	1302	Str C8C9 (11%) + Str N3C4 (-12%) + Be C8HC9 (21%) + Be C8C9H (-13%)	1256	1281	Str C8C9 (12%) + Str N3C4 (-10%) + Be C8HC9 (26%)+ Be C8C9H (-11%)
1245	1264	Str N7C8 (11%) + Be N7HC8 (13%)	1162	1198	Be C8C9H (-15%) + Be C5N7C8 (13%)
1174	1188	Str C2N3 (23%) + Str N1C2 (27%) + Be C2N3H (12%) + Be N1HC2 (21%)			
1121	1137	Str N7C8 (29%) + Be N7HC8 (21%) + Be C8HC9 (-18%)			
1073	1098	Str C8C9 (18%) + Be C8HC9 (20%) + Be C8C9H (51%)			

[a]Abbreviations: Str, stretch; Be, bend; Py, pyrimidine; Sci, scissors; Pu, purine.

3.4 Assessment of the performance of DFT

DFT is one of the most widely used and cost-effective procedures to determine vibrational spectra of molecules. The hybrid functional wB97XD accounts for dispersive forces and had previously been shown to predict the compact structural parameters well [179]. Dispersion also affects chemical bonds and thus use of such a functional minimizes the general over-estimation of bond order by DFT calculations. Further, the structural parameters obtained using this functional have been found to differ from those predicted by B3LYP [179]. Since, a correct structure is a pre-requisite to calculate vibrational frequencies, I chose wB97XD hybrid functional to determine the structural parameters and vibrational frequencies.

In the following, the performance of DFT (wB97XD/6-31G (d, p)) in predicting vibrational wavenumbers in nucleobases and H→D induced isotopic shifts is discussed. Though the experiments are carried out in solution and the calculations are conducted *in vacuo*, the H→D induced isotopic shift is reproduced reliably. Furthermore, the isotopic shifts in the region from 1100 cm^{-1} to 1500 cm^{-1} are reproduced moderately well as compared to the wavenumbers above 1500 cm^{-1} in 9DAG as well as in 9DAH. In particular, an exceptionally huge difference in the —NH_2 scissoring mode in neutral 9DAG is observed where a computed isotopic downshift of 397 cm^{-1} (1655 cm^{-1} to 1258 cm^{-1}) is predicted against an observed isotopic shift of 217 cm^{-1} (1608 cm^{-1} to 1391 cm^{-1}). This indicates the limitations of DFT in prediction of the normal mode composition accurately. A lower magnitude of isotope induced shift in observed spectra suggests that in D_2O spectrum, the band at 1391 cm^{-1} retains the contribution from —ND_2 moiety more than that predicted by DFT (32%). Also, the calculated wavenumbers are obtained under harmonic approximation. The substantial differences in the higher wavenumber region between the UVRR experiments and calculations are attributed to the anharmonicity of the system. In cytosine and uracil, it has been reported that even higher level DFT calculations, done under *in vacuo* conditions, predict erroneous wavenumbers [194]. The wavenumbers predicted above 1300 cm^{-1} are overestimated by more than 80 cm^{-1}. Incorporation of PCM model did not

improve the results. DFT methods, however, are by far the most widely used methods to predict the normal mode assignments which are the pre-requisite for using resonance Raman spectroscopy as a probe to report on the nucleobase-protein interaction.

3.5 Conclusion

The present chapter reports on the solution structures of 9-deazapurines at different pH values. The systematic observation of purine spectra and their assignments to normal mode vibrations in the present study provides the basis to examine these molecules in their enzyme-bound forms. In 9DAG and GMP, the neutral species bears a proton at N1 position. Deprotonation at higher pH occurs from N1 position in both the molecules. However, the two molecules have different structures at lower pH. Whereas N3 is protonated in 9DAG, in case of GMP protonation occurs at N7 position at lower pH. In case of 9DAH, N1 is the site of deprotonation at pH 12.5 whereas no deprotonation is observed at N7. In the corresponding nucleobase Hx, the first deprotonation, at pH 10, occurs from N7 of purine ring followed by a second deprotonation from N1 at pH 12.5. Apart from the protons at N1 and N7 positions in neutral form, 9DAH bears an additional proton at N3 position at lower pH. Protonated Hx, on the other hand, bears proton at N1, N7 and N9 positions. Further, in IMP which possesses a sugar moiety at N9 position, protonation at lower pH occurs at N1 and N7 positions.

A localized carbonyl stretch mode captures the effect of protonation and deprotonation in 9DAG as well as 9DAH. This result is remarkably similar in 9DAG and GMP, and in 9DAH and IMP across different pH values in H_2O and D_2O. Also, the purine base analogues, studied here, exist in keto (C6=O) form instead of (C6—OH) form in solution at all pHs. Since, these purine analogues bind to a number of enzymes of nucleotide synthesis pathway thus the work presented here can be extrapolated to the complexes of these molecules with the enzymes. Effect of isotope labeling at N1 position is manifested in the form of shift in the carbonyl stretch. This makes the carbonyl stretch a suitable marker band of hydrogen bonding interactions between N1 of purine ring and the active-site residues. Further, intense bands

arising from pyrimidine and pyrrole ring in 9DAG and 9DAH can serve as a probe to report on the local environment changes of these ligands upon encountering the amino-acid residues at the active-site.

Comparison of isotopic (H→D) induced shifts between experimental and computed wavenumbers have been used as an important criterion for the normal mode assignments of the observed UVRR bands in the solution state. Further, calculated Raman shifts upon protonation and deprotonation show similar trend as that of observed shifts. These results corroborate the assignments of the observed protonation state at lower and higher pH.

This study has the direct implication on the structural studies of PNP and HGPRT catalysis which are the integral enzymes of purine salvage pathway. Since the *de novo* nucleotide synthesis pathway is absent in *Plasmodium falciparum*, Hx derived from the salvage pathway is the sole source of purines in these parasites. Hence, PNP and HGPRT are considered as the potential targets of anti-malarials. In this regard, elucidating the solution structure and protonation-state in potent nucleobase inhibitors is indispensable in any type of structural studies. Further, it will help in future vibrational studies of the nucleobase analogues at the active-site of enzyme.

"Spoken words fly away, written words remain."

Latin proverb

4

Differential Distortion of Purine Nucleobases in Human and *Plasmodium falciparum* HGPRT

4.1 Introduction

Enzymes are central to all biochemical processes exhibiting enormous rate accelerations with extraordinary specificity. Several general strategies that reveal the mechanistic in enzyme catalysis have been proposed [1, 2, 38-40]. With the proposal of transition-state theory, the idea that the active-site is complementary to the transition-state of the reaction propelled [37]. This is the most widely accepted proposal which is now known as transition-state stabilization (TSS). Previous work has also shown that enzymes employ an elusive strategy called ground-state destabilization (GSD) [4-11]. The energy of enzyme•substrate complex (E•S) is raised by the distortion or strain caused due to non-covalent interactions formed at the active-site of enzyme. Further, it may also happen that at the active-site, the charges of the substrate molecules are placed next to the similar charges of amino-acid residues at the active-site. This is the basis of electrostatic destabilization. Using site directed mutagenesis, Herschlag and co-workers have shown that orotate phosphoribosyltransferase employs similar strategy to enhance the rate of the reaction [11, 12]. Such distortions lead to structural changes in the enzyme-bound substrate, which are quite small. For instance, catalysis by ketosteroid

isomerase employs shortening of hydrogen bond distance between ligand and active-site residue [14]. Peptide bond hydrolysis involves lengthening of carbonyl bond from 1.2 to 1.4 Å , an elongation of 0.2 Å in the bond length [16]. Obtaining such a resolution and level of precision from other biophysical technique is technically challenging. Thus, I have employed a vibrational technique, ultraviolet resonance Raman spectroscopy (UVRR), to experimentally observe such distortions in enzyme bound ligands. Vibrational spectroscopy is a very sensitive technique which can measure structural changes in enzyme bound ligands, on the order of a bond-length [7, 15, 17-22].

This chapter of my thesis is aimed at understanding the extent of such ground-state distortion in E•S complex. For this, I have worked with hypoxanthine guanine phosphoribosyltransferase (HGPRT) from human (h) and *Plasmodium falciparum* (Pf). HGPRT catalyzes the Mg^{2+} dependent phosphoribosylation of guanine and hypoxanthine. PfHGPRT, in addition to catalyzing the two nucleobases, can also convert xanthine to xanthosine-5'-monophosphate (XMP). The reason of this disparity in substrate specificity remains elusive in literature. Thus, this part of my thesis addresses the fundamental question of ground-state distortion as well as the reason behind the differential substrate specificity in these two homologues.

4.2 Methodology

4.2.1 HGPRT Sample Preparation

PRPP, magnesium chloride and sodium nitrate were obtained from Sigma-Aldrich Co. 9-deazaguanine (9DAG) and 9-deazahypoxanthine (9DAH) were a gift from Dr. Vern Schramm. UVRR Samples were prepared in 20 mM Tris-HCl pH 7 for hHGPRT experiments and 20 mM potassium phosphate pH 7 for PfHGPRT experiments. Concentration of nucleobases, HGPRT and PRPP in each sample was 500 µM, 150 µM and 1 mM, respectively. Spectra were recorded in buffer containing 12 mM $MgCl_2$, 30 mM $NaNO_3$ and 1 mM PRPP. hHGPRT was activated by incubating overnight

at 4°C in the buffer containing 5 mm DTT. Similarly, PfHGPRT was activated by adding 60 μM IMP and 5 mm DTT, three hours prior to experiment [193].

4.2.2 Structure determination of nucleobases bound to the amino-acid residues

The active site was modeled using dispersion corrected density functional wB97XD [198] with a 6-31G (d, p) basis set as implemented in Gaussian 09 [149]. Ground state structures of 9DAG and 9DAH *in vacuo* and in the protein-bound form (along with active-site residues D137, D193, K165, F186 and V187) were obtained through energy minimization. Initial coordinates for the structure determination were obtained from the structure of hHGPRT and ImmucillinGP complex (1BZY) as follows. Hydrogen atoms were added using GaussView 5.0 [199]. The nucleobase was modified to 9DAG and the ribose-5'-monophosphate group was replaced with a proton at C9 position. Coordinates of the backbone (carboxylic group, Cα and amino group) of all the residues were frozen and those of the side-chains and the nucleobase were allowed to be varied for location of the ground state structure through energy minimization. F186 stacks over the nucleobase at the active-site of hHGPRT and thus was incorporated in the QM calculations. H-bond distances between 9DAG and interacting residues were determined and compared with those in 1BZY to ensure that the overall structure was preserved. Mulliken partial atomic charges and structural parameters of 9DAH in presence and absence of amino-acid residues were also determined. Raman vibrational spectra were computed at the minimum energy geometry at the same level of theory. Shifts in the computed wavenumbers of 9DAG in presence and absence of active-site residues were determined. The resultant shift in each band was compared with the corresponding experimental shift. Similar protocol was used to model the complex between 9DAH and HGPRT.

4.3 Section I: Elucidating distortion in purine ligands using UVRR

Using a highly sensitive, UVRR spectroscopy, I have studied complexes of both the homologues bound to substrate analogues, 9DAG and 9DAH. I have elaborated the technique in great detail in Chapter 1 and a brief account is

mentioned herein. UVRR is a powerful technique which can report on the structural changes at sub-angstrom level of a molecule. Band positions in a vibration spectrum are directly related to the force constants of bonds. Thus, distortion in the substrate molecule that results in a small change in bond strength can manifest as an altered vibrational shift. Also, UVRR is the experimental method of choice for studying enzyme-nucleobase complexes because of the high cross-section of nucleobases at UV wavelengths. In addition, different cross-sections in the absorption spectra of enzymes and nucleobase provide selective enhancement of the substrate spectra without interference from protein vibrations (Figure 4.1) which in turn allows studying of distorted ligand bound to the enzyme. These spectra inform on the conformation, protonation-state and structure of bound nucleotides.

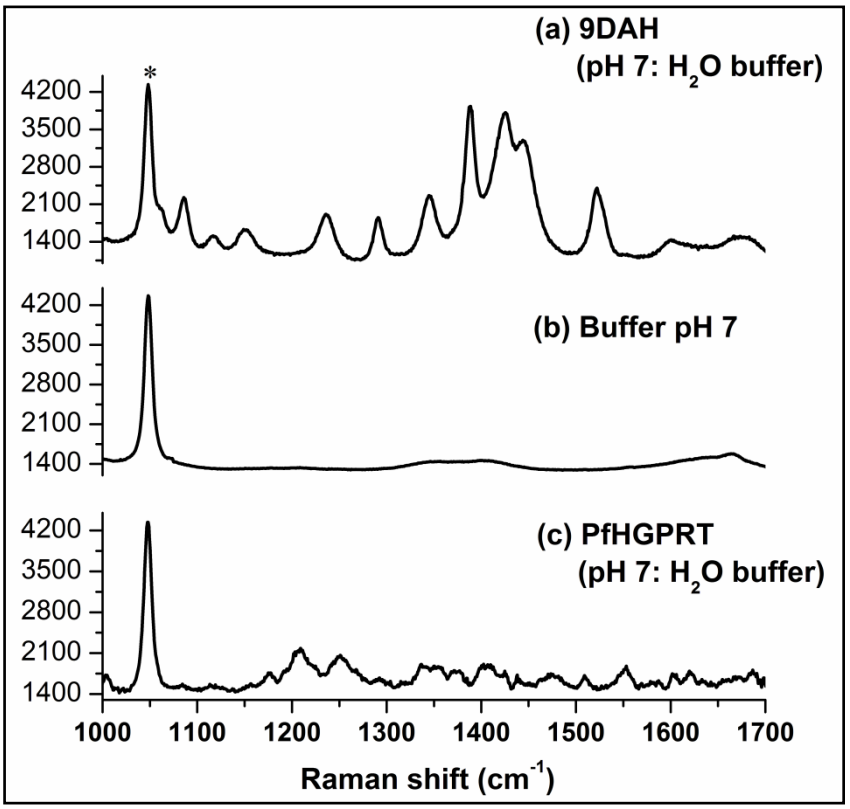

Figure 4.1: Raman spectra of (a) 9DAH, (b) Tris-HCl, pH 7 and, (c) *Pf*HGPRT; acquired at the excitation wavelength of 260 nm. The $NaNO_3$ band (internal standard) at 1049 cm^{-1} is marked with (*).

4.3.1 9DAG bound to human and Pf HGPRT

UVRR spectra of guanine analogue, 9DAG, in complex with hHGPRT and PfHGPRT, are shown in Figure 4.2. The Spectral contributions from

enzyme and unbound ligand have been removed. As elaborated in Chapter 3, observed bands were assigned to the computed normal modes of vibrations of 9DAG through density functional theory (DFT) calculations. Comparison of UVRR spectra of 9DAG in solution and bound at the active-site of hHGPRT and PfHGPRT show marked differences in the position and intensity of the bands. These differences reflect distortion in the structure of 9DAG upon binding to the active site of the enzymes. In the following, the observed wavenumber and change in the intensity pattern of the bound nucleobases have been discussed in detail.

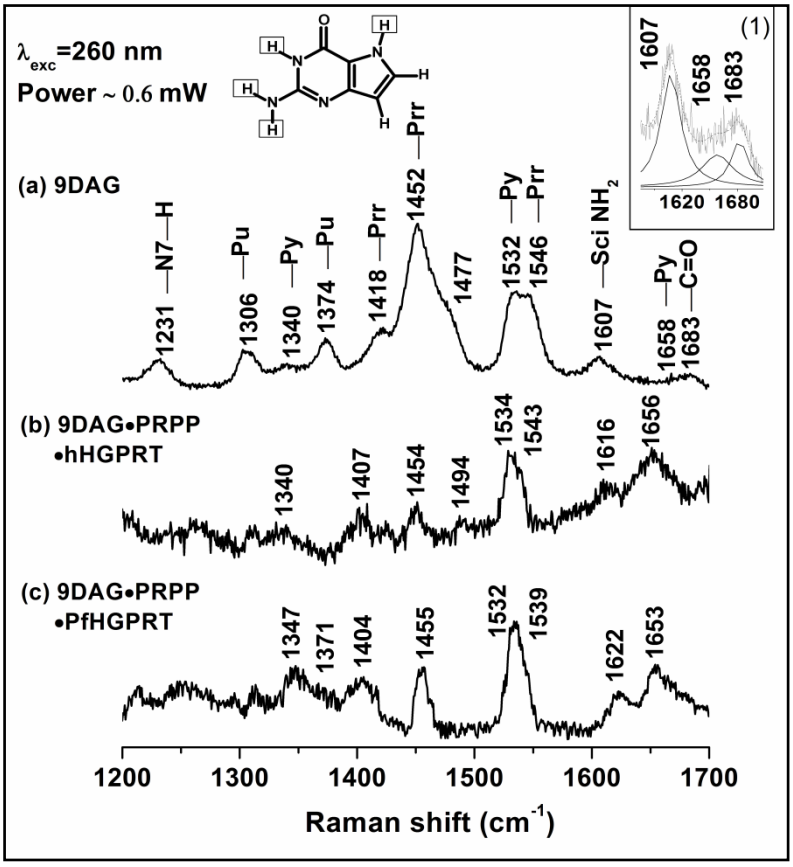

Figure 4.2: Binding of 9DAG to HGPRT homologues in presence of PRPP and Mg^{2+}. UVRR spectrum of: (a) 9DAG, inset (1) shows an enlarged region with fit to the band at 1658 cm^{-1}, (b) 9DAG•PRPP•hHGPRT in Tris-HCl buffer, pH 7, (c) 9DAG•PRPP•PfHGPRT in potassium phosphate buffer, pH 7, obtained with 260 nm excitation. Assignment to each band is shown as superscript above the corresponding wavenumbers in spectrum (a). Chemical structure of 9DAG is shown.

HGPRT distorts the bound nucleobase towards the transition-state structure and orientation

Carbonyl stretching vibration, at 1683 cm^{-1} of 9DAG, is downshifted to 1656 cm^{-1} (27 cm^{-1}) in hHGPRT•9DAG to 1657 cm^{-1} (25 cm^{-1}) in PfHGPRT•9DAG (Table 4.1). The downshift results from the hydrogen bond interaction between C6=O and Lys165 in hHGPRT (Lys 176 in PfHGPRT), as observed in crystal structures and quantifies the extent of weakening of the C6—O bond. Corresponding downshift in the previously reported product complex, HGPRT•GMP, is much higher (-40 cm^{-1}) [193]. Lower downshift indicates that the bond order of the C=O is higher in the forward complex than in the product complex. Scheiner and Latajka [202] have found that the magnitude of Raman wavenumber shift in carbonyl stretch is more sensitive to the angle of approach between C=O and the proton donor (θ_{DA}) than to the interaction energy. There is an inverse correlation so that θ_{DA}=120° will produce greater downshift in the C=O wavenumber than θ_{DA}=180°. This reflects the nature of the in-plane, lone-pair orbitals of the oxygen that are involved in forming the H-bond with the Lys resdiue. In the structure of the product complex, hHGPRT•GMP, θ_{DA} is found to be closer to the optimal hydrogen bond angle, at 134.6° [90] corresponding to a large downshift ($\Delta\nu$=40 cm^{-1}) in the Raman wavenumber [193]. The smaller downshift observed in complexes of the substrate analogues, indicates that θ_{DA} in hHGPRT must be larger than in the product complex and not optimal for hydrogen bonding (Table 4.2). Indeed, the two known crystal structures of human and Pf enzyme with TS analogues show θ_{DA}~140° [74, 88]. Thus in the HGPRT•9DAG•PRPP complex, UVRR spectra show that 9DAG is already bound in an orientation and structure close to that of the transition-state. It also shows that the active-site residues are oriented in the reactive conformation.

The 9DAG band at 1658 cm^{-1} (Inset 1 in Figure 4.2) is a coupled vibration with contributions from C2—N3, C2—NH_2 stretch (localized on the pyrimidine ring) and exocyclic —NH_2 scissoring. The large but different average downshifts of 43 cm^{-1} (hHGPRT) and 38 cm^{-1} (PfHGPRT) in this mode indicate the strong but differential influence of 9DAG with the two

enzymes. To delineate the effects of hydrogen bonding from those due to electrostatic and stacking interactions, we obtained spectra of these complexes in D_2O buffer (Figure 4.3, Table 4.3). As mentioned in Chapter 3, the Raman band assignments of the nucleobases are done by comparing the isotopic shifts (H→D) in the experimental and calculated Raman spectra. Wavenumber positions in the two cases are not used to assign normal modes to a particular band in a Raman spectrum. In D_2O, the labile hydrogens at N1, exocyclic N2 and N7 of bases are replaced with deuterium. In the free substrate, this band is downshifted to 1596 cm^{-1} ($\Delta\nu$ H/D = 62 cm^{-1}). At the active-site of HGPRT, the large downshift in this band is the result of H-bonds formed by the exocyclic —NH_2 group of 9DAG with backbone carbonyl of Val187 and Asp193 (hHGPRT numbering, V198 and Asp204 in PfHGPRT) in HGPRT (Figure 4.4). Formation of this hydrogen bond weakens the N2—H bond and thus results in the downshift in the position of this band.

Table 4.1: Comparison of shifts in wavenumber (cm^{-1}) observed in the UVRR spectra of 9DAG•PRPP•hHGPRT and 9DAG•PRPP•*Pf*HGPRT complexes with respect to 9DAG.

Mode description	UVRR		
	9DAG	9DAG•PRPP•hHGPRT*	9DAG•PRPP•PfHGPRT*
Str C6=O	1683	1656 (-27)	1653 (-25)
Py ring [Str C2N3-C2N2]	1658	1616 (-43)	1620 (-38)
Sci NH_2	1607	1576 (-30)	1576 (-31)
Prr ring [Str C4C5-C9C8-N3C4 + Be N7H + N1H + NH2]	1546	1543 (-5)	1539 (-7)
Py ring [Str C4C5N7 + Sci NH_2 + Be N3C4C5 + C9H + C8H + N1H]	1532	1534 (1)	1531
Prr ring [Be N7HC5-N7C8C9 + Str C5N7 + N7C8 ++ N1H]	1452	1454	1454 (2)
Prr ring [Str C4C5-N1C2 + Be C4C5N7]	1418	1407 (-13)	1405 (-13)

***Values in parentheses are the average shifts in the band positions obtained from three data sets ($\nu_{9DAG•PRPP•HGPRT}$-ν_{9DAG})**

Table 4.2: Bond angles between C6=O of nucleobase and proton donor (Lys residue) observed in different crystal structures of HGPRT

Crystal structure	Interaction	Bond angle between C=O…H
PfHGPRT•ImmHP (1CJB)	C=O…H9 (Lys176)	143.181°
hHGPRT•ImmGP (1BZY)	C=O…H9 (Lys165)	140°
hHGPRT•GMP (1HMP)	C=O…H9 (Lys165)	134.6°

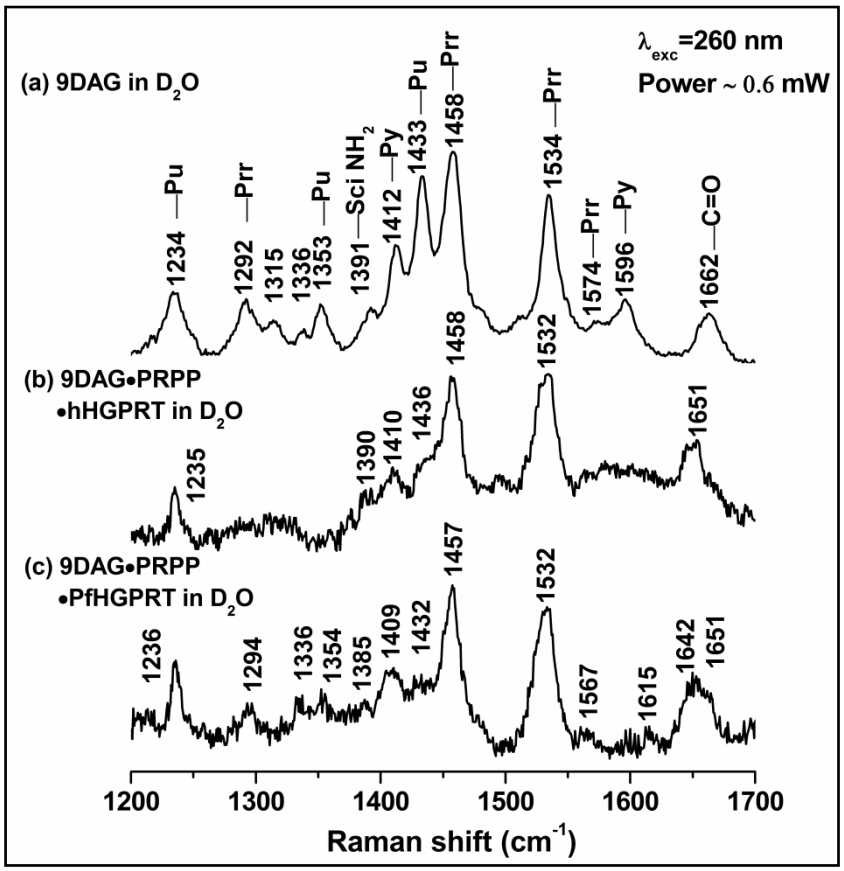

Figure 4.3: Binding of 9DAG to HGPRT homologues in D_2O in presence of PRPP and Mg^{2+}. UVRR spectrum of: (a) 9DAG, (b) 9DAG•PRPP•hHGPRT in Tris-HCl buffer, pD 7, (c) 9DAG•PRPP•PfHGPRT in potassium phosphate buffer, pD 7, obtained with 260 nm excitation.

Table 4.3: Effect of isotope labeling (H→D) on the wavenumber (cm^{-1}) of bound 9DAG. Shifts in the positions of nucleobase bands in the 9DAG•PRPP•hHGPRT (Tris-HCl buffer in D_2O) and 9DAG•PRPP•PfHGPRT (potassium phosphate buffer in D_2O) complexes with respect to unbound 9DAG in Tris-HCl buffer (pD 7.0).

Mode description	DFT	9DAG	9DAG• PRPP•hHGPRT	9DAG• PRPP•PfHGPRT
Str C6=O (68%) + Be C6N1C2 (-13%)	1843	1661	1651 (-11)	1651 (-11)
Str C2N3 (57%)	1693	1597	not observed	1615 (19)
Str C4C5 (41%) + Str C9C8 (-22%) + strN3C4 (14%)	1616	1573	not observed	1567 (-8)
Be C4C5N7 (19%) + Be N3C4C5 (19%) + Be C8HC9 (-10%)	1588	1432	1436 (8)	1432
Str C8C9 (32%) + Be C8HC9 (-16%)	1530	1535	1532 (-3)	1532 (-4)
Str C5N7 (36%) + Be C9C8N7 (20%) + Str C4C5 (-12%)	1485	1457	1458 (1)	1457 (-1)
Str N1C2 (31%) + Str C2N2 (-15%) + Str C4C5 (-14%) + Be N2D2a	1461	1412	1410 (-4)	1409 (-3)
Sci $N2D_2$ (40%) + Be N1DC6 (-12%)	1258	1390	1390 (-1)	1385 (-5)
Str N3C4 (25%) + Str N7C8 (-19%) + Be C9HC8 (11%)	1388	1352	-	1354 (2)
Str N7C8 (23%) + Str N1C6 (18%) + Be C8HC9 (-11%)	1320	1336	-	1336
Be C5N7C8 (15%) + Be C9HC8 (-13%) + Be C8HC9 (11%) + C9C8N7 (10%)	1193	1291	1287 (-2)	1294 (1)
Be N2D2a (21%) + Be N1DC2 (15%) + Str C2N3 (11%) + Be N7D+Be C9H	1184	1235	1235 (1)	1236 (2)

***Values in parenthesis represent average shift in wavenumbers ($\nu_{9DAG•PRPP•HGPRT}-\nu_{9DAG}$)**

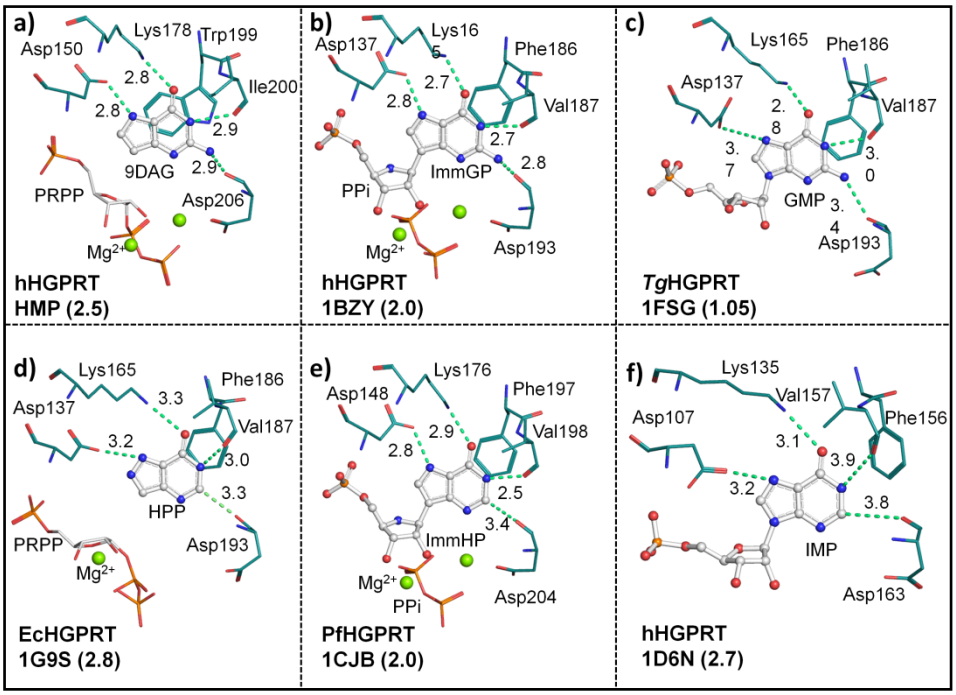

Figure 4.4: Hydrogen bonding network at different stages of HGPRT catalyzed reaction. (a), (b) and (c) are hHGPRT complexes with substrate analog (9DAG), TS analog (ImmGP) and product (GMP), respectively. (d), (e) and (f) are PfHGPRT complexes with substrate analog (HPP), TS analog (ImmHP) and product (IMP), respectively. Resolutions (Å) of crystal structures are shown in parentheses.

Stacking interactions play a key role in determining the rigidity of the active-site in two homologues

While the above mentioned bands show shifts in wavenumbers, other bands in the 9DAG•PRPP•HGPRT spectrum show marked changes in the intensity pattern. Band at 1452 cm^{-1} loses intensity by approximately 88% and 60% in 9DAG•PRPP•hHGPRT and 9DAG•PRPP•PfHGPRT complexes, respectively (Table 4.4). Also, the band at 1547 cm^{-1} shows loss in intensity in 9DAG•PRPP•hHGPRT and 9DAG•PRPP•PfHGPRT. Raman intensity modulation was observed in GMP•hHGPRT and GMP•PfHGPRT as well which was attributed to pi-stacking between GMP and Phe186 in hHGPRT (Phe198 in PfHGPRT) [193]. Comparatively greater intensity modulation observed here in 9DAG•PRPP•HGPRT complexes is also attributed to pi-stacking with the same residues but with improved packing at the active site due to loop closure in the Michaelis complex [80]. This finding is supported by pi-stacking distances observed in the respective crystal structures: in GMP•hHGPRT (1HMP: 4.15 Å), where the flexible loop remains open; and in

ImmucillinGP•hHGPRT (1BZY: 3.84 Å) and ImmucillinHP•PfHGPRT (1CJB: 3.95 Å) in the closed-loop conformation (Figure 4.5 and Table 4.5). The loss in Raman cross-section provides a quantitative measure of the differences in susbtrate•enzyme packing within the active-sites of ternary complexes. Greater loss of Raman cross-section quantifies tighter stacking in 9DAG•PRPP•hHGPRT as compared to 9DAG•PRPP•PfHGPRT.

Further corroborative evidence is obtained from the spectrum in deuterated buffer in which the band at 1432 cm^{-1} (corresponding to 1452 cm^{-1} in H_2O) drops down in intensity at the active-site of hHGPRT as well as PfHGPRT. This further suggests that in the Michaelis complex of HGPRT in solution-state, loop lies closed onto the active-site and thus the complexes in solution resembles the pre-transition state of HGPRT catalyzed reaction.

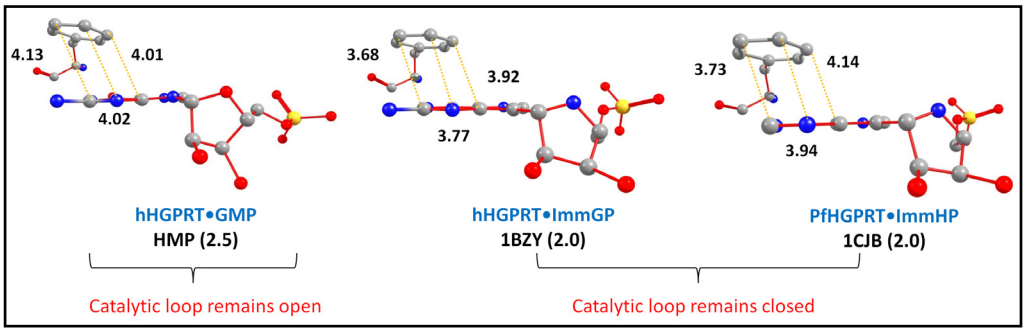

Figure 4.5: The interplanar distance between nucleobase moiety and Phe residue (a) 4.15 Å (distance between the two dummy atoms, each placed at the center of the nucleobase and the Phe residue) in hHGPRT with GMP where catalytic loop remains open, (b) 3.84 Å and (c) 3.95 Å in HGPRT with TS analogue ImmucillinGP and ImmucillinHP, respectively. Note that the catalytic loop remains closed in (b) and (c). All distances and resolution of crystal structures (in parentheses) are in Å.

Table 4.4: Comparison of different Raman band intensities in free and HGPRT bound 9DAG and in free and HGPRT bound 9DAH.

9DAG			**9DAG●PRPP●hHGPRT**				**9DAG●PRPP●PfHGPRT**			
Band position	Area	I1*	Band position	Area	I2*	Percentage change[a]	Band position	Area	I3*	Percentage change[a]
1417	2499.7	0.83	1406	1612.9	0.59	-29.59	1408	1359.4	1.33	59.76
1452	14923.8	4.97	1451	1660.8	0.6	-87.86	1454	2038.1	2	-59.88
1532	3000.3	1	1533	2749.5	1	0	1531	1021.3	1	0
9DAH			**9DAH●PRPP●hHGPRT**				**9DAH●PRPP●PfHGPRT**			
Band position	Area	I4*	Band position	Area	I5*	Percentage change[a]	Band position	Area	I6*	Percentage change[a]
1345	5916.0	0.54	1338	5763	0.67	22.7	1343	1911.0	0.97	77.73
1388	10858.8	1	1382	8620.7	1	0	1387	2620.7	1	0
1424	23151.9	2.13	1414	16391	1.9	-10.82	1419	5219.1	1.02	-6.6
1445	7936.9	0.73	1442	5603.3	0.65	-11.07	1446	1959.1	1.04	42.63
1454	3846.8	0.35	1452	6744.3	0.78	120.84	1457	534.96	1.05	196.52

***I1; intensity of different bands in 9DAG relative to 1532 cm^{-1} band, I2; intensity of different bands in 9DAG●hHGPRT relative to 1533 cm^{-1} band, I3; intensity of different bands in 9DAG●PfHGPRT relative to 1531 cm^{-1} band. I4; intensity of different bands in 9-deazahypoxanthine relative to 1388 cm^{-1} band, I5; intensity of different bands in 9DAH●hHGPRT relative to 1382 cm^{-1} band, I6; intensity of different bands in 9DAH●PfHGPRT relative to 1387 cm^{-1} band. [a]The percentage of band in E●S complex was calculated with respect to that band in free form. Value with '(-)' sign indicates loss while the '(+)' sign indicates increase in intensity.**

Table 4.5: Distances between the different atoms of two rings (phenylalanine from HGPRT and nucleobase) involved in stacking.

Phe (Atom 1)	Nucleobase (Atom 2)	Distance (Å)		
		GMP•hHGPRT	ImmGP•hHGPRT	ImmHP•PfHGPRT
ε2	C2	4.13	3.68	3.73
Z	N3	4.02	3.77	3.94
ε1	C4	4.01	3.92	4.14
Dummy*	**Dummy***	**4.15**	**3.84**	**3.95**

***Dummy atoms are placed at the centre of Phe and the pyrimidine moiety of nucleobase (Figure 4.5).**

Linewidths of Raman bands report on entropic effect

Apart from the intensity losses and wavenumber shifts observed upon enzyme binding, further evidence of tight control of the substrate environment at the active site is provided by changes in linewidths of Raman bands. The bending mode at 1236 cm^{-1} (Figure 4.3, 9DAG in D_2O) undergoes narrowing with the full width at half maxima (FWHM) decreasing at the active-site of both the homologues with respect to free 9DAG. The effect is more prominent in this band because the normal mode composition of the band is such that all exocyclic atoms involved in this mode are in contact with residues in the protein. Thus the reduced number of accessible conformations of 9DAG resulting from the interactions formed at the active-site contributes in the rate enhancement of HGPRT catalyzed reaction [203]. This is an entropic effect where reduction in number of conformations favours the binding of substrate to the active-site and assists catalysis.

4.3.2 9DAH complexes of human and Pf HGPRT

A complete set of studies was carried out on the complexes of human and Pf enzyme with 9DAH as well which is a hypoxanthine analogue. UVRR spectra of 9DAH•PRPP•hHGPRT and 9DAH•PRPP•PfHGPRT have been recorded at an excitation wavelength of 260 nm (Figure 4.6).

Hydrogen bonding of H7 with Asp 137 distorts the N7—H bond

An intense band at 1523 cm^{-1} in the UVRR spectrum of 9DAH in solution is attributed to N7H—C8 bending (primary) and pyrrole ring vibrations. Binding of 9DAH to hHGPRT and PfHGPRT shifts this band down to 1515 cm^{-1} and 1516 cm^{-1}, respectively (Table 4.6). Also, the band at 1424 cm^{-1} with similar composition shifts down to 1415 cm^{-1} in hHGPRT and 1419 cm^{-1} PfHGPRT and loses intensity. These downshifts indicate a lowering of the force constant for the vibrations involved in these modes, which in turn results from the binding of the ligand with the enzymes. For instance, the hydrogen bonding of the N7H with the Asp residues in both the homologues causes weakening of N7—H bond. Thus the shifts in Raman wavenumbers quantify the effect of hydrogen bonding and show that 9DAH is distorted into a catalytically conducive state in the ternary complex. Further, the vibrational shifts also show the modulation in electron density of the substrate in forward reaction complex which in turn changes the force constant of the bonds in the pyrrole ring. Using NMR spectroscopy, Almo and co-workers have determined the downfield shifts of 1H (N7—H) peak of the TS analogue complexes of hHGPRT and PfHGPRT [74]. These NMR shifts have been found out to be different in two complexes corroborating the differential shifts obtained from UVRR spectra.

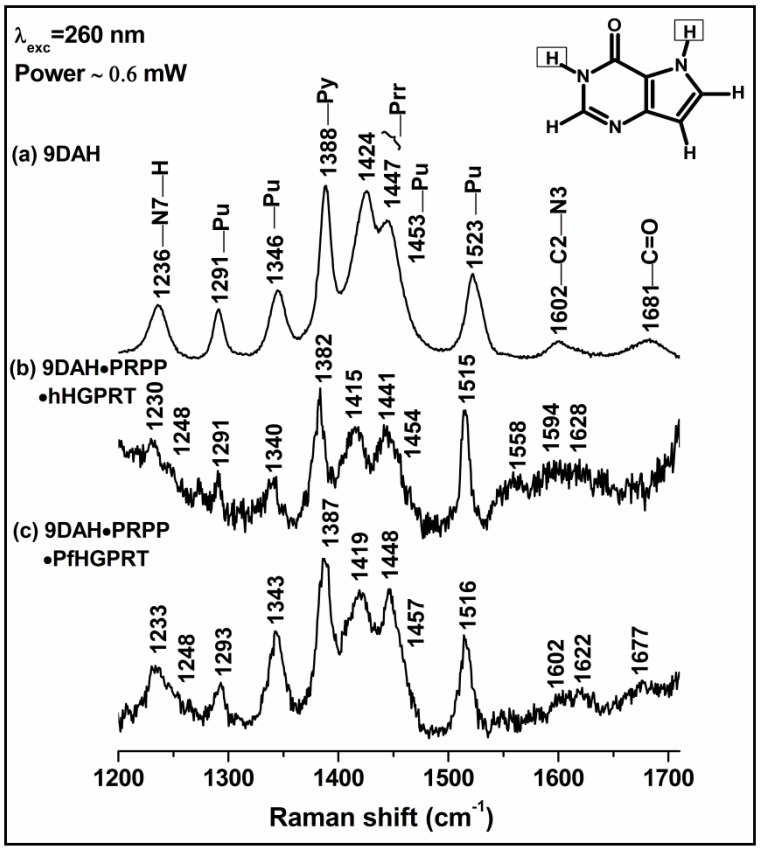

Figure 4.6: Binding of 9deazahypoxanthine to HGPRT homologues in presence of PRPP and Mg^{2+}. UVRR spectrum of: (a) 9DAH, (b) 9DAH•PRPP•hHGPRT in Tris-HCl buffer, pH 7, (c) 9DAH•PRPP•PfHGPRT in potassium phosphate buffer, pH 7; obtained with 260 nm excitation. Assignment to each band is shown as superscript above the corresponding wavenumbers in spectrum (a). Chemical structure of 9DAH is shown.

In case of 9DAG complexes, significant alteration in Raman intensity was observed which was attributed to the pi-stacking with Phe of active-site. In order to see the similar effect in 9DAH complexes, the percentage loss in intensity of the band at 1424 cm^{-1} with respect to the band at 1388 cm^{-1} was determined. Unlike in case of 9DAG complexes, a modest change in the intensities of the band at 1424 cm^{-1} in 9DAH•PRPP•hHGPRT (11%) and 9DAH•PRPP•PfHGPRT (7%) is observed (Table 4.4). The results show that the active-site packing in 9DAH complexes is not as compact as that in 9DAG complexes. A larger magnitude of intensity loss in hHGPRT further confirms rigid active-site interaction in hHGPRT than in PfHGPRT.

The purine ring mode at 1346 cm^{-1} downshifts to a lower wavenumber (-6 cm^{-1}) in 9DAH•PRPP•hHGPRT compared to 9DAH•PRPP•PfHGPRT

complex (-3 cm^{-1}). On the other hand, C4—C5 stretch at 1453 cm^{-1} shifts up to 1459 cm^{-1} in both the homologues of HGPRT.

Table 4.6: Comparison of shifts in wavenumber (cm^{-1}) observed in the UVRR spectra of 9DAH•PRPP•hHGPRT and 9DAH•PRPP•PfHGPRT complexes with respect to 9DAH.

Mode description	UVRR		
	9DAH	9DAH•PRPP•hHGPRT*	9DAH•PRPP•PfHGPRT*
Str C6=O + C6N1C2-N1H	1681	1628 (-64)	
Str C4C5-C8C9- N3C4	1523	1515 (-6)	1516 (-8)
Pu ring [Be C4C5N7-C5N7C8]	1453	1452 (3)	1457 (4)
Prr ring [Str C8C9+Be C8HC9]	1447	1441 (-6)	1448
Prr ring [Str C4C5-C5N7+ Be N7C8C9-C5N7C8]	1424	1415 (-5)	1419 (-8)
Py ring [Be C2HN3-N1HC6 + Str N3C4-C2N3]	1388	1382 (-3)	1387 (-2)
Pu ring [Be C2HN3-N7HC8 + Str N7C8-C5N7-N3C4]	1346	1340 (-6)	1343 (-3)
Be C2HN3-N7HC8 + Str N7C8-C5N7-N3C4	1291	1291 (1)	1292 (1)
Be N7HC8-C8C9H	1236	1230 (-2)	1233 (-2)

***Values in parentheses are the average shifts in the band positions obtained from three data sets ($\nu_{9DAH•PRPP•HGPRT}$-ν_{9DAH})**

The previously proposed reaction mechanism of the HGPRT catalyzed reaction suggests that the abstraction of proton on N7 is the key step [90]. Asp137 in hHGPRT (Asp148 in PfHGPRT) acts as a general base in this reaction [89]. Structure of hHGPRT with substrate analogue 7-hydroxypyrazolopyrimidine (HPP) [9] shows that the donor-acceptor distance is 3.2 Å (Asp137—N7) and is lower in ImmucillinHP•PfHGPRT at 2.9 Å (Asp148—N7) [74]. It is important to notice here that the pKa of N7—H hydrogen is expected to be different from that in Hx. However, this hydrogen atom served as a probe of the Asp137—H7 interaction.

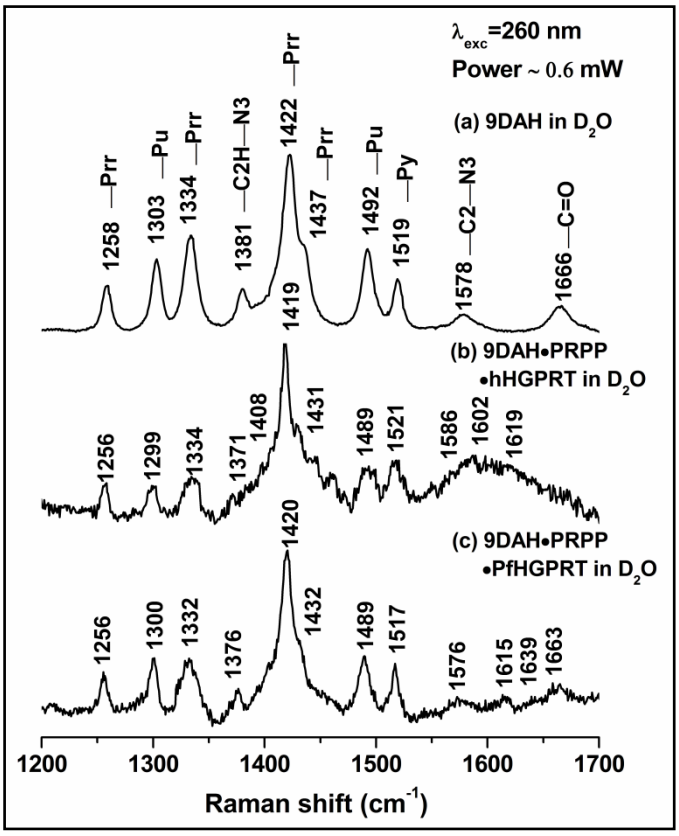

Figure 4.7: Binding of 9deazahypoxanthine to HGPRT homologues in presence of PRPP and Mg^{2+} in buffers made in D_2O. UVRR spectrum of: (a) 9DAH, (b) 9DAH•PRPP•hHGPRT in Tris-HCl buffer, pD 7, (c) 9DAH•PRPP•PfHGPRT in potassium phosphate buffer, pD 7; obtained with 260 nm excitation. Assignment to each band is shown as superscript above the corresponding wavenumbers in spectrum (a).

The band at 1388 cm^{-1} (C2H—N3 + N1H—C2 bending) shows a downshift in the bound form of 9DAH in both the homologues. The intense nature of this band and also an isotope (H→D) induced downshift of 8 cm^{-1} in this band make it a reliable marker of hydrogen bonding at N1—H position (Table 4.7). Crystal structures of hHGPRT with HPP (1D6N) and PfHGPRT with ImmucillinHP (1CJB) show that H1 is involved in hydrogen bonding with the backbone carbonyl of Val187 in hHGPRT (Val198 in PfHGPRT). Also, Asp193 and Asp204 lie at close proximity from C2 of nucleobase in hHGPRT (2.96 Å) and PfHGPRT (3.25 Å), respectively. Unlike in case of 9DAG, these residues do not form a direct contact with 9DAH which lacks the amino group at C2. Nonetheless, greater downshift of bands in 9DAH complex of hHGPRT implies larger distortion in the pyrimidine ring due to close proximity of Asp193 and Val187 in hHGPRT. A similar and prominent trend is observed in D_2O, where the band at 1380 cm^{-1} in solution further

downshifts to 1371 cm^{-1} (9DAH•PRPP•hHGPRT) and 1376 cm^{-1} (9DAH•PRPP•PfHGPRT) (Figure 4.7).

The band at 1236 cm^{-1} in the UVRR spectrum of free 9DAH splits into two bands when it is bound at the active-site of HGPRT. Interestingly, similar split is observed in 9DAH spectrum in solution upon H→D labeling, i.e. two bands appear at 1163 cm^{-1} and at 1519 cm^{-1}. Computated normal mode analysis shows that internal coordinates involved in the mode at 1236 cm^{-1} are redistributed into two new modes on deuterium labeling. These results show that the binding of 9DAH to HGPRT active-site causes not only weakening of N—H bonds but also reorganizes this normal mode to resemble the effects of replacing the labile hydrogen at N1—H and N7—H with deuterium.

It is important to notice that the vibrations of purine ring are also influenced by contacts of exocyclic purine atoms with the active-site residues. The N7—C8 stretch mode at 1346 cm^{-1} has a larger downshift in 9DAH•PRPP•hHGPRT (-6 cm^{-1}) as compared to 9DAH•PRPP•PfHGPRT complex (-3 cm^{-1}). The trend is conserved in D_2O with the 9DAH band in solution at 1303 cm^{-1} further downshifted to 1299 cm^{-1} (9DAH•PRPP•hHGPRT) and 1300 cm^{-1} (9DAH•PRPP•PfHGPRT). The slightly larger downshift at the active site of hHGPRT suggests that there is more extensive distortion in this analogue.

Table 4.7: Comparison of the shifts in wavenumber (cm^{-1}) observed in the UVRR spectra of 9DAH•PRPP•hHGPRT (in D_2O) and 9DAH•PRPP•PfHGPRT (in D_2O) complexes with respect to 9DAH alone in buffer pD 7.0.

Mode description	DFT	9DAH	9DAH• PRPP•hHGPRT	9DAH• PRPP•PfHGPRT
Str C6=O (72%) + Be C6N1C2 (-11%)	1843	1665	1619 (-44)	1639 (-26)
Str C2N3 (58%) + Be C2H	1690	1577	1586 (8)	
Str C4C5 (35%) + Str C8C9 (-21%) + StrN3C4 (-16%)	1595	1492	1489 (-3)	1489 (-2)
Be C4C5N7 (29%) + Be C8HC9 (-19%) + Be C5N7C8 (10%) + Be C2H	1568	1439	1431 (-7)	1432 (-6)
Str C8C9 (40%) + Be C4C5N7 (-16%)	1516	1422	1419 (-4)	1420 (-1)
Str C5N7 (34%) + Be N7C8C9 (20%) + Str C4C5 (-17%) + Be C5N7C8 (-10%)	1487	1333	1334 (1)	1332 (-2)
Be C2HN3 (58%)	1439	1380	1371 (-11)	1376 (-6)
Str N1C2 (30%) + Str N7C8 (10%)	1371	1519	1521	1517 (-2)
Str N7C8 (24%) + Str N1C2 (-14%) + Str N1C6 (11%) + Be N1H + C2H	1342	1303	1299 (-4)	1300 (-3)
Be C8HC9 (20%) + Str N7C8 (-18%)	1296	1258	1256 (-6)	1256

***Values in parenthesis represent average shift in wavenumbers ($\nu_{9DAG•PRPP•HGPRT}$-ν_{9DAG})**

4.4 Section II: Computational modeling of the nucleobases with the amino-acid residues forming non-covalent interactions

4.4.1 9DAG bound to hHGPRT

9DAG bound to the HGPRT enzyme was modeled through quantum chemical methods with explicit description of the nucleobase and the amino acid residues that line the binding pocket (Figure 4.8). The latter included D137, D193, K165, F186 and V187. A detailed description of the preparation of the initial input and final energy minimized structure is provided in the Methods section.

Shifts in the Raman band position of 9DAG upon binding to the protein were obtained by subtracting the Raman wavenumbers of 9DAG•HGPRT complex from those of 9DAG *in vacuo* (Table 4.8). Shifts thus obtained were compared with those obtained in the experimental UVRR spectra. Raman wavenumber of the C=O mode at 1850 cm^{-1} in 9DAG shifts down to 1787 cm^{-1} in 9DAG•HGPRT. This carbonyl stretch mode is shifted down because of the hydrogen bond with Lys165 of hHGPRT and reproduces the experimentally observed trend. The C2N2 and C2N3 stretching mode computed at 1721 cm^{-1} is downshifted to 1711 cm^{-1}. The corresponding downshift in experiments is much larger at 42 cm^{-1}. Further, the triene stretching mode appears at 1595 cm^{-1} in 9DAG and shifts up to 1608 cm^{-1} in the enzyme bound form. This upshift is also observed in experimental spectra, though of less magnitude at 2 cm^{-1}. Finally, the trend in the pyrrole ring mode is also similar in both experiments and computed shifts at -11 cm^{-1} and -2 cm^{-1}, respectively.

While D137, D193 and K165 are involved in direct hydrogen bonds, F186 forms a stack with the purine base. All the hydrogen bonding distances were reproduced well in the modeled structure (Table 4.9). The resultant structural parameters of 9DAG have been compared with free 9DAG and with those observed in crystal structure (PDB ID: 1BZY) (Table 4.10).

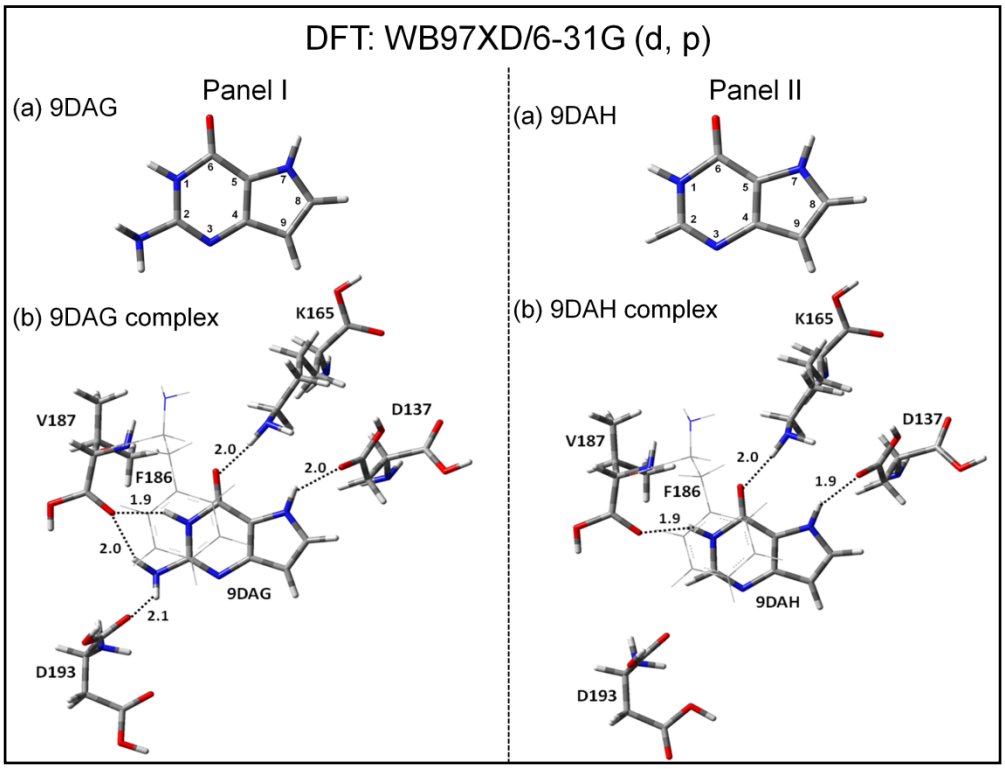

Figure 4.8: DFT (wB97XD/6-31G (d, p)) optimized structures of 9-deazapurines with active-site amino residues of HGPRT (D137, D193, K165, F186 and V187). Panel I: (a) 9DAG and (b) 9DAG complex. Panel II: (a) 9DAH and (b) 9DAH complex.

Table 4.8: Comparison of computed (DFT: wB97XD/6-31G (d, p)) Raman wavenumbers of 9DAG/9DAH and 9DAG/9DAH along with the active-site residues (D137, D193, K165, F186 and V187).

Mode description	9DAG	9DAG complex*	Mode description	9DAH	9DAH complex*
Str C6=O	1850	1787 (-63)	Str C6=O + C6N1C2-N1H	1850	1791 (-59)
Py ring [Str C2N3-C2N2]	1721	1711 (-10)	Str C4C5-C8C9- N3C4	1604	1605 (1)
Sci NH2	1655	1686 (31)	Pu ring [Be C4C5N7-C5N7C8]	1584	1591 (7)
Prr ring [Str C4C5-C9C8-N3C4 + Be N7H + N1H + NH2]	1624	1624	Prr ring [Str C8C9+Be C8HC9]	1526	1536 (10)
Py ring [Str C4C5N7 + Sci NH2 + Be N3C4C5 + C9H + C8H + N1H]	1595	1608 (13)	Prr ring [Str C4C5-C5N7+ Be N7C8C9-C5N7C8]	1500	1509 (9)
Prr ring [Be N7HC5-N7C8C9 + Str C5N7 + N7C8 ++ N1H]	1516	1512 (-4)	Py ring [Be C2HN3-N1HC6 + Str N3C4-C2N3]	1443	1438 (-5)
Prr ring [Str C4C5-N1C2 + Be C4C5N7]	1485	1483 (-2)	Pu ring [Be C2HN3-N7HC8 + Str N7C8-C5N7-N3C4]	1371	1375 (4)
Pu ring[StrN3C4 (29%)+StrC5N7 (-21%)+StrN7C8 (-14%)]+beN1H	1406	1416 (10)	Be C2HN3-N7HC8 + Str N7C8-C5N7-N3C4	1323	1349 (26)
Be N1HC6(29%)+str C2N2(10%)+rock NH2b	1344	1382 (38)	Be N7HC8-C8C9H	1251	1273 (22)

*Values in parenthesis represent shift in wavenumbers, for instance, ($\nu_{9DAG\ complex} - \nu_{9DAG}$)

Table 4.9: Comparison between the donor-acceptor distances (Å) obtained from the computed 9DAG and 9DAH complexes with the distances observed in the crystal structure (1BZY).

Proton donor-acceptor		H-bond distances (Å)		
Atom 1 (9DAG)	**Atom 2 (residues)**	**ImmucillinGP• hHGPRT**	**9DAG complex**	**9DAH complex**
N7	Oxygen atom of side-chain carbonyl of D137	2.8	2.8	2.8
C6=O	Nitrogen atom of side-chain of K165	2.8	3.0	3.0
C6=O	Nitrogen atom of backbone amide of V187	3.5	3.5	3.5
N1	Oxygen atom of backbone carbonyl of V187	2.7	2.8	2.8
Exocyclic N (C2 in 9DAH)	Oxygen atom of backbone carbonyl of V187	2.8	2.9	3.6
Exocyclic N	Oxygen atom of backbone carbonyl of D193	2.8	2.9	

Table 4.10: Structural parameters of computed structure of 9DAG with and without amino-acid residues.

Structural parameters								
Bond distances					Mulliken partial atomic charges			
	1BZY	Calculated				Calculated		
Bond	ImmucillinGP•hHGPRT	Gua	9DAG	9DAG Complex	Atom	Gua	9DAG	9DAG Complex
N1—C2	1.41	1.38	1.38	1.38	N1	-0.65	-0.65	-0.64
N1—H	1.07	1.01	1.01	1.02	C2	0.69	0.68	0.68
C2—N2	1.34	1.30	1.38	1.37	N2	-0.69	-0.69	-0.70
N2—Ha	1.07	1.01	1.01	1.01	N1H	0.30	0.30	0.32
N2—Hb	1.07	1.01	1.01	1.01	N2Ha	0.29	0.31	0.28
C2—N3	1.37	1.30	1.30	1.30	N2Hb	0.31	0.28	0.31
N3—C4	1.39	1.37	1.38	1.37	N3	-0.56	-0.57	-0.57
C4—C5	1.41	1.39	1.39	1.40	C4	0.39	0.22	0.22
C5—C6	1.44	1.43	1.43	1.42	C5	0.20	0.19	0.19
C6—O	1.23	1.22	1.22	1.24	C6	0.61	0.61	0.63
C5—N7	1.40	1.37	1.37	1.37	O6	-0.54	-0.55	-0.59
N7—H		1.01	1.01	1.01	N7	-0.61	-0.61	-0.61
N7—C8	1.30	1.36	1.36	1.36	N7H	0.31	0.31	0.29
C8—H	1.09	1.08	1.08	1.08	C8	0.27	0.07	0.06
C8—C9	1.41	1.32	1.38	1.38	C9	-0.49	-0.19	-0.20
C9—H	1.53		1.08	1.08	C8H	0.16	0.15	0.14
					C9H		0.13	0.13

4.4.2 9DAH bound to hHGPRT

In the energy minimized structure of the 9DAH•HGPRT complex, the bond most critical to the catalytic mechanism is the hydrogen bond between N7—H and D137, which shows a donor-acceptor (D-A) distance of 2.8 Å. This distance is same as that observed in the crystal structure (1BZY) of hHGPRT with TS analogue ImmucillinGP (Table 4.11). Similarly, all other calculated H-bond distances are also found to be similar to those observed in the crystal structure of TS analogue complex (Figure 4.8 and Table 4.9). Raman wavenumber shifts between 9DAH and 9DAH surrounded by the amino-acid residues were calculated and the same were compared with experimental UVRR frequencies.

Experimental trend is best reproduced in the carbonyl stretching mode which has a large downshift of 51 cm^{-1} in the UVRR spectra. Computed vibrational wavenumber of the carbonyl stretch at 1850 cm^{-1} in 9DAH is shifted down to 1791 cm^{-1} in computed 9DAH•hHGPRT, leading to a downshift of 59 cm^{-1} in good agreement with experiment. Thus the polarization of the C6—O bond due to the hydrogen bonding with Lys165 is captured well by the current model.

The computed C2N3 stretch band at 1698 cm^{-1} in 9DAH shifts down to 1593 cm^{-1} in 9DAH•hHGPRT ($\Delta\nu$=5 cm^{-1}), a slight underestimate of the corresponding experimental shift at 9 cm^{-1}. Better reproduced is the shift in the pyrimidine ring stretch at 5 cm^{-1} in computed spectra and 6 cm^{-1} in experiment.

Table 4.11: Structural parameters of computed structure of 9DAH with and without amino-acid residues.

Structural parameters								
Bond Length					Mulliken partial atomic charges			
	1BZY	Calculated				Calculated		
Bond	ImmucillinGP• hHGPRT	Hx	9DAH	9DAH complex	Atom	Hx	9DAH	9DAH complex
N1—C2	1.41	1.37	1.37	1.37	N1	-0.60	-0.60	-0.58
N1—H	1.07	1.01	1.01	1.02	C2	0.27	0.27	0.28
C2—H	1.34 (C2—N2)	1.09	1.09	1.09	N1H	0.31	0.31	0.33
C2—N3	1.37	1.29	1.29	1.29	C2H	0.16	0.15	0.15
N3—C4	1.39	1.37	1.38	1.37	N3	-0.49	-0.50	-0.52
C4—C5	1.41	1.39	1.39	1.40	C4	0.37	0.21	0.20
C5—C6	1.44	1.43	1.43	1.43	C5	0.21	0.20	0.21
C6—O	1.23	1.22	1.22	1.24	C6	0.62	0.61	0.63
C5—N7	1.40	1.37	1.36	1.37	O6	-0.53	-0.54	-0.59
N7—H		1.01	1.01	1.01	N7	-0.61	-0.61	-0.62
N7—C8	1.30	1.36	1.37	1.37	N7H	0.31	0.31	0.31
C8—H	1.09	1.08	1.08	1.08	C8H	0.17	0.15	0.14
C8—C9	1.41	1.31	1.38	1.38	C9H		0.14	0.13
C9—H	1.53 (C9—C1')		1.08	1.08	C8	0.27	0.07	0.06
					C9	-0.48	-0.18	-0.18

4.5 Assessment of the performance of DFT

The agreement of the computed and experimental wavenumber shifts in both, magnitude and direction, indicate that the minimal model chosen in this study to present the enzyme-substrate analogue captures major influences of the protein on the substrate. 9DAG and 9DAH mimic Gua and Hx, respectively to allow probing of the pre-TS environment of HGPRT catalyzed reaction. The similarities between the D-A distances calculated in the present study with the one observed in the crystal structure (1BZY) and with the natural substrates Gua and Hx suggest that these 9-deazapurines make similar non-covalent interactions at the active-site of HGPRT. The discrepancies between experimentally and computationally observed Raman shifts in few other wavenumbers, for instance, 1607 cm^{-1}, 1546 cm^{-1}, and 1452 cm^{-1} in 9DAG and 1523 cm^{-1}, 1447 cm^{-1}, 1424 cm^{-1}, 1346 cm^{-1}, and 1236 cm^{-1} in 9DAH may arise due to the absence of incorporation of all the effects which distort the ligand at the active-site. Apart from hydrogen bonding, such effects may include packing interactions, orientation of other active-site residues and allosteric effects from distant residues which are not taken into account in the present calculations.

The inability of DFT to fully reproduce the experimentally observed Raman shifts has previously been mentioned by Hildebrandt and co-workers [204]. The discrepancies between experimentally and computationally observed Raman shifts may arise due to several reasons: use of harmonic approximation, inadequacies of the quantum mechanical method employed and inadequate representation of the protein in the model, specifically, the absence of incorporation of all the effects which distort the ligand at the active-site. All these limitations are present in the current computation model. In modeling the protein environment, apart from hydrogen bonding, packing interactions, orientation of other active-site residues and allosteric effects from distant residues are not taken into account in the present calculations.

Despite these issues, these calculations serve a useful purpose. The structural parameters of the pre-transition-state of HGPRT catalyzed reaction

could be obtained from these calculations which provide an insight into the distortion of substrate upon binding to the active-site of enzyme. Although the magnitude and direction of the frequency shifts is not same in all the experimental and computational wavenumbers, hydrogen bonding distances between donor and acceptor molecule is very well reproduced in calculations and consistent with trends in experimental spectra. Hydrogen bonding (non-covalent interaction) between substrate and active-site residues results in the distortion of the structural parameters in the molecule which has been obtained through these calculations.

4.6 Discussion

4.6.1 Implications of these findings on HGPRT structure

hHGPRT and PfHGPRT with 80% sequence similarity are structural and functional analogues [84]. They have similar active-site interactions and kinetic mechanism and share common substrates and products. However they differ in their substrate specificity. The inability of hHGPRT to convert xanthine into XMP strongly suggests that the homologues are structurally different and such differences may be exploited to design molecules which specifically bind to PfHGPRT.

Since, the specific interactions are formed only with the nucleobase (as all other moieties remain same in all nucleotides), it becomes crucial to distinguish the two HGPRT homologues with respect to the nucleobase moiety. A plethora of crystal structures of HGPRT do not explain the reason behind such disparity in the two homologues. A QM/MM study to compare the reaction-mechanisms in two enzymes suggest that the difference in the specificity is not due to a chemical step involved in the reaction mechanism but due to the greater flexibility in the base binding region of PfHGPRT [82].

In the present chapter, I have shown that HGPRT destabilizes and distorts the substrate and this distorted substrate resembles its TS (Figure 4.9). Structure of TgHGPRT at 1.05 Å resolution suggests that the proton at N7 is firmly attached to it (N7—H is 0.88 Å) [80]. Thomas et al. used MD simulations to rationalize the differential substrate specificity among human

and PfHGPRT through calculations of the free energy surface for hHGPRT with Hx [84]. In this study, two feasible sequential reaction mechanisms were proposed. One, involving the abstraction of a proton from N7 leading to the formation of anionic Hx and then the phosphoribosylation reaction takes place. In the second pathway, phosphoribosyl group adds on to Hx, leading to the formation of IMPH+, followed by removal of H+. In the data presented in this chapter, clear downshifts in the Raman bands with the contribution from N7—H suggest that although the proton at N7 is still attached, the bond between the two is weakened. Hence, the present data show proton abstraction is most likely the initial step in the HGPRT catalyzed reaction. Interestingly, weakening of N7—H bond is more evident in the 9DAH complex than in 9DAG complex corroborating the kinetic results ($K_{m,\ Gua}$ =4.5 μM; $K_{m,\ Hx}$ =1.4 μM) [29].

The loss in intensity in the present Raman data suggests that upon addition of 9DAG, PRPP and Mg^{2+}, the flexible-loop closes onto the active-site of HGPRT and in the absence of any product formation remains closed over it. Stopped-flow fluorescence experiments with Y74W mutant of *Tritrichomonas foetus* HGXPRT reported the conformational change in the flexible loop during HGPRT catalyzed reaction [28].

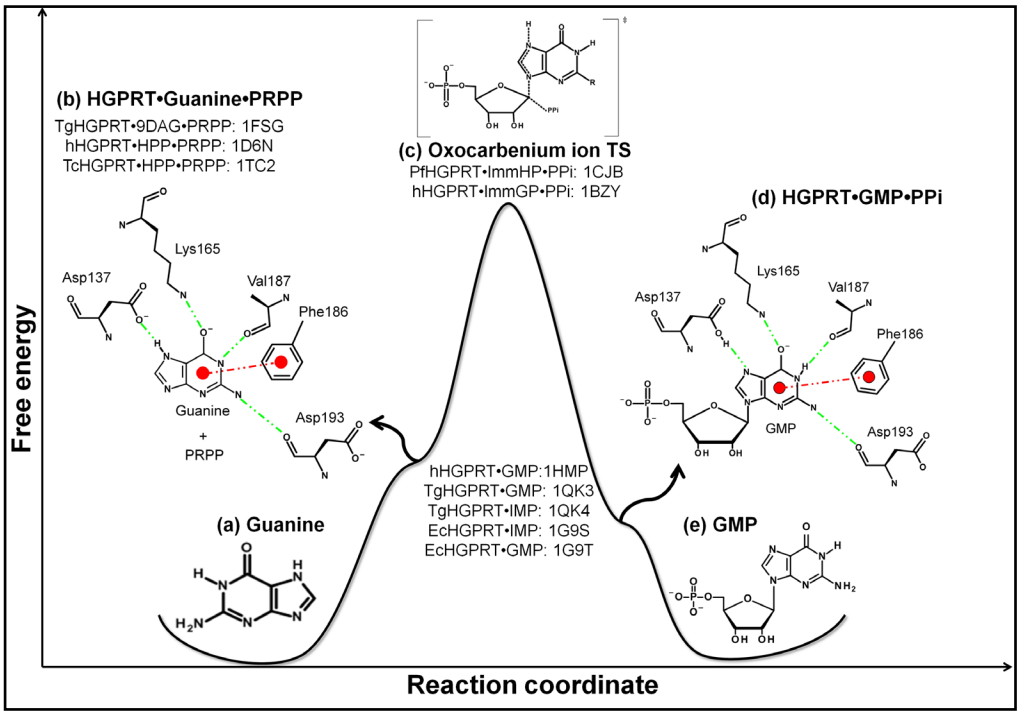

Figure 4.9: Distortion in guanine at the active-site of HGPRT is depicted on a schematic free energy profile. (a) Guanine and PRPP bind to HGPRT at different sites. (b) Interaction with the amino-acids of the active site distorts guanine into a high energy structure in which the C—O distance of the carbonyl group of guanine is larger, the pyrimidine ring is distorted and there is an overall delocalization of the electron density over the triene at the pyrimidine-imidazole ring junctions (C4—C5—C6 and C4—C5—N7). The stacking of Phe186 on the guanine ring further modulates the electron distribution of the purine. (C) At the transition state, formation of an oxocarbenium ion is proposed. (d) the product, GMP, is produced in a high-energy configuration at the active-site[193] in which the guanine ring is still distorted to resemble the guanine anion. (e) release of PPi facilitates the release of GMP.

4.7 Conclusion

The results obtained from the use of highly sensitive UVRR have the bearing on many important attributes in hHGPRT catalysis. The work done here establishes that the substrate distortions, indistinguishable in other biophysical techniques, seem to play an important role in generating differential substrate specificity in the two homologues. The results obtained in this work explicitly show the contribution of stacking interaction in providing this specificity to hHGPRT. Raman spectra obtained in this work reveal the enzymatic control of different substrates, Gua and Hx during catalysis. The differential magnitude of Raman wavenumber shifts and

differential loss in intensity in the Raman spectra of 9-deazapurines bound to hHGPRT and PfHGPRT suggest closer packing in hHGPRT active-site. Tighter interaction with the nucleobase is implicated in rigid, non-covalent hydrogen bonding network at hHGPRT active-site whereas the comparatively loosely stacked Phe197 in PfHGPRT with nucleobase is in agreement with a more flexible active-site environment of PfHGPRT.

The structural and molecular details explained in the present chapter provide improved understanding of potent inhibitors against parasitic protozoa, and in future, could be incorporated to develop a species-selective inhibitor of HGPRT.

"A route differs from a road not only because it is solely intended for vehicles, but also because it is merely a line that connects one point with another. A route has no meaning in itself; its meaning derives entirely from the two points that it connects. A road is a tribute to space. Every stretch of road has meaning in itself and invites us to stop. A route is the triumphant devaluation of space, which thanks to it has been reduced to a mere obstacle to human movement and a waste of time."

Milan Kundera

5

Solution Structure of Ligands involved in Adenylosuccinate Synthetase Catalyzed Reaction

5.1 Introduction

Adenylosuccinate synthetase (ADSS) is an enzyme of purine nucleotide synthesis pathway which commits the conversion of inosine-5'-monophosphate (IMP) to adenosine-5'-monophosphate (AMP). This reaction is a two step process; first, ADSS converts IMP to succinyl AMP (sAMP). This step involves formation of a transient intermediate 6-pIMP which is stable only at the active-site of ADSS. In the second step, sAMP is converted to AMP with the help of adenylosuccinate lyase (ADL) (Scheme 5.1). A few enzymes of purine salvage pathway like hypoxanthine guanine phosphoribosyltransferase (HGPRT), adenosine deaminase (ADA) and purine nucleoside phosphorylase (PNP) are well characterized [59]. On the other hand, comparatively little is known about the enzymes ADSS, ADL and their ligands.

Scheme 5.1

The enzymes of salvage pathway are identified as potential therapeutic targets against protozoan parasites like *Plasmodium*, *Leshmania*, *Tritrichomonas* and *Trypanosoma*. These parasites lack the *de novo* pathway and thus depend solely on the salvage pathway to recycle the nucleotide pool. In order to develop suitable drug molecules against these enzymes, a thorough understanding of the structure of the natural substrates and intermediates is important. In this chapter, I have elucidated the solution structures of 6-pIMP and sAMP, a comparatively less understood intermediates, and compared the same with the structure of purine riboside. In the following, I report the UVRR spectra of 6-pIMP and sAMP, acquired using light of excitation wavelength 260 nm. I assign these spectra to the vibrational normal modes, computed on the energy minimized structure of these molecules using density functional theory (DFT, B3LYP/6-31G (d, p)). The assignments are further validated by comparing the experimental and theoretical data, along with a comparison of isotope (H→D) induced shifts in the two cases.

5.2 Methodology

5.2.1 Sample preparation for absorption and UVRR spectroscopy

sAMP and $NaNO_3$ were purchased from Sigma-Aldrich Co. and were used without further purification. Appropriate amount of sAMP was dissolved in 30 mM HEPES pH 7.0 to obtain the final concentration of 50 μM for absorption and 500 μM for UVRR experiments. Deuterium labeled sAMP was prepared by dissolving the sample in D_2O and incubating overnight to ensure complete H→D labeling. 30 mM $NaNO_3$ was used as an internal standard in all samples. Appropriate buffer controls were recorded along with the samples.

5.2.2 Computational methods

Computed structure of nucleosides viz. succinyl adenosine (sAdenosine), 6-phosphoryl inosine (6-pI) and purine riboside were obtained using DFT calculations. Since, Raman excitation wavelength chosen for sAMP was 260 nm at which Raman bands from only nucleobase are resonance enhanced and therefore, phosphate was not included in any calculation. In view of maintaining the effect of bulky group at N9 position of nucleobase, ribose sugar was also optimized in each case. DFT calculations were performed using B3LYP parameterization. Basis set used was 6-31G (d, p) as implemented in Gaussian 09. Initial coordinates for the energy minimization of sAMP were obtained from the crystal structure of mouse muscle ADSS with its product sAMP (PDB ID: 1MEZ) [107]. Hydrogen atoms were added in GaussView 5.0. Phosphate group at C5' position of the ribose sugar of sAMP molecule was replaced with a proton. Mulliken partial atomic charges and structural parameters for all the molecules were also determined. Raman vibrational spectra were computed at the minimum energy geometry with the same level of theory. Vibrational energy distribution analysis (VEDA) 4.0 [180] program was used to calculate potential energy distribution (PED). The effect of isotopic shift was determined by replacing the mass of exchangeable hydrogen with the heavier mass of deuterium. Mode assignments of the experimentally observed bands were done by matching the isotopic shifts in experiment and calculations. Analysis of the computed vibrational spectra was done using Chemcraft 1.6 software *(http://www.chemcraftprog.com)*.

5.3 Results and Discussion

Exocyclic modification on the purine ring moiety (Figure 5.1 (a)) results in the formation of different purines which are the part of nucleotide synthesis pathway. sAdenosine and 6-pI may be regarded as the analogues of AMP because of the presence of similar conjugation in all these rings (Figure 5.1 (b), (c) and (d)).

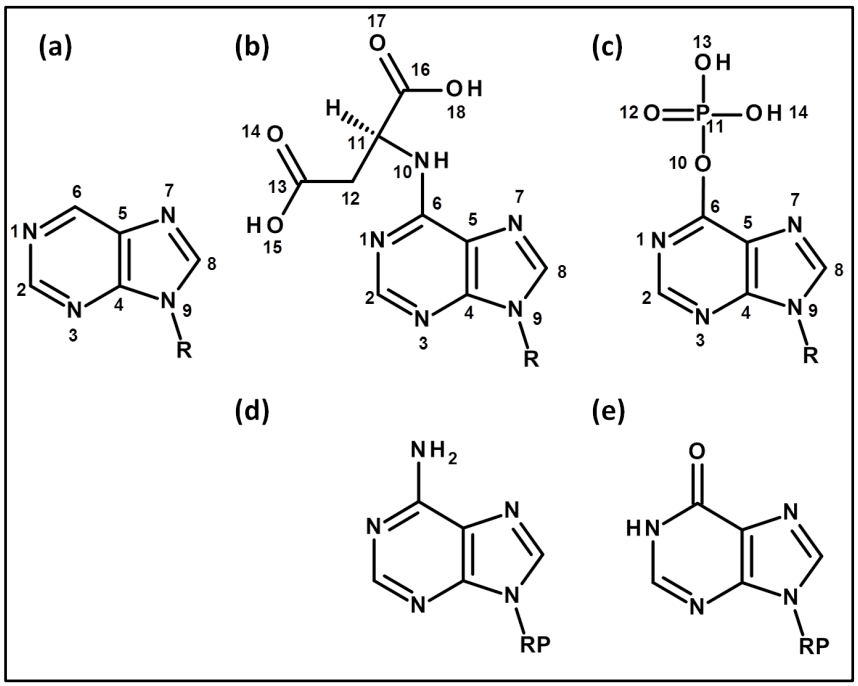

Figure 5.1: Structures of (a): purine riboside, (b) sAdenosine, (c) 6-pI, (d) AMP, and (e) IMP. Abbreviation: RP-ribose-5'-monophosphate.

5.3.1 Purine ribonucleotide (Parent molecule of nucleotides and model compound for 6-pIMP)

Purine is the parent nucleobase molecule which contains two rings: the pyrimidine ring and the imidazole ring. Most of the nucleotides which are the important part of purine synthesis pathway are modified on the pyrimidine ring. Substituted purines also form the part of majority of antitumor drugs. Further, study of such parent molecule establishes a necessary foundation for understanding the distortion in the ring upon substitution.

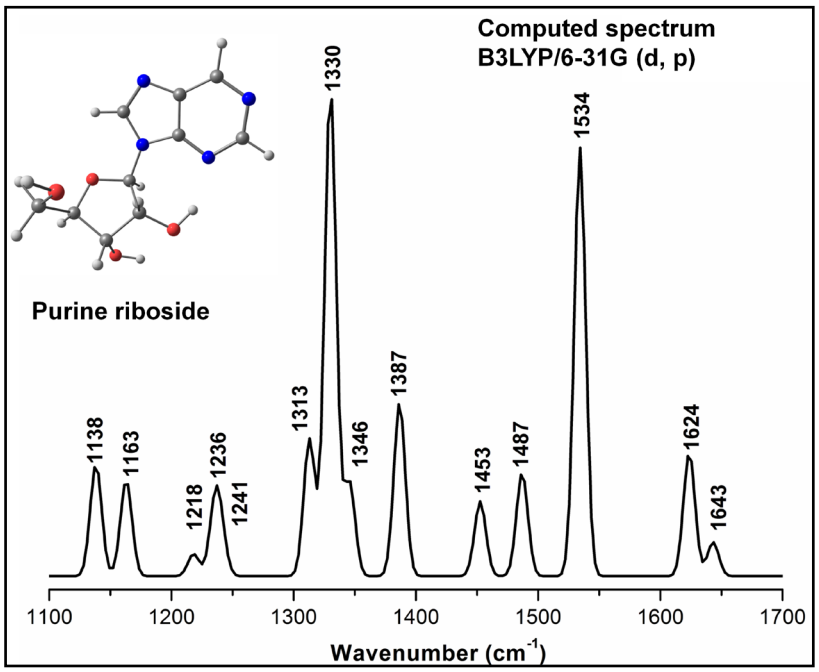

Figure 5.2: Computed Raman spectrum of purine riboside. Structure was energy minimized using DFT at the level of B3LYP/6-31G (d, p). Raman wavenumber calculations were done on the energy minimized structure.

Earlier Majoube et al. [205] has acquired resonance Raman spectrum of purine in aqueous solution using light of 257 nm wavelength and concluded that in aqueous solution, N7H tautomer of purine dominates whereas in gas phase, N9H tautomer dominates. Normal mode analysis of observed spectrum was done on the basis of the calculated spectrum at 3-21G level. In the work done in this thesis, I have computed the spectrum of purine riboside using DFT calculations at B3LYP/6-31G (d, p) level (Figure 5.2). Since, the DFT calculations in the present study are done at higher level of theory and thus the previously observed resonance Raman bands of N9H tautomer of purine, obtained at the excitation wavelength of 260 nm, have been reassigned with the mode composition predicted in the present study (Table 5.1). Difference in the normal mode composition as observed between the present study and the study done by Majoube et al. [205] arises mainly due to different methods used in calculations. Perturbations in the pyrimidine ring and imidazole ring mode upon substitution on the purine ring in case of sAMP and 6-pIMP are elaborated in discussion section. This study forms the basis of understanding distortion in these ligands upon binding at the active-site of ADSS.

Table 5.1: DFT (B3LYP/6-31G (d, p)) computed Raman wavenumbers of purine riboside and experimental resonance Raman shifts (λ_{exc} = 257 nm) of purine.

Mode assignments[a]	DFT	UVRR at 257 nm[b]
Pyrimidine ring distortion [Be N3C4C5 (19%) + Str C2N3 (14%) + Str N1C6 (-14%) + Str N7C8 (-11%)]	1643	1617
Imidazole ring distortion [Str N3C4 (23%) + Be C4N9C8 (-16%) + Be C5N7C8 (-15%) + C2H]	1624	1597
Imidazole ring distortion [Str N7C8 (29%) + Be N7C8H (-16%) + Be C4N9C8 (12%) + C6H]	1534	1470
Purine ring distortion [Be N1C2H (30%) + Be C5N7C8 (18%) + Str N1C6 (-14%) + Str C4N9 (-11%)]	1487	1408
Be N1C2H (23%) + Str N7C8 (16%) + Str C4N9 (11%)	1453	1335
Str N7C8 (14%) + Be C5N7C8 (13%) + Be N1C6H (12%)	1387	1301
Ribose ring	1346	
Be N1C6H (26%) + Str C5N7 (19%)	1330	1236
Pyrimidine ring distortion [Str N1C2 (21%) + Str C2N3 (-20%)]	1313	
Imidazole ring distortion [Be N7C8H (18%) + Str N9C8 (-11%)]	1241	1109
Str N9C8 (12%)	1236	
Be N7C8H (22%) + Str N7C5 (11%)	1218	943
Ribose ring	1163	
Str N1C2 (24%) + Str N1C6 (22%) + Be N1C6H (11%)	1138	798

[a]Abbreviations: Str, stretch; Be, bend; Py, pyrimidine; Sci, scissors; Pu, purine
[b]: taken from ref. [205]

5.3.2 sAMP (product of ADSS catalyzed reaction)

sAMP has an absorption maximum at 269 nm (Figure 5.3) and thus the excitation wavelength of 260 nm falls within this absorption envelope and leads to resonance enhancement of the UVRR spectrum of sAMP. Ultraviolet resonance Raman spectra of sAMP were acquired in both H_2O and D_2O buffers (HEPES, pH 7.0) (Figure 5.4). Isotopic shifts obtained from H→D labeling of molecule, fundamental wavenumber positions and DFT calculations were used for normal mode assignments of the bands observed in the UVRR spectrum of sAMP. Structure of sAdenosine was energy minimized at the B3LYP level of theory using 6-31G (d, p) basis set as implemented in

Gaussian 09. Raman wavenumber calculation was done on the energy minimized structure with the same basis set. In the following I focus on the discussion of bands in the region from 1200 cm^{-1} to 1600 cm^{-1} which may act as marker of hydrogen bonding interactions and enzyme-induced distortion of the purine ring. The mode composition of each band is described in detail in Table 5.2.

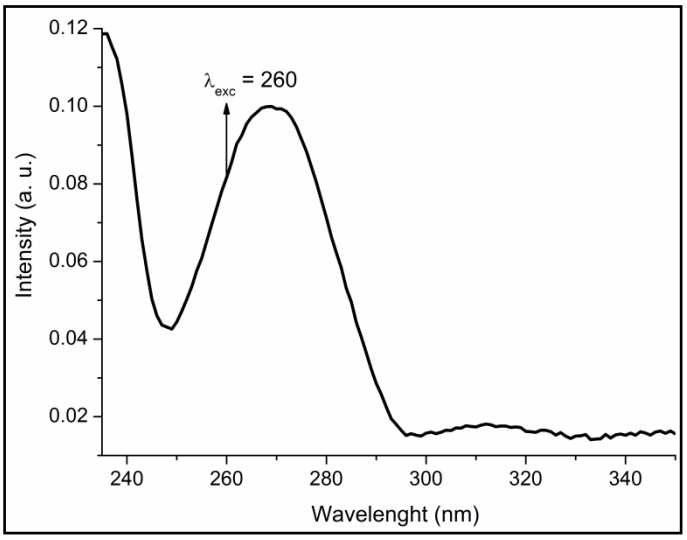

Figure 5.3: Absorption spectrum of sAMP. An arrow depicts 260 nm at which the UVRR spectra of sAMP are acquired. The spectrum was acquired in HEPES buffer, pH 7.

Pyrimidine ring mode along with a contribution from C6—N6—H bending vibrations (bend) is observed at 1633 cm^{-1} (Table 5.2). Upon deuterium isotopic labeling, this band downshifts to 1620 cm^{-1} ($\Delta\nu_{HtoD}$ = -13 cm^{-1}). The only labile hydrogen at the exocyclic N of the pyrimidine ring is the likely cause of the observed downshift. This band, though of less intensity, can act as a marker of hydrogen bonding interaction at N6—H position in the active-site of the enzyme. DFT calculations predict an isotope induced downshift of 13 cm^{-1}, which is in agreement with experiments.

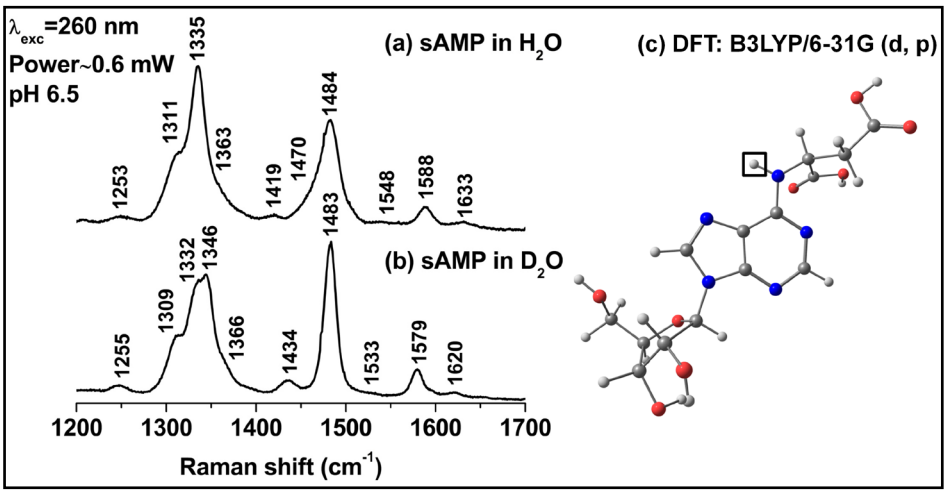

Figure 5.4: Resonance Raman spectra (λ_{exc}=260 nm) in HEPES buffer, pH 7.0 (a) sAMP in H_2O buffer, (b) sAMP in D_2O buffer. (c) DFT (B3LYP/6-31G (d, p)) computed structure of sAMP.

The band at 1588 cm^{-1} is assigned to N3—C4 and N1—C6 stretching vibrations (str) along with C4—N9—C8 bend. This band shows a minor downshift of 2 cm^{-1} upon H→D labeling. A downshift of 9 cm^{-1} is predicted by DFT calculations.

The intense band at 1484 cm^{-1} in H_2O buffer has primary contribution from pyrimidine ring str. Upon H→D labeling, though the band does not show a large shift in wavenumber, computed normal modes show a large re-organization in the composition of the normal mode. In D_2O buffer, this band reorganizes to have primary contribution from imidazole ring distortion with a slight contribution from C6—N6 str. DFT calculations predict a downshift of 2 cm^{-1} upon H→D labeling which agrees well with the experimental observed downshift (1 cm^{-1}).

Table 5.2: Experimental resonance Raman shifts (λ_{exc}=260 nm) at pH=7.0 in neutral sAMP in H_2O and D_2O, and computed (B3LYP/6-31G (d, p)) vibrational wavenumbers with mode assignments[a]

Mode assignments in H_2O	DFT	Scaled DFT[b]	UVRR	Mode assignments in D_2O	DFT	Scaled DFT[a]	UVRR
Str C2N3 (16%) + Be C6N1C2 (14%) + Be N3C4C5 (13%) + Be C6N6H (10%)	1660	1627	1633	Str C2N3 (17%) + Be N3C4C5 (14%) + Be C6N1C2 (14%)	1647	1631	1620
Str N3C4 (25%) + Str N1C6 (17%) + Be C4N9C8 (-13%)	1632	1599	1588	Str N3C4 (22%) + Str N1C6 (18%)	1630	1614	1579
Str N7C8 (23%) + Str C6N10 (-12%) + Be C4N9C8 (13%) + Be N7C8H (-12%) + Be C6N6H (10%)	1563	1532	1548	Str C6N10 (26%) + Str N7C8 (-19%) + Be C2HN3 (-10%)	1551	1535	1533
Str N1C6 (17%) + Str N7C8 (-16%) + Str C2N3 (-14%) + Str C6N10 (-13%) + Be C2HN3 (13%)	1526	1495	1484	Str N7C8 (25%) + Str C6N10 (-16%) + Be N7C8H (-14%) + Be C4N9C8 (13%)	1524	1509	1483
Be C6N6H (29%) + Be C5N7C8 (12%) + Str C4N9 (-10%)	1493	1463	1470				
Str C4N9 (-10%) + Ribose ring mode	1434	1405	1419	Str C4N9 (16%) + Ribose ring mode	1471	1456	1434
Be C2HN3 (29%) + Be C11HN10 (-	1412	1384	1363	Be C2HN3 (20%) + Str C4N9	1462	1447	1366

17%) + Be C6N6H (10%)				(11%)			
Pyrimidine ring mode [Str N1C2 (31%) + Str C2N3 (-22%) + Be C2HN3 (-12%) + Be C6N6H]	1350	1323	1335	**Pyrimidine ring mode** [Str N1C6 (12%) + Str N3C4 (-11%) + Str N1C2 (-11%)]	1360	1346	1346
				Str C2N3 (21%) + Be C2HN3 (13%)	1350	1337	1332
Purine ring Stretch + Be C2H	1397	1369	1311	Str C5N7 (24%) + Str N1C2 (15%)	1375	1361	1309
Be N7C8H (37%) + Str N9C1' (14%)	1260	1235	1253	Be N7C8H (25%) + Str N1C2 (13%)	1268	1255	1255

[a]**Abbreviations: Str, stretch; Be, bend; Py, pyrimidine; Sci, scissors; Pu, purine**

[b]**Scaling factor used: 0.98 and 0.99 in H_2O and D_2O, respectively.**

The band at 1363 cm^{-1} in the UVRR spectrum of sAMP in H_2O buffer is essentially a bending mode with contributions from H—C2—N3 and C6—N10—H bends. This band upshifts by 3 cm^{-1} upon H→D labeling of sAMP. It is well established that bending vibrations upshift upon isotopic labeling (H→D) which may happen due to reorganization of the mode composition and decoupling of some of the bending vibrations. Here, DFT calculations predict an upshift of 50 cm^{-1} in this band with an altered mode composition in which the contribution from bending C6—N10—H is lost. Since HD labeling results in the upshift and hence this band can act as a marker of hydrogen bonding interactions between N10—H of sAMP with the active-site residues of enzyme.

Another intense band at 1335 cm^{-1} in sAMP spectrum is assigned to the pyrimidine ring mode. This band splits into two bands upon deuterium labeling, at 1347 cm^{-1} and 1332 cm^{-1}. Both bands in D_2O buffer comprise of the vibrations from pyrimidine ring distortion. Since, this band shows very high sensitivity to the change in environment of sAMP molecule and thus can act as a marker of distortion of sAMP molecule upon binding to the enzymes of nucleotide synthesis pathway.

The band at 1311 cm^{-1} ($\Delta\nu_{HtoD}$ = -2 cm^{-1}) in the sAMP spectrum, though of less intensity, is very important band since it involves the vibrations from the complete purine ring. DFT calculations predict a downshift of 22 cm^{-1} upon H→D labeling. Calculations predict that in H_2O buffer the mode composition is highly delocalized over the whole purine ring. However, the deuterium labeling at N10—H position seems to localize the vibrations to only pyrimidine ring str which also involves C5—N7 and N1—C2 str. This marked change is predicted in the form of larger downshift in calculated wavenumber. A smaller downshift in experimental wavenumber suggests that the DFT calculations overestimate the effect of H→D labeling in this case.

The band at 1253 cm^{-1} ($\Delta\nu_{HtoD}$ = +2 cm^{-1}) is assigned to N7—C8—H bend. DFT calculations predict an upshift of 8 cm^{-1} upon H→D labeling along with the re-organization of the mode.

Effect of substitution of succinyl group on purine ring: a comparison with AMP

Although the purine ring structures of sAMP and AMP are very similar and differ only at exocyclic N (N10) of the pyrimidine ring, the wavenumber positions in these two spectra are conspicuously different. Detailed normal mode assignments for the UVRR spectrum of AMP are taken from Wen and Thomas [36] and a comparison with sAMP have been given in Appendix (Table A.1).

It is important to notice that the wavenumber region from 1400-1700 cm^{-1} is upshifted in sAMP with respect to AMP. The band at 1633 cm^{-1} is majorly attributed to pyrimidine ring vibrations. The corresponding band in AMP appears at 1604 cm^{-1}. Also, the band at 1588 cm^{-1} which arises from the C4—C5 and N3—C4 stretch appears at 1581 cm^{-1} in AMP. Since, the Raman band positions are directly related to the force constant of the bond between the atoms undergoing vibrations, a systematic upshift in sAMP in this region suggests that the conjugation in the pyrimidine ring of sAMP is increased upon addition of succinyl group. Moreover, the effect of substitution on the purine ring is manifested as a shortening of bond lengths (C2—N3 and C4—C5) in sAMP as compared to the purine ring parameters (Table 5.3). This further emphasizes the utility of UVRR in identifying a slight substitution on the purine ring.

Interestingly, the band positions in the region from 1100-1400 cm^{-1} are remarkably similar in sAMP and AMP. Normal mode assignments of the bands in this region suggest a major contribution from imidazole ring. This implies that the substitution at N10 position in sAMP does not influence the bond order in the imidazole ring.

Table 5.3: Structural parameters of computed structure of purine, 6-phophoryl inosine and succinyl adenosine.

Purine				6-phosphoryl inosine					Succinyl adenosine				
Bond distances		Atomic charges		Bond distances		1LNY[a]	Atomic charges		Bond distances		1MEZ[a]	Atomic charges	
N1—C2	1.34	N1	-0.44	N1—C2	1.34	1.34	N1	-0.52	N1—C2	1.34	1.34	N1	-0.54
C2—H	1.09	C2	0.24	C2—H	1.09		C2	0.25	C2—H	1.09		C2	0.23
C2—N3	1.34	N3	-0.56	C2—N3	1.34	1.33	N3	-0.46	C2—N3	1.33	1.33	N3	-0.52
N3—C4	1.34	C4	0.56	N3—C4	1.34	1.34	C4	0.45	N3—C4	1.34	1.34	C4	0.54
C4—C5	1.41	C5	0.21	C4—C5	1.40	1.38	C5	0.21	C4—C5	1.40	1.38	C5	0.16
C5—C6	1.39	C6	0.10	C5—C6	1.41	1.40	C6	0.53	C5—C6	1.41	1.40	C6	0.55
C6—H	1.09	N7	-0.52	C6—010	1.35	1.24	N7	-0.44	C6—N10	1.37	1.39	N7	-0.54
C5—N7	1.38	C8	0.30	C5—N7	1.39	1.39	C8	0.27	C5—N7	1.38	1.39	C8	0.29
N7—C8	1.31	N9	-0.55	N7—C8	1.32	1.31	N9	-0.55	N7—C8	1.31	1.31	N9	-0.54
C8—H	1.08	C2H	0.12	C8—H	1.08		O10	-0.57	C8—H	1.08		N10	-0.57
C8—N9	1.38	C8H	0.15	C8—N9	1.37	1.37	C2H	0.13	C8—N9	1.39	1.37	C11	-0.03
N9—C1'	1.47	C6H	0.12	N9—C1'	1.47	1.46	C8H	0.13	N9—C1'	1.45	1.46	C12	-0.24
				O10—P11	1.68	1.63	P11	1.11	N10—H	1.01		C13	0.59
				P11—O12	1.48	1.53	O12	-0.56	N10—C11	1.45	1.48	O14	-0.47
				P11—O13	1.60	1.53	H13	0.32	C11—C12	1.54	1.55	O15	-0.49
				O13—H	0.97		O14	-0.56	C12—C13	1.51	1.54	C16	0.62
				P11—O14	1.58	1.53	H15	0.32	C13—O14	1.21	1.25	O17	-0.47
				O14—H	1.00		O16	-0.31	C13—O15	1.36	1.25	O18	-0.48
									O15—H	0.97		C2H	0.10
									C11—C16	1.54	1.53	C8H	0.13
									C16—O17	1.21	1.25	N10H	0.29
									C16—O18	1.35	1.25	C15Ha	0.15
									O18—H	0.97		C15Hb	0.18
												O15H	0.32
												O18H	0.33

[a]1LNY and [a]1MEZ [107, 206] are the crystal structures of mouse muscle ADSS co-crystallized with 6-pIMP and sAMP, respectively.

5.3.3 6-phosphoryl inosine-5'-monophosphate (intermediate of ADSS catalyzed reaction)

6-phosphoryl inosine-5'-monophosphate (6-pIMP) is the intermediate in the reaction catalyzed by ADSS. It is unstable when free in solution and rapidly converts to IMP [115]. It is stable only when bound to ADSS. Due to its transient nature, studies on 6-pIMP are scant. To detect or quantify the intermediate in ADSS catalyzed reaction and also to be able to determine the enzyme induced distortion in 6-pIMP, it is very important to first decipher the structure of this molecule in solution. Since, the flux of purines in the nucleotide synthesis pathway flows from IMP to AMP, the formation of the intriguing intermediate 6-pIMP can be tracked by knowing its marker bands in the UVRR spectrum which distinguish it from IMP molecule.

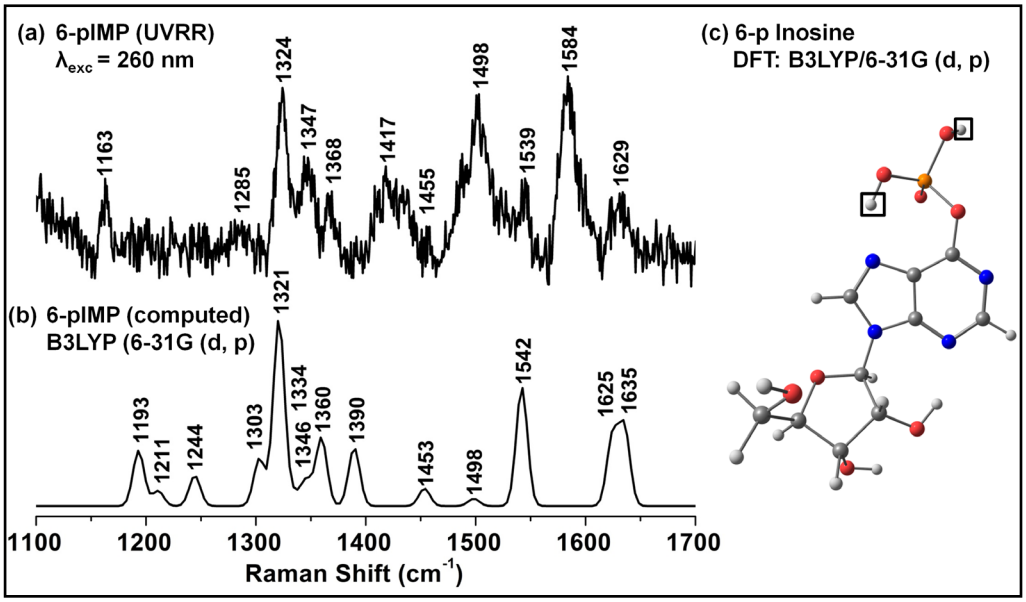

Figure 5.5: Spectrum of 6-pIMP; (a) experimentally observed resonance Raman spectrum at an excitation wavelength of 260 nm, (b) and (c) are DFT (B3LYP/6-31G (d, p)) predicted Raman spectrum and energy minimized geometry of 6-pIMP.

In this context, the structure of 6-phosphoryl inosine (6-pI) is energy minimized at B3LYP/6-31G (d, p) level and the Raman wavenumber calculations were performed on this structure (Table 5.4, Figure 5.5). Similar procedure was followed by replacing the labile protons with deuterons to obtain the wavenumber shift upon H→D labeling. It is important to mention

that none of the bands in the region comprising from 1600 cm^{-1} to 1400 cm^{-1} show a significant isotope induced shift in the calculated wavenumber. This is due to the absence of any exchangeable proton on the purine ring moiety. The observed UVRR spectrum of 6-pIMP was obtained as mentioned in the Appendix (Figure A.4).

The band at 1629 cm^{-1} in the observed resonance Raman spectrum is exclusively assigned to the pyrimidine ring distortion. This band does not involve any contribution from exocyclic phosphate moiety and thus no H→D induced shift is predicted by DFT calculations. Also, the band at 1583 cm^{-1} is attributed to purine ring vibrations. The normal mode composition of this band does not seem to alter upon H→D labeling at the 6 -phosphoryl group in DFT calculations. Further, the band at 1539 cm^{-1} is predicted as a more localized vibration which is restricted to the N7—C8 str. The band at 1498 cm^{-1} in the observed Raman spectrum arises from the pyrimidine ring vibrations which involve N1—C6 str and H—C2—N3 bend. Due to its intense nature, this band can be monitored in an enzymatic conversion of IMP to 6-pIMP.

The band at 1455 cm^{-1} in the observed spectrum of 6-pIMP involves the contribution from N3—C4 and N7—C8 str. While most bands in the calculated Raman spectrum of 6-pIMP do not show isotopic shifts due to lack of any replaceable proton on the purine ring, two bands at 1360 cm^{-1} and 1346 cm^{-1} show different trends. The band at 1360 cm^{-1} is comprised of the vibrations from C2HN3 bending and C6—O6 stretching. The effect of deuteration at the exocyclic phosphate is manifested in the form of decoupling of C6—O6 and an upshift to 1366 cm^{-1}. C6—O6 str reorganizes to appear at 1353 cm^{-1} in deuterated 6-pIMP. This band is sensitive to H→D labeling and change in environment, and is unique to 6-pIMP. Thus, the formation of 6-pIMP from IMP, in an enzymatic reaction, can be traced by observing the appearance of this marker band. Another band at 1346 cm^{-1} which involves the contribution from N1—C2, C2—N3 and N7—C8 str downshifts to 1343 cm^{-1} upon deuteration.

Table 5.4: DFT (B3LYP/6-31G (d, p)) computed Raman wavenumbers and mode assignments of 6-pI.

Mode assignments[a] in H_2O	DFT	UVRR	Mode assignments[a] in D_2O	DFT
Str N3C4 (23%) + Str N1C6 (21%)	1635	1629	Str N3C4 (22%) + Str N1C6 (19%) + Be N3C4C5 (-11%)	1635
Str C2N3 (19) + Be C4N9C8 (-15%) + Be N3C4C5 (12%) + Be C2N3C4 (-10%)	1625	1583	Str C2N3 (18) + Be C4N9C8 (-15%) + Be N3C4C5 (13%) + Be C2N3C4 (-11%)	1624
Str N7C8 (27%) + Be N7C8H (-18%)	1542	1539	Str N7C8 (27%) + Be N7C8H (-17%)	1541
Be C2HN3 (41%) + Str N1C6 (24%)	1498	1497	Be C2HN3 (40%) + Str N1C6 (24%)	1498
Str N3C4 (19%) + Str N7C8 (15%)	1453	1455	Str C4N9 (23%) + Str N7C8 (21%) + Str N3C4 (-10%)	1454
Purine ring stretching + C2H bending	1390	1418	Str N1C2 (16%) + Be C2HN3 (15%) + Str C5N7 (13%) + Be C5N7C8 (-12%) + Str N1C6 (-10%)	1390
Be C2HN3 (23%) + Str C6O6 (12%)	1360	1367	Str C8N9 (10%) + Be C2HN3 (10%)	1366
			Str C6O6 (15%) + Str N1C2 (-15%) + Be C2HN3 (14%)	1353
Str N1C2 (24%) + C2N3 + N7C8	1346	1348	Str N1C2 (16%)	1343
Str C2N3 (-15%)	1321	1323	C2N3 (-13%) + Phosphate	1320
Be N7C8H (-23%)	1244	1285	Be N7C8H (40%) + Str C8N9 (-13%)	1244
Be N7C8N9 (-17%)	1211		Be N7C8N9 (23%) + Str N9C1' (-13%)	1214
Be N7C8H (26%) + Str C5N7 (18%) + Str N1C6 (-11%) + Str C2N3 (-11%)+Str N1C2 (-10%)	1193	1164	Be N7C8H (21%) + Str C5N7 (20%) + Str N1C6 (-11%) + Str C2N3 (-10%) + Str N1C2 (-10%)	1195

[a]**Abbreviations: Str, stretch; Be, bend; Py, pyrimidine; Sci, scissors; Pu, purine**

Effect of substitution of phosphoryl group on purine ring: a comparison with IMP

The 6-pI band at 1629 cm^{-1} is attributed to pyrimidine ring distortion. A band with similar normal mode composition in purine appears at 1617 cm^{-1}. An upshift in the mode upon substitution at C6 position shows that addition of the phosphoryl group enhances the bond strength in the pyrimidine ring in 6-pI. Further, the pyrimidine ring distortion in IMP appears at 1593 cm^{-1} which shows that the presence of double bond between C6=O reduces the bond strength of the pyrimidine ring by breaking the conjugation of the ring. A comparison between the Raman wavenumbers of 6-pI and IMP has been provided in Appendix (Table A.2) [34]. The structure of 6-pI differ from IMP in terms of aromatic character of pyrimidine which is greater in former than latter. Such structural differences are manifested in the form of shifts in the calculated Raman spectra of the two molecules.

Further, purine ring mode in 6-pI and purine appears at 1418 cm^{-1} and 1408 cm^{-1}, respectively. In IMP, the corresponding band appears at 1468 cm^{-1}. These differences in wavenumber positions suggest change in the bond strength. However, DFT calculations predict similar bond strength and Mulliken partial atomic charges in the pyrimidine ring. This shows that the subtle changes in bond length which are indistinguishable in DFT calculations are manifested in the form of different Raman shifts in the UVRR spectrum of these molecules. Thus, Raman spectroscopy serves as an important tool to identify and characterize sublte changes in the structure and conformation of nucleic-acids and proteins.

5.4 Conclusion

The first step in determining the enzyme-induced distortion is to understand the molecular structure of the free ligands at physiological pH. Vibrational spectroscopy has long been regarded as a potential tool to determine the structure of small molecules. In the work done in this chapter, I have determined the structure of purine riboside, 6-pIMP and sAMP experimentally and/or computationally. These molecules form a part of the nucleotide synthesis pathway and are substrates catalyzed by ADSS. Very little information is available on these molecules. Understanding the structures of intermediates of purine synthesis can provide useful clues for designing potent inhibitors of enzymes of this pathway. The experimental and computational results obtained in the present study on sAMP show that the molecule exists in neutral form with a proton at the exocyclic N (N10). The results also identify the bands which are sensitive to the hydrogen bonding interaction and change in the environment of sAMP when it is transferred from the solution to the active-site of ADSS. In case of 6-pIMP, the structural comparison with IMP is drawn based on the previously published UVRR spectrum of IMP.

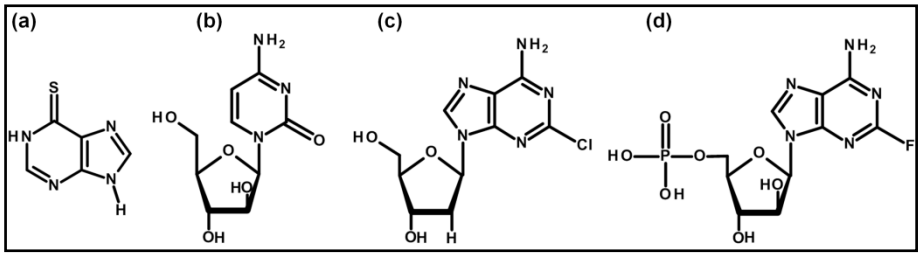

Figure 5.6: Chemical structures of nucleobase and nucleoside analogues which are employed as drug molecules. (a) 6-mercaptopurine, (b) cytarabine, (c) cladribine, and (d) fludarabine.

A recent review discusses the development of nucleoside and nucleotide inhibitors for cancer and viral disease [207]. It addresses the need to develop new analogues because of recurrence of drug resistance, and the need to provide drug with improved bioavailability and solubility. Another category of more recent nucleotide based inhibitors are phosphoramidate and phosphorodiamidates which are being developed as anti-tumour and anti-viral agents. Based on the current information available in the literature, this is, by

far, the first UVRR study which discusses the structure of sAMP. Further, understanding the structure of purine and its substituents is the pre-requisite for the development of novel nucleoside and nucleotide analogues. These analogues which include variety of purines and pyrimidines have been exploited as drug molecules for almost half a decade (Figure 5.6). 6-mercaptopurine (6MP), an analogue of purine which differs at C6 position (instead of a proton attached to C6 in purine, 6MP has sulphur atom at this place) is an immunosuppressive drug which is used to treat Leukemia [207]. It competes with hypoxanthine and guanine to HGPRT binding site and is itself gets converted to thioinosinic acid and thus inhibits the formation of AMP and GMP. Also, the first nucleoside analogue cytarabine (cytidine analogue) is known to inhibit haematological malignancies [208]. Two major purine analogues which have been extensively used to treat blood malignancies are cladribine and fludarabine (both are the analogues of adenosine and hence blocks adenosine deaminase). These analogues have been proved as promising nucleoside analogues against cancer activity [208]. Development of such analogues is possible based on the prior information of the nucleotides involved in the metabolic pathways. This study is one step forward towards exploiting the enzymes of nucleotide synthesis pathway as a potential therapeutic target against infectious diseases.

"Real obstacles don't take you in circles. They can be overcome. Invented ones are like a maze."

Barbara Sher

6

Recognition, Distortion and Allosteric Control of Purine Ligands by Adenylosuccinate Synthetase

6.1 Introduction

6.1.1 Overview of ADSS

Adenylosuccinate synthetase (ADSS) catalyzes the Mg^{2+} dependent condensation of a molecule of inosine-5'-monophosphate (IMP) with L-Aspartate to form succinyl adenosine-5′-monophosphate (sAMP), in a reaction coupled with the hydrolysis of guanosine-5'-triphosphate (GTP) to guanosine-5'-diphosphate (GDP) [93]. The reaction proceeds in two steps; the first step is a phosphoryl transfer reaction where, Asp43 (mouse muscle numbering) abstracts a proton from N1—H of IMP leading to the formation of 6-oxy anionic IMP. His71, on the other hand, provides a proton from its ND1 position to the leaving β-phosphate group of GDP. The γ-phosphate group of GTP is transferred to 6-oxo position of IMP resulting in the formation of an intermediate 6-phosphoryl IMP (6-pIMP). The second step is the phosphoryl displacement reaction where, the nucleophilic displacement of 6-phosphoryl group by L-Aspartate takes place to form sAMP. In this step, Asp43 and His71 both acts as a catalytic acid. His71, from NE2 position donates a proton to 6-phosphoryl group leading to its expulsion. At the same time, Asp43 returns proton to N1 position of nucleotide which results in the resonance stabilization

of C6 carbonium ion. This leads to the nucleophilic attack of L-Aspartate at C6 position leading to the formation of sAMP [93]. In this catalytic mechanism, Mg^{2+} ion helps in assembly of the reactants to facilitate the final catalytic step [94].

6.1.2 Information from crystal structures

Extensive structural studies at various steps of the catalytic cycles in *E. coli* (Ec) and mouse muscle (mm) ADSS are available [99, 107, 109, 110, 206, 209, 210]. These studies suggest that the active-site loops in apo ADSS without ligands are disordered [109, 110, 123], binding of ligands results in organization of loops. These loops in mmADSS have been divided into Pre-switch loop (65-69), Switch loop (70-83), IMP loop (152-165), Val loop (304-310), GTP loop (448-452) and Asp loop (330-336) [209]. Largest displacement of 9 Å is observed in the Switch loop in mmADSS and EcADSS [106, 209]. Conformational change in loop 299-304 is driven by the ligation of L-Aspartate pocket [106]. Further, the enzyme does not undergo any conformational change in response to the binding of guanine nucleotide and IMP and/or Mg^{2+} is required for the recognition of pyrophosphate group of GTP [110]. A complete active-site of IMP requires two subunits as Arg177 from one subunit anchors IMP of symmetry related subunit by forming hydrogen bond with 5′-phosphoryl group [206].

6.1.3 *Methanocaldococcus jannaschii* adenylosuccinate synthetase

ADSS from a thermophilic archaea *Methanocaldococcus jannaschii* (Mj) is truncated to 345 amino-acids against an average length of 430-457 amino-acids. Amino-acid sequences from MjADSS and *Pyrococcus horikoshii* show 68% sequence identity [32]. X-ray crystal structure of the latter has been solved (PDB: 2D7U and PH0438). Comparative studies of MjADSS with other homologues establish that the deleted segments in MjADSS are mapped at the region which is involved in ligand binding and subunit interface; the residues in these segments contribute to neither of these. Furthermore, the active-site residues which are playing a key role in catalysis and in formation

of non-covalent interactions with the ligand are conserved in PhADSS, EcADSS, mmADSS and MjADSS [32]. The thermophilic enzyme shows continuous increase in activity till 85°C. Interestinglyat 25°C, not only does the enzyme show binding to all substrates but it also leads to the formation of product at low catalytic-rate. k_{cat} of the enzyme at 70°C and 25°C is determined to be 4.2 s^{-1} and 0.45 s^{-1}, respectively [32].

6.1.4 Kinetic mechanism of MjADSS

MjADSS binds to its ligands in a sequential manner which involves rapid equilibrium random and ordered mechanism (Figure 6.1). Here, IMP and GTP bind randomly to the enzyme and L-Aspartate binds to the preformed ternary complex (ADSS•IMP•GTP) [32]. Release of product follows the similar pattern where Pi leaves the active-site first followed by the random release of sAMP and GDP.

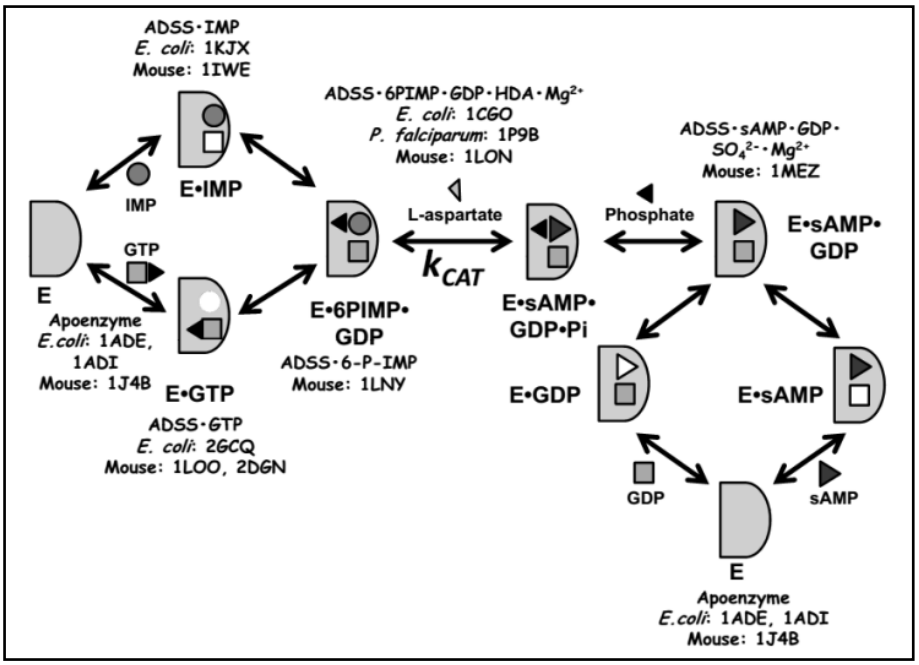

Figure 6.1: Kinetic mechanism of MjADSS. Crystal structures from various homologues at different kinetic steps are mentioned.

This chapter of my thesis is aimed at understanding ADSS induced distortion and allosteric control of the ligands at each step of the kinetic cycle. For this, I have studied complexes of MjADSS with substrates, intermediates,

analogues and products with the help of UVRR. In view of absence of crystal structure of MjADSS, structural information of ADSS from *P. horikoshii*, mouse and *E. coli* have been used to infer the information obtained from UVRR spectra. These interpretations are extrapolated to the structure and function of MjADSS and implications to the distortion of the ligand are suggested.

6.2 Methodology

6.2.1 ADSS sample preparation

IMP, GTP, GDP, sAMP, L-Aspartate, magnesium acetate and sodium nitrate were purchased from Sigma-Aldrich Co. Hadacidin (HDA) was procured from Develomental Therapeutic Programme, NIH. UVRR Samples were prepared in 30 mM MES pH 6.5. UVRR spectra of enzyme and nucleobase were acquired in buffer containing 5 mM magnesium acetate, 30 mM $NaNO_3$ and 10 mM HDA. 500 μM of nucleobase and 150 μM of enzyme were used for the Raman experiments.

6.2.2 C18 column run

A reaction volume of 50 μL containing MES buffer pH 6.5 (30 mM), magnesium acetate (15 mM), sodium phosphate (10 mM), sAMP (500 μM) and GDP (500 μM) was prepared. MjADSS was added at a concentration of 150 μM. Two different reactions of MjADSS were incubated at 25°C and 70°C. After 25 minutes of incubation period, enzyme was denatured by adding 0.1% SDS solution. 20 μL of supernatant was loaded onto the Luna 5 μm C18 (2) 100 Å, 260 x 4.60 mm (Phenomenex) column. The nucleotides were separated using a protocol employed by Ogawa et al. [116] with minor modification, in an isocratic flow of KH_2PO_4 (73 mM), tetrabutyl ammonium hydroxide (5 mM) and methanol (25%) at a flow rate of 0.5 mL/min for 25 minutes. Chromatogram was obtained at 251 nm (λ_{max} for IMP).

6.3 Results: Section I

6.3.1 Forward reaction complexes of MjADSS

UVRR spectra of enzyme•nucleotide complexes were acquired at the excitation wavelength of 260 nm. At 260 nm, selective resonance enhancement from nucleotides, without any interference from protein spectrum, was obtained (Figure 6.2). Perturbations in the structure of bound ligands at the active-site of MjADSS were observed in the form of Raman shifts and intensity modulation in the UVRR spectra. UVRR spectrum of bound ligand was obtained by subtracting the spectrum of apoenzyme and unbound ligand from the enzyme-ligand complex. Raman band assignments of IMP and GTP are taken from previous studies [34-36] (Table 6.1).

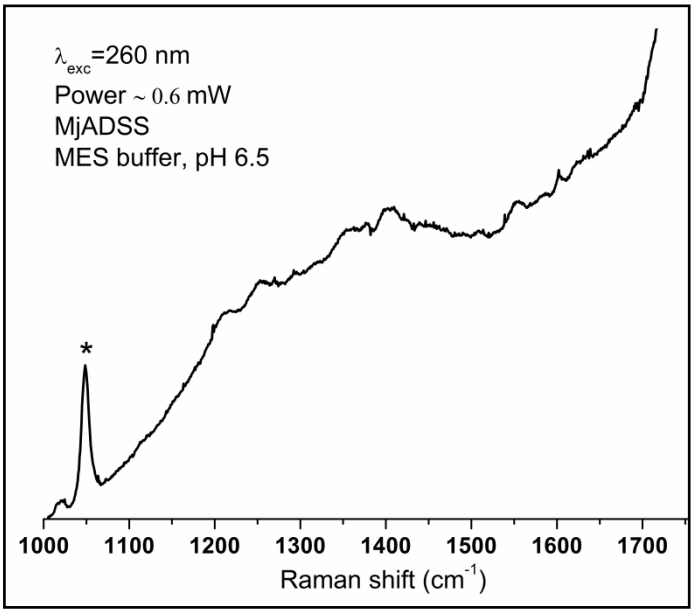

Figure 6.2: Raw Raman spectrum of MjADSS in MES buffer, pH 6.5 at 260 nm. The internal standard ($NaNO_3$) band at 1049 cm^{-1} is marked with asterisk (*). No spectral interference from enzyme is observed at 260 nm.

IMP•MjADSS: MjADSS distorts IMP towards its deprotonated form

The intense broad band at 1468 cm^{-1} is the UVRR spectrum of IMP is primarily a N1—H bending vibration (bend) (Figure 6.3 (a)). This band upshifts to 1472 cm^{-1} in the IMP•MjADSS (Figure 6.3 (b)). Similar upshift is observed when IMP is deprotonated at N1—H at higher pH. The UVRR spectrum of deprotonated IMP, acquired at an excitation wavelength of 260

nm is shown in Appendix (Figure A.5) [34]. Thus, upshift in the band at 1470 cm^{-1} reports on the distortion towards deprotonation.

The triene stretch mode appears as an intense band at 1555 cm^{-1} ($\Delta\nu_{HtoD}$ = -5 cm^{-1}). The corresponding band in the deprotonated IMP is observed at 1512 cm^{-1}, the intensity of which is markedly reduced. Binding of IMP to ADSS not only results in the downshift of 5 cm^{-1} but also shows a marked loss of intensity which is implicated in the weakening of N1—H bond (distortion towards deprotonated IMP) in IMP•MjADSS complex.

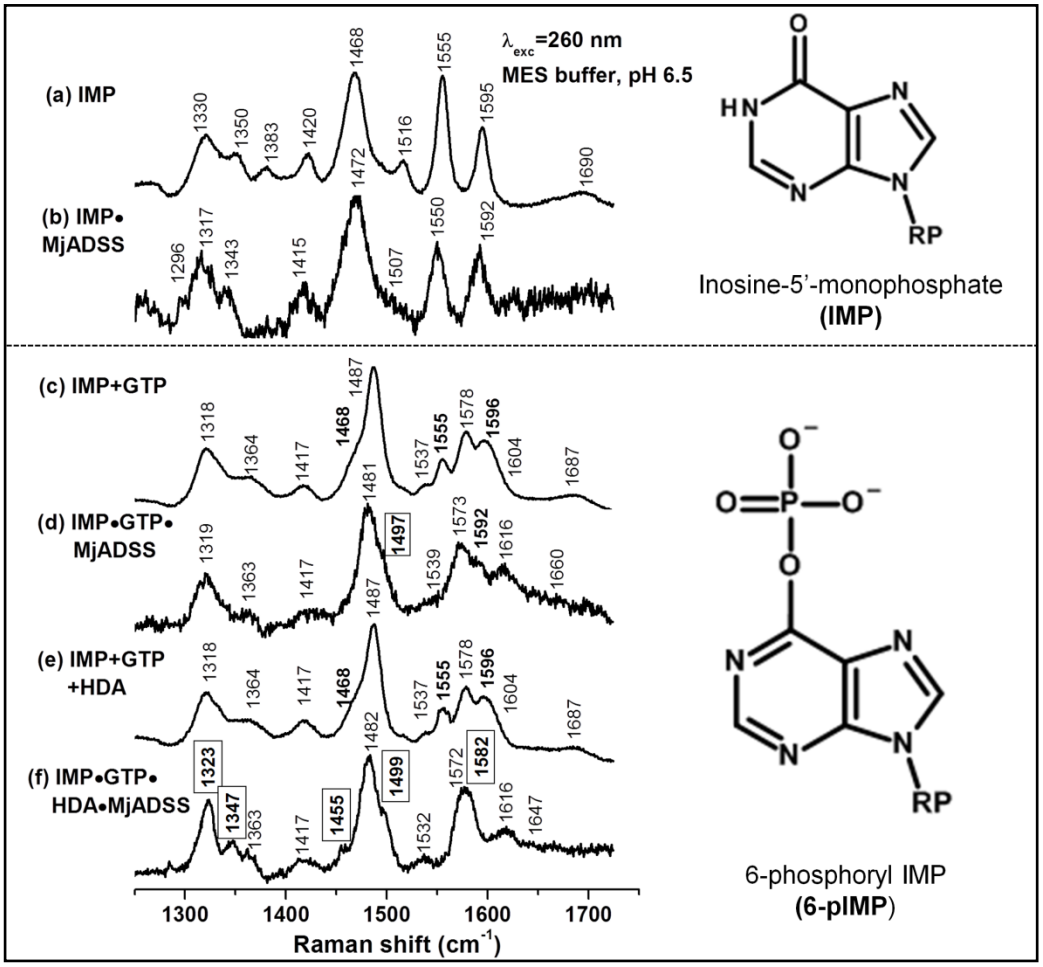

Figure 6.3: Resonance Raman spectra (λ_{exc}=260 nm) of forward reaction complexes of MjADSS in MES buffer in H_2O, pH 6.5. (a) IMP free in solution, (b) IMP bound to MjADSS, (c) IMP and GTP in solution, (d) IMP and GTP bound to MjADSS, (e) IMP, GTP and HDA in solution and (f) IMP, GTP and HDA bound to MjADSS. Wavenumbers in bold are the IMP bands and in boxes are the 6-pIMP bands.

The pyrimidine ring stretching mode is observed at 1595 cm^{-1} in IMP and downshifts to 3 cm^{-1} in IMP•MjADSS. This downshift results from the hydrogen bonding interactions at C6=O and N1—H moiety of pyrimidine ring [206] (Figure 6.4). The corresponding mode in deuterated IMP reorganizes to include the contribution from C6—N1 stretch and appears at 1580 cm^{-1} (Figure 6.5, Table 6.2). An upshift of 4 cm^{-1} in this band at IMP•MjADSS is implicated in decoupling of N1—H bend. It is well established that strong hydrogen bond formation between N—H and O—H of ligand with neighbor amino-acids increases the bending mode wavenumber [136]. Such upshift in the band with N1—H bending contribution was also observed previously in case of adenosine deaminase [136].

Raman bands in the 1300-1400 cm^{-1} region are contributed by the delocalized vibrational modes of the purine ring. The downshift observed in these bands in the IMP•MjADSS complex is corroborated by the further downshift observed in the corresponding D_2O spectrum.

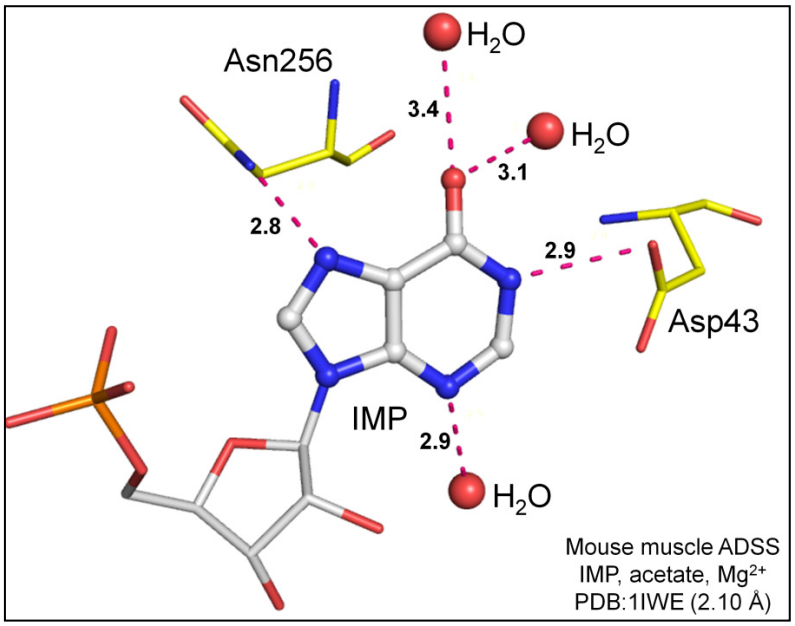

Figure 6.4: Non-covalent interactions between the nucleobase of IMP with active-site residue of ADSS from mouse muscle ADSS (1IWE: 2.10 Å) [206].

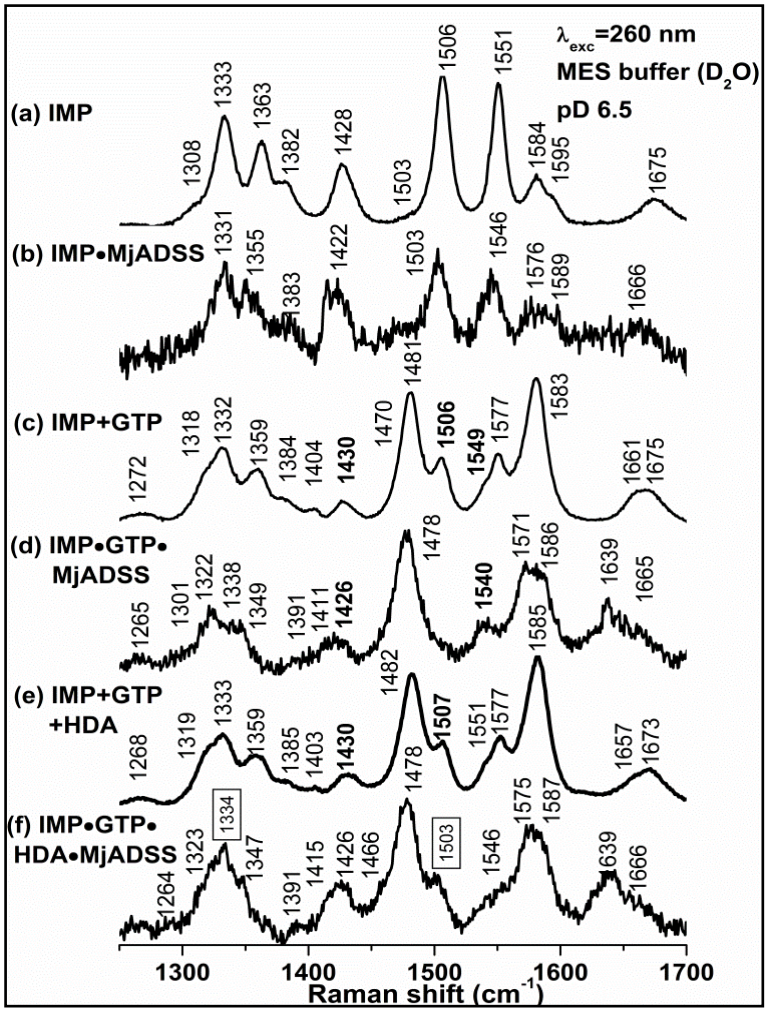

Figure 6.5: Resonance Raman spectra (λ_{exc}=260 nm) of forward reaction complexes of MjADSS in MES buffer in D_2O, pD 6.5. (a) IMP free in solution, (b) IMP bound to MjADSS, (c) IMP and GTP in solution, (d) IMP and GTP bound to MjADSS, (e) IMP, GTP and HDA in solution and (f) IMP, GTP and HDA bound to MjADSS. Wavenumbers in bold are the IMP bands and in boxes are the 6-pIMP bands.

GTP•MjADSS: GTP provides maximum intrinsic binding energy to MjADSS complexes

The band at 1684 cm^{-1} is attributed to the carbonyl stretch coupled to N1—H bend (Figure 6.6 (a) and (b)). The observed downshift of 27 cm^{-1} in this band GTP•MjADSS is attributed to the hydrogen bond between the C6=O of the purine ring with the backbone amide of Lys363 and Gly447 [206] (Figure 6.7). In D_2O, the band at 1665 cm^{-1} shows a downshift of 27 cm^{-1} in GTP•MjADSS (Figure 6.6 (c) and (d)).

The band at 1604 cm^{-1} in the GTP spectrum (N1—H bend and C2—N2 str) shows an upshift of 12 cm^{-1} in GTP•MjADSS. Hydrogen bonding between Asp365 with N1—H and exocyclic —NH_2 of guanine ring results in the decoupling of —NH_2 sci causing the resultant vibration to shift towards higher wavenumber [136].

Pyrimidine ring stretch coupled to —NH_2 sci and N1—H bend appears at 1578 cm^{-1} and downshift to 1571 cm^{-1} in GTP•MjADSS. The downshift results from the distortion in the pyrimidine ring which is caused due to the formation of hydrogen bond between Asp333 and —NH_2 and N1—H. A downshift in this band against an upshift observed in 1604 cm^{-1} suggests that the delocalized C2N2 stretch remains coupled to —NH_2 sci in this mode.

The imidazole ring mode appears as a most intense band at 1487 cm^{-1} and downshift by 6 cm^{-1} in GTP•MjADSS. Corresponding band in D_2O also shows downshifts by 3 cm^{-1} in GTP•MjADSS. X-ray structure of EcADSS reports on the interactions between side-chain hydroxyl group of Ser414 with N7 (D—A= 2.8 Å) [109].

Large magnitude of shifts in the spectrum of GTP•MjADSS with respect to GTP indicates that though the guanine nucleobase of GTP does not take part in chemical transformation by ADSS, it is held tightly by several non-covalent interactions at the active-site. These shifts in the Raman wavenumber are implicated in the formation of non-covalent interactions in GTP•MjADSS complex and thereby providing a significant amount of intrinsic binding energy to E•S. Furthermore, although shifts in wavenumber are observed, spectral pattern of the GTP at the active-site of MjADSS is preserved. Absence of any radical changes in GTP•MjADSS spectrum corroborates the catalytic mechanism of ADSS where no chemical transformation is observed at the nucleobase moiety [93].

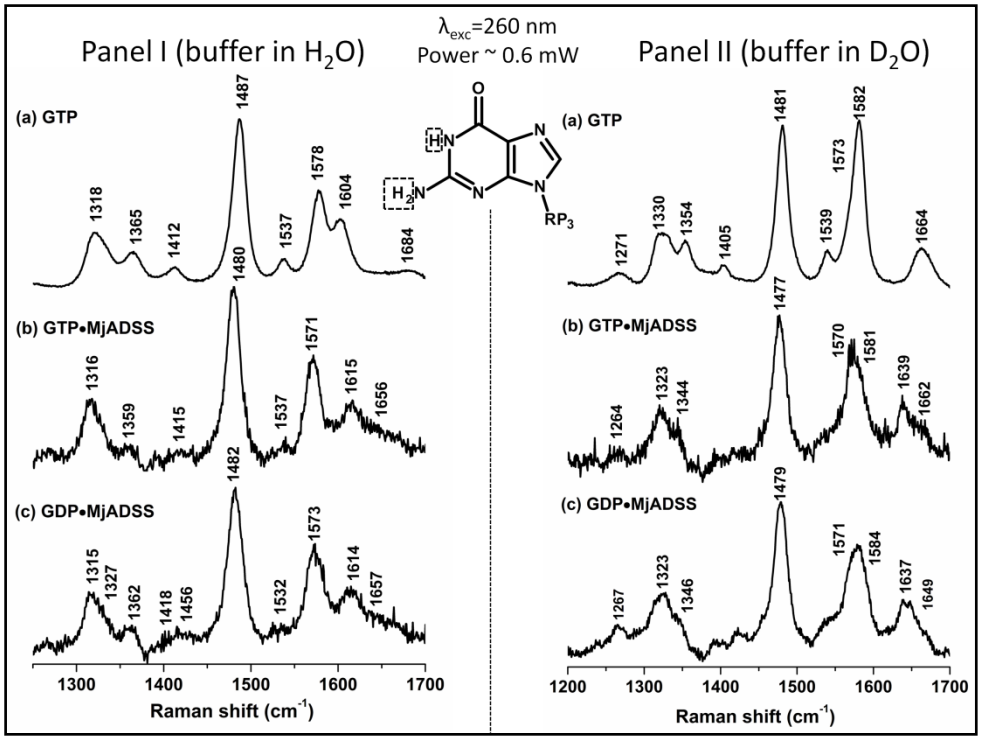

Figure 6.6: Resonance Raman spectra (λ_{exc}=260 nm) of guanine nucleotides with MjADSS. Panel I depicts the spectra obtained in MES buffer prepared in H_2O at pH 6.5, (a) Free GTP, (b) GTP•MjADSS and (c) GDP•MjADSS. Panel II depicts the spectra obtained in MES buffer prepared in D_2O at pD 6.5, (a) Free GTP, (b) GTP•MjADSS and (c) GDP•MjADSS. Chemical structure of GTP is shown (RP_3: ribose-5'-tri-phosphate).

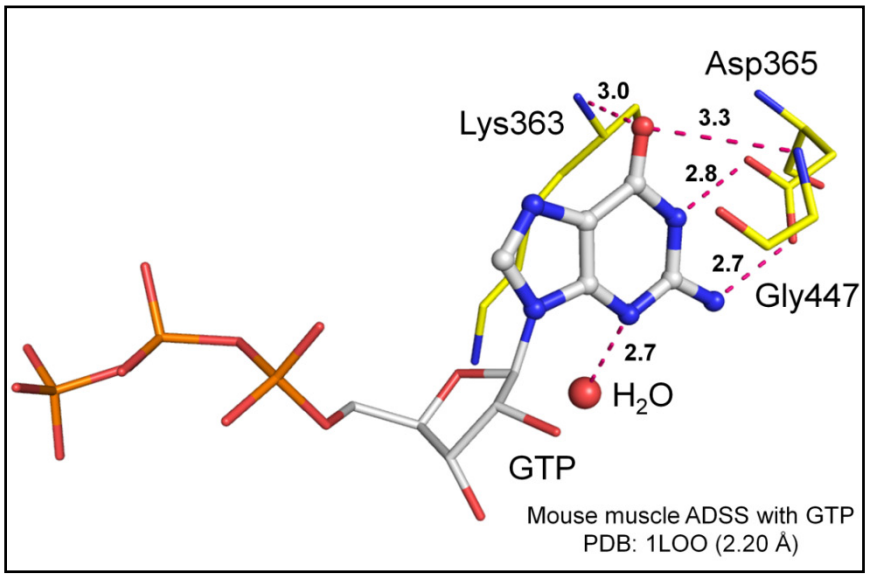

Figure 6.7: Non-covalent interactions between the nucleobase of GTP with active-site residue of ADSS from mouse muscle ADSS (1LOO: 2.20 Å) [206].

6.3.2 Intermediate complexes in the forward reaction of MjADSS

Extensive kinetic studies on ADSS from various organisms such as *E.coli* [211], mouse [209], *Zea mays* [212], *Saccharomyces cerevisiae* [117] suggest that IMP and GTP bind randomly to the enzyme and in different binding pockets. Once both these ligands are bound, structural studies suggest that the first catalytic intermediate, 6-pIMP, is formed even in the absence of L-Aspartate in these enzymes [93, 96]. By contrast, in case of MjADSS, it was reported that complete utilization of GTP and thus formation of 6-pIMP takes place in presence of HDA [115]. In absence of HDA, GTP was not completely hydrolysed to GDP. UVRR is a very sensitive technique which can distinguish a slight substitution and distortion in a molecule. Thus, complexes of MjADSS with IMP and GTP, in presence and absence of HDA, have been reported in this part of the thesis. Spectra of IMP•GTP•MjADSS and IMP•GTP•HDA•MjADSS were obtained by subtracting the spectra of apoenzyme and unbound ligands from enzyme•ligand spectrum.

IMP•GTP•MjADSS: 6-pIMP formation initiates in the absence of L-Aspartate ligation

In the UVRR spectrum of (free IMP + free GTP), a few bands belonging to IMP and GTP overlap in terms of wavenumbers because of similar normal modes of vibrations while a few other bands act as marker bands of IMP and GTP. For example, the band at 1468 cm^{-1}, 1555 cm^{-1} and 1595 cm^{-1} act as marker for IMP in the spectrum of (IMP+GTP) whereas the band at 1487 cm^{-1}, 1578 cm^{-1} and 1604 cm^{-1} are the marker bands for GTP (Figure 6.3 (c), also see Appendix (Figure A.6 and A.7)).

The spectrum of IMP•GTP•MjADSS evidently shows that the GTP bands are preserved whereas the IMP bands, apart from showing downshifts, disappear (Figure 6.3 (d)). For instance, the IMP band at 1555 cm^{-1} ($\Delta\nu$=-7 cm^{-1}, area under the curve is reduced) and 1595 cm^{-1} ($\Delta\nu$=-3 cm^{-1}) show shifts similar to the one observed in the IMP•MjADSS. Further, the band at 1468 cm^{-1} disappears instead a new shoulder appears at 1497 cm^{-1}. The same is also

evident in D_2O, where the corresponding band at 1506 cm^{-1} in (IMP+GTP), which has sole contribution from IMP, shows a loss in intensity in IMP•GTP•MjADSS (Figure 6.5 (c) and (d)).

In the catalytic mechanism of ADSS, Asp43 abstracts a proton from N1 of purine ring leading to the formation of deprotonated IMP [93, 96, 206]. Because of the similarity in the wavenumber position in deprotonated IMP (1512 cm^{-1}, Figure 6.8 (d)), appearance of new band at 1497 cm^{-1} is attributed to the formation of new species resembling the deprotonated form of IMP. Further, the spectra of deprotonated IMP in H_2O and D_2O are identical owing to the absence of any labile hydrogen. Thus, a meagerly intense band at 1512 cm^{-1} in the spectrum of IMP•GTP•MjADSS in D_2O buffer also, corroborates the observation of the corresponding spectrum in H_2O buffer.

Similar observation of change in protonation-state was also reported by Callender and co-workers in adenosine-5'-diphosphate ribose bound to malate dehydrogenase. Appearance of new band in the region from 1300-1400 cm^{-1} was interpreted as the protonation of N3 position of adenine moiety by a proximal aspartate residue [213].

The results obtained from this complex suggest that at the active-site of MjADSS, apart from IMP a new species is also present. On the basis of the previously proposed reaction mechanism, 6-pIMP formation takes place in this complex. UVRR data here evidently show that the formation of 6-pIMP does not require ligation of L-Aspartate pocket.

GTP in IMP•GTP•MjADSS

Marker bands of GTP retain their identity in IMP•GTP•MjADSS. The bands at 1487 cm^{-1} and 1684 cm^{-1} show a downshift of 7 cm^{-1} and 30 cm^{-1}, respectively. Similarly, the band at 1604 cm^{-1} shows an upshift of 12 cm^{-1} (Figure 6.3 (d)).

Table 6.1: Comparison of shifts in wavenumber (cm^{-1}) observed in the UVRR spectra of IMP•MjADSS, IMP•GTP•MjADSS, IMP•GTP•HDA•MjADSS and GTP•MjADSS complexes with respect to IMP in MES, pH 6.5.

Assignments	IMP	IMP•MjADSS	Band	IG or IGH[a]	IMP•GTP•MjADSS	IMP•GTP•HDA•MjADSS	Assignments	GTP	GTP•MjADSS
Str C6=O (76%) + Be N1H + C6N1C2 (-12%)	1690		IMP+GTP	1687	1660 (-27)	1653 (-34)	Str C6=O + C5C6 + BeN1H	1684	1657 (-27)
			GTP	1604	1616 (12)	1618 (12)	Be N1H+ Str C2N	1604	1614 (10)
Str C2N3 (55%) — C4C5 — C5C6 + Be C2H (-12%) + N1H	1595	1591 (-3)	IMP	1595	1592 (-3)				
			GTP	1578	1573 (-5)	1578 (0)	Str N3C4 + C4C5 + C5N7	1578	1574 (-4)
Str C4N9 (12%) — N3C4 (-22%) + N7C8 + Be N9H (15%) + C8H	1555	1552 (-5)	IMP	1555					
			GTP	1537	1539 (2)	1536 (-1)	Str C4N9 + C6=O + N1C2	1537	1534 (-3)
			GTP	1487	1481 (-6)	1481 (-6)	Be C8H + Str C8N9 + N7C8	1487	1483 (-4)
Str C4C5—N7C8 (30%) + C2N3 + Be	1515	1510 (-5)							

N1H + C8H + N7C8N9 (21%)									
Be N1H (-23%) + C8H + N9H + Str N7C8 (-15%) — C4N9 (-11%) + N1C2	1468	1473 (+3)	IMP	1468		1455 (-15)			
Be N1H (17%) + C2H (18%) + C5N7C8 (-10%) + Str N1C2 (17%) — C4N9 (10%)	1421	1418 (-3)	IMP+GTP	1417	1422 (5)	1418 (0)	Str C4N9 + C5N7	1413	1417 (+4)
			IMP+GTP	1364	1363 (-1)	1363 (-1)	Str N7C8 + NIC6 + C5N7	1366	1361 (-5)
Be N9H (20%) + C2H (-17%) + N1H + Str C8N9 (-17%) - C5N7C8 (-10%)	1381								
Be C2H (24%) + C8H + N1H + Str C5N7 (28%) — N7C8	1350	1340							
Be C8H (-13%) + N9H + C2H (-10%) + Str C4N9 (-10%) + C2N3C4 (10%)	1322	1314	IMP+GTP	1318	1319 (1)	1322 (4)			

[a]IG is (IMP+GTP) and IGH is (IMP+GTP+HDA).

Table 6.2: Comparison of shifts in wavenumber (cm^{-1}) observed in the UVRR spectra of IMP•MjADSS, IMP•GTP•MjADSS, IMP•GTP•HDA•MjADSS and GTP•MjADSS complexes with respect to IMP in MES, pD 6.5.

Assignments	IMP	IMP•MjADSS	Band Contribution	IG or IGH[a]	IMP•GTP•MjADSS	IMP•GTP•HDA•MjADSS	Assignments	GTP	GTP•MjADSS
Str C6=O (78%) + C6N1C2 (-10%) + Be N1H	1676		IMP	1673	1648 (-10)	1672 (-7)			
			GTP	1659	1637 (-22)	1639 (-18)	Str C6O + Be N1H	1665	1638 (-27)
Str C2N3 (55%) - C4C5— C5C6— C6N1 + Be C2H (-11%)	1580	1584 (+4)	IMP+GTP	1580	1586 (+4)	1586 (+10)	Sci NH2 + Py ring + Be N1H	1582	1580 (-2)
			1561 in IMP-		1572 (0)	1573 (-5)	Py ring + Sci NH2 + Be N1H	1572	1570 (-2)
Str C4N9 (-10%) - N3C4 (26%) — C5N7C8 (12%) + Be C8H	1551	1545 (-6)	IMP	1550		1553 (+1)			
			GTP	1538	1540 (-2)	1540	Pu ring + Be N1H + C8H + Sci NH2	1540	1539 (-1)
C5N9C8 (19%) + C2N3 + Be C8H (-10%)	1506	1503 (-3)	IMP	1506	1508 (0)	1503 (-4)			
			GTP	1481	1478 (-3)	1478 (-4)	Str N7C8 + Py ring + Be C8H + N1H + N2H2b	1481	1479 (-2)

Str C5N7C8 (20%) - C4N9 (-24%) — N3C4C5 (-11%) + Be C2H + C8H	1428	1421 (-7)	IMP	1428	1421 (-7)	1425 (-5)			
			GTP	1404	1397 (-7)	1362 (-22)	Py ring + Str N7C8 + rock NH2 + Be N1H	1404	1410 (6)
Be C2H (47%) + N9H + C8H + Str C5N7 (11%) - C8N9 + C2N3 (13%)	1383	1383 (0)	IMP	1383					
Str N7C8 (-12%) + N1C2 (-11%) + Be C2H (12%) + C8H (-16%)	1363	1355 (-8)	IMP+GTP	1359	1346 (-13)	1348 (-11)	Pu ring + Be N2H2a	1355	1346 (-9)
Be C2H + C8H (13%) + N1H + N9H + Str N1C2 (25%) + N7C8 (14%) — C8N9 (14%)	1333	1332 (0)	IMP+GTP	1332	1324 (-8)	1334	Imidazole ring vibration + N7H bending	1330	1326 (-4)
Str C2H (28%) + C8H + N9H + N7C8 (-13%) — N9C4 (-10%)	1308		IMP+GTP	1318		1321 (+3)	Be N1H + N2H2b + C8H + Str C5N7 — C2N2	1318	

[a]IG is (IMP+GTP) and IGH is (IMP+GTP+HDA).

IMP•GTP•HDA•MjADSS: Ligation of L-Aspartate pocket stabilizes 6-pIMP at the active-site of MjADSS

HDA does not absorb light at 260 nm. Consequently, its spectrum is not resonance enhanced at this excitation wavelength and does not interfere with the spectrum of the E•S. In the absence of the enzyme, the spectra of (IMP+GTP) and (IMP+GTP+HDA) are identical (Figure 6.3 (c) and (e)). The differences between the spectra of (IMP+GTP+HDA) and its corresponding enzyme bound complex in MES buffer pH 6.5 are conspicuous (Figure 6.3 (e) and (f). Marker bands of IMP at 1468 cm^{-1}, 1555 cm^{-1} and 1595 cm^{-1} completely disappear. New bands at 1499 cm^{-1} and 1455 cm^{-1} become more intense in the presence of HDA. The band at 1363 cm^{-1} which had contribution from both IMP (1350 cm^{-1}) and GTP (1366 cm^{-1}) is replaced by two new bands at 1347 cm^{-1} and at 1363 cm^{-1} in the enzyme bound form. Such radical changes in IMP•GTP•HDA•MjADSS spectrum indicate transformation of IMP to a new species which is most likely 6-pIMP.

Carbonyl stretch at 1686 cm^{-1} in (IMP+GTP+HDA) shows a downshift of 30 cm^{-1} in the corresponding enzyme bound complex (IMP•GTP•HDA•MjADSS). This shift is similar to the one observed in the spectrum of IMP•GTP•MjADSS (31 cm^{-1}). This suggests that GDP remains bound to the enzyme until the product sAMP is formed. Further, this carbonyl stretch is more prominent in the E•S spectrum in D_2O. Here, a broad carbonyl stretch band, characteristic of free IMP and GTP, becomes intense and narrow in E•S.

The band at 1323 cm^{-1} has a contribution from IMP as well as GTP. This band downshifts by 4 cm^{-1} in IMP•MjADSS and GTP•MjADSS complexes, but in IMP•GTP•HDA•MjADSS this band shows an upshift of 4 cm^{-1}. The band also gains intensity with the area under the curve increasing by a factor of 2.5 with respect to that of free ligands.

Establishing the formation and UVRR identity of 6-pIMP

To further confirm the identity of the species formed in the presence of HDA, I performed isotope labeling (H→D) of the substrates. The E•S complexes were prepared in D_2O. This allows substitution of the labile hydrogens with deuterium atoms. The effect of isotope substitution on individual bands of the starting substrates, IMP and GTP is known. The spectrum in Figure 6.5 (f) shows that the new species formed in the presence of HDA has novel isotope induced shifts. A new, intense band appears at 1503 cm^{-1} in IMP•GTP•HDA•MjADSS spectrum in D_2O that corresponds to the characteristic band of 6-pIMP at 1500 cm^{-1} in H_2O (Figure 6.3 (f)). The IMP marker band at 1428 cm^{-1} seen in the spectrum of (IMP+GTP+HDA) in D_2O disappears and is replaced by a band at 1424 cm^{-1}. Another IMP marker band at 1383 cm^{-1} that is present in the (IMP+GTP) spectrum is absent in the spectrum of the IMP•GTP•HDA•MjADSS complex consistent with the transformation of IMP into 6-pIMP.

Table 6.3: Experimental resonance Raman wavenumbers of 6-pIMP[a] and DFT (B3LYP/6-31G (d, p)) predicted vibrational wavenumbers with mode assignments.

Mode assignments	DFT	UVRR
Str N1C6 (21%) + Str N3C4 (23%)	1635	1629
Str C2N3 (-19) + Be C2N3C4 (10%) + Be N3C4C5 (-12%) + Be C4N9C8 (15%)	1625	1583
Str N7C8 (27%) + Be N7C8H (-18%)	1542	1539
Str N1C6 (24%) + Be C2HN3 (41%)	1498	1498
Str N7C8 (15%) + Str N3C4 (19%)	1453	1455
Purine ring stretching+C2H bending	1390	1418
Str C6N6 (12%) + Be C2HN3 (23%)	1360	1366
Str N1C2 (24%) + C2N3 + N7C8	1346	1346
Str C2N3 (-15%)	1321	1324
Be N7C8H (-23%)	1244	1284

[a]Spectral identity of 6-pIMP is obtained by subtracting the spectrum of GTP•MjADSS from IMP•GTP•HDA•MjADSS.

In order to obtain the spectral identity of the species that is formed in the fully ligated ADSS complex, the spectrum of GTP•MjADSS was subtracted from the spectrum of IMP•GTP•HDA•MjADSS. The resultant spectrum, containing bands only from the new species, was compared with the DFT predicted Raman spectrum of 6-pIMP (Figure 6.8 (a) and (b)). Computed Raman spectrum agrees well in the wavenumber positions with the experimental values (Table 6.3). I have also compared the UVRR spectra of AMP and deprotonated IMP with that of 6-pIMP (Figure 6.8 (c) and (d)). This is because of the similarity in their structures which arises from, first, the presence of a single bond between C6 and exocyclic group attached to it, and second, absence of any hydrogen at the N1 position which results in similar purine ring properties in 6-pIMP, AMP and deprotonated IMP.

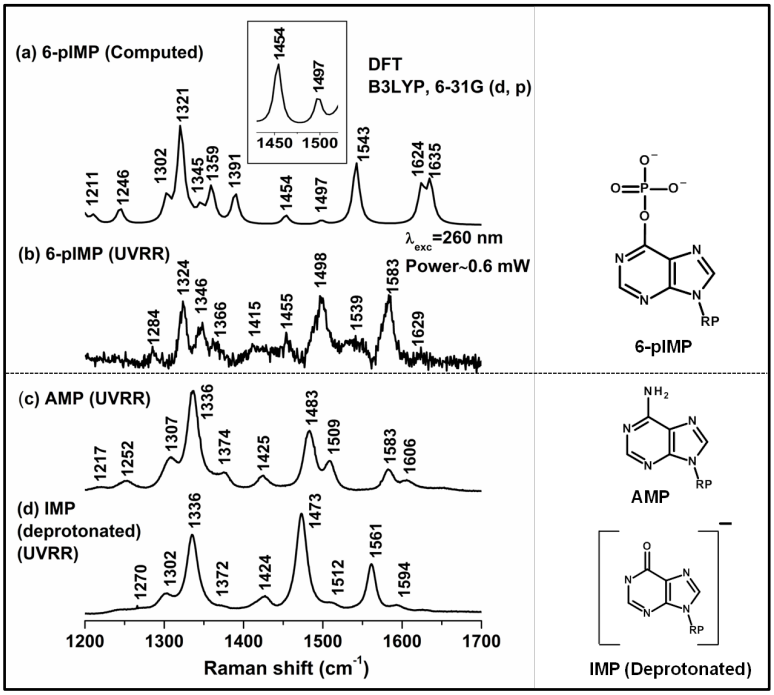

Figure 6.8: Raman spectra of 6-pIMP and its model compounds. (a) DFT (B3LYP/6-31G (d, p) predicted Raman spectrum of 6-pIMP, the wavenumber region from 1450-1500 cm^{-1} is zoomed in the inset. Experimental UVRR spectra of (b) 6-pIMP obtained by subtracting the spectrum of GTP•MjADSS from that of IMP•GTP•HDA•MjADSS spectrum, (c) AMP, (d) deprotonated IMP; acquired at the excitation wavelength of 260 nm. Chemical structures of 6-pIMP, AMP and deprotonated IMP are also shown.

To further prove that the changes observed in the E•S spectrum are due to the formation of 6-pIMP and not mere distortion of IMP, control experiments of MjADSS with (IMP+GDP), (IMP+GMP-PNP) and (IMP+GDP+L-Aspartate) were carried out. The (IMP+GDP+L-Aspartate) complex serves as control for the (IMP+GTP+HDA) complex. GDP serves as an analogue for GTP and binds at the same active-site, but the absence of a transferable phosphate group renders the complex incapable of forming 6-pIMP. Consistent with this expectation, the spectral pattern of the corresponding E•S complex (IMP•GDP•L-Aspartate•MjADSS) does not change and the characteristic marker bands of IMP are present (Figure 6.9 (a) and (b)). GMP-PNP is a non-hydrolysable analogue of GTP and thus cannot transfer its γ-phosphate group to C6 carbonyl of IMP. Further, none of the above mentioned controls are capable of forming 6-pIMP in the view of absence of transferrable γ-phosphate group. Figure 6.9 (c), (d) and (e) show the spectra of GMP-PNP, IMP•GMP-PNP•MjADSS and IMP•GMP-PNP•HDA•MjADSS, respectively. The band at 1499 cm^{-1} which was regarded as a marker band of 6-pIMP in IMP•GTP•HDA•MjADSS is not observed in these control experiments. Further, IMP bands are intact in the control E•S spectrum, but the distortion in this E•S complex similar to the one observed in the productive complex (IMP•GTP•MjADSS) is evident. Also, no new bands are observed in the E•S complex. Thus, while the presence of GMP-PNP is sufficient to bring about the changes in conformation of the active-site of IMP, it is incapable of transferring the phosphate to the IMP. These shifts also highlight the role of the guanine moiety of GTP as the allosteric modulator of IMP active-site.

Previous studies with GDP along with IMP and Mg^{2+} show the complete organization of dynamic loops in active conformation [110]. Our results show that the guanine moiety in GTP is most likely to be the allosteric effector of IMP binding site. Thus, structural distortions of IMP molecule in presence of GDP/GMP-PNP are similar to those observed in the IMP+GTP+MjADSS complex. However, in the absence of γ-phosphate further transition in the

protonation-state of IMP from neutral to deprotonated form is not observed in these controls.

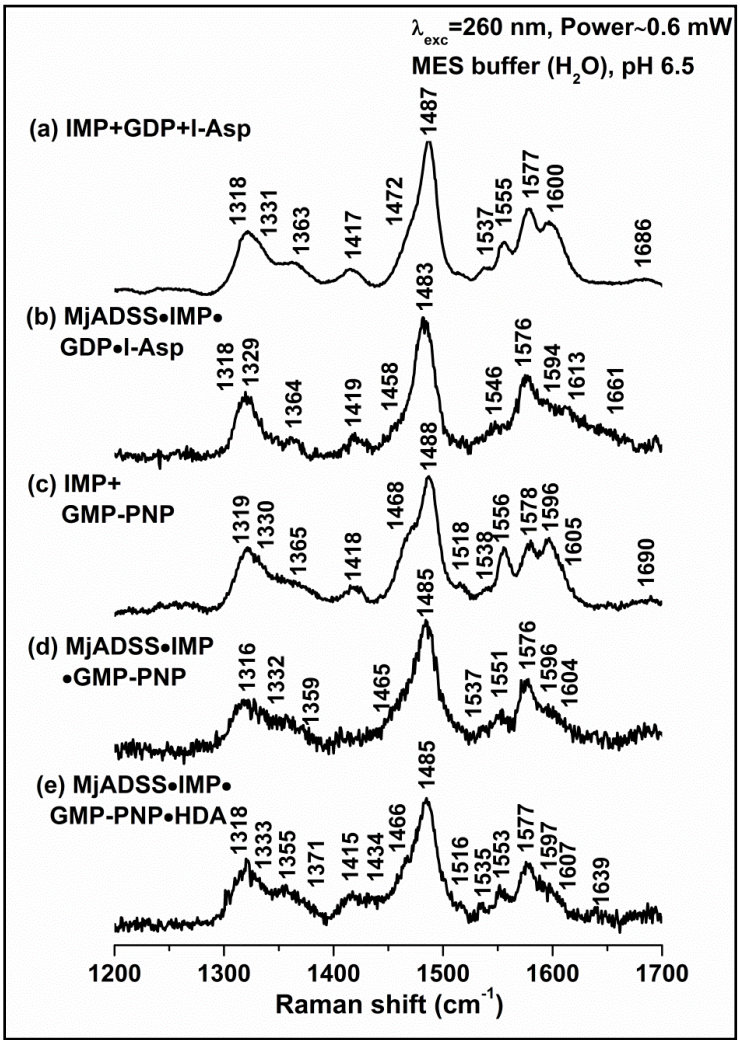

Figure 6.9: Resonance Raman spectra (λ_{exc}=260 nm) of various guanine nucleotide complexes of MjADSS in MES, pH 6.5. (a) (IMP+GDP+L-Aspartate), (b) MjADSS•IMP•GDP•L-Aspartate, (c) (IMP+GMP-PNP), (d) MjADSS•IMP•GMP-PNP, and (e) MjADSS•IMP•GMP-PNP•HDA. The characteristic band at 1499 cm^{-1} is not observed in any of these complexes.

In general, although the bands in a Raman spectrum of an E•S complex show positional shift with respect to the free ligand spectrum, the spectral pattern is preserved. Only if a covalent bond is formed or broken does the spectral pattern change drastically. In IMP•GTP•HDA•MjADSS where, 6-pIMP is formed, aromaticity of the purine ring is expected to change considerably and this leads to the large change in the vibrational modes

pattern. Here, the difference between (IMP+GTP+HDA) and IMP•GTP•HDA•MjADSS spectra is so drastic that mere environmental effect of the active-site residues on highly polarisable groups like C=O, C=N, O—H and N—H (enzyme induced electronic perturbations) cannot explain the reason behind the same. These changes pointed to a covalent modification of IMP. The new molecule is identified as 6-pIMP based on the Raman band positions and comparison with computed spectrum.

6.3.3 Attempt to isolate 6-pIMP in solution

The Raman spectrum of 6-pIMP depicts the MjADSS bound form of the intermediate. An attempt was made to isolate 6-pIMP using RP-HPLC. 20 μL of the reaction mixture containing MjADSS (150 μM), GTP (500 μM), IMP (500 μM), HDA (10 mM) and magnesium acetate (15 mM) in MES pH 6.5 (30 mM) was loaded onto the Luna reverse phase-high performance liquid chromatography (RP-HPLC) C18 column (Phenomenex). The column was eluted in an isocratic run with a buffer containing methanol (25%), tetra butyl ammonium hydroxide (5 mM) and potassium dihydrogen monophosphate (73 mM) [116]. The absorbance was monitored at 251 nm (λ_{max}=IMP). The chromatograms have been shown in Appendix (Figure A.8). Control nucleotides were also run under identical conditions to obtain the retention time of each molecule. Retention time for IMP, GDP, GTP and sAMP is 8 min, 10 min, 13 min and 18 min, respectively. MjADSS reaction mixture which was incubated at 25°C for 25 min shows peak at 8 min, 10 min and 13 min corresponding to IMP, GDP and GTP, respectively. A separate peak of 6-pIMP could not be obtained presumably because upon denaturation of enzyme, 6-pIMP falls off from the active-site and reverts back to IMP.

6.4 Discussion on the forward reaction complexes

There is a plethora of structural information about Michaelis complex and enzyme-product complex, acquired using various techniques such as x-ray crystallography and NMR. However, a precise explanation of the mechanism of enzymatic catalysis which also involves enzyme-induced substrate

distortion requires understanding of all the enzyme bound complexes including transient intermediates of a kinetic cycle. Using a sensitive technique, UVRR, I have investigated the extent of enzyme induced distortion at each step of kinetic mechanism. This chapter also delineates the systematic transition in the structure of IMP at the active-site of MjADSS along the reaction pathway.

IMP binding: The results discussed in this chapter suggest that binding of IMP to the active-site of MjADSS accompanies substantial molecular distortion towards deprotonated form, however, the N1 of purine is not deprotonated as the spectral pattern of IMP is preserved in IMP•MjADSS. The catalytic mechanism of ADSS involves abstraction of proton from N1 of IMP (donor-acceptor (D-A) distance: 2.9 Å, 1IWE) [206] resulting in the delocalization of C6=O bond and formation of C6 oxyanion which in turn is converted to 6-pIMP. This is the first step of the catalytic mechanism which involves phosphoryl transfer and is expected to have a transition-state where the N1 is deprotonated. The data presented here evidently suggest distortion of the IMP towards deprotonated form and thus capture the pre-transition state of the phosphoryl transfer step. Further, the distortions in the bands comprised of imidazole ring mode arise from the interactions between the N7 of purine ring and Asn256 (D-A: 2.8 Å, 1IWE) and between the C6=O and Asn256 (D-A: 4.0 Å, 1IWE).

GTP binding: GTP transfers the γ-phosphate group to C6 oxy anion of IMP. Substantial shifts in the band positions of GTP•MjADSS with respect to GTP in solution is implicated in hydrogen bond interactions at the active-site, and suggest that the GTP is held tightly at the active-site. A large downshift of 30 cm^{-1} in the carbonyl stretching wavenumber of GTP•MjADSS directly captures this important interaction. Interestingly, the shift in this band is similar in IMP•GTP•MjADSS (-31 cm^{-1}) and also in IMP•GTP•HDA•MjADSS (-30 cm^{-1}). This implies that the enthalpy of hydrogen bond formation at carbonyl of guanine moiety does not vary much from ground-state to transition-state. Shift in carbonyl also suggests that GTP

after donating the γ-phosphate group remains bound to the active-site until the product sAMP is formed.

(IMP+GTP) binding: Although IMP•MjADSS shows shifts in the wavenumber with respect to the free IMP in solution, they have similar spectral identity. When IMP and GTP are added together to *Mj*ADSS, not only do the downshifts in IMP bands suggest greater distortion but the appearance of new band at 1497 cm^{-1} suggests the formation of 6-pIMP. However, intact IMP bands suggest the presence of IMP•MjADSS along with 6-pIMP•MADSS. This implies that in the absence of its stabilization, 6-pIMP formed in the ternary complex (IMP•GTP•MjADSS) falls off from the active-site and reverts back to IMP. Thus, the spectrum of IMP•GTP•MjADSS is contributed by bound IMP as well as bound 6-pIMP.

(IMP+GTP+HDA) binding: It is evident that the spectrum of IMP•GTP•HDA•MjADSS features a number of new bands. Complete disappearance of the marker bands of IMP and appearance of new bands suggest that IMP is completely transformed to 6-pIMP. The new observed spectrum agrees well with the DFT predicted spectrum of 6-pIMP. Most conspicuous new bands in the resultant spectrum are the bands at 1583 cm^{-1}, 1498 cm^{-1} and 1324 cm^{-1}. Further, the position of these bands is compared with the UVRR spectrum of AMP, a model compound which has an intense shoulder at 1509 cm^{-1} in water [36]. The protonation-state of purine ring at N1 position and aromatic character of the ring in AMP and 6-pIMP are similar. Thus, it is evident from IMP•GTP•HDA•MjADSS spectrum that 6-pIMP is formed.

6.4.1 6-pIMP is stabilized in the presence of HDA/L-Aspartate

The complete transition of IMP to 6-pIMP upon ligation of L-Aspartate pocket suggests that the stabilization of 6-pIMP at the active-site of *Mj*ADSS is not facile in absence of Asp/HDA. Addition of HDA stabilizes 6-pIMP at the active-site. This is also corroborated by a previous study where upon addition of IMP and GTP to MjADSS, in the absence of L-Aspartate, GDP

was not formed instantaneously but was built over time. On the other hand, upon addition of HDA, complete utilization of GTP within 30 s was observed [115]. Ligation of L-Aspartate pocket by either L-Aspartate or HDA is known to bring about the conformational changes in the binding pockets of ADSS, more specifically in the Asp loop. Raman spectra at various steps of kinetic cycle capture these subtle local conformational changes around the ligands. These conformational changes are summarized in Figure 6.10.

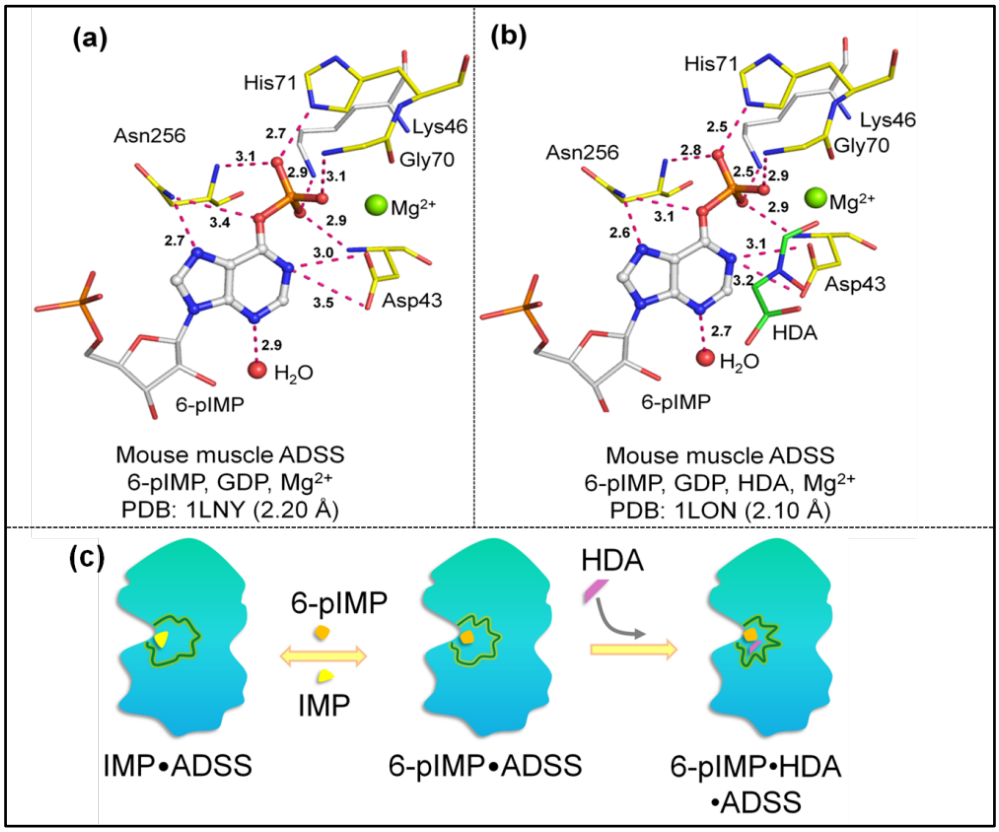

Figure 6.10: Active-site interactions of 6-pIMP [206] (a) in absence of HDA (1LNY: 2.20 Å) and (b) in presence of HDA (1LON: 2.10 Å). Orientation of amino-acid residues is similar in two cases. (c) cartoon depicting the effect of binding of HDA to the complex, 6-pIMP•ADSS on the local conformational re-organization of the active-site, as inferred from the present study.

6.4.2 His residue plays a key role in stabilizing 6-pIMP

Crystal structure of EcADSS with IMP, HDA and NO_3^- suggests that His41 acts as catalytic acid in the phospho-transfer step and donates a proton from its ND2 position to GDP to stabilize the charge development while gamma-phosphate leaves to 6-oxy anionic IMP [109]. In the second step

where phosphoryl displacement occurs, His41 undergoes a rotation by 90 degrees around Cβ-Cγ bond and donates a ε' proton to the 6-phosphoryl group. The rotation of His41 is driven by the ligation of L-Aspartate pocket. The interaction of HDA at L-Aspartate pocket stabilizes the hydrogen bond between His41 and 6-phopshoryl group [93, 96, 109, 210] (Figure 6.10). Direct observation of this hydrogen bond has been possible in the UVRR spectrum where 6-pIMP is found to be stabilized upon ligation of L-Aspartate pocket. Due to the least stability of this intermediate, its isolation has been difficult. However, this is the first study in ADSS where resonance Raman spectrum of 6-pIMP is observed in solution-state.

In conclusion, it is evident that in MjADSS, formation of 6-pIMP does not require ligation of aspartate pocket but the stabilization does. Absence of any stabilization of 6-pIMP in PfADSS mutant (Thr307Val) which does not bind to the HDA indicates that the conformational change in the His41 is brought about by the ligation of HDA only. It is also observed that if no HDA binds then Asp13 does not lie in the inner coordination sphere of Mg^{2+}. In such case, His41 is not capable of bringing about the phosphoryl displacement reaction in ADSS.

Based on the analysis of available crystal structure of EcADSS (IMP•GDP•HDA•EcADSS: 1GIM), it is observed that if no 6-pIMP forms then Asp13 (equivalent to Asp43 in mmADSS) does not lie in the inner coordination sphere of Mg^{2+} (D-A distance: 3.2 Å). In a structure (6-pIMP•HDA•EcADSS: 1CGO), where 6-pIMP is formed and HDA is also present, then a conformational change in the side-chain of His41 causes Asp13 to enter the inner coordination sphere of Mg^{2+} [106]. A coordinate bond between Asp13 and Mg^{2+} (D-A distance: 2.1 Å) makes Asp13 a strong catalytic acid which can now return a proton to N1 of purine ring. This distance is greater (4.1 Å) in IMP bound complex of mmADSS (1IWE) [206]. In another complex (IMP•HDA•PPi•EcADSS:1KKF), when no 6-pIMP is formed at the active-site then even in the presence of HDA, Asp13 does not lie in the inner coordination sphere of Mg^{2+}. These observed conformational

changes in crystal structures along with the present Raman data suggest that the coordination of Asp43 with Mg^{2+} and a hydrogen bond between His71 and 6-pIMP stabilize the intermediate at the active-site of ADSS. The conformational changes necessary for the formation of these bonds are driven by the ligation of HDA.

6.5 Results: Section II

6.5.1 Reverse reaction complexes of MjADSS

While there is a plethora of information available on the forward reaction complexes, structural studies on the product complexes of ADSS are scant [107]. sAMP, a product of ADSS catalyzed reaction, has an absorption maximum at 269 nm and thus at the excitation wavelength of 260 nm, resonance enhancement in the spectral features of sAMP is observed.

UVRR spectrum of sAMP was acquired in buffers made in H_2O and D_2O. In D_2O, the labile hydrogen at C6—N6H gets replaced by deuterium. DFT calculations were carried out on the energy minimized structure of sAMP to obtain the normal modes composition. To predict the effect of deuterium labeling in solution state, calculations were carried out by replacing the hydrogen at N6H position by deuterium. Experimental spectrum was assigned to the DFT predicted spectrum based on the comparison between deuterium labeled isotopic shift obtained in the two cases. A detail account of the normal mode assignments to sAMP in H_2O and D_2O buffers has been provided in Chapter 5.

Spectra of complexes of MjADSS with sAMP; GDP; (sAMP+GDP) and (sAMP+GDP+Pi) were obtained and compared with the spectra of corresponding free substrates in solution. AMP differs from IMP in having $–NH_2$ group at C6 instead of =O in IMP. Though both the moieties are completely opposite in their hydrogen bonding capacity, they bind the same active-site and hence AMP acts as a competitive inhibitor of IMP in ADSS [107]. In this part of the chapter, I have delineated the distortions in these ligands upon binding to the enzyme. Extensive comparisons have been made

between all the product complexes of ADSS. Conformational changes upon binding to the individual ligand and plausible reaction mechanism in the reverse direction is also discussed.

sAMP•MjADSS: sAMP alone is sufficient to organize the dynamic loops around active-site

The only crystal structure with sAMP along with GDP, SO_4^{2-} and Mg^{2+} suggests that the dynamics loops (basically Switch loop and Val loop) are oriented in a closed loop conformation [107]. Since, no crystal structure with sAMP alone is available, conformational changes in various dynamics loops can only be presumed depending on the basis of Raman shifts observed in this complex.

Changes in the spectral region from 1300-1600 cm^{-1} of sAMP•MjADSS spectrum as compared to sAMP in solution are clearly observed (Figure 6.11 (a) and (b)). Raman bands in this region are highly coupled delocalized vibrations basically assigned to purine ring mode, C=C and C=N stretch. The band at 1633 cm^{-1} ($\Delta\nu_{H\ toD}$ = -11 cm^{-1}) in sAMP spectrum is attributed to C6—N1—C2 bend and C2N3—C6NH str and shows a downshift of 5 cm^{-1} in the sAMP•MjADSS (Table 6.4). Shifts in the bands comprising of C6—NH vibrations suggest hydrogen bonding interactions between N6H and Asn68 of active-site. In D_2O, C6—NH str decouples from this mode and this may well be the reason of absence of any shifts in this band in sAMP•MjADSS in D_2O ((Figure 6.12 (a) and (b)), Table 6.5).

In the absence of a crystal structure of MjADSS with sAMP, I have compared the observations with the crystal structure of mmADSS along with sAMP, GDP, SO_4^{2-} and Mg^{2+} (Figure 6.13). This structure shows that sAMP occupies the same binding pocket as IMP. The N1 of sAMP, though not protonated, lies in the vicinity of Asp43. Neither sAMP nor Asp43 is protonated at physiological pH and thus Raman shifts in the bands corresponding to the N1 of sAMP imply the presence of non-bonding interactions with Asp43 [107]. A steric interaction between Asp43…N1

(sAMP) may contribute to the distortion observed in sAMP. Such destabilization may be a strategy employed by the enzyme to facilitate easy release of product from the active-site.

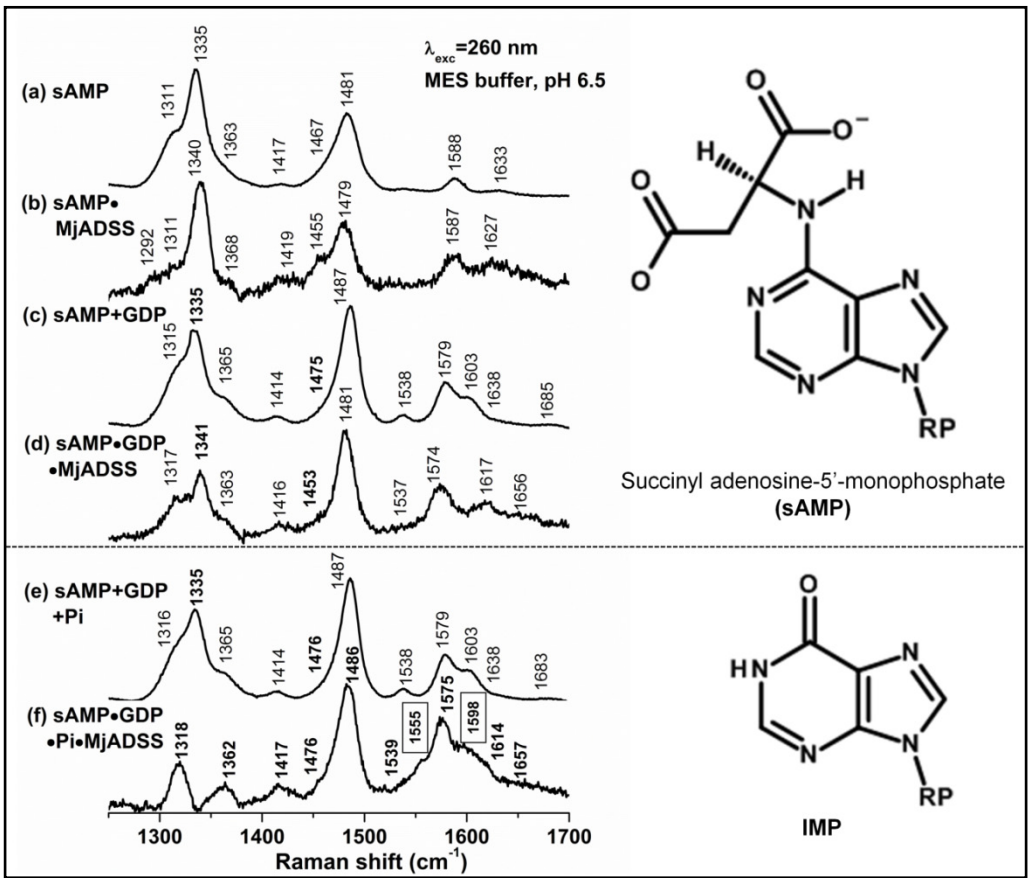

Figure 6.11: Resonance Raman spectra (λ_{exc}=260 nm) of reverse reaction complexes of MjADSS in MES, pH 6.5. (a) sAMP free in solution, (b) sAMP bound to MjADSS, (c) sAMP and GDP in solution, (d) sAMP and GDP bound to MjADSS, (e) sAMP, GDP and Pi in solution and (f) sAMP, GDP and Pi bound to MjADSS.

A very intense marker band of sAMP at 1335 cm^{-1} ($\Delta\nu_{HtoD}$ = +12 cm^{-1}) shows an upshift to 1340 cm^{-1} in sAMP•MjADSS spectrum. This band is attributed to C=N str along with C2H and N6H bends. DFT calculations predict that deuterium labeling leads to the decoupling of C2H and N6H bends and thus results in upshift. An upshift in the band in sAMP•MjADSS spectrum with respect to free sAMP spectrum, arises from the decoupling of N6H from the main vibrations due to the hydrogen bond formation between N6H and Asn68.

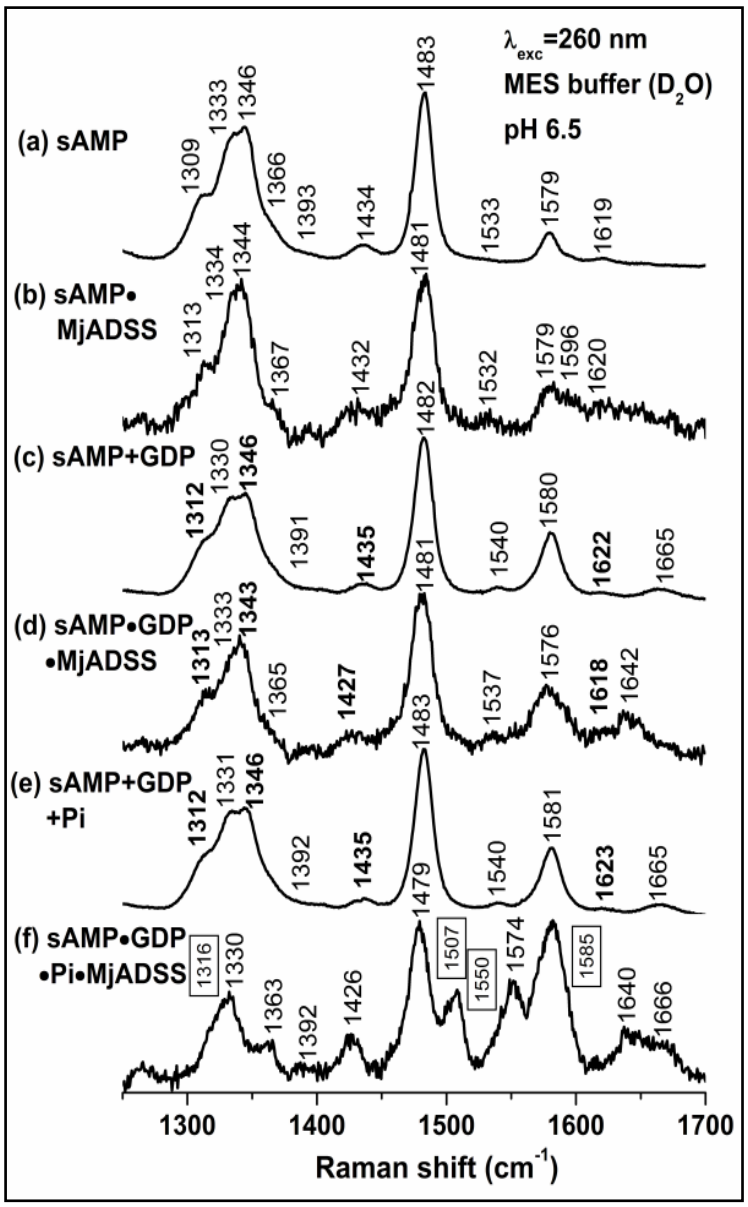

Figure 6.12: Resonance Raman spectra (λ_{exc}=260 nm) of product complexes of MjADSS in MES, pD 6.5. (a) sAMP free in solution, (b) sAMP bound to MjADSS, (c) sAMP and GDP in solution, (d) sAMP and GDP bound to MjADSS, (e) sAMP, GDP and Pi in solution, and (f) sAMP, GDP and Pi bound to MjADSS

Table 6.4: Comparison of shifts in wavenumber (cm^{-1}) observed in the UVRR spectra of sAMP•MjADSS, sAMP•GDP•MjADSS, sAMP•GDP•Pi•MjADSS and GDP•MjADSS complexes with respect to sAMP in MES, pH 6.5.

Assignments	UVRR	sAMP• MjADSS	Band Contribution	SG or SGP[a]	sAMP•GDP• MjADSS	sAMP•GDP• Pi•MjADSS	Assignments	GDP	GDP• MjADSS
			GDP	1685	1656 (-29)	1657 (-26)	StrC6=O+C5C6+ Be N1H	1683	1657 (-26)
			GDP	1603	1617 (14)	1614 (11)	Be N1H+ Str C2N	1604	1614 (10)
Be C6N1C2 (15%) + Str C2N3 (14%) + C6N10H (11%) + Be N3C4C5 (11%)	1633	1627 (-6)							
						1598 (0)			
Str N3C4 (23%) + Str N1C6 (11%) + Be C4N9C8 (-11%) + Be C4N9H (10%) + Be C5N7C8 (-10%)	1588	1587 (-1)	sAMP +GDP	1579	1574 (-5)	1575 (-4)	Str N3C4 + C4C5 + C5N7	1577	1573 (-4)
						1555 (0)			
Str N7C8 (22%) + Str C6N10 (-16%) + Be C4N9C8 (10%) + Be C6N10H(12%) + Be NH2	1546	1535 (-11)	sAMP +GDP	1538	1537 (-1)	1539 (1)	Str C4N9 + C6=O + N1C2	1537	1532 (-5)
Str N7C8 (24%) + Str N1C6 (-19%) + Str C2N3 (11%) + Be C2HN3 (-11%) + Str	1481	1479 (-2)	sAMP +GDP	1487	1481 (-6)	1486 (-1)	Be C8H+ Str C8N9 + N7C8	1487	1482 (-5)

C6N10 (10%) + Be C8H + Be N9H									
Be C6NH (29%) + Be C5N7C8 (15%) + Be C2H + Be C8H	1467	1455 (-12)	sAMP	1475	1453 (-22)	1476 (0)			
Be C2HN3 (39%) + Be C4N9H (20%) + Be N6H	1417	1419 (2)	sAMP +GDP	1414	1416 (2)	1417 (3)	Str C4N9 + C5N7	1412	1418 (6)
Str N3C4 (11%) + Str C8N9 (-13%) + Be N6H + Be N9H + Be + C2H + Be C8H	1363	1368 (5)	sAMP +GDP	1365	1363 (-2)	1362 (-3)			
Str C5N7 (23%) + Str N1C2 (20%) + Str N7C8 (-10%) + Be N6H + Be C8H + Be C2H	1335	1340 (5)	sAMP	1335	1341 (6)		StrN7C8 + NIC6 + N5N7	1365	1362 (-3)
Str C2N3 (31%) + Str N1C2 (-22%) + Be C2HN3 (17%) + Be N9H	1311		sAMP +GDP	1315	1317 (2)	1318 (3)			

[a]SG is (sAMP+GDP) and SGP is (sAMP+GDP+Pi)

Table 6.5: Comparison of shifts in wavenumber (cm^{-1}) observed in the UVRR spectra of sAMP•MjADSS, sAMP•GDP•MjADSS, sAMP•GDP•Pi•MjADSS and GDP•MjADSS complexes with respect to sAMP in MES, pD 6.5.

Assignments	DFT	UVRR	sAMP• MjADSS	Band Contribution	SG or SGP[a]	sAMP•GDP• MjADSS	sAMP•GDP• Pi•MjADSS	Assignments	GDP	GDP•MjADSS
				GDP	1665	1642 (-23)	1640 (-25)	Str C6O+Be N1H	1666	1643 (-23)
Str C2N3 (17%) + Be C6N1C2 (18%) + Be N3C4C5 (11%) + Be NH2 + Be C8H + Be C2H	1647	1619	1620 (1)	sAMP	1622	1618 (-4)				
Str N3C4 (25%) + Str N1C6 (17%) Be NH2+ Be N9H + Be C8H+ Be C2H	1632	1579	1596 (17)							
Str C6N (26%) + Str N7C8 (-19%) + Be C2HN3 (-10%)	1541	1533	1532 (-1)	sAMP+GDP	1580	1592 (12)	1585 (4)	Sci NH2 + Py ring + Be N1H	1581	1583 (2)
				GDP		1576	1574 (-1)	Py ring + Sci NH2 + Be N1H	1573	1569 (-4)
				GDP	1540	1537 (-3)	1550 (10)	Pu ring + Be N1H + C8H + Sci NH2	1541	1540 (-1)
							1507			
Str N7C8 (32%) + Str C2N3 (13%) + Str	1516	1483	1481 (-2)	sAMP+GDP	1482	1481 (-1)	1479 (-4)	Str N7C8 + Py ring + Be C8H	1481	1478 (-3)

N1C6 (-14%) + Be C2HN3 (-12%) + Be N7C8H (-10%)								+ N1H + N2H2b		
Str C4N9 (-21%) + Be C5N7C8 (18%) + Be C2HN3 (-17%)	1460	1434	1432 (-2)	sAMP	1435	1427 (-8)	1426 (-9)	Py ring + Str N7C8 + rock NH2 + Be N1H	1405	1424 (19)
Str N1C2 (14%) + Str C5N7 (17%) + Tors aspartate (21%) + Be C8H + Be C2H	1368	1393								
Str C4N9 (-19%) + Be C2HN3 (26%) + Be C8H	1403	1366	1367 (1)	sAMP+GDP		1365	1363	Pu ring + Be N2H2a	1356	1347 (-9)
		1346	1344 (-2)							
Str N7C8 (13%) + Be N7C8H (13%) + Str C2N3 (-10%) + Str N1C2 (10%)	1339	1333	1334 (1)	sAMP+GDP	1346	1340 (-6)	1330 (-16)	Imidazole ring vibration + N7H bending	1331	1322 (-9)
Str C2N3 (-14%) + Str N1C2 (-18%)+ Str N9C8 (19%) + Be N9H + Be C8H + Be NH2	1238	1309	1313 (4)	sAMP+GDP	1312	1314 (2)	1316 (4)	Be N1H + N2H2b + C8H+ Str C5N7 ―C2N2	1318	

[a]SG is (sAMP+GDP) and SGP is (sAMP+GDP+Pi)

AMP•MjADSS: Active-site remains exposed to solvent

AMP is a competitive inhibitor of IMP in ADSS. Earlier, crystal structures of AMP with mmADSS and EcADSS have been reported [107, 214]. It was observed that when bound alone, AMP drives conformational changes similar to the one observed in the IMP complex whereas when AMP binds along with GDP and SO_4^{2-}, the resulting conformation changes in ADSS resemble to that of sAMP binding [107] (Figure 6.13). Previously, Raman bands in AMP spectrum have been shown to respond to the external perturbations caused upon binding to the hydrophobic environment of the active-site [215, 216]. The similar spectral pattern of AMP free in solution and bound to MjADSS suggests that AMP alone does not bring enough conformational change so as to sequester itself from the solvent.

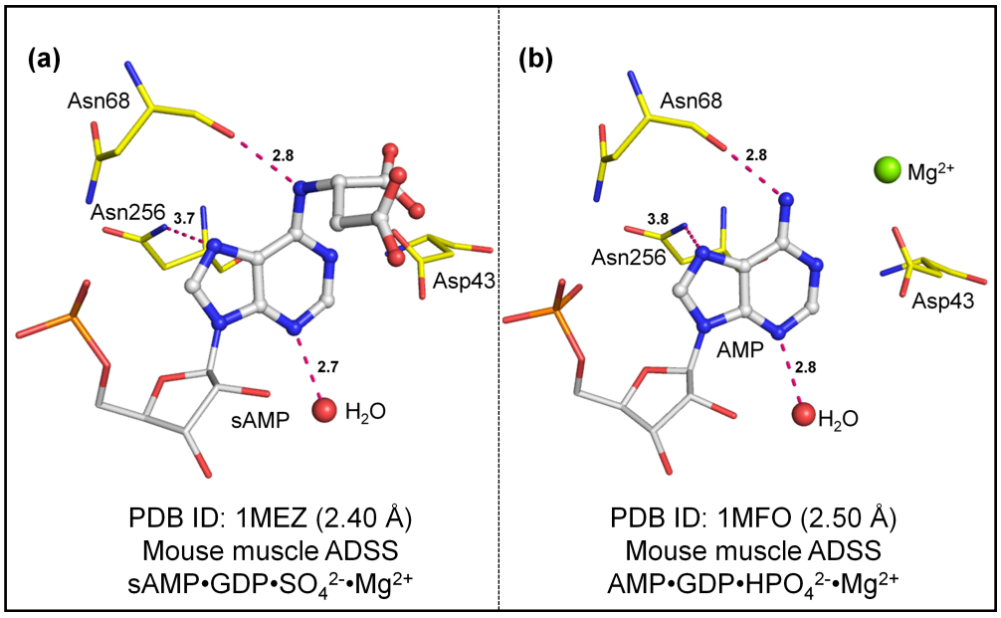

Figure 6.13: Active-site interactions of sAMP (1MEZ) and AMP (1MFO) in mouse muscle ADSS [107].

GDP•MjADSS: GDP remains bound till the product sAMP is formed

Kinetic mechanism suggests the random binding and release order of sAMP and GDP to MjADSS. Spectrum of GDP•MjADSS shows shifts in Raman band positions that corroborate this observation (Figure 6.6 (c)). The direction and magnitude of the shifts observed in the spectrum of GDP•MjADSS are similar to that observed in the GTP•MjADSS complex

above. This suggests that the guanine moiety of GDP binds with similar strength as compared to that of GTP at the active-site though the presence of gamma phosphate in GTP may provide the larger over-all binding energy to the ligand. This may be the reason of higher affinity and thus lower K_m value (15 μM) of GTP as compared to the K_i value of GDP (30 μM) [98]. Raman shifts observed in GDP•MjADSS complex are summarized in Table 6.3.

6.5.2 Intermediate complexes in the reverse reaction of MjADSS

Intermediate complexes of MjADSS in the reverse reaction include sAMP•GDP•MjADSS and sAMP•GDP•Pi•MjADSS. Since, inorganic phosphate (Pi) does not have any absorption at the excitation wavelength of 260 nm thus UVRR spectra of free (sAMP+GDP) and (sAMP+GDP+Pi) in solution are identical (Figure 6.11 (c) and (e), also see Appendix (Figure A.9 and A.10)). However, corresponding spectra in MjADSS bound form are markedly different.

sAMP•GDP•MjADSS: sAMP and GDP bind synergistically

UVRR spectrum of sAMP•GDP•MjADSS was acquired at 260 nm in solution of MES buffer pH 6.5, from which the spectra of apoenzyme and unbound ligands were subtracted. The spectrum of (sAMP+GDP), free in solution, have few overlapping bands arising from sAMP as well as GDP. This is due to similar normal modes of vibrations in these molecules. Yet, few bands viz. 1335 cm^{-1} and 1475 cm^{-1} in (sAMP+GDP) spectrum act as marker of sAMP while the bands at 1604 cm^{-1} and 1684 cm^{-1} are solely contributed by GDP.

The band at 1335 cm^{-1} ($\Delta\nu_{HtoD}$ =+12 cm^{-1}) shows an upshift of 4 cm^{-1} in sAMP•GDP•MjADSS spectrum, similar to the upshift observed in sAMP•MjADSS. Similar upshift is observed when sAMP is deuterium labeled at N6H position. In both cases, the upshift in this band marks decoupling of N6H bend from the main vibration. While the isotope labeling (H→D) leads to reorganization of the normal mode, in sAMP•GDP•MjADSS the decoupling occurs due to the hydrogen bonding between N6H…Asn68.

The band at 1475 cm^{-1} is solely contributed by sAMP and largely arises from C6—NH and C5—N7—C8 bends. This shows a huge downshift of 20 cm^{-1} in sAMP•GDP•MjADSS. In sAMP•MjADSS, a downshift of 11 cm^{-1} is observed. In deuterium labeled sAMP, this mode is observed at 1435 cm^{-1} ($\Delta\nu_{HtoD}$=-35 cm^{-1}) which further downshifts to 1432 cm^{-1} in sAMP•MjADSS. However, in the presence of GDP, this mode shows much higher downshift to 1427 cm^{-1} in sAMP•GDP•MjADSS spectrum. The larger downshift in the presence of GDP indicates greater distortion in sAMP molecule in presence of GDP. Thus, GDP allosterically modulates the sAMP binding to the enzyme.

Distortion in GDP in presence of sAMP

The GDP band at 1487 cm^{-1} shows a downshift of 5 cm^{-1} in sAMP•GDP•MjADSS spectrum, similar to that observed in GDP•MjADSS. Also, the band at 1604 cm^{-1} shows a larger upshift (13 cm^{-1}) in sAMP•GDP•MjADSS than in GDP•MjADSS (8 cm^{-1}). The shift in carbonyl stretching mode ($\Delta\nu$= -27 cm^{-1}) is similar in GDP•MjADSS and sAMP•GDP•MjADSS spectra.

sAMP•GDP•Pi•MjADSS: The fully ligated product complex results in the reverse reaction

A comparison between the UVRR spectra of (sAMP+GDP+Pi) and sAMP•GDP•Pi•MjADSS shows that the marker band of sAMP at 1336 cm^{-1} disappears and new bands at 1555 cm^{-1} and 1598 cm^{-1} are observed (Figure 6.11 (e) and (f)). Such a radical change in the spectral pattern is possible only when a covalent bond is formed or broken. A comparison with the spectrum of IMP•GDP•L-Aspartate•MjADSS complex immediately reveals that the new species formed is IMP. The finding that IMP is formed in reverse reaction is significantly evident in the corresponding D_2O spectrum where comparatively fewer bands of sAMP and GDP overlap with each other in (sAMP+GDP) spectrum (Figure 6.12 (e)) and thus the IMP bands can be reliably identified. Bands at 1507 cm^{-1}, 1550 cm^{-1} and 1574 cm^{-1} observed in sAMP•GDP•Pi•MjADSS complex in D_2O (Figure 6.12 (f)) are characteristic

bands of IMP clearly showing that MjADSS is capable of catalyzing the reaction in reverse direction in the presence of phosphate.

To further substantiate the results, UVRR experiments with GMP-PNP instead of (GDP+Pi) were performed. The resulting spectrum does not show any conversion of sAMP to IMP and resembles the spectrum of sAMP•GDP•MjADSS. This further confirms the occurrence of reverse reaction and formation of IMP in sAMP•GDP•Pi•MjADSS (Figure 6.14).

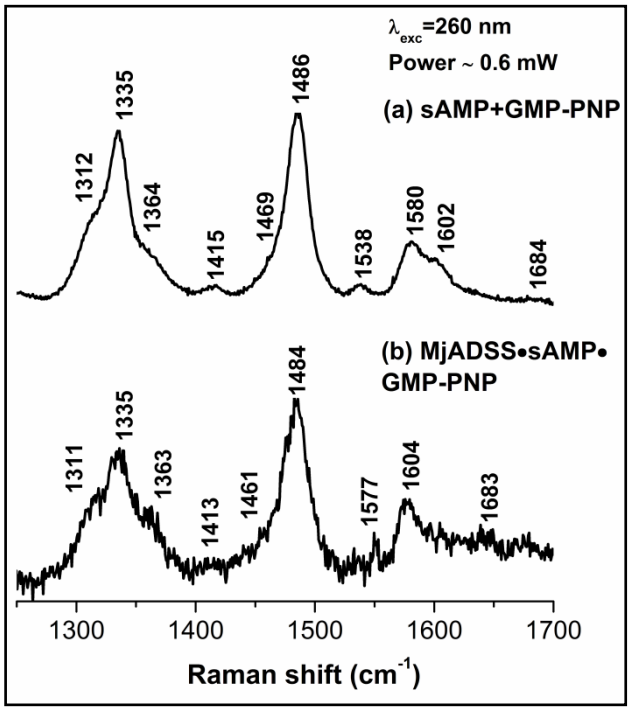

Figure 6.14: Resonance Raman spectra (λ_{exc}=260 nm) of (a) sAMP+GMP-PNP free in solution, (b) sAMP•GMP-PNP•MjADSS; acquired in MES buffer, pH 6.5 at the excitation wavelength of 260 nm.

Reverse phase HPLC confirms formation of IMP and GTP in reverse direction

In order to demonstrate the occurrence of ADSS assisted reverse reaction, the products of the reverse reaction were monitored using HPLC. 20 µL of the reaction mixture, containing MjADSS (150 µM), GDP (500 µM), sAMP (500 µM), magnesium acetate (15 mM) in MES pH 6.5 (30 mM), was loaded onto the Luna reverse phase-high performance liquid chromatography (RP-HPLC) C18 column (Phenomenex). The column was eluted in an

isocratic run with a buffer containing methanol (25%), tetra butyl ammonium hydroxide (5mM) and potassium dihydrogen monophosphate (73 mM) [116]. The absorbance was monitored at 251 nm (λ_{max}=IMP) (Figure 6.15). Control nucleotides were also run under identical conditions to obtain the retention time of each molecule. Retention time for IMP, GDP, GTP and sAMP is 8 min, 10 min, 13 min and 18 min, respectively. MjADSS reaction mixture which was incubated at 25°C for 25 min shows peaks at 8 min and 13 min corresponding to IMP and GTP, respectively along with the peaks of GDP (10 min) and sAMP (18 min). However, in the reaction mixture of MjADSS which was incubated at 70°C only the peaks at 8 min (IMP) and 10 min (GDP) were observed. This is due to unstability of GTP at higher temperature resulting in its hydrolysis to GDP and Pi.

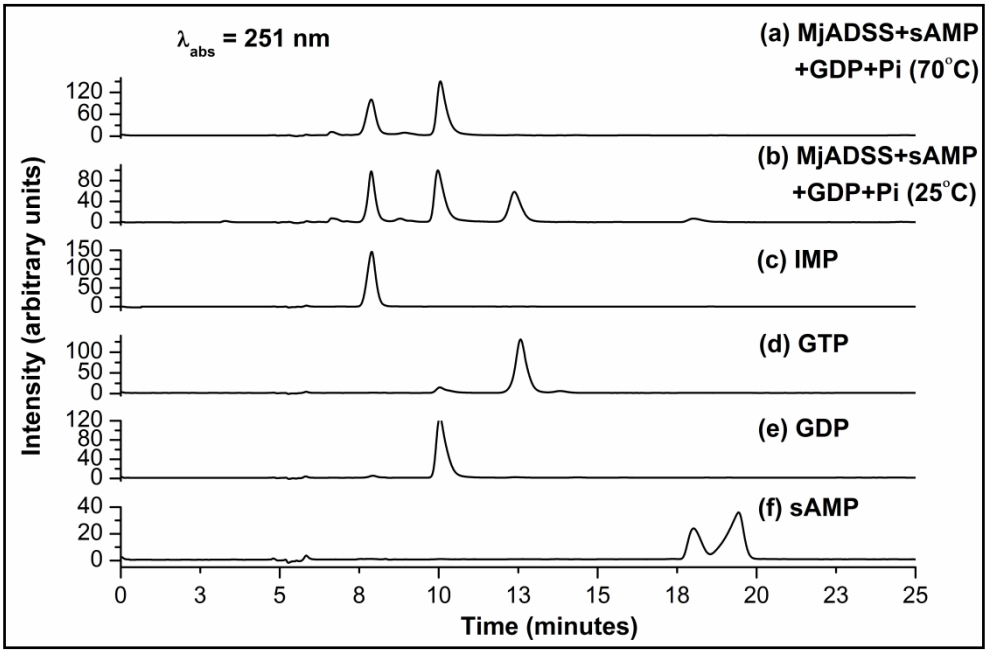

Figure 6.15: RP-HPLC Chromatogram of MjADSS reaction mixture, containing MjADSS (150 µM), GDP (500 µM), sAMP (500 µM), Pi (10mM) and magnesium acetate (15 mM) in MES pH 6.5 (30 mM), at 251 nm. (a) MjADSS reaction mixture at 70°C; no peaks for GTP (13 minutes) and sAMP (18 minutes) are observed, (b) MjADSS reaction mixture at 25 °C; GTP peak and a minor peak of sAMP is observed. 500 µM each of (c) IMP (8 minutes), (d) GTP (13 minutes), (e) GDP (10 minutes) and (f) sAMP (18 minutes) were run as controls. All the controls were treated in the same way as that of MjADSS reaction mixture.

Information from literature suggesting enzyme-assisted formation of GTP in ADSS, under in vitro conditions

Previously, using a slowly hydrolysable analogue, GTPγS, Markham and Reed have reported the occurrence of reverse reaction in EcADSS. They observed that in the forward reaction, IMP, L-Aspartate and GTPγS leads to the formation of GDP, thiophosphate (SPi) and sAMP. In the reverse reaction, the products combine to give GTP and 6-mercaptopurine ribotide. The rate with the SPi reaction is 14% of the rate obtained with phosphate [113]. In *Azotobacter vinelandii* ADSS, steady state kinetic measurements of the forward and reverse reactions were reported [217]. The maximum velocity of reverse reaction was found out to be 10% of the forward reaction. Authors found that sAMP is degraded only when GDP, Pi and Mg^{2+} are included in the reaction mixture. Fluorophosphate and phosphite were ineffective in reversing the reaction [217].

6.6 Discussion on the reverse reaction complexes

While the order of release of product molecules is known in ADSS from different organism, the conformational changes driven by the binding of individual ligand are elusive. This is because of the paucity of information on the product complexes of ADSS. A very few structures viz. EcADSS with AMP [214], mmADSS with (AMP+GDP) [214] and with (sAMP+GDP+SO_4^{2-}) [107] are available.

sAMP binding: Marked differences in the wavenumber position of sAMP•MjADSS spectrum with repect to free sAMP spectrum in solution suggests distortion in the nucleobase upon binding to ADSS. The shift in the band comprised of N6H bend (1335 cm^{-1}) evidently captures hydrogen bond between N6H and Asn68 (D-A distance: 2.8 Å) [107]. Downshifts in the bands at 1475 cm^{-1} and 1588 cm^{-1} capture hydrogen bonds between N7 of sAMP and side-chain amide of Asn256.

GDP binding: The observed distortion in the guanine moiety in GDP is essentially same as that observed in GTP and GMP-PNP (*vide-supra*) which suggests that GDP remains bound even after formation of products.

(sAMP+GDP) binding: The magnitude of Raman shifts in the marker bands of sAMP and GDP is increased when bound together to ADSS as compared to the shifts observed when bound individually. Thus, a synergism in binding of these ligands is observed. Further, the spectral pattern of (sAMP+GDP) is maintained in the E•S spectrum which implies that no covalent bond is formed or broken in this ternary complex.

(sAMP+GDP+Pi) binding: Intriguingly, the whole spectral pattern of sAMP•GDP•Pi•MjADSS is different from that of (sAMP+GDP+Pi) spectrum. Marker band of sAMP at 1335 cm^{-1} is disappeared. Appearance of new bands is implicated in the formation of IMP. Reports on the reverse reaction of ADSS are scant. Nevertheless, the results obtained in the present study confirm the occurrence of reverse reaction by ADSS in solution under in vitro conditions. This finding is further corroborated by the absence of these bands when GMP-PNP was used in place of GDP and Pi, and by RP-HPLC data.

6.6.1 Plausible mechanism of the reverse reaction

Reverse reaction in ADSS may take place in two sequential steps. In the first step, sAMP and Pi react at the active-site of ADSS to result in the formation of 6-pIMP, L-Aspartate is formed as a by-product (Step 1). In the second step, 6-pIMP and GDP react which in turn results in the formation of IMP and GTP (Step 2). Degradation of 6-pIMP may also result in the formation of IMP and Pi but the fact that a GTP peak is observed in RP-HPLC suggests that 6-pIMP is converted to IMP and GTP.

sAMP + Pi → L-Aspartate + 6-pIMP…….. (Step 1)

6-pIMP + GDP → IMP + GTP…… (Step 2)

6.6.2 Local conformational changes at the active-site of MjADSS when both sAMP and GDP are bound together

A feedback inhibition study has shown that Asp loop is organized in sAMP•mmADSS complex where GDP, SO_4^{2-} and Mg^{2+} are also present [107]. However, the conformational changes driven by the binding of the individual ligand remains elusive. In the present chapter, using UVRR spectra at each step of the kinetic cycle, I have elucidated the conformational changes brought about by the binding of each ligand in solution-state. The difference between the band positions of free ligand and that of the enzyme•ligand captures non-covalent interactions. The magnitude of the wavenumber shifts reports on whether the interactions are optimum or not. A ligand which is bound in a more organized active-site is likely to undergo a greater extent of distortion due to the formation of more stable interactions between the active-site residues and the ligand. An improvement in the binding of a ligand at the active-site upon binding of another ligand in the neighbouring site will be manifested as an increase in the magnitude of wavenumber shifts in the enzyme•ligands complex. Crystal structures of ADSS show that the active-site is completely organized in the fully ligated complex, thus shifts in this complex may be taken as a references for the most stable interactions. Similar shifts resulting from the binding of an individual ligand suggests that this ligand alone is sufficient to organize the active-site in a way which is similar to that observed in the fully ligated complex. In this context, similar directions and trends of shifts in the bands of sAMP in sAMP•MjADSS and sAMP•GDP•MjADSS show that sAMP alone drives conformational changes in sAMP•MjADSS. These results, for the first time to the bestt of my knowledge, suggest that even when GDP is not added, sAMP alone is sufficient to drive conformational changes similar to those observed in the fully ligated complex in the reverse direction. However, the magnitude of the shifts increases in the complex where sAMP and GDP are bound together. Larger magnitude of shifts has been correlated earlier with the greater enthalpy of hydrogen bond formation (Badger-Bauer relationship) [21]. Thus, larger magnitude of shifts in sAMP•GDP•MjADSS complex suggests stronger

hydrogen bond interactions. In other words, it is evident that the strength of hydrogen bond interactions and hence distortion in ligands increases when both the ligands are bound together at the active-site.

6.7 Estimation of enthalpy of hydrogen bond formation in the active-site of ADSS

Callender and co-workers have determined the relationship between magnitude of Raman wavenumber shifts and corresponding enthalpy of hydrogen bond formation [21, 136]. With the help of Badger-Bauer relationship, they established, specifically in purines, that every 100 cm^{-1} shift in stretching wavenumber corresponds to 1.1-1.3 kcal/mol of the enthalpy of hydrogen bond formation. Further, the shifts in bending wavenumber suggest a greater binding energy involved in stabilizing the transient intermediates. Every 10 cm^{-1} shift in bending wavenumber was found to be related to the 1-1.2 kcal/mol of the enthalpy of hydrogen bond formation [136]. Badger-Bauer relationship establishes a correlation between enthalpy of formation of hydrogen bond and the vibrational wavenumber shifts ($-\Delta H = a\Delta\nu + b$), where H is in kcal/mol and ν is in cm^{-1}; 'a' and 'b' are slope and intercept, respectively which are found to vary with the strength of the hydrogen bond [21].

An estimate of interaction energies between ADSS and its ligands has been made depending on the above mentioned relationship (Table 6.6). This estimate provides us with the relative energies involved in stabilizing the transient intermediates (6-pIMP) and distorted ligands (IMP, sAMP and GTP) in case of ADSS. Such species are captured in the form of characteristic changes in the Raman spectrum of IMP. Radical changes in the fully ligated ADSS complex spectrum are assigned to the intermediate, 6-pIMP. Other transient intermediates are discussed based on the distortion in the key molecules (IMP in forward and sAMP in backward reaction).

Table 6.6 shows the estimate of hydrogen-bonding enthalpy in the active-site of ADSS. Considering the hydrogen bonds which are common

across two different intermediate complexes in the forward reaction, it is observed that the total enthalpy of such hydrogen bond formation is more in the quinternary complex (IMP•GTP•HDA•MjADSS) than the ternary complex (IMP•GTP•MjADSS). This implies that maximum stabilization of 6-pIMP intermediate occurs in the former, which in turn suggests greater extent of pre-organization of the active-site in the former complex. This pre-organization eventually stabilizes the highly polar transition-state.

In the product complexes, as sAMP is transformed to IMP thus only the hydrogen-bonding interactions between GDP and the active-site residues are taken into account to estimate the enthalpy of hydrogen bond formation. Estimated enthalpy in the ternary product complex is maximum suggesting that both sAMP and GDP are held tightly at the active-site till the next step is ensured.

Table 6.6: Interaction energies (ΔH, kcal/mol) of various substrate complexes of MjADSS at different steps of the catalytic cycle. Magnitude of shifts in wavenumber (cm^{-1}) was used as a criterion to determine the interaction energies.

IMP•MjADSS			**GTP•MjADSS**			**IMP•GTP•MjADSS**			**IMP•GTP•HDA•MjADSS**		
Band	Δν	ΔH	Band	Δν	ΔH	Band	Δν	ΔH	Band	Δν	ΔH
1595	-3	-0.039	1684	-27	-2.26	1687	-27	-2.26	1687	-34	-2.88
1555	-5	-0.065	1604	12	-1.2	1604	12	-1.2	1604	12	-1.2
1515	-5	-0.065				1595	-3	-0.039	1595		
1468	3	-0.3	1578	-7	-0.091	1578	-5	-0.065	1578		
			1487	-6	-0.078	1487	-6	-0.078	1487	-6	-0.078
						1468	-15	-1.5	1468	-15	-1.5
Total		**-0.469**			**-3.629**			**-5.142**			**-5.658**
sAMP•MjADSS			**GDP•MjADSS**			**sAMP•GDP•MjADSS**			**sAMP•GDP•Pi•MjADSS**		
Band	Δν	ΔH	Band	Δν	ΔH	Band	Δν	ΔH	Band	Δν	ΔH
1633	-6	-0.6	1683	-26	-2.14	1685	-29	-2.64	1685	-26	-2.14
1588	-1		1604	10	-1	1603	14	-1.4	1603	11	-1.1
1546	-11	-0.143	1577	-4	-0.052	1579	-5	-0.065	1579	-4	-0.052
1481	-2		1487	-5	-0.065	1487	-6	-0.078	1487	-1	
1467	-12	-1.2									
Total		**-1.943**			**-3.257**			**-4.183**			**-3.292**

6.8 Conclusion

In this chapter, I have investigated enzyme-induced distortion and allosteric control in substrate, intermediate and product complexes of MjADSS. The results show that IMP alone, though distorted towards deprotonated form, remains bound in the neutral form in the absence of GTP and L-Aspartate. GTP provides maximum specific interactions with the active-site amino-acid residues and hence contributes maximum to the intrinsic binding energy. Addition of IMP and GTP to ADSS, results in the formation of an intermediate 6-pIMP. This intermediate is not stable at the active-site until the L-Aspartate pocket of ADSS is ligated by HDA. In the reverse reaction, sAMP is found to organize the active-site conformation even in the absence of any other ligand. sAMP and GDP allosterically modulate the active-site of each other. Occurrence of reverse reaction is observed upon addition of sAMP, GDP and Pi in presence of Mg^{2+}. Results obtained in this study have the bearing on important attributes such as the extent of substrate distortion in the mechanism of enzyme action and development of potent drug molecules against ADSS.

"What we call the beginning is often the end. And to make an end is to make a beginning. The end is where we start from."

T.S. Elliot

7

Distortion and Allosteric Control of Purine Ligands by *Plasmodium falciparum* Adenylosuccinate Synthetase

7.1 Introduction

7.1.1 Overview of PfADSS

Development of drugs against parasitic protozoa requires understanding the difference between the metabolic pathways of host and pathogens [27]. An essential nucleotide synthesis pathway provides major differences between the two which can be exploited to design potent inhibitors against the enzyme of the pathway. However in a few cases, the inhibitors are also shown to bind to the host enzymes. Thus, targeting a parasitic enzyme specifically requires understanding the specific non-covalent interactions between a ligand and the active-site residues of the enzyme.

In this context, I have studied the enzyme adenylosuccinate synthetase (ADSS) from the protozoan parasite, *Plasmodium falciparum* (Pf). This parasite lacks *de novo* pathway for nucleotide synthesis and thus depends solely on salvage pathway for fulfilling the requirement of nucleotides [27]. It is becasue of this reason that the enzymes of the *de novo* and the salvage pathways of the nucleotide synthesis have been regarded as potential target for

anti-parasitic chemotherapy [25-28]. ADSS is one such enzyme in the parasite which can be targeted against malaria. This enzyme constitutes the part of the *de novo* as well as the salvage pathway for nucleotide synthesis. It is the first enzyme which commits the conversion of inosine-5'-monophosphate (IMP) to the formation of adenosine-5'-monophosphate (AMP). ADSS catalyzes the condensation of IMP and L-Aspartate to the product succinyl adenosine-5'-monophosphate (sAMP) with the simultaneous hydrolysis of GTP to GDP.

7.1.2 Structural studies of PfADSS

Although ADSS has been extensively investigated but the structural studies on PfADSS are scant. The only crystal structure of PfADSS co-crystallized with an intermediate 6-pIMP suggests several active-site interactions which putatively stabilize the intermediate at the active-site until the next catalytic step is ensured [95]. Kinetic studies suggest the occurrence of an ordered binding mechanism where IMP binds first and then only can the GTP bind leading to the formation of a ternary complex [33] (Figure 7.1). This is followed by the binding of L-Aspartate to this complex. Release of products is also ordered where phosphate (Pi) leaves the active-site first, followed by the release of GDP and at last sAMP leaves the binding pocket of PfADSS. Mutational studies evidently suggest the role of various residues which result in the unique ordered binding mechanism of ADSS [124].

The aim of the present study is to develop a better understanding towards the contribution of ground-state (GS) distortion in enzyme catalysis. By using a highly sensitivity technique, ultraviolet resonance Raman spectroscopy (UVRR), I have delineated the sequential distortion in the ligands resulting from the binding to the PfADSS active-site. Further, these distortions reflect the change in bond order of the catalytically important bonds involved in an ADSS catalyzed reaction. Studying such interactions between ligand and the active-site residues of the enzyme provides us with the rationale behind the tight binding of a few ligands with respect to the other. Also, the reason behind the high specificity of enzymes can be determined. The present study emphasizes on the distortion of IMP at every step of the

kinetic cycle in the forward reaction, and on the sAMP molecule in the reverse reaction. To achieve this, I used analogues of L-Aspartate (HDA), GTP (GMP-PNP) and sAMP (AMP).

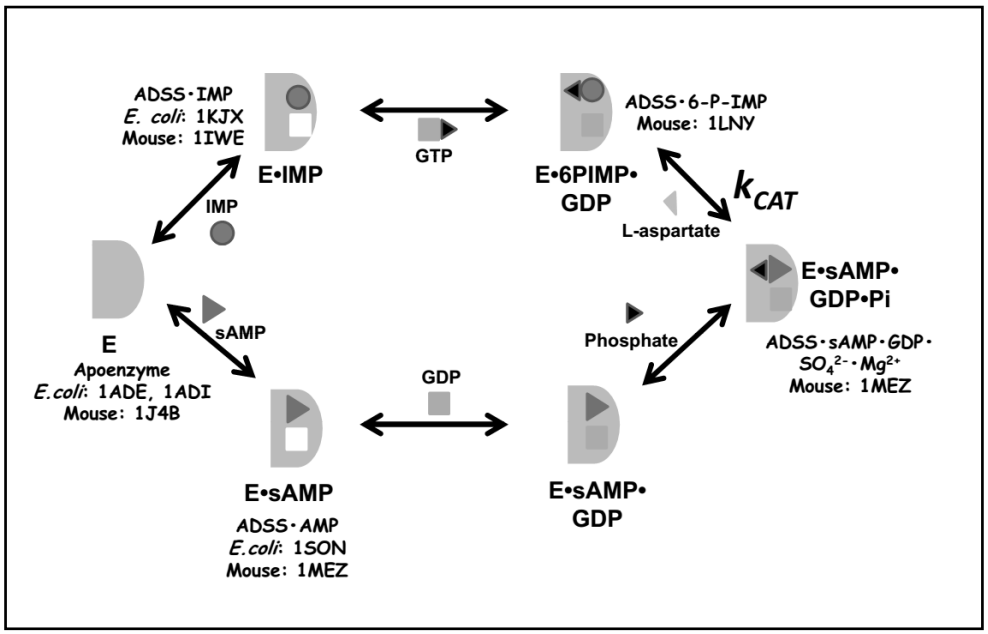

Figure 7.1: Kinetic mechanism of PfADSS. Crystal structures from various homologues at different kinetic steps are mentioned.

7.2 Methodology

7.2.1 ADSS sample preparation

IMP, GTP, GDP, sAMP, L-Aspartate, magnesium acetate and sodium nitrate were purchased from Sigma-Aldrich Co. HDA was procured from Developmental Therapeutic Programme, NIH. UVRR Samples were prepared in 30 mM HEPES pH 7. UVRR spectra of the enzyme and the nucleobases were recorded in the buffer containing 5 mM magnesium acetate, 30 mM $NaNO_3$ and 5 mM HDA. 500 μM of nucleobase and 150 μM of enzyme were used for the Raman experiments.

7.3 Results

7.3.1 Forward complexes of PfADSS

Forward reaction complexes include complexes of PfADSS with IMP; GTP; (IMP+GTP); and (IMP+GTP+HDA). All the experiments have been

carried out at an excitation wavelength of 260 nm, the selection of which was made based on the absorption spectra of PfADSS ligands (mononucleotides). In the previous chapter, I have shown that at 260 nm, protein spectrum does not interfere and a resonance enhanced spectrum from nucleobase can be obtained selectively. The UVRR spectrum of the enzyme complexed with ligand is obtained by subtracting the spectrum of apoenzyme and the spectrum of unbound ligand from the enzyme•ligand spectrum.

IMP•PfADSS: Binding of IMP to PfADSS is weak until other ligands are bound

The UVRR spectra of free IMP and IMP•PfADSS in HEPES, pH 7.0 are shown in Figure 7.2. The IMP band at 1469 cm^{-1} which has been attributed to N1—H bending vibrations (bend) shows a downshift of 2 cm^{-1} in IMP•PfADSS (Table 7.1). This downshift in the band is similar to the one observed when the proton at N1 position of IMP is replaced with a deuteron ($\Delta\nu_{HtoD}$ = -2 cm^{-1}) [34]. By contrast, this band in IMP•MjADSS showed an upshift of 3 cm^{-1}. This upshift was attributed to the weakening of N1—H bond resulting from the hydrogen bond formation with a catalytic base residue, Asp26 (Pf numbering). Absence of such upshift in IMP•PfADSS depicts that in the absence of other ligands, activation of IMP for the next step of catalysis, which in this case is deprotonation of N1—H, does not occur.

Triene stretch mode in IMP at 1555 cm^{-1} shows a downshift of 2 cm^{-1} in IMP•PfADSS whereas the intensity of the Raman band remains unperturbed. Pyrimidine stretch mode at 1595 cm^{-1} shows no significant shift in the E•S complex. These results are markedly different from the results obtained in case of MjADSS where a larger magnitude of shifts were implicated in the greater distortion of IMP in IMP•MjADSS.

A significant downshift of 6 cm^{-1} in the band at 1352 cm^{-1} which arises from the delocalized vibrations of the purine ring, suggests that IMP is held at the active-site. A larger downshift (9 cm^{-1}) in IMP•MjADSS quantifies greater distortion in IMP in addition to stronger hydrogen bond between N7 of purine ring and Asn232.

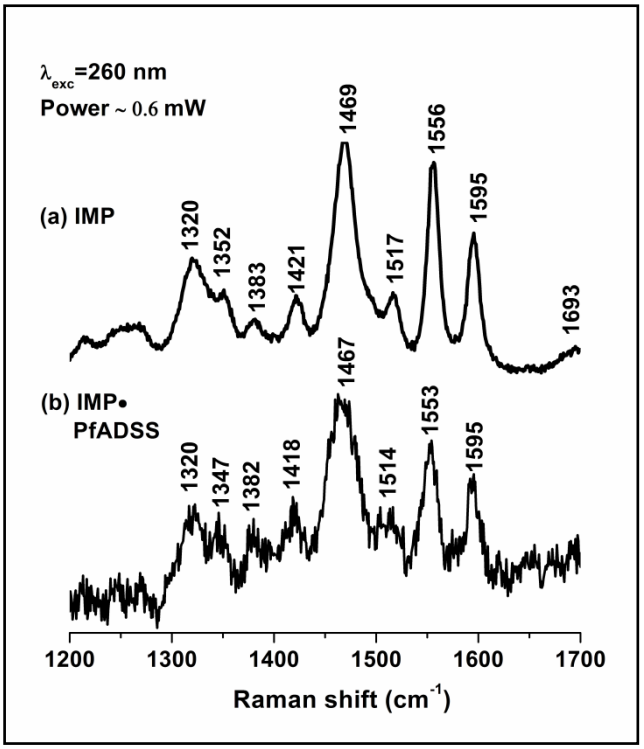

Figure 7.2: Resonance Raman spectra (λ_{exc}=260 nm) of (a) IMP free in solution, (b) IMP bound to PfADSS; acquired in HEPES buffer, pH 7.0.

A larger magnitude of Raman wavenumber shifts in IMP•MjADSS than in IMP•PfADSS suggests that the nucleobase moiety is distorted to a greater extent in the former than in the latter. This larger magnitude of Raman wavenumber shifts implies greater enthalpy of hydrogen bond formation which constitutes larger intrinsic binding energy and hence results in a more stable complex with the base. When IMP is bound alone, the magnitude of wavenumber shifts is smaller in IMP•PfADSS spectrum as compared to that in IMP•MjADSS spectrum. We note that our experiments report only on the interactions between the nucleobase moiety and the active-site residues, whereas the interactions with the sugar and phosphate moieties are not captured in the present resonance Raman experiment. Thus, a larger magnitude of wavenumber shifts in IMP•MjADSS suggests that the nucleobase moiety is bound strongly to MjADSS. However, if one takes the K_m values as a measure of overall affinity between an enzyme and the ligand then a lower K_m value of IMP in PfADSS (23 ± 4 μM) as compared to that in MjADSS (75.5 ± 4.6 μM) implies that IMP binds with greater affinity to PfADSS than to MjADSS [32, 33]. As the nucleobase moiety is bound

comparatively weakly in PfADSS (as suggested by wavenumber shifts) and thus a lower K_m value in PfADSS may arise from stronger hydrogen bonding interactions of active-site residues with the sugar and phosphate moieties of IMP.

Table 7.1: Comparison of the shifts in wavenumber (cm^{-1}) between different ligand complexes of MjADSS and PfADSS

	Wavenumber (cm^{-1})					
IMP	**1595**	**1555**	**1515**	**1468**	**1421**	**1352**
MjADSS	-3	-5	-5	3	-3	-9
PfADSS	1	-3	-3	-2	-4	-6
GTP	**1684**	**1604**	**1578**	**1537**	**1487**	**1366**
MjADSS	-27	10	-4	-3	-4	-5
PfADSS	-32	6	-4	-3	-4	-3
sAMP	**1633**	**1481**	**1467**	**1363**	**1335**	
MjADSS	-6	-2	-12	5	5	
PfADSS	-5	-1	-9	5	5	
GDP	**1684**	**1604**	**1578**	**1537**	**1487**	**1366**
MjADSS	-26	10	-4	-5	-5	-3
PfADSS	-28	5	-5	-3	-4	-3

A ligand which is bound in a more organized active-site is likely to undergo a greater extent of distortion, due to the formation of interactions between active-site residues and the ligand. Thus, a greater distortion in MjADSS implies that IMP alone is sufficient to drive complete organization of the dynamic loops at the active-site in the IMP•MjADSS complex. Whereas minor shifts in the PfADSS complex suggest that the binding of IMP to PfADSS is weak until the other ligands are also bound to the enzyme. This is further confirmed by observing the spectrum of IMP•GTP•PfADSS (*vide-infra*) where the presence of GTP further organizes the loops around IMP and results in larger magnitude of shifts.

Conformational changes brought about by the binding of IMP alone cannot be deduced from the only crystal structure of PfADSS along with 6-pIMP, GDP, HDA and Mg^{2+} [95]. However, UVRR results obtained from this study show that in PfADSS, ligation of GTP and L-Aspartate pocket drives conformational changes which improve the binding of IMP at the active-site. Based on the observed Raman shifts in this study, it seems that not only the

GTP loop is organized upon binding of IMP to switch loop, as suggested by the crystal structure, but also GTP binding organizes the switch loop to fully optimize the interactions with IMP. Interaction between GTP loop and Switch loop (Figure 7.3) suggests that this indeed is the case. Binding of GTP organizes the GTP loop which in turn reorganizes the switch loop resulting in the more compact IMP binding site. These conformational changes along with the other factors like TS stabilization and GSD reduce the activation energy barrier of ADSS catalysis [10-12, 14]. These UVRR results are novel and unique to the structure of PfADSS, observation of which has been possible because of the use of the highly sensitive technique, UVRR.

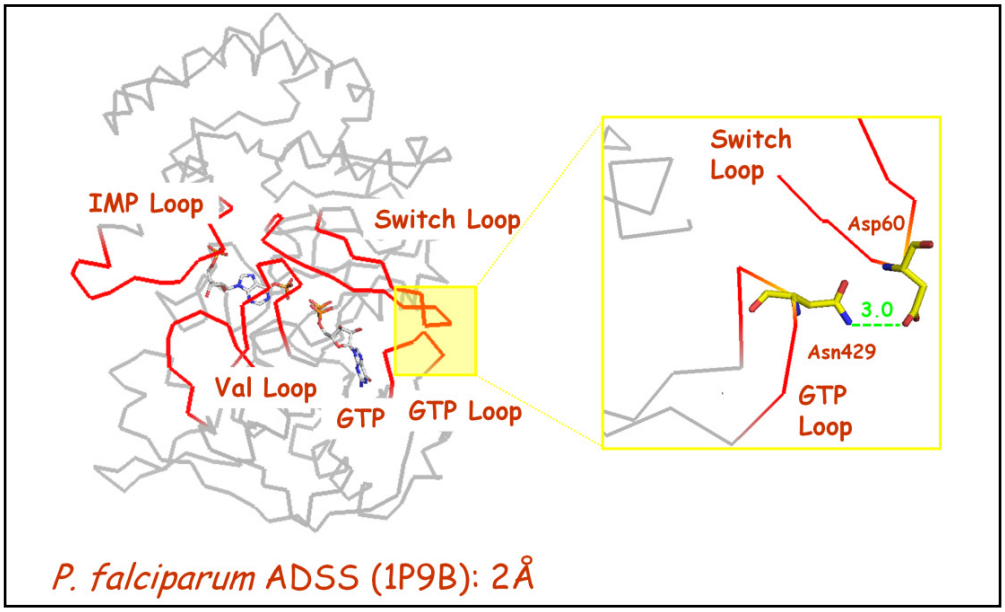

Figure 7.3: Crystal structure of PfADSS depicting various dynamic loops (Adapted from Mehrotra et al., Biochim. Biophys. Acta, 2010). Interaction between Asn429 of GTP loop with Asp60 of IMP loop is shown in inset.

GTP•PfADSS: UVRR reports conformational heterogeneity in PfADSS

The GTP band at 1487 cm^{-1} is an imidazole ring mode (Figure 7.4) and therefore, a downshift of 4 cm^{-1} in the band in GTP•PfADSS spectrum is attributed to the hydrogen bonding between N7 of imidazole ring and Lys31 residue. The band at 1604 cm^{-1} which is an N1—H bend and C2—N2 stretching vibration (str) shows an upshift of 4 cm^{-1} in GTP•PfADSS resulting from the hydrogen bonding contacts between —NH_2 moiety and Asp341

residue. Also, the carbonyl stretch at 1684 cm^{-1} shows a downshift of 32 cm^{-1} in GTP•PfADSS which is attributed to the interactions between C6=O and Lys31, Lys339 and Val426 [95] (Figure 7.5).

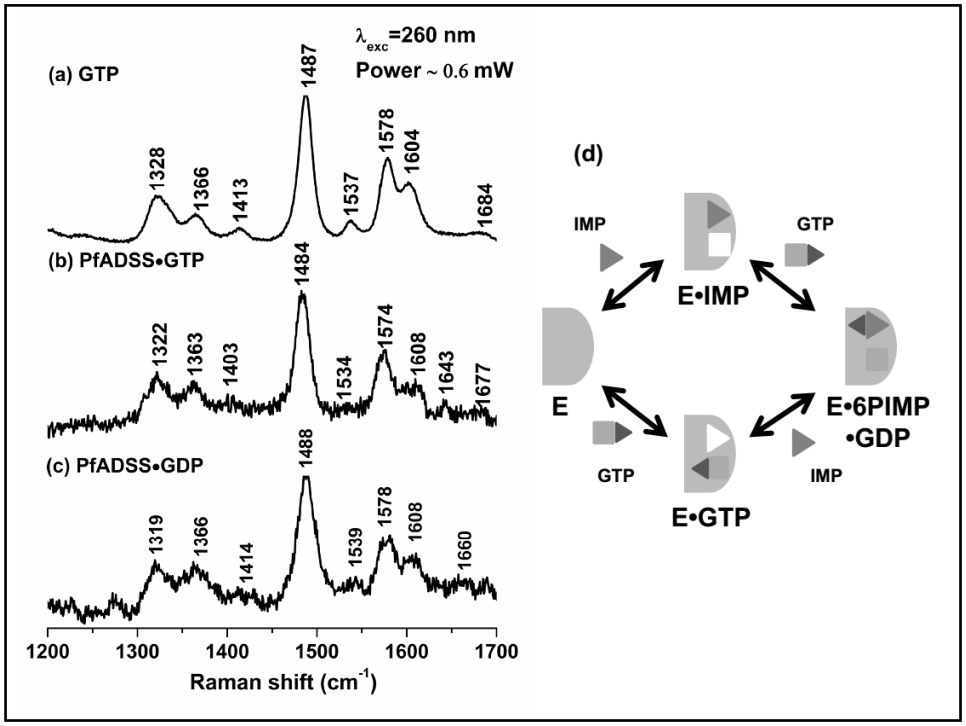

Figure 7.4: Resonance Raman spectra (λ_{exc}=260 nm) of (a) GTP free in solution, (b) GTP bound to PfADSS, (c) GDP bound to PfADSS; acquired in HEPES buffer, pH 7.0. (d) a cartoon depicting the binding of a minor population of PfADSS to GTP in absence of IMP.

The sequential ordered binding of ligands in PfADSS implies that GTP can bind only if IMP is bound to PfADSS i.e. GTP can bind to the IMP•PfADSS complex only. However, the difference in the band positions (cm^{-1}) observed in the spectrum of GTP•PfADSS as compared to the free GTP in solution suggests that GTP is bound at the active-site even in the absence of any other ligands (Figure 7.4). The shifts in band position in GTP•PfADSS spectrum may arise from the basal level of GTP binding to PfADSS. The result evidently shows conformational heterogeneity of ADSS in solution-state. There may be major population of ADSS in a conformation which cannot bind to GTP but a small percentage which can readily bind to GTP is also present in the ensemble. In this study, detection of the conformational

heterogeneity in ADSS has been possible because of the immense sensitivity of UVRR and the greater resolution at which information is obtained.

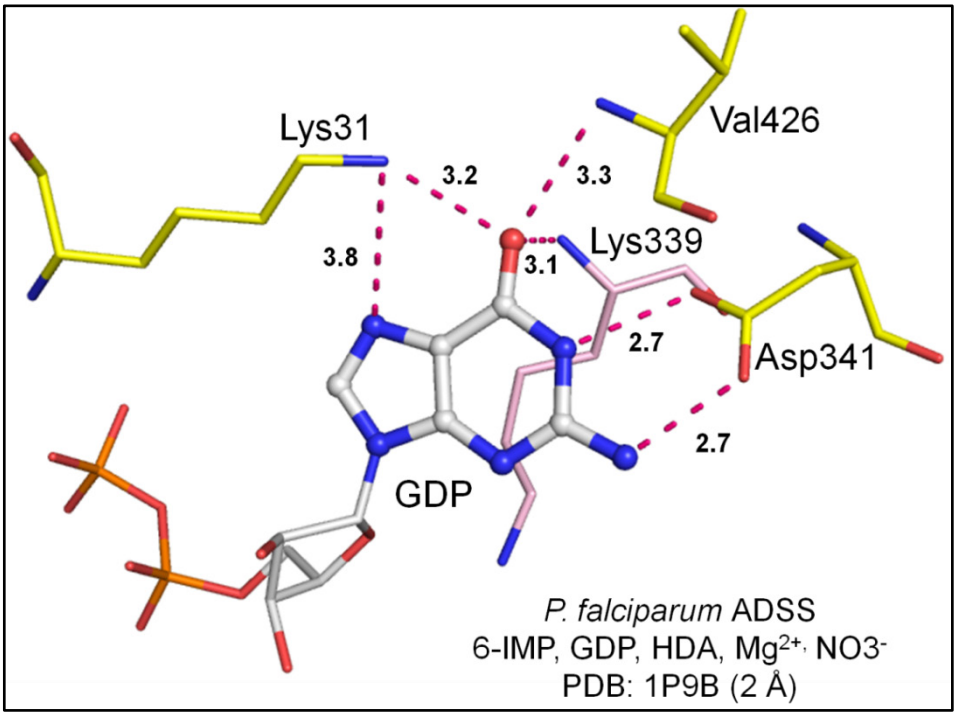

Figure 7.5: Hydrogen bonding interactions between GDP and active-site residues of PfADSS [95]. All distances are in Å.

K_m values suggest that GTP binds with an overall greater affinity to PfADSS (K_m value = 18.4 ± 2 µM [33]) than to MjADSS (K_m value = 42.6 ± 2.8 µM [32]). These K_m values of GTP are determined in a reaction mixture where all the other substrates of ADSS are also present. However, when GTP is bound alone to PfADSS, the magnitude of wavenumber shifts is smaller in GTP•PfADSS spectrum. These shifts report on the binding of guanine moiety with the active-site residues and evidently show that although GTP alone may bind to PfADSS, the binding is weaker until IMP is also bound at the active-site (vide-infra). The implication of the same is observed as a difference in the kinetic mechanisms of the two homologues. The results presented in this study show that the active-site of GTP is preformed and it is only upon IMP binding that the binding of GTP is further stabilized suggesting the allosteric control of IMP binding site upon GTP binding.

7.3.2 Intermediate complexes in forward direction

Intermediate complexes of PfADSS include a ternary complex, IMP•GTP•PfADSS, and a quinternary complex, IMP•GTP•HDA•PfADSS. Since, HDA does not have any resonance enhancement at the excitation wavelength of 260 nm and hence the spectra of free ligand i.e. (IMP+GTP) and (IMP+GTP+HDA) are identical. In the following section, I have discussed the implication of Raman shifts, obtained in the above mentioned complexes, to the structure of PfADSS.

IMP•GTP•PfADSS: 6-pIMP reverts back to IMP in the absence of the ligation of L-Aspartate pocket

The complex IMP•GTP•PfADSS was obtained by adding IMP and GTP together to PfADSS. From the spectrum of this ternary complex, the spectra of apoenzyme and (IMP+GTP) were subtracted to obtain the spectrum of IMP•GTP bound to the enzyme. Similarity in normal modes of vibrations in IMP and GTP results in many overlapping bands which can be attributed to both IMP and GTP. A few bands of IMP and GTP are unique and thus act as marker bands of these molecules. Perturbations in these marker bands indicate distortion in the nucleobase moiety from which they arise. For instance, in the spectrum of (IMP+GTP) bands at 1468 cm^{-1}, 1555 cm^{-1} and 1595 cm^{-1} are marker bands of IMP. Similarly, the bands at 1578 cm^{-1}, 1604 cm^{-1} and at 1487 cm^{-1} are marker bands of GTP.

Distortion in IMP in IMP•GTP•PfADSS: All the bands of IMP, though show minor downshifts, remain intact in IMP•GTP•PfADSS. For example, the band at 1555 cm^{-1} in (IMP+GTP) shows a downshift of 2 cm^{-1} in IMP•GTP•PfADSS spectrum (Figure 7.6 (a) and (b)). The band at 1595 cm^{-1} shows an upshift of 3 cm^{-1} and the band at 1468 cm^{-1} downshifts to 1461 cm^{-1} in IMP•GTP•PfADSS spectrum.

Distortion in GTP in IMP•GTP•PfADSS: The GTP bands at 1486 cm^{-1} and 1578 cm^{-1} in (IMP+GTP) spectrum show a downshift of 3 cm^{-1} and 2

cm^{-1}, respectively in IMP•GTP•PfADSS. Also, the band at 1604 cm^{-1} upshifts to 1614 cm^{-1} in the enzyme bound form.

Greater shifts in IMP (1595 cm^{-1}) and GTP (1604 cm^{-1} and 1684 cm^{-1}) bands in the ternary complex than their individual complexes capture the allosteric effect in PfADSS. Larger magnitude of shifts observed in IMP•GTP•PfADSS spectrum imply stronger active-site interactions and thus suggests that binding of IMP to GTP•PfADSS (or GTP to IMP•PfADSS) drives conformational re-organization in a way that results in a more compact active-site of PfADSS. These results also show that the dynamic loops of ADSS attain a 'closed-conformation' only when both IMP and GTP are bound.

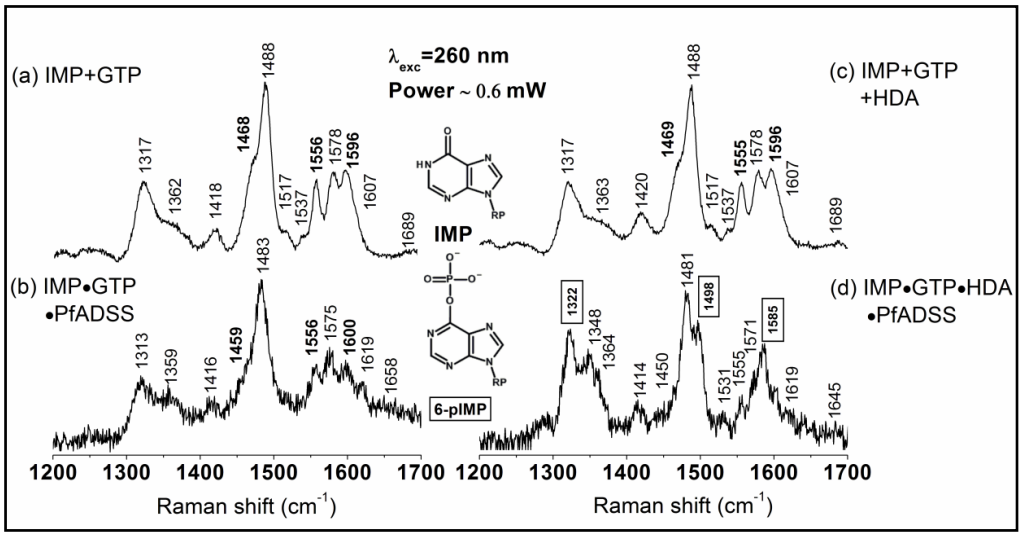

Figure 7.6: Resonance Raman spectra (λ_{exc}=260 nm) of intermediate complexes of PfADSS in forward direction of kinetic mechanism in HEPES, pH 7. (a) IMP+GTP free in solution, (b) IMP and GTP bound to PfADSS, (c) IMP, GTP and HDA in solution and (d) IMP, GTP and HDA bound to PfADSS.

IMP•GTP•HDA•PfADSS: Ligation of L-Aspartate pocket stabilizes 6-pIMP at the active-site of PfADSS

Distortion of IMP in IMP•GTP•HDA•PfADSS: A comparison of the spectrum of free (IMP+GTP+HDA) in solution with IMP•GTP•HDA•PfADSS shows marked differences between the two (Figure 7.6 (c) and (d)). For instance, the IMP bands at 1468 cm^{-1}, 1555 cm^{-1} and 1595 cm^{-1} are not observed in the enzyme bound spectrum. This indicates substitution or

modification in the IMP molecule. In addition, a clear band at 1498 cm^{-1} suggests the formation of an intermediate 6-phosphoryl inosine-5'-monophosphate (6-pIMP). Further, the band at 1320 cm^{-1} becomes very sharp and intense in the spectrum of the enzyme•ligand complex. These results are similar to the results obtained in case of MjADSS in the previous chapter, where formation of 6-pIMP have been shown by using computational calculations and control experiments.

To further prove the formation of 6-pIMP at the active-site of PfADSS in the quinternary complex, experiment with GDP in place of GTP was carried out. Since, GDP cannot provide the γ-phosphate group which can be transformed to 6-oxy anionic IMP thus formation of 6-pIMP cannot take place in a reaction mixture containing IMP, GDP, L-Aspartate and PfADSS. In such situation, mere enzyme-induced distortion does not result in appearance of new bands and disappearance of IMP bands. This is found out to be indeed the case. The spectrum of IMP•GDP•L-Aspartate•PfADSS evidently shows that no covalent bonds are formed or broken in this complex (Figure 7.7). Further, since all the binding pockets are occupied in this complex thus the enzyme attains the fully ligated conformation i.e. dynamic loops of the enzyme acquire 'the closed conformation' leading to distortion of the bound ligands. These results also report on similar distortions of IMP in IMP•GDP•L-Aspartate•PfADSS and IMP•GTP•PfADSS complexes. Intensity loss in the band at 1555 cm^{-1} and at 1468 cm^{-1} in the spectrum of IMP•GDP•L-Aspartate•PfADSS depicts that the active-site becomes more compact upon ligation of the L-Aspartate pocket leading to a larger distortion of bound ligands. The effect of the same is manifested in the form of larger shifts in wavenumbers in the quinternary complex. This is the direct evidence of the allosteric effect in PfADSS which is captured in the form of varied magnitude of wavenumber shifts in the fully ligated enzyme complex.

Further, the carbonyl stretch at 1687 cm^{-1} which is attributed to both IMP and GTP shows a huge downshift of 46 cm^{-1} in this complex. A larger downshift in this band shows a greater contribution to the stabilization energy

which results in the proper positioning and orientation of the ligand at the active-site.

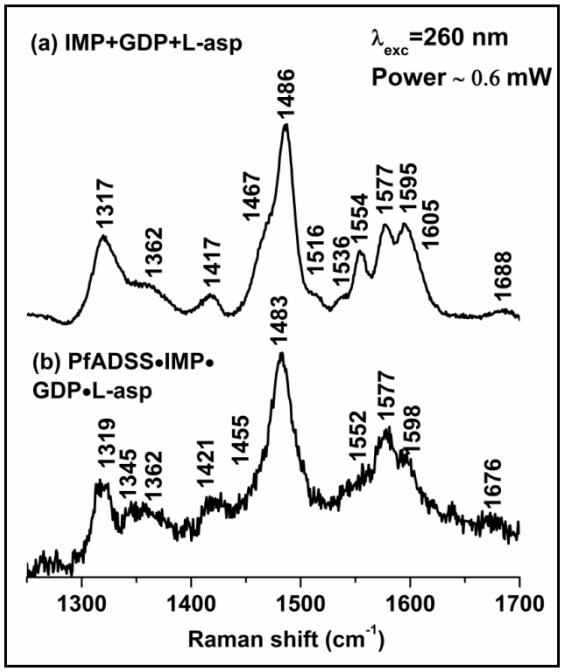

Figure 7.7: Resonance Raman spectra (λ_{exc}=260 nm) of (a) (IMP+GDP+L-Aspartate) free in solution, (b) IMP, GDP and L-Aspartate bound to PfADSS; acquired in HEPES buffer, pH 7.0.

Distortion of GTP in IMP•GTP•HDA•PfADSS: The marker bands of GTP in this complex show the shifts similar to those observed in IMP•GTP•PfADSS. For instance, the shifts observed in intense bands at 1486 cm^{-1} ($\Delta\nu$= -6 cm^{-1}) and at 1604 cm^{-1} ($\Delta\nu$= +10 cm^{-1}) are similar to the preceding enzyme complex.

Table 7.2: Comparison of shifts in wavenumber (cm^{-1}) observed in the UVRR spectra of IMP•PfADSS, IMP•GTP•PfADSS, IMP•GTP•HDA•PfADSS and GTP•PfADSS complexes in HEPES, pH 7.

Assignments	IMP	IMP•PfADSS	Band	IG or IGH[a]	IMP•GTP•PfADSS	IMP•GTP•HDA•PfADSS	Assignments	GTP	GTP•PfADSS
Str C6=O (76%) + Be N1H + C6N1C2 (-12%)	1693		IMP+GTP	1689	1658 (-43)	1645 (-46)	Str C6=O + C5C6 + BeN1H	1684	1650 (-32)
			GTP	1607	1619 (10)	1619 (10)	Be N1H+ Str C2N	1604	1614 (6)
Str C2N3 (55%) -C4C5- C5C6 + Be C2H (-12%) + N1H + N9H	1595	1595 (+1)	IMP	1596	1600 (+3)	1603 (+5)			
			GTP	1578	1575 (-2)	1571 (-7)	Str N3C4 + C4C5 + C5N7	1578	1575 (-4)
Str C4N9 (12%) - N3C4 (-22%) + N7C8 + Be N9H (15%) + C8H	1556	1553 (-3)	IMP	1556	1556 (-2)	1555 (-2)			
			GTP	1537		1531 (-7)	Str C4N9 + C6=O + N1C2	1537	1544 (-3)
			GTP	1488	1483 (-5)	1481 (-6)	Be C8H + Str C8N9 + N7C8	1487	1483 (-4)
Str C4C5-N7C8 (30%) + C2N3 + Be N1H + C8H + N7C8N9 (21%)	1517	1514 (-3)							

Be N1H (-23%) + C8H + N9H + Str N7C8 (-15%) - C4N9 (-11%) + N1C2	1468	1467 (-2)	IMP	1468	1459 (-9)	1450 (-8)			
Be N1H (17%) + C2H (18%) + C5N7C8 (-10%) + Str N1C2 (17%) - C4N9 (10%)	1421	1418 (-4)	IMP+GTP	1418	1416 (-2)	1414 (-5)	Str C4N9 + C5N7	1413	1419
			IMP+GTP	1362	1359 (-3)	1364 (+1)	Str N7C8 + NIC6 + C5N7	1366	1361 (-3)
Be N9H (20%) + C2H (-17%) + N1H + Str C8N9 (-17%) - C5N7C8 (-10%)	1383	1382							
Be C8H (-13%) + N9H + C2H (-10%) + Str C4N9 (-10%) + C2N3C4 (10%)	1320	1320 (-1)	IMP+GTP	1317	1313 (-4)	1322 (4)			

[a]IG or IGH represents (IMP+GTP) or (IMP+GTP+HDA)

7.3.3 Product complexes of PfADSS

Ligands of the reverse reaction in PfADSS are least characterized. It is important to mention that the ligands and their analogues falling at any step in the kinetic cycle can be exploited to develop a drug molecule which can effectively block the enzyme. However, structural and mechanical details of PfADSS bound to the ligands of the reverse reaction are negligible. In view of the difficulties involved in crystallization of enzymes, most of the crystal structures generally involve information on either the substrate or the product complexes.

A more holistic approach taken in this work where the ligands of the forward as well as reverse reaction have been studied provides thorough information of the conformational changes taking place at each step in PfADSS catalysis. An excitation wavelength of 260 nm enables the observation of ligands complexed with enzymes. All the spectra of product complexes of PfADSS were acquired in HEPES buffer, pH 7.0. At 260 nm, no spectral contribution from HEPES buffer was obtained.

Such complexes in the reverse reaction of PfADSS include sAMP•PfADSS, GDP•PfADSS, sAMP•GDP•PfADSS and sAMP•GDP•Pi•PfADSS. Results on product complexes are particularly valuable because of the paucity of data from other studies. Further, AMP which is a competitive inhibitor of IMP has also been studied.

sAMP•PfADSS: sAMP alone is sufficient to organize the active-site in PfADSS

sAMP has an absorption maximum at 269 nm and thus at 260 nm selective resonance enhancement of sAMP spectrum is observed. Spectral contribution of enzyme and unbound ligand have been subtracted from the enzyme•ligand spectrum. The spectra of sAMP free in solution and sAMP•PfADSS are shown in (Figure 7.8 (a) and (b)). A similar spectral pattern of bound and free form shows that sAMP is bound in the neutral form to the active-site. Shifts in the wavenumbers in sAMP•PfADSS with respect to

sAMP evidently show the presence of non-covalent interactions between sAMP and active-site residues (*vide-infra*).

The band at 1631 cm^{-1} ($\Delta\nu$= -5 cm^{-1}) in the sAMP spectrum arises from pyrimidne str along with N10—H bend. The band at 1363 cm^{-1} ($\Delta\nu$= +5 cm^{-1}) is attributed to N3—C4 and C8—N9 str and C6—N10—H bend (Table 7.3). The substantial shifts observed in these bands in sAMP•PfADSS, as mentioned in parentheses, capture distortion in the pyrimidine ring due to hydrogen bond between exocyclic —NH of sAMP and Ala68 residue [95]. The band at 1335 cm^{-1} ($\Delta\nu$= +3 cm^{-1}) in sAMP spectrum is a purine ring mode and thus reports on the distortion in the nucleobase moiety of sAMP. Further, the band at 1483 cm^{-1} in sAMP spectrum shows no shifts on an average in the sAMP•PfADSS spectrum. Interestingly, no isotope induced shift in this band is observed when sAMP is transferred from H_2O to D_2O. This suggests that though the band at 1483 cm^{-1} is intense but cannot be used as the marker of hydrogen bonding interactions.

In the previous chapter, complex of sAMP with MjADSS shows similar trends but larger magnitudes of wavenumber shifts. This comparison across two homologues of ADSS quantifies larger extent of distortion in sAMP bound at the active-site of MjADSS.

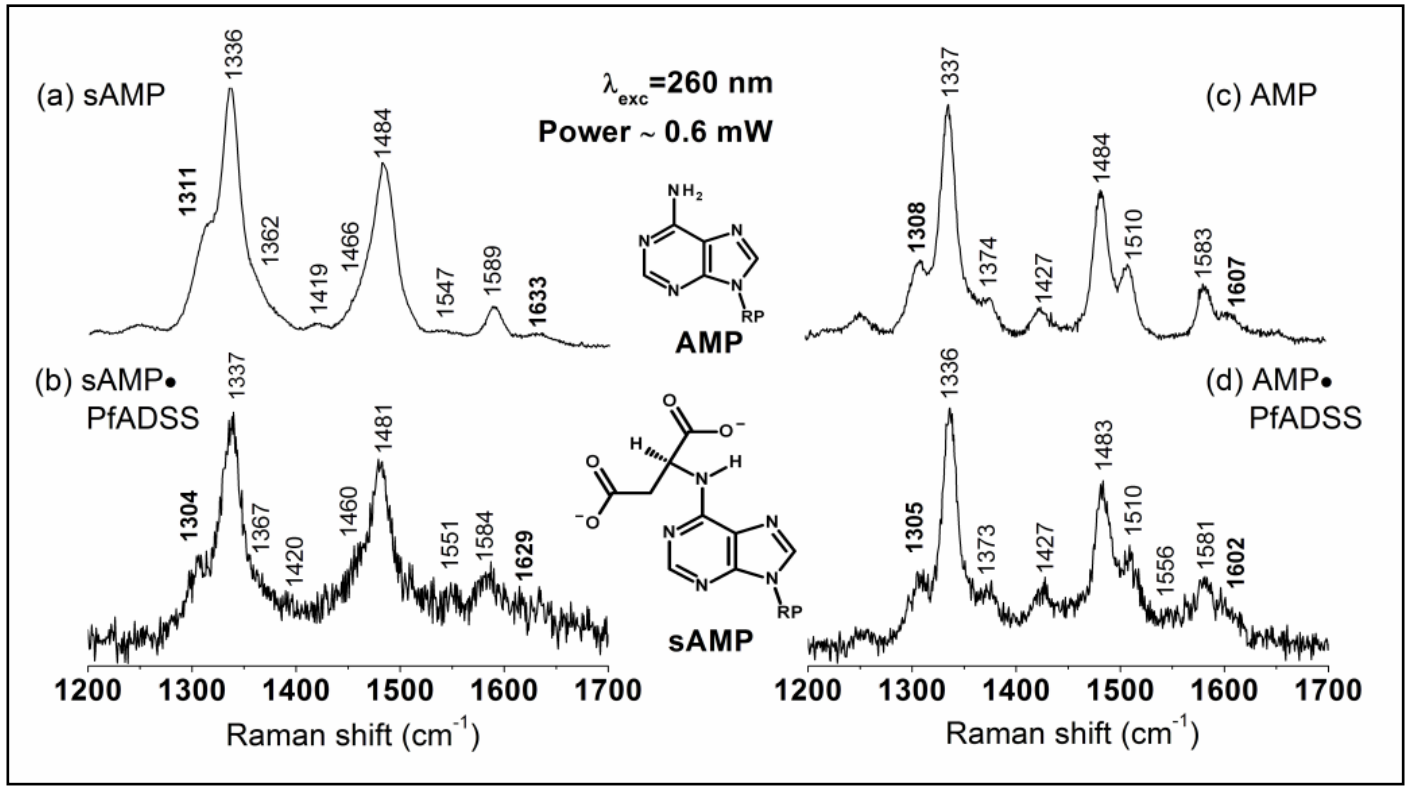

Figure 7.8: Resonance Raman spectra (λ_{exc}=260 nm) of (a) sAMP free in solution, (b) sAMP bound to PfADSS, (c) AMP free in solution and, (d) AMP bound to PfADSS; acquired in HEPES buffer, pH 7.0.

Table 7.3: Comparison of shifts in wavenumber (cm^{-1}) observed in the UVRR spectra of sAMP•PfADSS, sAMP•GDP•PfADSS, sAMP•GDP•Pi•PfADSS and GDP•PfADSS complexes in HEPES, pH 7.

Assignments	sAMP	sAMP• PfADSS	Band	SG or SGP[a]	sAMP•GDP • PfADSS	sAMP•GDP• Pi•PfADSS	Assignments	GDP	GDP• PfADSS
			GDP	1684	1665 (-29)	1672 (-25)	Str C6=O+C5C6+ Be N1H	1684	1661 (-28)
			GDP	1602	1609 (6)	1603 (+1)	Be N1H+ Str C2N	1603	1606 (5)
Be C6N1C2 (15%) + Str C2N3 (14%) + C6N10H (11%) + Be N3C4C5 (11%)	1633	1629 (-5)	sAMP	1641	1637				
						1595 (IMP)			
Str N3C4 (23%) + Str N1C6 (11%) + Be C4N9C8 (-11%) + Be C4N9H (10%) + Be C5N7C8 (-10%)	1589	1584 (-1)	sAMP +GDP	1579	1580 (-2)	1577 (-5)	Str N3C4 + C4C5 + C5N7	1577	1573 (-5)
						1554 (IMP)			
Str N7C8 (22%) + Str C6N10 (-16%) + Be C4N9C8 (10%) + Be C6N10H(12%) + Be NH2	1547	1551 (+2)	sAMP +GDP	1538		1536 (+3)	Str C4N9 + C6=O + N1C2	1536	1534 (-3)

Str N7C8 (24%) + Str N1C6 (-19%) + Str C2N3 (11%) + Be C2HN3 (-11%) + Str C6N10 (10%) + Be C8H + Be N9H	1484	1481 (-1)	sAMP +GDP	1487	1486 (-2)	1487	Be C8H+ Str C8N9 + N7C8	1486	1483 (-4)
Be C6NH (29%) + Be C5N7C8 (15%) + Be C2H + Be C8H	1466	1460 (-9)	sAMP	1477	1468 (-9)	1466 (-6)			
Be C2HN3 (39%) + Be C4N9H (20%) + Be N6H	1419	1420 (+5)	sAMP +GDP	1414	1418 (3)	1416 (+1)	Str C4N9 + C5N7	1411	1414
Str N3C4 (11%) + Str C8N9 (-13%) + Be N6H + Be N9H + Be + C2H + Be C8H	1362	1367 (+5)	sAMP +GDP	1365	1364	1363 (-2)			
Str C5N7 (23%) + Str N1C2 (20%) + Str N7C8 (-10%) + Be N6H + Be C8H + Be C2H	1336	1337 (5)	sAMP	1335	1340 (3)		Str N7C8 + NIC6 + N5N7	1364	1361 (-4)
Str C2N3 (31%) + Str N1C2 (-22%) + Be C2HN3 (17%) + Be N9H	1311	1304 (-3)	sAMP +GDP	1314	1319 (2)	1322 (5)		1317	1322 (+2)

[a]SG or SGP represents (sAMP+GDP) or (sAMP+GDP+Pi)

AMP•PfADSS: distortions in AMP and sAMP are similar

The AMP band at 1607 cm^{-1} ($\Delta\nu$= -5 cm^{-1}) is analogous to the sAMP band at 1631 cm^{-1} ($\Delta\nu$= -5 cm^{-1}) which arises from the C6—N6—H bend (Figure 7.8 (c) and (d)). The shifts observed in this band in the two cases evidently suggest that the enthalpic contribution of the hydrogen bond between N6H and Ala68 (Pf) is same in the two cases. The band at 1308 cm^{-1} ($\Delta\nu$= -3 cm^{-1}) in AMP spectrum is a pyrimidine ring mode. The corresponding band in sAMP spectrum lies at 1311 cm^{-1} and shows a similar shift ($\Delta\nu$= -3 cm^{-1}) in sAMP•PfADSS. Similar shifts in AMP•PfADSS and sAMP•PfADSS show that the geometric distortion is similar in AMP and sAMP which may arise from the similar electrostatic environment of PfADSS active-site.

In the absence of crystal structure of PfADSS with the product ligands, the spectral shifts are interpreted with respect to the structure of homologous ADSS from mouse muscle (mm). In mmADSS, N1 and N3 position of bound AMP interacts with Asp (non bonded contact) and water molecule, respectively. The structure also shows a putative hydrogen bond contact between N6—H of AMP and Ala69 (D-A: 3.2 Å) [107].

GDP•PfADSS: Interactions of guanine moiety in GDP and GTP are essentially same

Similar shifts observed in the spectrum of GDP•PfADSS and that of GTP•PfADSS quantifies similar strength of hydrogen bond at the guanine moiety in the two complexes. This implies that the absence of one phosphate group does not influence the interactions at the nucleobase moiety in two cases.

7.3.4 Intermediate complexes in reverse direction

sAMP•GDP•PfADSS: sAMP and GDP are not distorted any further

UVRR spectrum of sAMP•GDP•PfADSS is obtained by subtracting the spectrum of unbound (sAMP+GDP) and apoenzyme. Due to similar normal modes of vibration in sAMP and GDP, many bands in (sAMP+GDP) spectrum are attributed to both the molecules. A few bands that can be observed clearly

are assigned as the marker bands of individual ligands. For instance, the bands at 1335 cm^{-1}, 1470 cm^{-1}, 1589 cm^{-1} and 1641 cm^{-1} arise solely from sAMP while the bands at 1538 cm^{-1}, 1604 cm^{-1} and 1682 cm^{-1} arise from GDP only.

Distortion of sAMP in sAMP•GDP•PfADSS complex: Downshift in the band at 1631 cm^{-1} ($\Delta\nu$= -3 cm^{-1}) is similar to the one observed in the corresponding band at 1631 cm^{-1} ($\Delta\nu$= -5 cm^{-1}) in PfADSS•sAMP (Figure 7.9 (a) and (b)). Also, the sAMP band at 1335 cm^{-1} shows an upshift of +3 cm^{-1} in sAMP•GDP•PfADSS against an upshift of +5 cm^{-1} in sAMP•PfADSS. Similar direction and trend of shifts in sAMP bands in sAMP•PfADSS and sAMP•GDP•PfADSS suggest that sAMP alone is sufficient for bringing about the reorganization of all the dynamic loops in case of PfADSS. However, the magnitudes of shifts in the two cases are different, particularly being lower in the sAMP•GDP•PfADSS spectrum, suggesting strategic preparation of the active-site to facilitate the release of the product sAMP at this step of kinetic cycle.

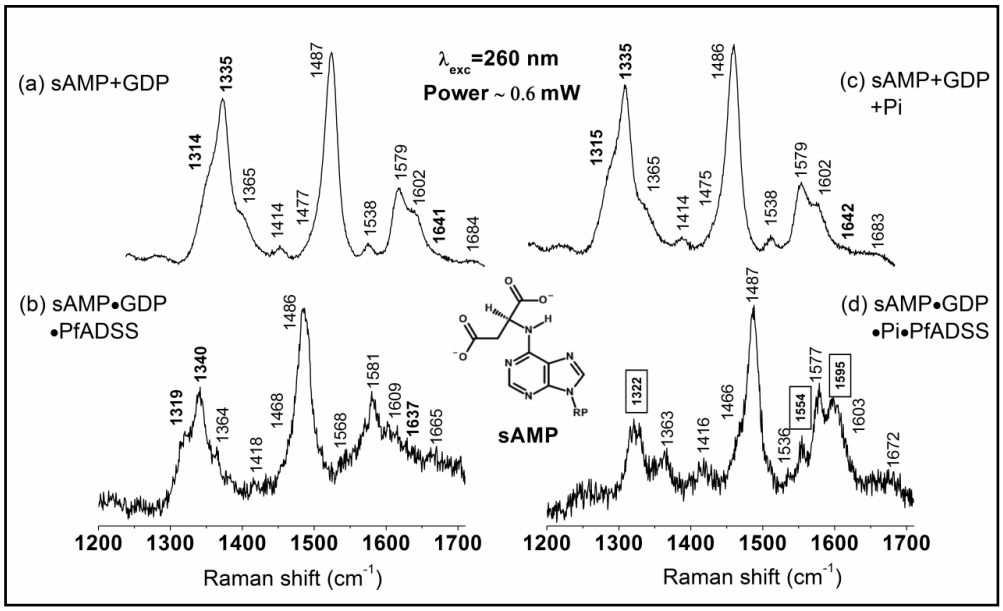

Figure 7.9: Resonance Raman spectra (λ_{exc}=260 nm) of (a) sAMP and GDP free in solution, (b) sAMP and GDP bound to PfADSS, (c) sAMP, GDP and Pi free in solution and, (d) sAMP, GDP and Pi bound to PfADSS; acquired in HEPES buffer, pH 7.0. The wavenumbers marked in bold are sAMP marker bands and the boxed wavenumbers are marker bands of IMP.

Distortion of GDP in sAMP•GDP•PfADSS complex: The band at 1602 cm^{-1} ($\Delta\nu$= +6 cm^{-1}) shows an upshift similar to the one observed in GDP•PfADSS ($\Delta\nu$= +5 cm^{-1}). The band at 1684 cm^{-1} is the carbonyl stretch contributed by the spectrum of GDP alone. This band shows an average downshift of 29 cm^{-1} in sAMP•GDP•PfADSS. These shifts suggest that GDP remains bound to the active-site until the product sAMP is formed.

sAMP•GDP•Pi•PfADSS: PfADSS catalyzes reverse reaction

The spectrum of phosphate (Pi) is not resonance enhanced at the excitation wavelength of 260 nm chosen for the experiments and thus as reported in Figure 7.9 (a) and (c), UVRR spectra of (sAMP+GDP+Pi) and (sMAP+GDP) are identical. Thus, the perturbations in the sAMP•GDP•Pi•PfADSS spectrum reports on the distortion in the enzyme bound sAMP and GDP in the presence of Pi.

Distortion in sAMP in sAMP•GDP•Pi•PfADSS complex: The spectrum of sAMP•GDP•Pi•PfADSS shows radical changes with repect to the (sAMP+GDP+Pi) spectrum (Figure 7.9 (c) and (d)). The sAMP bands at 1335 cm^{-1}, 1315 cm^{-1} and 1643 cm^{-1} are disappeared. New bands appear at the position of 1555 cm^{-1}, 1595 cm^{-1}, 1466 cm^{-1} and 1322 cm^{-1}. Similar to the observation in the sAMP•GDP•Pi•MjADSS spectrum, appearance of these new bands also suggests the occurrence of reverse reaction resulting in the formation of IMP, as shown in Appendix (Figure A.11). The new bands are attributed to the IMP spectrum. Further, it is important to notice that the experiment in which (GDP+Pi) of sAMP•GDP•Pi•PfADSS is replaced by GMP-PNP (a non hydrolysable analogue of GTP), showed no detectable bands of IMP (Figure 7.10).

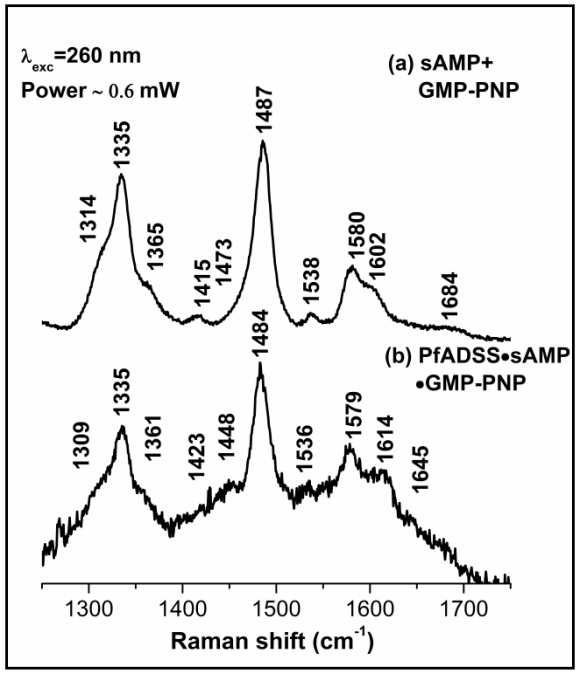

Figure 7.10: Resonance Raman spectra (λ_{exc}=260 nm) of (a) sAMP and GMP-PNP free in solution, (b) sAMP and GMP-PNP bound to PfADSS; acquired in HEPES buffer, pH 7.0.

7.4 Discussion

7.4.1 Comparison between PfADSS and MjADSS and implications on ligand binding

Forward reaction complexes: PfADSS and MjADSS catalyze the same reaction via different kinetic mechanisms. This suggests disparity in terms of the way allostery functions in two cases. New Raman bands pertaining to 6-pIMP were captured in the ternary complex of MjADSS. This is because the enzyme is maximally active at 80°C and hence at room temperature the rate of formation of the intermediate is slowed down. However, PfADSS is a mesophilic enzyme and hence in view of the absence of L-Aspartate or HDA, required to trap the intermediate at the active-site, 6-pIMP reverts back to IMP during the time-period of experiments.

In the crystal structure of fully ligated PfADSS (1P9B), 6-phosphoryl group of the intermediate seems to make several contacts with the active-site residues [95] (Figure 7.11). Most important of which is with the His54 (PfADSS) residue in the Switch loop which acts as a catalytic acid and donates a proton form NE2 position to the intermediate. This interaction can occur

only when the Asp pocket is occupied. This triggers a conformational change of 90° in His residue about its Cβ-Cγ bond. The hydrogen bonding interaction of His54 with one of the oxy-anions of the 6-phosphoryl group results in the stabilization of the intermediate at the active-site of PfADSS.

This interpretation is also supported by the observed downshifts in the combined carbonyl vibrations of IMP and GTP which lies at 1687 cm^{-1} in IMP•GTP•PfADSS complex. A continuous increase in the carbonyl shift quantifies the energy of hydrogen bond formation at each stage of the kinetic cycle. For instance, the carbonyl of GTP in PfADSS is downshifted more than that in MjADSS suggesting a more stable binding of the ligand in PfADSS. This implies that GTP is held tightly at the active-site of PfADSS. This is also corroborated by the kinetic constants ($K_{m\ (GTP•MjADSS)}$: 42.6 µM [32] and $K_{m\ (GTP•PfADSS)}$: 18.4 µM [33]). The evolutionary importance is to avoid non-productive hydrolysis of GTP. This is because the protozoan parasite maintains low level of guanine nucleotide pool [125].

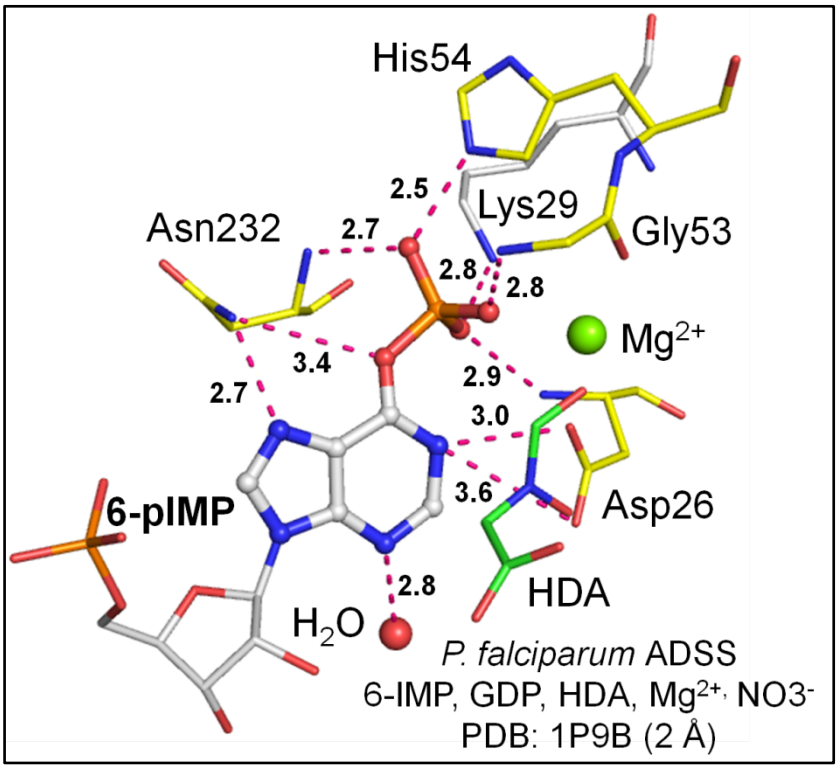

Figure 7.11: Active-site interactions of 6-pIMP with amino-acid residues in PfADSS (1P9B: 2 Å).

Reverse reaction complexes: Previously, it was observed in MjADSS that the downshifts in the marker bands of sAMP and GDP were larger when they are bound together at the active-site than when bound individually. This was rationalized as the implication of the random binding mechanism where both the ligands can bind in a random order but at a greater strength in the ternary complex. However, an ordered kinetic mechanism in PfADSS suggests that GDP alone should not form any complex with PfADSS. Interestingly, UVRR results capture the binding of GDP alone to PfADSS which is ascribed to the very high sensitivity of the technique. Further, no synergism is observed in their binding which is counter-intuitive to the ordered binding of ligands to PfADSS. The shifts in the marker bands of sAMP and GDP remain similar to the shifts observed when they are bound separately to PfADSS.

Further, in case of the fully ligated product complexes, both MjADSS and PfADSS show the occurrence of reverse reaction. The results obtained in the form of Raman shifts evidently show that the reactivity of IMP at N1H differ by a large amount in IMP•MjADSS and IMP•PfADSS. Differential wavenumber shifts in the band corresponding to the N1—H bending vibrations (1468 cm^{-1}) immediately suggest that N1—H bond is weaker in IMP•MjADSS as compared to that in IMP•PfADSS. Combining the kinetic data (k_{cat}) with our results suggests greater activation energy for PfADSS catalyzed reaction, provided that the other conditions are optimum in two cases [32, 33]. This can be rationalized by perceiving that the pre-organization of the active-site in the two cases is different. While the random kinetic mechanism in *E. coli* ADSS leads to the organization of all the dynamic loops upon binding of IMP, ordered kinetic mechanism in PfADSS keeps a constrain on full activation of ligand until a fully ligated complex is formed. Furthermore, non bonded contacts clearly seem to destabilize sAMP, suggesting the reduced binding strength of nucleobase moeity in the products which results in the easy release of the product.

7.5 Conclusion

The results reported in this study bear on a number of important attributes concerning the allosteric control of enzymes. For instance, the comparison between MjADSS and PfADSS reveals that homologous enzymes with conserved active site residues can distort the same substrate to different extents. Multiple sequence alignment of the two homologues suggests that the hydrogen bonding network is conserved in the two enzymes. This is corroborated by the overall similarity of relative intensities and band positions of the spectra of ligands bound to MjADSS and PfADSS. However, the <10 cm-1 difference in the magnitude of wavenumber shifts between the two complexes implies that interactions of the nucleobase with the two enzyme active sites is not identical. Relative shifts between the band positions in the two complexes imply that subtle changes in the overall protein conformations influence hydrogen bonding strengths and overall packing at the active site. These effects manifest in Raman experiments because a small change in the force constant of the bonds of a molecule significantly alters the associated vibrational wavenumbers. This ability of UVRR to report on the subtle distortion in the ligand upon binding to enzymes suggests that the technique can be exploited to study the structures of enzyme inhibitors or substrate analogues.

"It is impossible to say just what I mean!
But as if a magic lantern threw the nerves in patterns on
a screen:
Would it have been worthwhile?
If one, settling a pillow or throwing off a shawl,
And turning toward the window, should say:
'That is not it at all,
That is not what I meant, at all'."

T.S. Eliot

Conclusion

In this thesis, I have documented the ligand complexes of two enzymes, HGPRT and ADSS, of purine nucleotide synthesis pathway. Using the highly sensitive technique of UVRR, I have elucidated the extent of ground-state distortion in ligands bound to the active-site of these enzymes. Altered Raman shift and cross-section of a band in a vibrational spectrum allowed direct observation of such perturbations in the structural parameters of ligands, which typically lie at sub-angstrom level. A comparison between the two homologues of each enzyme led the quantification of these distortions. The work done in the thesis establishes a significant advancement in understanding the mechanistic details involved in enzyme catalysis. In case of HGPRT, the work provides the first and novel explanation for the differential substrate specificities between human and Pf HGPRTs. The work also elucidates the allosteric control of such distortions in two different homologues of ADSS which involve a thermophilic MjADSS and a mesophilic PfADSS. I found that the two homologues catalyzing same reaction employ different mechanistics.

Section I: Hypoxanthine guanine phosphoribosyltransferase

- In order to capture the ternary complex in forward reaction of HGPRT, I used 9-deazapurines, 9DAG and 9DAH which are substrate analogues of guanine and hypoxanthine, respectively. The structures of these analogues in solution at acidic, physiological and alkaline pH

values were established using UVRR and DFT. The work elucidated that both the analogues exist in neutral form at physiological pH with the proton at N1 and N7 position. The protonated species at lower pH bear a proton at N3 position of the pyrimidine ring. Deprotonation at higher pH occurs from the N1 position whereas proton at the N7 position remains intact even at pH 12.5, in both the analogues.

- The distortions in the structure of enzyme bound ligands which are integral to catalysis have been captured. The distorted structure of 9-deazapurines, when bound to HGPRT, resembles the transition-state of the phosphoribosyltransferase reaction.
- Perturbations in the Raman wavenumber positions establish that the hydrogen bonding network at the active-site of hHGPRT is more rigid as compared to that in PfHGPRT. This quantifies different mechanistics employed by identical hydrogen bonding environments in the two homologues.
- Loss in Raman cross-section of the 9-deazapurines, bound to both the HGPRTs, has been attributed to the stacking interaction between Phe residue and the nucleobase at the active-sites.
- The loss in Raman cross-section is greater in hHGPRT than in PfHGPRT suggesting a closer stacking interaction in the former than in the latter. These results establish that non-covalent interactions (hydrogen bonding and stacking) provide greater rigidity and hence specificity to hHGPRT as compared to PfHGPRT.
- UVRR results of 9DAH bound to both the HGPRTs show comparatively less compact active-site interaction with 9DAH than with 9DAG. This is manifested in the forms of lower magnitude of Raman shifts.

Section II: *M. jannaschii* adenylosuccinate synthetase

- In my PhD work, I have determined solution structure of the product, sAMP, of ADSS catalyzed reaction. sAMP exists as a neutral species with proton at exocyclic N6 position of pyrimidine ring. RP-HPLC profile establishes the presence of two isomers of sAMP in solution.

- The solution structure and Raman identity of highly transient intermediate, 6-pIMP, in complex with ADSS, has been established. The isolation of free form of 6-pIMP has been difficult because of the unstability of this species in solution. In the present work also, RP-HPLC did not result in a separate peak for 6-pIMP upon denaturation of the enzyme.
- The results of the forward reaction complex establish that although IMP bound to MjADSS is distorted towards its deprotonated form, it remains bound as a neutral species in the absence of GTP.
- GTP alone is held at the active-site with strong non-covalent interactions. The larger magnitude of Raman shifts in the GTP•MjADSS spectrum establishes that GTP provides maximum intrinsic binding energy in ADSS catalyzed reaction.
- Absence of any radical changes in the GTP•MjADSS spectrum corroborates the literature which suggest that the guanine moiety does not take part in chemical transformation of ADSS catalyzed reaction.
- IMP and GTP when bound together to MjADSS show the formation of 6-pIMP which is not stabilized at the active-site. This establishes that the formation of the intermediate, 6-pIMP, at the active-site of ADSS does not require ligation of L-Aspartate pocket.
- Addition of HDA to the ternary complex of ADSS results in complete transformation of IMP to 6-pIMP. This intermediate is stabilized at the active-site of ADSS upon ligation of L-Aspartate pocket.
- The results of the ternary and the quinternary complexes of ADSS capture local conformational changes which take place upon ligation of L-Aspartate pocket and in turn stabilize 6-pIMP at the active-site. Such subtle conformational changes play an important role in catalysis by lowering the activation energy barrier; however, these are indistinguishable in other biophysical techniques.
- The direct implication of this finding lies in the identification of potential drug molecules against the parasitic ADSS. The present data suggest that a mimic of 6-pIMP alone cannot act as a potential

therapeutic agent but it should be provided along with a mimic of L-Aspartate.

- Not only does the present study capture distortion in the product sAMP which is attributed to the hydrogen bonding interactions, but it also elucidates the conformational re-organization in the dynamic loops of the active-site of ADSS upon binding to sAMP. The results show that sAMP alone is sufficient to organize the dynamic loops around the active-site.
- Distortion in guanine moiety of GDP is essentially same as that in GTP and GMP-PNP which suggests unaltered active-site interactions in the guanine moiety in GDP•MjADSS, GTP•MjADSS and GMP-PNP•MjADSS complexes.
- Enhanced magnitude of shifts in marker bands of sAMP and GDP in the sAMP•GDP•MjADSS spectrum suggests that both the ligands bind synergistically to ADSS.
- Addition of phosphate to sAMP•GDP•MjADSS results in the occurrence of reverse reaction, under in vitro conditions, at the active-site of ADSS.

Section III: *P. falciparum* adenylosuccinate synthetase

- Absence of substantial shifts in the wavenumber of IMP•PfADSS spectrum shows that IMP alone is not sufficient to completely organize the active-site of PfADSS.
- A comparison between the UVRR spectrum of IMP•PfADSS with that of IMP•MjADSS shows that while in MjADSS, IMP is activated for the next catalytic step, binding of IMP to PfADSS does not lead to significant distortion until the other ligands of ADSS catalyzed reaction are also bound. This implies differences in the mechanistics employed by the two homologues to catalyze the identical substrates.
- Whereas kinetic results suggest that GTP binds only to IMP•PfADSS, UVRR results sample a PfADSS population which is capable of binding to GTP even in the absence of IMP.

- Addition of GTP to the IMP•PfADSS complex further distorts the structure of IMP which is evident from the increase in the magnitude of shifts in the IMP•GTP•PfADSS complex with respect to the IMP•PfADSS complex.
- Unlike in case of MjADSS, the ternary complex of PfADSS does not show any signature of 6-pIMP while in the quinternary complex, complete transformation of IMP to 6-pIMP is observed. This shows that even in the mesophilic enzyme, PfADSS, local conformational changes stabilize 6-pIMP at the active-site for indefinite period of time.
- In the reverse reaction of PfADSS, sAMP alone is sufficient to organize the active-site conformation.
- The active-site interactions and the conformation organization in GDP•PfADSS resemble to that in GTP•PfADSS.
- In the ternary product complex of PfADSS, no synergism in the binding of sAMP and GDP was observed which means that the release of the products is less controlled in PfADSS as compared to MjADSS.
- Likewise MjADSS, reverse reaction is also observed in fully ligated product complex of PfADSS, which is further corroborated by the RP-HPLC data.

Utility of Raman spectroscopy in drug development

- The enzymes, HGPRT and ADSS, studied in the present work are essential in the nucleotide synthesis pathway of the protozoan parasite, *Plasmodium falciparum* [218, 219]. Development of potent drug molecules which can be specifically targeted against the parasitic enzymes while leaving the host enzymes unaffected requires thorough understanding of the non-covalent interactions between the drug molecule and the active-site residues in enzyme. Structural information at lower resolutions may not provide a clear understanding of differential substrate specificity between parasitic and host enzymes. In this respect, the use of Raman spectroscopy in the present study provides a quantitative measure of specific non-covalent contacts

which are responsible for providing differential substrate specificity to the parasitic and the host enzymes.

- In case of HGPRT, the present study, in combination with the previous Raman study from our lab, suggests that interactions of the substrate with hHGPRT and PfHGPRT are not identical. Despite the homology of sequence and participating residues of the active-sites, the overall differences between the enzymes influence the strength of hydrogen bonding and other interactions with the nucleobase of the substrate. We also find that the packing interactions of the base with the active-site are stronger in the forward complex as compared to those in the product complexes. This suggests that while a mimic of the reactant may specifically bind to PfHGPRT, that of the product may not prove an effective drug molecule.
- In case of ADSS, the present work suggests that a drug molecule mimicking the intermediate, 6-pIMP, may not prove effective unless supplemented by the presence of L-Aspartate analogue. This is because the work done in the present thesis suggest that in the absence of HDA, the ternary complex, IMP•GTP•ADSS, does not drive enough conformational changes so as to hold the intermediate, 6-pIMP, at the active-site. Addition of HDA to the complex re-organizes the active-site and captures 6-pIMP. Thus, a combination of 6-pIMP and HDA can inhibit the enzymatic turn-over and thereby blocking the pathway of nucleotide synthesis.
- The present Raman study establishes that once an enzyme is studied with its natural ligands, subsequent study with other analogues of the enzyme can be performed easily. Moreover, the information obtained is in solution state which is a physiologically relevant condition. Many parasites are known to develop resistance against the existing drug molecules. In this respect, the present study provides the utility of Raman spectroscopy in providing the differential information at sub-angstrom level which can be exploited to develop species-specific drug molecules.

Appendix

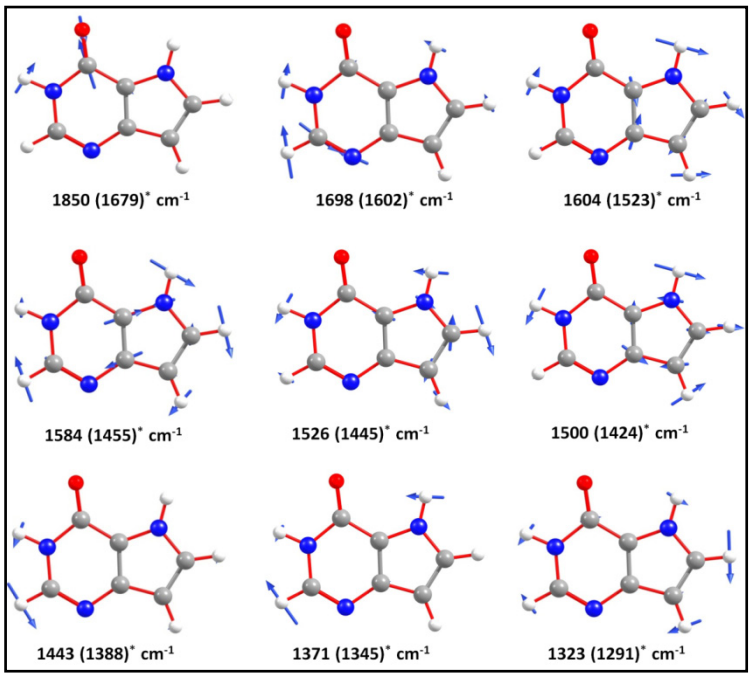

Figure A.1: Normal mode vectors of 9DAH. Structure of 9DAH was computed using dispersion corrected density functional theory in Gaussian 09. wB97XD/6-31G (d, p) level of theory was used for the purpose. Wavenumber calculations were performed on the optimized structure using same level of theory and basis set.*represents the wavenumber obtained in UVRR experiment.

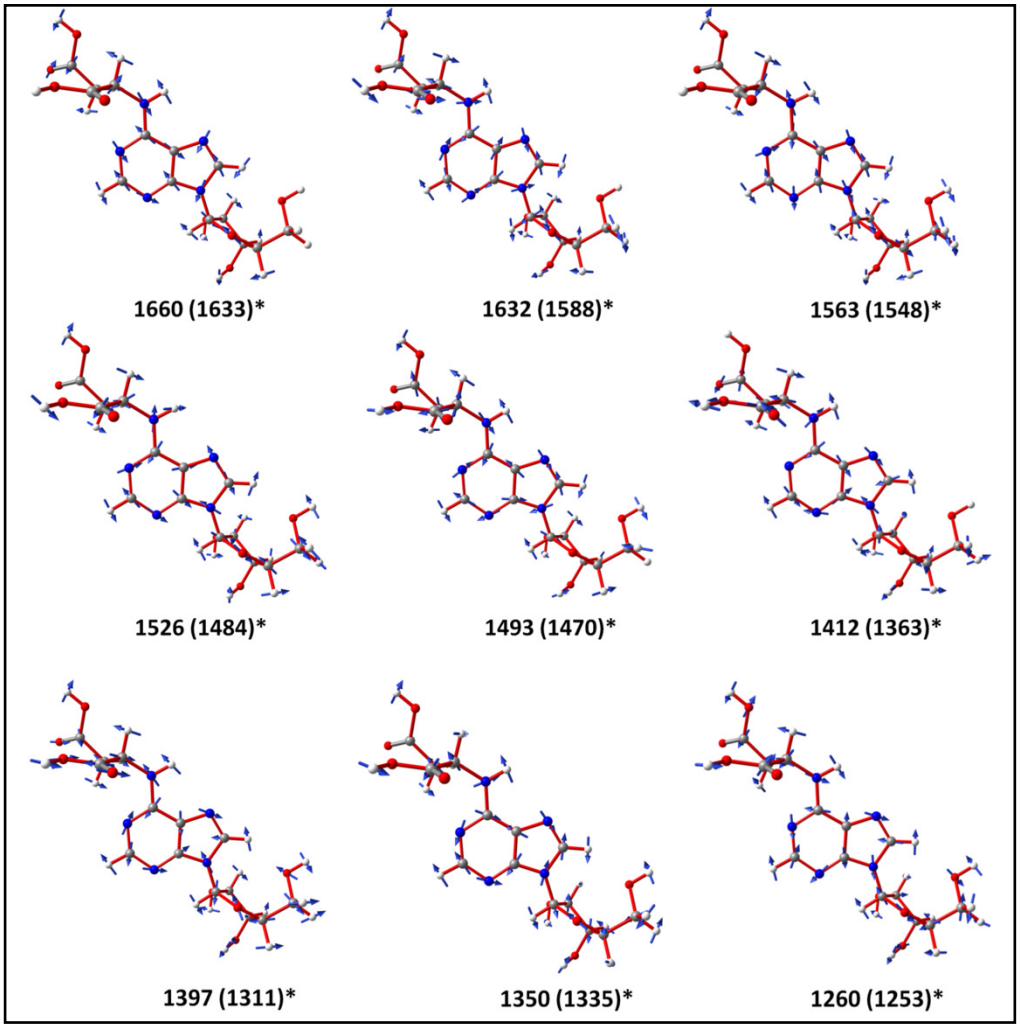

Figure A.2: Normal mode vectors of succinyl-Adenosine. Structure of succinyl-Adenosine was computed using density functional theory in Gaussian 09. B3LYP/6-31G (d, p) level of theory was used for the purpose. Wavenumber calculations were performed on the optimized structure using same level of theory and basis set.*represents the wavenumber obtained in UVRR experiment.

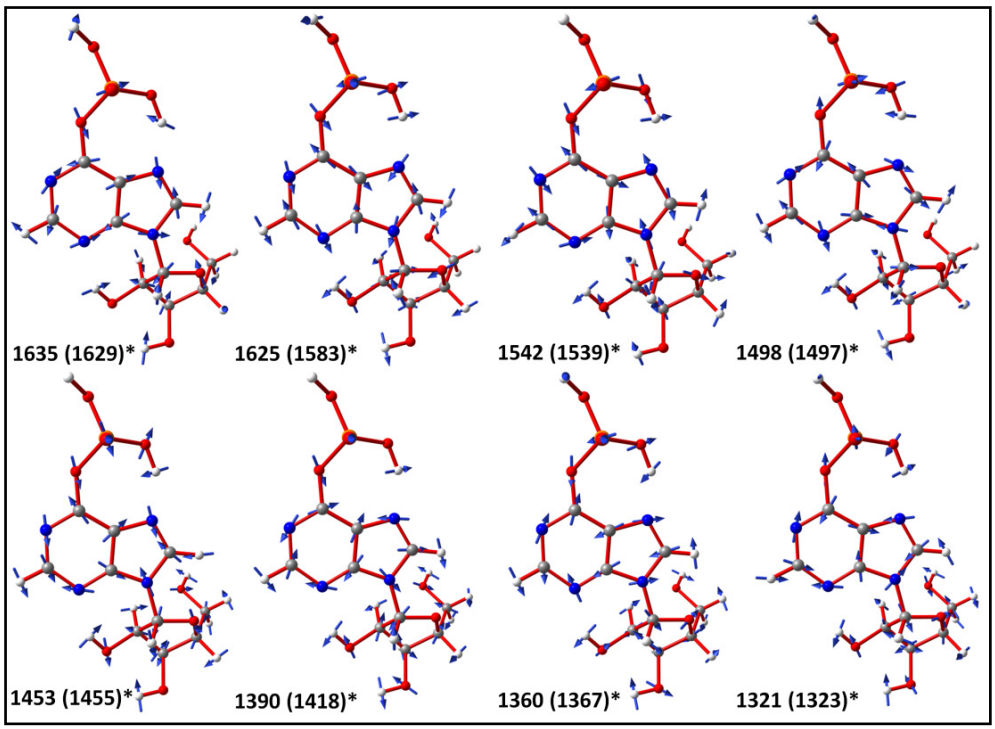

Figure A.3: Normal mode vectors of 6-phosphoryl inosine. Structure of 6-phosphoryl inosine was computed using density functional theory in Gaussian 09. B3LYP/6-31G (d, p) level of theory was used for the purpose. Wavenumber calculations were performed on the optimized structure using same level of theory and basis set.*represents the wavenumber obtained in UVRR experiment.

Table A.1: Comparison between the experimentally observed Raman wavenumbers of sAdenosine and AMP.

Mode assignments (sAdenosine)	UVRR	
	sAdenosine	**AMP[a]**
Str C2N3 (16%)+ Be C6N1C2 (14%)+ Be N3C4C5 (13%) + Be C6N6H (10%)	1633	1604
Str N3C4 (25%)+ Str N1C6 (17%) + Be C4N9C8 (-13%)	1588	1581
Str N7C8 (23%)+ Str C6N10 (-12%) + Be C4N9C8 (13%) + Be N7C8H (-12%)+ Be C6N6H (10%)	1548	1509
Str N1C6 (17%) + Str N7C8 (-16%)+ Str C2N3 (-14%) + Str C6N10 (-13%) + Be C2HN3 (13%)	1484	1482
Be C6N6H (29%) + Be C5N7C8 (12%) + Str C4N9 (-10%)	1470	1423
Str C4N9 (-10%) + Ribose ring mode	1419	
Be C2HN3 (29%) + Be C11HN10 (-17%)+ Be C6N6H (10%)	1363	1376
Pyrimidine ring mode [Str N1C2 (31%)+ Str C2N3 (-22%) + Be C2HN3 (-12%) + Be C6N6H]	1335	1339
Purine ring Stretch + Be C2H	1311	1309
Be N7C8H (37%) + Str N9C1' (14%)	1253	1254

[a]Raman wavenumbers are taken from ref. [36].

Raman Spectrum of 6-pIMP (a detail account is mentioned in Chapter 6 (under the Section 'Establishing the formation and UVRR identity of 6-pIMP'))

In order to obtain the spectral identity of the species that is formed in the fully ligated ADSS complex in the forward direction, the spectrum of GTP•MjADSS was subtracted from the spectrum of IMP•GTP•HDA•MjADSS.

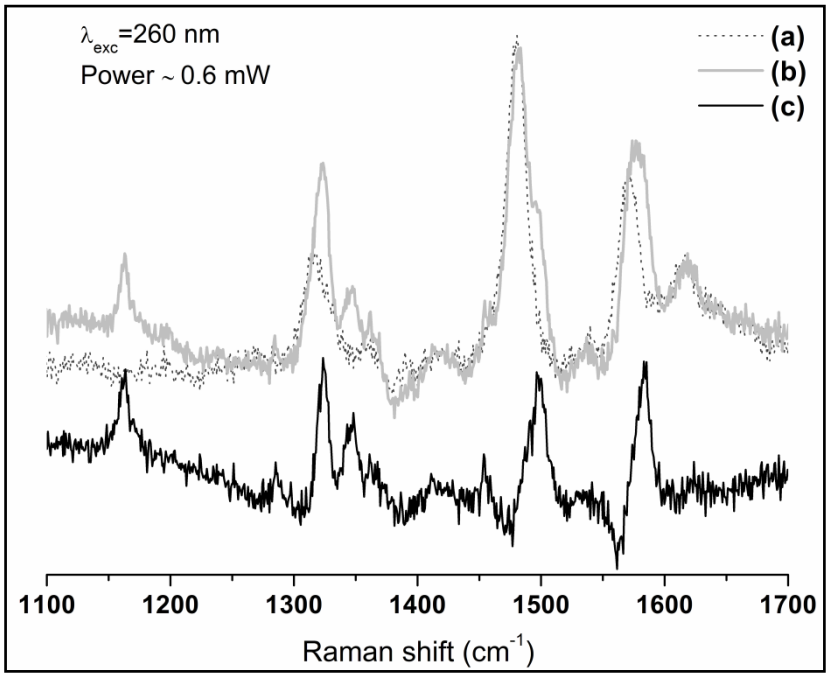

Figure A.4: UVRR spectrum of GTP•MjADSS (a) was subtracted from the UVRR spectrum of IMP•GTP•HDA•MjADSS (b). The resultant spectrum of 6-pIMP is shown in black (c).

Table A.2: Comparison between DFT (B3LYP/6-31G (d, p)) computed normal modes of 6-phosphoryl inosine and experimentally observed Raman wavenumbers (λ_{exc}=260 nm) with IMP bands.

6-phosphoryl Inosine	UVRR	IMP	UVRR
		Str C6O (76%) + Be N1H + C6N1C2 (-12%)	1690
Str N3C4 (23%) + Str N1C6 (21%)	1629	Str C2N3 (55%) - C4C5 - C5C6 + Be C2H (-12%) + N1H + N9H/N7H	1593
Str C2N3 (19) + Be C4N9C8 (-15%) + Be N3C4C5 (12%) + Be C2N3C4 (-10%)	1583	Str C4N9 (12%) -N3C4 (-22%) + N7C8 + Be N9H (15%) + C8H	1554
Str N7C8 (27%) + Be N7C8H (-18%)	1539		
Be C2HN3 (41%) + Str N1C6 (24%)	1497		
Str N3C4 (19%) + Str N7C8 (15%)	1455	Str C4C5 - N7C8 (30%) + C2N3 + Be N1H + C8H + N7C8N9 (21%)	1515
Purine ring stretching + C2H bending	1418	Be N1H (-23%) + C8H + N9H + Str N7C8 (-15%) - C4N9 (-11%) + N1C2	1468
Be C2HN3 (23%) + Str C6O6 (12%)	1367		
Str N1C2 (24%) + C2N3 + N7C8	1348	BeN1H(17%)+C2H(18%)+ C5N7C8(-10%)+St N1C2(17%)-C4N9(10%)	1421
		BeN9H (20%) + C2H (-17%) + N1H + Str C8N9(-17%) - C5N7C8 (-10%)	1381
Str C2N3 (-15%)	1323		
Be N7C8H (-23%)	1285		
Be N7C8N9 (-17%)			
Be N7C8H (26%) + Str C5N7 (18%) + Str N1C6 (-11%) + Str C2N3 (-11%)+Str N1C2 (-10%)	1164	Be C2H(24%) + C8H + N1H + St C5N7 (28%) - N7C8	1350
		Be C8H (-13%) + N9H + C2H (-10%) + Str C4N9 (-10%) + C2N3C4 (10%)	1322

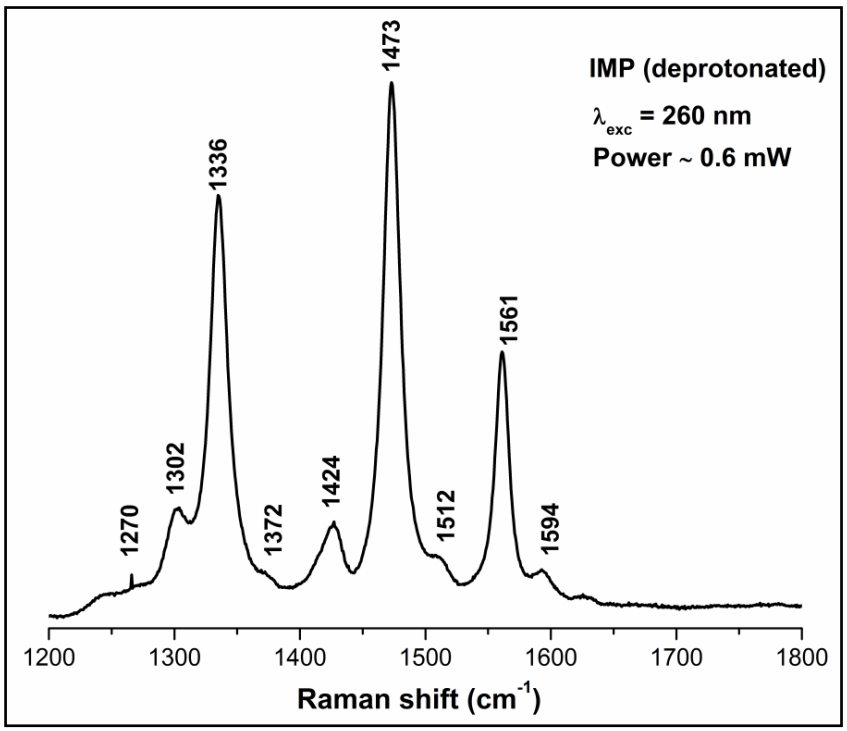

Figure A.5: UVRR spectrum of deprotonated IMP at pH 1.5; acquired at an excitation wavelength of 260 nm.

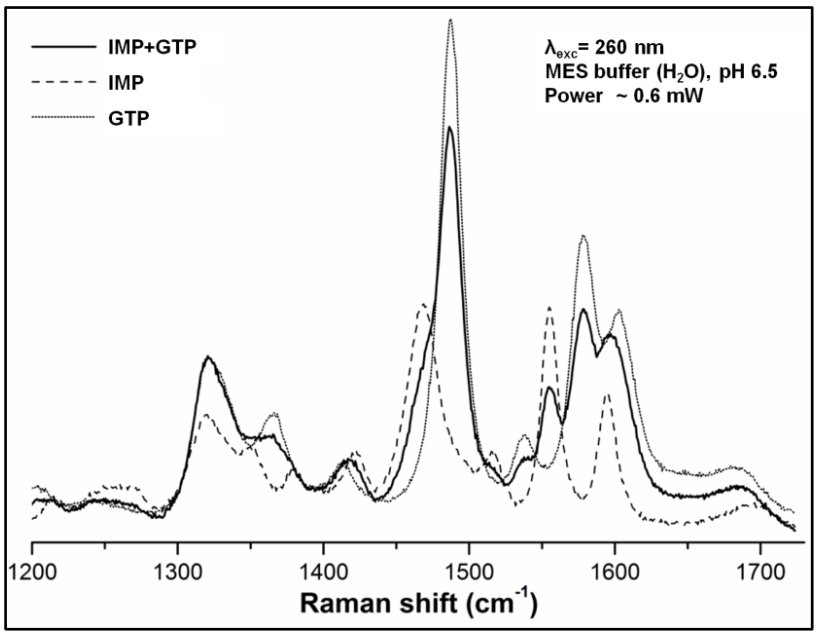

Figure A.6: Resonance Raman spectra (λ_{exc}=260 nm) of different mononucleotides in H_2O buffer (MES, pH 7.0). Solid line is (IMP+GTP), dashed line is IMP only and light dotted line is GTP only.

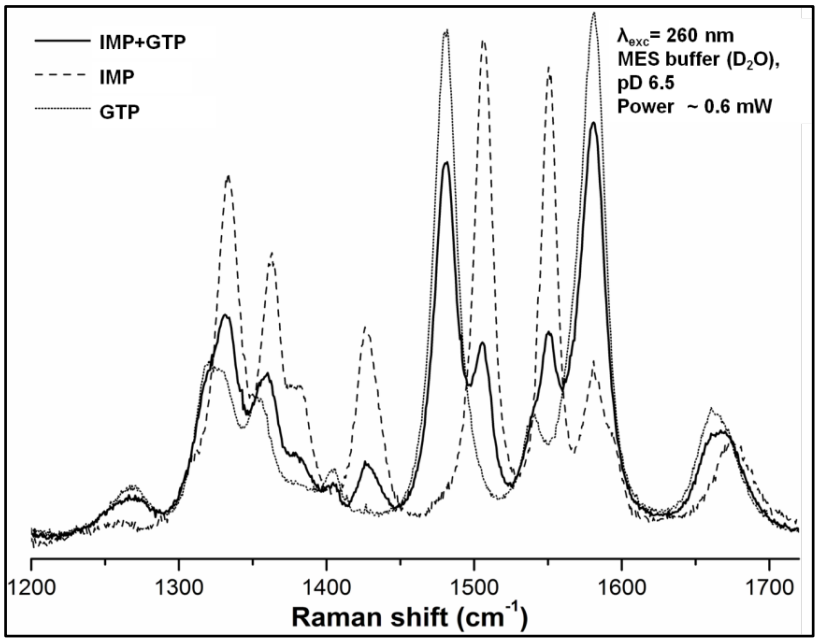

Figure A.7: Resonance Raman spectra (λ_{exc}=260 nm) of different mononucleotides in D_2O buffer (MES, pD 7.0). Solid line is (IMP+GTP), dashed line is IMP only and light dotted line is GTP only.

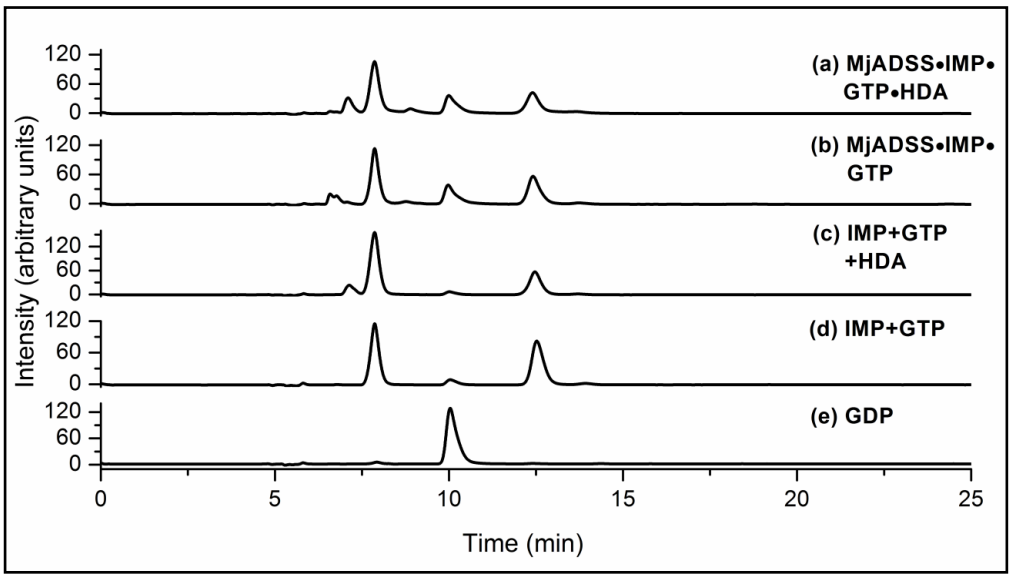

Figure A.8: RP-HPLC Chromatogram (λ= 251 nm) of MjADSS reaction mixture containing MjADSS (150 µM), GTP (500 µM), IMP (500 µM), HDA (10 mM) and magnesium acetate (15 mM) in MES pH 6.5 (30 mM), at 251 nm and 25 °C. (a) MjADSS reaction mixture containing IMP, GTP and HDA; peaks for GTP (13 min) and GDP (10 min) and IMP (8 min) are observed, (b) MjADSS reaction mixture containing IMP and GTP without HDA; GTP, GDP and IMP peaks are observed. IMP+GTP+HDA (c), IMP+GTP (d) and GDP (e) were run as controls. Concentration of IMP, GTP and GDP were maintained at 500 µM each, while HDA and MjADSS were used at 10 mM and 150 µM, reapectively. All the controls were treated in the same way as that of MjADSS reaction mixture.

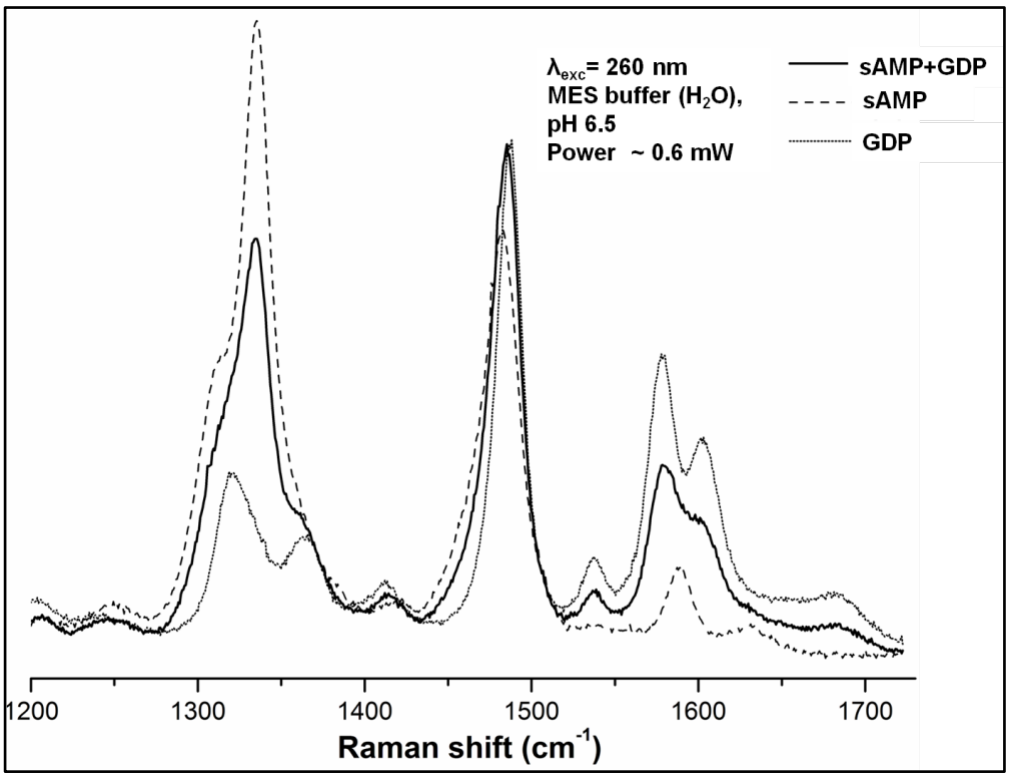

Figure A.9: Resonance Raman spectra (λ_{exc}=260 nm) of different mononucleotides in H_2O buffer (MES, pH 7.0). Solid line is (sAMP+GDP), dashed line is sAMP only and light dotted line is GDP only.

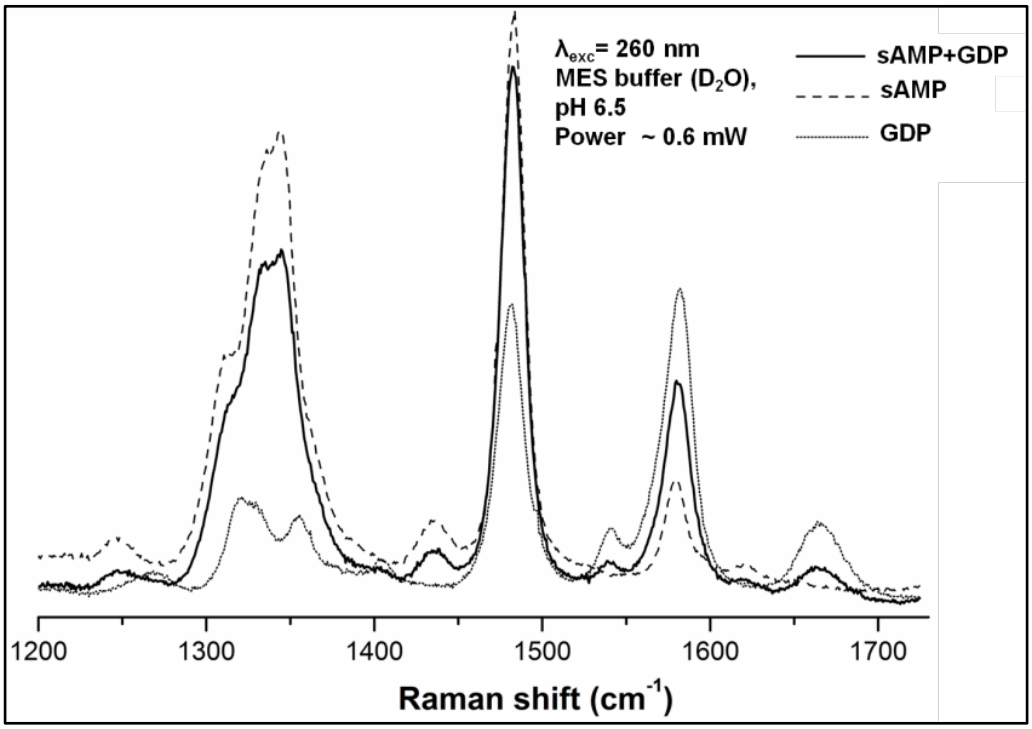

Figure A.10: Resonance Raman spectra (λexc=260 nm) of different mononucleotides in D_2O buffer (MES, pD 7.0). Solid line is (sAMP+GDP), dashed line is sAMP only and light dotted line is GDP only.

A.2: C18 column run provides proof of the occurence of reverse reaction in PfADSS

A reaction volume of 50 µL containing HEES buffer pH 7 (30 mM), magnesium acetate (15 mM), sodium phosphate (10 mM), sAMP (500 µM) and GDP (500 µM) was prepared. PfADSS was added at a concentration of 150 µM. After 25 minutes of incubation period, enzyme was denatured by adding 0.1% SDS solution. 20 µL of supernatant was loaded onto the Luna 5 µm C18 (2) 100 Å column, 260 x 4.60 mm (Phenomenex) column. The nucleotides were separated using a protocol employed by Ogwa et al. [116] with minor modification in an isocratic flow of KH_2PO_4 (73 mM), tetrabutyl ammonium hydroxide (5 mM) and methanol (25%) at a flow rate of 0.5 mL/min for 25 minutes. Chromatogram was obtained at 251 nm (λ_{max} for IMP) (Figure A.6).

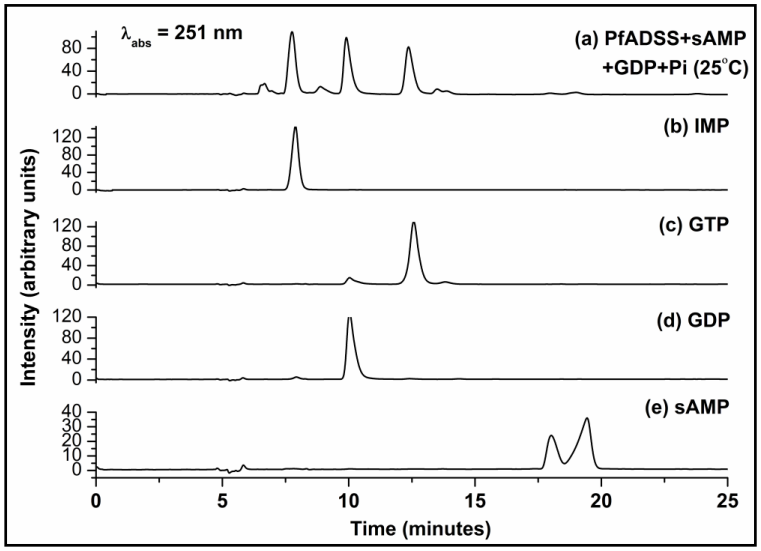

Figure A.11: RP-HPLC Chromatogram of PfADSS reaction mixture containing PfADSS (150 µM), GDP (500 µM), sAMP (500 µM), Pi (5 mM) and magnesium acetate (15 mM) in HEPES pH 7.0 (30 mM), at 251 nm. (a) PfADSS reaction mixture at 25 °C; GTP peak and a minor peak of sAMP is observed. 500 µM each of (c) IMP (8 minutes), (d) GTP (13 minutes), (e) GDP (10 minutes) and (f) sAMP (18 minutes) were run as controls. All the controls were treated in the same way as that of PfADSS reaction mixture (a).

References

[1] Jencks, W. P. **(1997)** From chemistry to biochemistry to catalysis to movement. *Annual Review of Biochemistry 66*, 1-18.

[2] Koshland, D. E. **(1994)** The Key-Lock Theory and the Induced Fit Theory. *Angewandte Chemie International Edition 33*, 2375-2378.

[3] Pauling, L. **(1948)** Nature of Forces between Large Molecules of Biological Interest. *Nature 161*, 707-709.

[4] Anderson, V. E. **(2005)** Quantifying energetic contributions to ground state destabilization. *Archives of Biochemistry and Biophysics 433*, 27-33.

[5] Andrews, L. D., Deng, H., and Herschlag, D. **(2011)** Isotope-Edited FTIR of Alkaline Phosphatase Resolves Paradoxical Ligand Binding Properties and Suggests a Role for Ground-State Destabilization. *Journal of the American Chemical Society 133*, 11621-11631.

[6] Andrews, L. D., Fenn, T. D., and Herschlag, D. **(2013)** Ground State Destabilization by Anionic Nucleophiles Contributes to the Activity of Phosphoryl Transfer Enzymes. *PLoS Biology 11*.

[7] Carey, P. R. **(2006)** Spectroscopic characterization of distortion in enzyme complexes. *Chemical Reviews 106*, 3043-3054.

[8] Griswold, W. R., Castro, J. N., Fisher, A. J., and Toney, M. D. **(2012)** Ground-State Electronic Destabilization via Hyperconjugation in Aspartate Aminotransferase. *Journal of the American Chemical Society 134*, 8436-8438.

[9] Balendiran, G. K., Molina, J. A., Xu, Y. M., Torres-Martinez, J., Stevens, R., Focia, P. J., Eakin, A. E., Sacchettini, J. C., and Craig, S. P. **(1999)** Ternary complex structure of human HGPRTase, PRPP, Mg2+, and the inhibitor HPP reveals the involvement of the flexible loop in substrate binding. *Protein Science 8*, 1023-1031.

[10] Ruben, E. A., Schwans, J. P., Sonnett, M., Natarajan, A., Gonzalez, A., Tsai, Y., and Herschlag, D. **(2013)** Ground State Destabilization from a Positioned General Base in the Ketosteroid Isomerase Active Site. *Biochemistry 52*, 1074-1081.

[11] Zhang, Y., and Schramm, V. L. **(2011)** Ground-State Destabilization in Orotate Phosphoribosyltransferases by Binding Isotope Effects. *Biochemistry 50*, 4813-4818.

[12] Zhang, Y., Deng, H., and Schramm, V. L. **(2010)** Leaving Group Activation and Pyrophosphate Ionic State at the Catalytic Site of Plasmodium falciparum Orotate Phosphoribosyltransferase. *Journal of the American Chemical Society 132*, 17023-17031.

[13] Alhambra, C., Wu, L., Zhang, Z. Y., and Gao, J. L. **(1998)** Walden-inversion-enforced transition-state stabilization in a protein tyrosine phosphatase. *Journal of the American Chemical Society 120*, 3858-3866.

[14] Sigala, P. A., Kraut, D. A., Caaveiro, J. M. M., Pybus, B., Ruben, E. A., Ringe, D., Petsko, G. A., and Herschlag, D. **(2008)** Testing geometrical discrimination within an enzyme active site: Constrained hydrogen bonding in the ketosterold isomerase oxyanion hole. *Journal of the American Chemical Society 130*, 13696-13708.

[15] Tonge, P. J., and Carey, P. R. **(1992)** Forces, Bond Lengths, and Reactivity - Fundamental Insight into the Mechanism of Enzyme Catalysis. *Biochemistry 31*, 9122-9125.

[16] Wilmouth, R. C., Edman, K., Neutze, R., Wright, P. A., Clifton, I. J., Schneider, T. R., Schofield, C. J., and Hajdu, J. **(2001)** X-ray snapshots of serine protease catalysis reveal a tetrahedral intermediate. *Nature Structural Biology 8*, 689-694.

[17] Asher, S. A. **(1988)** Uv Resonance Raman Studies of Molecular-Structure and Dynamics - Applications in Physical and Biophysical Chemistry. *Annual Review of Physical Chemistry 39*, 537-588.

[18] Callender, R., and Deng, H. **(1994)** Nonresonance Raman Difference Spectroscopy - a General Probe of Protein-Structure, Ligand-Binding, Enzymatic Catalysis, and the Structures of Other Biomacromolecules. *Annual Review of Biophysics and Biomolecular Structure 23*, 215-245.

[19] Carey, P. R. **(1999)** Raman spectroscopy, the sleeping giant in structural biology, awakes. *Journal of Biological Chemistry 274*, 26625-26628.

[20] Carey, P. R., and Tonge, P. J. **(1995)** Unlocking the Secrets of Enzyme Power Using Raman-Spectroscopy. *Accounts of Chemical Research 28*, 8-13.

[21] Deng, H., and Callender, R. **(1999)** Raman spectroscopic studies of the structures, energetics, and bond distortions of substrates bound to enzymes. *Enzyme Kinetics and Mechanism, Pt E 308*, 176-201.

[22] Deng, H., Wang, J. H., Callender, R., and Ray, W. J. **(1998)** Relationship between bond stretching frequencies and internal bonding for [O-16(4)]- and [O-18(4)]phosphates in aqueous solution. *Journal of Physical Chemistry B 102*, 3617-3623.

[23] Lehninger, A. L., Cox, M. M., and Nelson, D. L. **(2008)** Lehninger Principles of Biochemistry.

[24] Reginald H. Garrett, and Grisham, C. M. **(2010)** Biochemistry. *4th Edition*.

[25] Biagini, G. A., O'Neill, P. M., Nzila, A., Ward, S. A., and Bray, P. G. **(2003)** Antimalarial chemotherapy: young guns or back to the future? *Trends in Parasitology 19*, 479-487.

[26] Jana, S., and Paliwal, J. **(2007)** Novel molecular targets for antimalarial chemotherapy. *International Journal of Antimicrobial Agents 30*, 4-10.

[27] Wang, C. C. **(1984)** Parasite Enzymes as Potential Targets for Antiparasitic Chemotherapy. *Journal of Medicinal Chemistry 27*, 1-9.

[28] Craig, S. P., and Eakin, A. E. **(1997)** Purine salvage enzymes of parasites as targets for structure-based inhibitor design. *Parasitology Today 13*, 238-241.

[29] Xu, Y. M., Eads, J., Sacchettini, J. C., and Grubmeyer, C. **(1997)** Kinetic mechanism of human hypoxanthine-guanine phosphoribosyltransferase: Rapid phosphoribosyl transfer chemistry. *Biochemistry 36*, 3700-3712.

[30] Keough, D. T., Skinner-Adams, T., Jones, M. K., Ng, A.-L., Brereton, I. M., Guddat, L. W., and de Jersey, J. **(2006)** Lead compounds for antimalarial chemotherapy: Purine base analogs discriminate between human and P-falciparum 6-oxopurine phosphoribosyltransferases. *Journal of Medicinal Chemistry 49*, 7479-7486.

[31] Li, C. M., Tyler, P. C., Furneaux, R. H., Kicska, G., Xu, Y. M., Grubmeyer, C., Girvin, M. E., and Schramm, V. L. **(1999)** Transition-state analogs as inhibitors of human and malarial hypoxanthine-guanine phosphoribosyltransferases. *Nature Structural Biology 6*, 582-587.

[32] Mehrotra, S., and Balaram, H. **(2007)** Kinetic characterization of adenylosuccinate synthetase from the thermophilic archaea methanocaldococcus jannaschii. *Biochemistry 46*, 12821-12832.

[33] Raman, J., Mehrotra, S., Anand, R. P., and Balaram, H. **(2004)** Unique kinetic mechanism of Plasmodium falciparum adenylosuccinate synthetase. *Molecular and Biochemical Parasitology 138*, 1-8.

[34] Gogia, S., Jain, A., and Puranik, M. **(2009)** Structures, Ionization Equilibria, and Tautomerism of 6-Oxopurines in Solution. *Journal of Physical Chemistry B 113*, 15101-15118.

[35] Jayanth, N., Ramachandran, S., and Puranik, M. **(2009)** Solution Structure of the DNA Damage Lesion 8-Oxoguanosine from Ultraviolet Resonance Raman Spectroscopy. *Journal of Physical Chemistry A 113*, 1459-1471.

[36] Wen, Z. Q., and Thomas, G. J. **(1998)** UV resonance Raman spectroscopy of DNA and protein constituents of viruses: Assignments and cross sections for excitations at 257, 244, 238, and 229 nm. *Biopolymers 45*, 247-256.

[37] Fersht, A. **(1999)** Structure and Mechanism in Protein Science. *2nd Edition*.

[38] Benkovic, S. J., and Hammes-Schiffer, S. **(2003)** A perspective on enzyme catalysis. *Science 301*, 1196-1202.

[39] Bruice, T. C., and Benkovic, S. J. **(2000)** Chemical basis for enzyme catalysis. *Biochemistry 39*, 6267-6274.

[40] Kresge, N., Simoni, R. D., and Hill, R. L. **(2010)** The Role of Binding Energy in Catalysis: the Work of William P. Jencks. *Journal of Biology Chemistry 285*.

[41] Fujihashi, M., Ishida, T., Kuroda, S., Kotra, L. P., Pai, E. F., and Miki, K. **(2013)** Substrate Distortion Contributes to the Catalysis of Orotidine 5 '-Monophosphate Decarboxylase. *Journal of the American Chemical Society 135*, 17432-17443.

[42] Bruice, T. C. **(1976)** Some Pertinent Aspects of Mechanism as Determined with Small Molecules. *Annual Review of Biochemistry 45*, 331-373.

[43] Bruice, T. C. **(2002)** A view at the millennium: The efficiency of enzymatic catalysis. *Accounts of Chemical Research 35*, 139-148.

[44] Bruice, T. C. **(2006)** Computational approaches: Reaction trajectories, structures, and atomic motions. Enzyme reactions and proficiency. *Chemical Reviews 106*, 3119-3139.

[45] Bruice, T. C., and Kahn, K. **(2000)** Computational enzymology. *Current Opinion in Chemical Biology 4*, 540-544.

[46] Bruice, T. C., and Lightstone, F. C. **(1999)** Ground state and transition state contributions to the rates of intramolecular and enzymatic reactions. *Accounts of Chemical Research 32*, 127-136.

[47] Lightstone, F. C., and Bruice, T. C. **(1996)** Ground state conformations and entropic and enthalpic factors in the efficiency of intramolecular and enzymatic reactions .1. Cyclic anhydride formation by substituted glutarates, succinate, and 3,6-endoxo-Delta(4)-tetrahydrophthalate monophenyl esters. *Journal of the American Chemical Society 118*, 2595-2605.

[48] Lightstone, F. C., and Bruice, T. C. **(1997)** Separation of ground state and transition state effects in intramolecular and enzymatic reactions .2. A theoretical study of the formation of transition states in cyclic anhydride formation. *Journal of the American Chemical Society 119*, 9103-9113.

[49] Warshel, A. **(1977)** Interpretation of Resonance Raman-Spectra of Biological Molecules. *Annual Review of Biophysics and Bioengineering 6*, 273-300.

[50] Warshel, A. **(1998)** Electrostatic origin of the catalytic power of enzymes and the role of preorganized active sites. *Journal of Biological Chemistry 273*, 27035-27038.

[51] Warshel, A., and Florian, J. **(1998)** Computer simulations of enzyme catalysis: Finding out what has been optimized by evolution. *Proceedings of the National Academy of Sciences of the United States of America 95*, 5950-5955.

[52] Warshel, A., Sharma, P. K., Kato, M., Xiang, Y., Liu, H., and Olsson, M. H. M. **(2006)** Electrostatic basis for enzyme catalysis. *Chemical Reviews 106*, 3210-3235.

[53] Warshel, A., Strajbl, M., Villa, J., and Florian, J. **(2000)** Remarkable rate enhancement of orotidine 5 '-monophosphate decarboxylase is due to transition-state stabilization rather than to ground-state destabilization. *Biochemistry 39*, 14728-14738.

[54] Silva, R. G., Murkin, A. S., and Schramm, V. L. **(2011)** Femtosecond dynamics coupled to chemical barrier crossing in a Born-Oppenheimer enzyme. *Proceedings of the National Academy of Sciences of the United States of America 108*, 18661-18665.

[55] Schwartz, S. D., and Schramm, V. L. **(2009)** Enzymatic transition states and dynamic motion in barrier crossing. *Nature Chemical Biology 5*, 552-559.

[56] Deng, H., Lewandowicz, A., Schramm, V. L., and Callender, R. **(2004)** Activating the phosphate nucleophile at the catalytic site of purine nucleoside phosphorylase: A vibrational spectroscopic study. *Journal of the American Chemical Society 126*, 9516-9517.

[57] Lewandowicz, A., Shi, W. X., Evans, G. B., Tyler, P. C., Furneaux, R. H., Basso, L. A., Santos, D. S., Almo, S. C., and Schramm, V. L. **(2003)** Over-the-barrier transition state analogues and crystal structure with Mycobacterium tuberculosis purine nucleoside phosphorylase. *Biochemistry 42*, 6057-6066.

[58] Murkin, A. S., Tyler, P. C., and Schramm, V. L. **(2008)** Transition-state interactions revealed in purine nucleoside phosphorylase by binding isotope effects. *Journal of the American Chemical Society 130*, 2166-+.

[59] Schramm, V. L. **(2005)** Enzymatic transition states: thermodynamics, dynamics and analogue design. *Archives of Biochemistry and Biophysics 433*, 13-26.

[60] Schramm, V. L. **(2002)** Development of transition state analogues of purine nucleoside phosphorylase as anti-T-cell agents. *Biochimica Et Biophysica Acta-Molecular Basis of Disease 1587*, 107-117.

[61] Schramm, V. L. **(2013)** Transition States, Analogues, and Drug Development. *Acs Chemical Biology 8*, 71-81.

[62] Salerno, C., and Giacomello, A. **(1981)** Human Hypoxanthine Guanine Phosphoribosyltransferase - the Role of Magnesium-Ion in a Phosphoribosylpyrophosphate-Utilizing Enzyme. *Journal of Biological Chemistry 256*, 3671-3673.

[63] Musick, W. D. L. **(1981)** Structural Features of the Phosphoribosyltransferases and Their Relationship to the Human Deficiency Disorders of Purine and Pyrimidine Metabolism. *Crc Critical Reviews in Biochemistry 11*, 1-34.

[64] Gutensohn, W., Huber, M., and Jahn, H. **(1976)** Facilitated Purification of Hypoxanthine Phosphoribosyltransferase. *Hoppe-Seylers Zeitschrift Fur Physiologische Chemie 357*, 1379-1385.

[65] Holmes, E. W., Wyngaard.Jb, and Kelley, W. N. **(1973)** Human Glutamine Phosphoribosylpyrophosphate Amidotransferase - 2 Molecular Forms Interconvertible by Purine Ribonucleotides and Phosphoribosylpyrophosphate. *Journal of Biological Chemistry 248*, 6035-6040.

[66] Krenitsky.T. A, Papaioan.R, and Elion, G. B. **(1969)** Human Hypoxanthine Phosphoribosyltransferase .I. Purification Properties and Specificity. *Journal of Biological Chemistry 244*, 1263-&.

[67] Packman, P. M., and Jakoby, W. B. **(1965)** Crystalline Quinolinate Phosphoribosyltransferase. *Journal of Biological Chemistry 240*, 4107-&.

[68] Patel, P. I., Framson, P. E., Caskey, C. T., and Chinault, A. C. **(1986)** Fine-Structure of the Human Hypoxanthine Phosphoribosyltransferase Gene. *Molecular and Cellular Biology 6*, 393-403.

[69] Kohler, G., and Milstein, C. **(1975)** Continuous Cultures of Fused Cells Secreting Antibody of Predefined Specificity. *Nature 256*, 495-497.

[70] Kohler, G., and Milstein, C. **(2005)** Continuous cultures of fused cells secreting antibody of predefined specificity (Reprinted from Nature, vol 256, 1975). *Journal of Immunology 174*, 2453-2455.

[71] Hovejensen, B., Harlow, K. W., King, C. J., and Switzer, R. L. **(1986)** Phosphoribosylpyrophosphate Synthetase of Escherichia-Coli - Properties of the Purified Enzyme and Primary Structure of the Prs Gene. *Journal of Biological Chemistry 261*, 6765-6771.

[72] Wilson, J. M., Tarr, G. E., and Kelley, W. N. **(1983)** Human Hypoxanthine (Guanine) Phosphoribosyltransferase - an Amino-Acid Substitution in a Mutant Form of the Enzyme Isolated from a Patient with Gout. *Proceedings of the National Academy of Sciences of the United States of America-Biological Sciences 80*, 870-873.

[73] Wilson, J. M., Young, A. B., Kelley, W. N., Braunwald, E., Robinson, S. H., Grossman, W., Ingbar, S. H., Epstein, Einhorn, D., Rosa, R. M., Landsberg, L. L., Markis, J. E., and Spark, R. F. **(1983)** Hypoxanthine-Guanine Phosphoribosyltransferase Deficiency - the Molecular-Basis of the Clinical Syndromes. *New England Journal of Medicine 309*, 900-910.

[74] Shi, W. X., Li, C. M., Tyler, P. C., Furneaux, R. H., Cahill, S. M., Girvin, M. E., Grubmeyer, C., Schramm, V. L., and Almo, S. C. **(1999)** The 2.0 angstrom structure of malarial purine phosphoribosyltransferase in complex with a transition-state analogue inhibitor. *Biochemistry 38*, 9872-9880.

[75] Keough, D. T., Ng, A. L., Winzor, D. J., Emmerson, B. T., and de Jersey, J. **(1999)** Purification and characterization of Plasmodium falciparum hypoxanthine-guanine-xanthine phosphoribosyltransferase and comparison with the human enzyme. *Molecular and Biochemical Parasitology 98*, 29-41.

[76] Focia, P. J., Craig, S. P., and Eakin, A. E. **(1998)** Approaching the transition state in the crystal structure of a phosphoribosyltransferase. *Biochemistry 37*, 17120-17127.

[77] Focia, P. J., Craig, S. P., Nieves-Alicea, R., Fletterick, R. J., and Eakin, A. E. **(1998)** A 1.4 angstrom crystal structure for the hypoxanthine phosphoribosyltransferase of Trypanosoma cruzi. *Biochemistry 37*, 15066-15075.

[78] Heroux, A., White, E. L., Ross, L. J., and Borhani, D. W. **(1999)** Crystal structures of the Toxoplasma gondii hypoxanthine-guanine phosphoribosyltransferase-GMP and -IMP complexes: Comparison of purine binding interactions with the XMP complex. *Biochemistry 38*, 14485-14494.

[79] Heroux, A., White, E. L., Ross, L. J., Davis, R. L., and Borhani, D. W. **(1999)** Crystal structure of Toxoplasma gondii hypoxanthine-guanine phosphoribosyltransferase with XMP, pyrophosphate, and two Mg2+ ions bound: Insights into the catalytic mechanism. *Biochemistry 38*, 14495-14506.

[80] Heroux, A., White, E. L., Ross, L. J., Kuzin, A. P., and Borhani, D. W. **(2000)** Substrate deformation in a hypoxanthine-guanine phosphoribosyltransferase ternary complex: The structural basis for catalysis. *Structure 8*, 1309-1318.

[81] Munagala, N., Basus, V. J., and Wang, C. C. **(2001)** Role of the flexible loop of hypoxanthine-guanine-xanthine phosphoribosyltransferase from Tritrichomonas foetus in enzyme catalysis. *Biochemistry 40*, 4303-4311.

[82] Pitera, J. W., Munagala, N. R., Wang, C. C., and Kollman, P. A. **(1999)** Understanding substrate specificity in human and parasite phosphoribosyltransferases through calculation and experiment. *Biochemistry 38*, 10298-10306.

[83] Thomas, A., and Field, M. J. **(2002)** Reaction mechanism of the HGXPRTase from Plasmodium falciparum: A hybrid potential quantum mechanical/molecular mechanical study. *Journal of the American Chemical Society 124*, 12432-12438.

[84] Thomas, A., and Field, M. J. **(2006)** A comparative QM/MM simulation study of the reaction mechanisms of human and Plasmodium falciparum HG(X) PRTases. *Journal of the American Chemical Society 128*, 10096-10102.

[85] Wenck, M. A., Medrano, F. J., Eakin, A. E., and Craig, S. P. **(2004)** Steady-state kinetics of the hypoxanthine phosphoribosyltransferase from Trypanosoma cruzi. *Biochimica Et Biophysica Acta-Proteins and Proteomics 1700*, 11-18.

[86] Jardim, A., and Ullman, B. **(1997)** The conserved serine-tyrosine dipeptide in Leishmania donovani hypoxanthine-guanine phosphoribosyltransferase is essential for catalytic activity. *Journal of Biological Chemistry 272*, 8967-8973.

[87] Goodstadt, L., and Ponting, C. P. **(2001)** CHROMA: consensus-based colouring of multiple alignments for publication. *Bioinformatics 17*, 845-846.

[88] Shi, W. X., Li, C. M., Tyler, P. C., Furneaux, R. H., Grubmeyer, C., Schramm, V. L., and Almo, S. C. **(1999)** The 2.0 angstrom structure of human hypoxanthineguanine phosphoribosyltransferase in complex with a transition-state analog inhibitor. *Nature Structural Biology 6*, 588-593.

[89] Xu, Y. M., and Grubmeyer, C. **(1998)** Catalysis in human hypoxanthine-guanine phosphoribosyltransferase: Asp 137 acts as a general acid/base. *Biochemistry 37*, 4114-4124.

[90] Eads, J. C., Scapin, G., Xu, Y. M., Grubmeyer, C., and Sacchettini, J. C. **(1994)** The Crystal-Structure of Human Hypoxanthine-Guanine Phosphoribosyltransferase with Bound Gmp. *Cell 78*, 325-334.

[91] Hazleton, K. Z., Ho, M.-C., Cassera, M. B., Clinch, K., Crump, D. R., Rosario, I., Jr., Merino, E. F., Almo, S. C., Tyler, P. C., and Schramm, V. L. **(2012)** Acyclic Immucillin Phosphonates: Second-Generation Inhibitors of Plasmodium falciparum Hypoxanthine-Guanine-Xanthine Phosphoribosyltransferase. *Chemistry & Biology 19*, 721-730.

[92] Rosenthal, P. J. **(2003)** Antimalarial drug discovery: old and new approaches. *Journal of Experimental Biology 206*, 3735-3744.

[93] Honzatko, R. B., and Fromm, H. J. **(1999)** Structure-function studies of adenylosuccinate synthetase from Escherichia coli. *Archives of Biochemistry and Biophysics 370*, 1-8.

[94] Choe, J. Y., Poland, B. W., Fromm, H. J., and Honzatko, R. B. **(1999)** Mechanistic implications from crystalline complexes of wild-type and mutant adenylosuccinate synthetases from Escherichia coli. *Biochemistry 38*, 6953-6961.

[95] Eaazhisai, K., Jayalakshmi, R., Gayathri, P., Anand, R. P., Sumathy, K., Balaram, H., and Murthy, M. R. N. **(2004)** Crystal structure of fully ligated adenylosuccinate synthetase from Plasmodium falciparum. *Journal of Molecular Biology 335*, 1251-1264.

[96] Honzatko, R. B., Stayton, M. M., and Fromm, H. J. **(1999)** Adenylosuccinate synthetase: Recent developments. *Advances in Enzymology, Vol 73 73*, 57-102.

[97] Stayton, M. M., Rudolph, F. B., and Fromm, H. J. **(1983)** Regulation, Genetics, and Properties of Adenylosuccinate Synthetase - a Review. *Current Topics in Cellular Regulation 22*, 103-141.

[98] Borza, T., Iancu, C. V., Pike, E., Honzatko, R. B., and Fromm, H. J. **(2003)** Variations in the response of mouse isozymes of adenylosuccinate synthetase to inhibitors of physiological relevance. *Journal of Biological Chemistry 278*, 6673-6679.

[99] Iancu, C. V., Zhou, Y., Borza, T., Fromm, H. J., and Honzatko, R. B. **(2006)** Cavitation as a mechanism of substrate discrimination by adenylosuccinate synthetases. *Biochemistry 45*, 11703-11711.

[100] Siehl, D. L., Subramanian, M. V., Walters, E. W., Lee, S. F., Anderson, R. J., and Toschi, A. G. **(1996)** Adenylosuccinate synthetase: Site of action of hydantocidin, a microbial phytotoxin. *Plant Physiology 110*, 753-758.

[101] Wang, W. Y., Gorrell, A., Honzatko, R. B., and Fromm, H. J. **(1997)** A study of Escherichia coli adenylosuccinate synthetase association states and the

interface residues of the homodimer. *Journal of Biological Chemistry 272*, 7078-7084.

[102] Wang, W. Y., Hou, Z. L., Honzatko, R. B., and Fromm, H. J. **(1997)** Relationship of conserved residues in the IMP binding site to substrate recognition and catalysis in Escherichia coli adenylosuccinate synthetase. *Journal of Biological Chemistry 272*, 16911-16916.

[103] Kang, C. H., Sun, N., Poland, B. W., Gorrell, A., Honzatko, R. B., and Fromm, H. J. **(1997)** Residues essential for catalysis and stability of the active site of Escherichia coli adenylosuccinate synthetase as revealed by directed mutation and kinetics. *Journal of Biological Chemistry 272*, 11881-11885.

[104] Ryzhova, T. A., Andreichuk, Y. V., and Domkin, V. D. **(1998)** Adenylosuccinate synthetase of the yeast Saccharomyces cerevisiae: Purification and properties. *Biochemistry-Moscow 63*, 650-656.

[105] Kang, C. H., and Fromm, H. J. **(1994)** Characterization of the Putative Gtp-Binding Site Residues of Escherichia-Coli Adenylosuccinate Synthetase by Site-Directed Mutagenesis. *Archives of Biochemistry and Biophysics 310*, 475-480.

[106] Hou, Z. L., Wang, W. Y., Fromm, H. J., and Honzatko, R. B. **(2002)** IMP alone organizes the active site of adenylosuccinate synthetase from Escherichia coli. *Journal of Biological Chemistry 277*, 5970-5976.

[107] Iancu, C. V., Borza, T., Fromm, H. J., and Honzatko, R. B. **(2002)** Feedback inhibition and product complexes of recombinant mouse muscle adenylosuccinate synthetase. *Journal of Biological Chemistry 277*, 40536-40543.

[108] Clark, S. W., and Rudolph, F. B. **(1976)** Regulation of Purine Metabolism - Adenylosuccinate Synthetase from Novikoff Ascites Tumor-Cells. *Biochimica Et Biophysica Acta 437*, 87-93.

[109] Poland, B. W., Fromm, H. J., and Honzatko, R. B. **(1996)** Crystal structures of adenylosuccinate synthetase from Escherichia coli complexed with GDP, IMP hadacidin, NO3- and Mg2+. *Journal of Molecular Biology 264*, 1013-1027.

[110] Poland, B. W., Hou, Z. L., Bruns, C., Fromm, H. J., and Honzatko, R. B. **(1996)** Refined crystal structures of guanine nucleotide complexes of adenylosuccinate synthetase from Escherichia coli. *Journal of Biological Chemistry 271*, 15407-15413.

[111] Lieberman, I. **(1956)** Enzymatic synthesis of adenosine-5'-phosphate from inosine-5'-phosphate. *Journal of Biological Chemistry 223*, 327-339.

[112] Miller, R. W., and M.Buchanan, J. **(1962)** Biosynthesis of purines. *Journal of Biological Chemistry 237*, 485-490.

[113] Markham, G. D., and Reed, G. H. **(1978)** Reactions of Phosphorothioate Compounds Catalyzed by Adenylosuccinate Synthetase - Steady-State and

Pre-Steady State Kinetic Studies. *Journal of Biological Chemistry 253*, 6184-6189.

[114] Bass, M. B., Fromm, H. J., and Rudolph, F. B. **(1984)** The Mechanism of the Adenylosuccinate Synthetase Reaction as Studied by Positional Isotope Exchange. *Journal of Biological Chemistry 259*, 2330-2333.

[115] Mehrotra, S., and Balaram, H. **(2008)** Methanocaldococcus jannaschii adenylosuccinate synthetase: Studies on temperature dependence of catalytic activity and structural stability. *Biochimica Et Biophysica Acta-Proteins and Proteomics 1784*, 2019-2028.

[116] Ogawa, T., Ueda, Y., Yoshimura, K., and Shigeoka, S. **(2005)** Comprehensive analysis of cytosolic nudix hydrolases in Arabidopsis thaliana. *Journal of Biological Chemistry 280*, 25277-25283.

[117] Lipps, G., and Krauss, G. **(1999)** Adenylosuccinate synthase from Saccharomyces cerevisiae: homologous overexpression, purification and characterization of the recombinant protein. *Biochemical Journal 341*, 537-543.

[118] Fields, P. A. **(2001)** Review: Protein function at thermal extremes: balancing stability and flexibility. *Comparative Biochemistry and Physiology a-Molecular and Integrative Physiology 129*, 417-431.

[119] Georlette, D., Damien, B., Blaise, V., Depiereux, E., Uversky, V. N., Gerday, C., and Feller, G. **(2003)** Structural and functional adaptations to extreme temperatures in psychrophilic, mesophilic, and thermophilic DNA ligases. *Journal of Biological Chemistry 278*, 37015-37023.

[120] Jaenicke, R. **(1991)** Protein Stability and Molecular Adaptation to Extreme Conditions. *European Journal of Biochemistry 202*, 715-728.

[121] Vihinen, M. **(1987)** Relationship of Protein Flexibility to Thermostability. *Protein Engineering 1*, 477-480.

[122] Zavodszky, P., Kardos, J., Svingor, A., and Petsko, G. A. **(1998)** Adjustment of conformational flexibility is a key event in the thermal adaptation of proteins. *Proceedings of the National Academy of Sciences of the United States of America 95*, 7406-7411.

[123] Silva, M. M., Poland, B. W., Hoffman, C. R., Fromm, H. J., and Honzatko, R. B. **(1995)** Refined Crystal-Structures of Unligated Adenylosuccinate Synthetase from Escherichia-Coli. *Journal of Molecular Biology 254*, 431-446.

[124] Mehrotra, S., Mylarappa, B. N., Iyengar, P., and Balaram, H. **(2010)** Studies on active site mutants of P-falciparum adenylosuccinate synthetase: Insights into enzyme catalysis and activation. *Biochimica Et Biophysica Acta-Proteins and Proteomics 1804*, 1996-2002.

[125] Weber, J. L. **(1987)** Analysis of Sequences from the Extremely a+T-Rich Genome of Plasmodium-Falciparum. *Gene 52*, 103-109.

[126] Kippen, A. D., Sancho, J., and Fersht, A. R. **(1994)** Folding of Barnase in Parts. *Biochemistry 33*, 3778-3786.

[127] Hawkins, P. C. D., Warren, G. L., Skillman, A. G., and Nicholls, A. **(2008)** How to do an evaluation: pitfalls and traps. *Journal of Computer-Aided Molecular Design 22*, 179-190.

[128] Boehr, D. D., Dyson, H. J., and Wright, P. E. **(2006)** An NMR perspective on enzyme dynamics. *Chemical Reviews 106*, 3055-3079.

[129] Damblon, C., Raquet, X., Lian, L. Y., LamotteBrasseur, J., Fonze, E., Charlier, P., Roberts, G. C. K., and Frere, J. M. **(1996)** The catalytic mechanism of beta-lactamases: NMR titration of an active-site lysine residue of the TEM-1 enzyme. *Proceedings of the National Academy of Sciences of the United States of America 93*, 1747-1752.

[130] Carlomagno, T. (2005) Ligand-target interactions: What can we learn from NMR?, in *Annual Review of Biophysics and Biomolecular Structure* pp 245-266.

[131] Feng, W., Pan, L., and Zhang, M. **(2011)** Combination of NMR spectroscopy and X-ray crystallography offers unique advantages for elucidation of the structural basis of protein complex assembly. *Science China-Life Sciences 54*, 101-111.

[132] Wagner, G. **(1997)** An account of NMR in structural biology. *Nature Structural Biology 4*, 841-844.

[133] Deng, H., Wang, J. H., Callender, R. H., Grammer, J. C., and Yount, R. G. **(1998)** Raman difference spectroscopic studies of the myosin S1 center dot MgADP vanadate complex. *Biochemistry 37*, 10972-10979.

[134] Wang, J. H., Xiao, D. G., Deng, H., Webb, M. R., and Callender, R. **(1998)** Raman difference studies of GDP and GTP binding to c-Harvey ras. *Biochemistry 37*, 11106-11116.

[135] Deng, H., and Callender, R. **(1998)** Structure of dihydrofolate when bound to dihydrofolate reductase. *Journal of the American Chemical Society 120*, 7730-7737.

[136] Deng, H., Kurz, L. C., Rudolph, F. B., and Callender, R. **(1998)** Characterization of hydrogen bonding in the complex of adenosine deaminase with a transition state analogue: A Raman spectroscopic study. *Biochemistry 37*, 4968-4976.

[137] Dinakarpandian, D., Shenoy, B., PusztaiCarey, M., Malcolm, B. A., and Carey, P. R. **(1997)** Active site properties of the 3C proteinase from hepatitis A virus (a hybrid cysteine/serine protease) probed by Raman spectroscopy. *Biochemistry 36*, 4943-4948.

[138] Carey, P. R. (2006) Raman crystallography and other biochemical applications of Raman microscopy, in *Annual Review of Physical Chemistry* pp 527-554.

[139] Sahoo, S. K., Umapathy, S., and Parker, A. W. **(2011)** Time-Resolved Resonance Raman Spectroscopy: Exploring Reactive Intermediates. *Applied Spectroscopy 65*, 1087-1115.

[140] Nibbering, E. T. J., Fidder, H., and Pines, E. (2005) Ultrafast chemistry: Using time-resolved vibrational spectroscopy for interrogation of structural dynamics, in *Annual Review of Physical Chemistry* pp 337-367.

[141] Moore, J. N., Hansen, P. A., and Hochstrasser, R. M. **(1988)** Iron Carbonyl Bond Geometries of Carboxymyoglobin and Carboxyhemoglobin in Solution Determined by Picosecond Time-Resolved Infrared-Spectroscopy. *Proceedings of the National Academy of Sciences of the United States of America 85*, 5062-5066.

[142] Braiman, M. S., Bousche, O., and Rothschild, K. J. **(1991)** Protein Dynamics in the Bacteriorhodopsin Photocycle - Submillisecond Fourier-Transform Infrared-Spectra of the L-Photointermediates, M-Photointermediates, and N-Photointermediates. *Proceedings of the National Academy of Sciences of the United States of America 88*, 2388-2392.

[143] Thoenges, D., and Barth, A. **(2002)** Direct measurement of enzyme activity with infrared spectroscopy. *Journal of Biomolecular Screening 7*, 353-357.

[144] Deng, H., Callender, R., Schramm, V. L., and Grubmeyer, C. **(2010)** Pyrophosphate Activation in Hypoxanthine-Guanine Phosphoribosyltransferase with Transition State Analogue. *Biochemistry 49*, 2705-2714.

[145] Zanni, M. T., and Hochstrasser, R. M. **(2001)** Two-dimensional infrared spectroscopy: a promising new method for the time resolution of structures. *Current Opinion in Structural Biology 11*, 516-522.

[146] Singh, R. **(2002)** C. V. Raman and the discovery of the Raman effect. *Physics in Perspective 4*, 399-420.

[147] Friedrich, S., and Peter, H. **(2008)** Vibrational Spectroscopy in Life Sciences.

[148] Kim, M., Owen, H., and Carey, P. R. **(1993)** High-Performance Raman-Spectroscopic System Based on a Single Spectrograph, Ccd, Notch Filters, and a Kr+ Laser Ranging from the near-Ir to near-Uv Regions. *Applied Spectroscopy 47*, 1780-1783.

[149] Frisch, M. J., Trucks, G. W., Schlegel, H. B., Scuseria, G. E., Robb, M. A., Cheeseman, J. R., Scalmani, G., Barone, V., Mennucci, B., Petersson, G. A., Nakatsuji, H., Caricato, M., Li, X., Hratchian, H. P., Izmaylov, A. F., Bloino, J., Zheng, G., Sonnenberg, J. L., Hada, M., Ehara, M., Toyota, K., Fukuda, R., Hasegawa, J., Ishida, M., Nakajima, T., Honda, Y., Kitao, O., Nakai, H., Vreven, T., Montgomery, J. A., Jr., Peralta, J. E., Ogliaro, F., Bearpark, M., Heyd, J. J., Brothers, E., Kudin, K. N., Staroverov, V. N., Kobayashi, R., Normand, J., Raghavachari, K., Rendell, A., Burant, J. C., Iyengar, S. S., Tomasi, J., Cossi, M., Rega, N., Millam, M. J., Klene, M., Knox, J. E., Cross, J. B., Bakken, V., Adamo, C., Jaramillo, J., Gomperts, R., Stratmann, R. E., Yazyev, O., Austin, A. J., Cammi, R., Pomelli, C., Ochterski, J. W., Martin, R. L., Morokuma, K., Zakrzewski, V. G., Voth, G. A., Salvador, P.,

Dannenberg, J. J., Dapprich, S., Daniels, A. D., Farkas, Ö., Foresman, J. B., Ortiz, J. V., Cioslowski, J., and Fox, D. J. G., Revision D.01. **(2009)** Gaussian, Inc., Wallingford CT.

[150] Kim, M., and Carey, P. R. **(1993)** Observation of a Carbonyl Feature for Riboflavin Bound to Riboflavin-Binding Protein in the Red-Excited Raman-Spectrum. *Journal of the American Chemical Society 115*, 7015-7016.

[151] Doran, J. D., and Carey, P. R. **(1996)** alpha-helix dipoles and catalysis: Absorption and Raman spectroscopic studies of acyl cysteine proteases. *Biochemistry 35*, 12495-12502.

[152] Blackwood, M. E., Rush, T. S., Romesberg, F., Schultz, P. G., and Spiro, T. G. **(1998)** Alternative modes of substrate distortion in enzyme and antibody catalyzed ferrochelation reactions. *Biochemistry 37*, 779-782.

[153] Hu, S. Z., Smith, K. M., and Spiro, T. G. **(1996)** Assignment of protoheme Resonance Raman spectrum by heme labeling in myoglobin. *Journal of the American Chemical Society 118*, 12638-12646.

[154] Kitagawa, T., and Mizutani, Y. **(1994)** Resonance Raman-Spectra of Highly Oxidized Metalloporphyrins and Heme-Proteins. *Coordination Chemistry Reviews 135*, 685-735.

[155] Dong, S. L., and Spiro, T. G. **(1998)** Ground- and excited-state mapping of plastocyanin from resonance Raman spectra of isotope-labeled proteins. *Journal of the American Chemical Society 120*, 10434-10440.

[156] Macclement, B. A. E., Carriere, R. G., Phelps, D. J., and Carey, P. R. **(1981)** Evidence for 2 Acyl Group Conformations in Some Furylacryloylchymotrypsins and Thienylacryloylchymotrypsins - Resonance Raman Studies of Enzyme-Substrate Intermediates at Ph 3.0. *Biochemistry 20*, 3438-3447.

[157] Phelps, D. J., Schneider, H., and Carey, P. R. **(1981)** Correlations between Reactivity and Structure of Some Chromophoric Acylchymotrypsins by Resonance Raman-Spectroscopy. *Biochemistry 20*, 3447-3454.

[158] Carey, P. R., and Phelps, D. J. **(1983)** Vibrations of the Scissile C-O Bond in an Acyl-Chymotrypsin Observed by Resonance Raman-Spectroscopy. *Canadian Journal of Chemistry-Revue Canadienne De Chimie 61*, 2590-2595.

[159] Gill, D., Kilponen, R. G., and Rimai, L. **(1970)** Resonance Raman Scattering of Laser Radiation by Vibrational Modes of Carotenoid Pigment Molecules in Intact Plant Tissues. *Nature 227*, 743-&.

[160] Spiro, T. G. **(1974)** Resonance Raman-Spectroscopy - New Structure Probe for Biological Chromophores. *Accounts of Chemical Research 7*, 339-344.

[161] Huang, C. Y., Balakrishnan, G., and Spiro, T. G. **(2006)** Protein secondary structure from deep-UV resonance Raman spectroscopy. *Journal of Raman Spectroscopy 37*, 277-282.

[162] Fodor, S. P. A., Rava, R. P., Hays, T. R., and Spiro, T. G. **(1985)** Ultraviolet Resonance Raman-Spectroscopy of the Nucleotides with 266-Nm, 240-Nm, 218-Nm, and 200-Nm Pulsed Laser Excitation. *Journal of the American Chemical Society 107*, 1520-1529.

[163] Kubasek, W. L. **(1985)** Ultraviolet Resonance Raman Excitation Profiles of Nucleic-Acid Bases with Excitation from 200 to 300 Nanometers. *Biophysical Journal 47*, A69-A69.

[164] Kubasek, W. L., Hudson, B., and Peticolas, W. L. **(1985)** Ultraviolet Resonance Raman Excitation Profiles of Nucleic-Acid Bases with Excitation from 200-Nanometers to 300-Nanometers. *Proceedings of the National Academy of Sciences of the United States of America 82*, 2369-2373.

[165] Wang, Y., and Peticolas, W. L. **(1987)** A New Oxygen-Mediated Photoreaction of Uracil and Thymine in Aqueous-Solution Detected by Ultraviolet Resonance Raman-Scattering. *Journal of Physical Chemistry 91*, 3122-3124.

[166] Ernzerhof, M., and Scuseria, G. E. **(2000)** Perspective on "Inhomogeneous electron gas" - Hohenberg P, Kohn W (1964) Physical Reviews 136 : B864. *Theoretical Chemistry Accounts 103*, 259-262.

[167] Aqvist, J., and Warshel, A. **(1993)** Simulation of Enzyme-Reactions Using Valence-Bond Force-Fields and Other Hybrid Quantum-Classical Approaches. *Chemical Reviews 93*, 2523-2544.

[168] Gao, J. L. **(2000)** Perspective on "Theoretical studies of enzymic reactions: dielectric, electrostatic and steric stabilization of the carbonium ion in the reaction of lysozyme" - Warshel A, Levitt M (1976) J Mol Biol 103 : 227-249. *Theoretical Chemistry Accounts 103*, 328-329.

[169] Kamerlin, S. C. L., and Warshel, A. **(2009)** At the dawn of the 21st century: Is dynamics the missing link for understanding enzyme catalysis? *Proteins-Structure Function and Bioinformatics 78*, 1339-1375.

[170] Giese, B., and McNaughton, D. **(2002)** Density functional theoretical (DFT) and surface-enhanced Raman spectroscopic study of guanine and its alkylated derivatives - Part 1. DFT calculations on neutral, protonated and deprotonated guanine. *Physical Chemistry Chemical Physics 4*, 5161-5170.

[171] Giese, B., and McNaughton, D. **(2002)** Density functional theoretical (DFT) and surface-enhanced Raman spectroscopic study of guanine and its alkylated derivatives - Part 2: Surface-enhanced Raman scattering on silver surfaces. *Physical Chemistry Chemical Physics 4*, 5171-5182.

[172] Parker, S. F., Jeans, R., and Devonshire, R. **(2004)** Inelastic neutron scattering, Raman spectroscopy and periodic DFT study of purine. *Vibrational Spectroscopy 35*, 173-177.

[173] Toyama, A., Hanada, N., Abe, Y., Takeuchi, H., and Harada, I. **(1994)** Assignment of Adenine Ring Inplane Vibrations in Adenosine on the Basis of N-15 and C-13 Isotopic Frequency-Shifts and Uv Resonance Raman Enhancement. *Journal of Raman Spectroscopy 25*, 623-630.

[174] Subbayya, I. N. S., Sukumaran, S., Shivashankar, K., and Balaram, H. **(2000)** Unusual substrate specificity of a chimeric hypoxanthine-guanine phosphoribosyltransferase containing segments from the Plasmodium falciparum and human enzymes. *Biochemical and Biophysical Research Communications 272*, 596-602.

[175] Subbayya, I. N. S., and Balaram, H. **(2000)** Evidence for multiple active states of Plasmodium falciparum hypoxanthine-guanine-xanthine phosphoribosyltransferase. *Biochemical and Biophysical Research Communications 279*, 433-437.

[176] Raman, J., Sumathy, K., Anand, R. P., and Balaram, H. **(2004)** A non-active site mutation in human hypoxanthine guanine phosphoribosyltransferase expands substrate specificity. *Archives of Biochemistry and Biophysics 427*, 116-122.

[177] Jayalakshmi, R., Sumathy, K., and Balaram, H. **(2002)** Purification and characterization of recombinant Plasmodium falciparum adenylosuccinate synthetase expressed in Escherichia coli. *Protein Expression and Purification 25*, 65-72.

[178] Ferraro, J. R., and Nakamaoto, K. **(1994)** Introductory Raman spectroscopy. *Edition 1st*.

[179] Minenkov, Y., Singstad, A., Occhipinti, G., and Jensen, V. R. **(2012)** The accuracy of DFT-optimized geometries of functional transition metal compounds: a validation study of catalysts for olefin metathesis and other reactions in the homogeneous phase. *Dalton Transactions 41*, 5526-5541.

[180] Jamroz, M. H. **(2004)** Vibrational Energy Distribution Analysis VEDA 4, Warsaw.

[181] Wierzchowski, J., Bzowska, A., Stepniak, K., and Shugar, D. **(2004)** Interactions of calf spleen purine nucleoside phosphorylase with 8-azaguanine, and a bisubstrate analogue inhibitor: Implications for the reaction mechanism. *Zeitschrift Fur Naturforschung C-a Journal of Biosciences 59*, 713-725.

[182] Wierzchowski, J., Medza, G., Sepiol, J., Szabelski, M., and Shugar, D. **(1996)** Fluorescence emission properties of 8-azaisoguanine and its N-methyl derivatives: Ground- and excited-state tautomerism. *Journal of Photochemistry and Photobiology a-Chemistry 237*, 64-70.

[183] Wierzchowski, J., Stepniak, K., Bzowska, A., and Shugar, D. **(2005)** Spectroscopic and kinetic studies of interactions of calf spleen purine nucleoside phosphorylase with 8-azaguanine, and its 9-(2-phosphonylmethoxyethyl) derivative. *Nucleosides Nucleotides & Nucleic Acids 24*, 459-464.

[184] Wierzchowski, J., WielgusKutrowska, B., and Shugar, D. **(1996)** Fluorescence emission properties of 8-azapurines and their nucleosides, and application to the kinetics of the reverse synthetic reaction of purine nucleoside phosphorylase. *Biochimica Et Biophysica Acta-General Subjects 1290*, 9-17.

[185] Hikishima, S., Hashimoto, M., Magnowska, L., Bzowska, A., and Yokomatsu, T. **(2007)** Synthesis and biological evaluation of 9-deazaguanine derivatives connected by a linker to difluoromethylene phosphonic acid as multi-substrate analogue inhibitors of PNP. *Bioorganic & Medicinal Chemistry Letters 17*, 4173-4177.

[186] Kolossavary, I., and Guida, W. C. **(1999)** Low-mode conformational search elucidated: Application to C39H80 and flexible docking of 9-deazaguanine inhibitors into PNP. *Journal of Computational Chemistry 20*, 1671-1684.

[187] Keough, D. T., Hockova, D., Krecmerova, M., Cesnek, M., Holy, A., Naesens, L., Brereton, I. M., Winzor, D. J., de Jersey, J., and Guddat, L. W. **(2010)** Plasmodium vivax hypoxanthine-guanine phosphoribosyltransferase: A target for anti-malarial chemotherapy. *Molecular and Biochemical Parasitology 173*, 165-169.

[188] Mikleusevic, G., Stefanic, Z., Narczyk, M., Wielgus-Kutrowska, B., Bzowska, A., and Luic, M. **(2011)** Validation of the catalytic mechanism of Escherichia coli purine nucleoside phosphorylase by structural and kinetic studies. *Biochimie 93*, 1610-1622.

[189] Wielgus-Kutrowska, B., Antosiewicz, J. M., Dlugosz, M., Holy, A., and Bzowska, A. **(2007)** Towards the mechanism of trimeric purine nucleoside phosphorylases: Stopped-flow studies of binding of multisubstrate analogue inhibitor - 2-amino-9-[2-(phosphonomethoxy)ethyl]-6-sulfanylpurine. *Biophysical Chemistry 125*, 260-268.

[190] Wielgus-Kutrowska, B., and Bzowska, A. **(2006)** Probing the mechanism of purine nucleoside phosphorylase by steady-state kinetic studies and ligand binding characterization determined by fluorimetric titrations. *Biochimica Et Biophysica Acta-Proteins and Proteomics 1764*, 887-902.

[191] Stein, J. M., Stoeckler, J. D., Li, S. Y., Tolman, R. L., Maccoss, M., Chen, A., Karkas, J. D., Ashton, W. T., and Parks, R. E. **(1987)** Inhibition of Human Purine Nucleoside Phosphorylase by Acyclic Nucleosides and Nucleotides. *Biochemical Pharmacology 36*, 1237-1244.

[192] Stoeckler, J. D., Ryden, J. B., Parks, R. E., Chu, M. Y., Lim, M. I., Ren, W. Y., and Klein, R. S. **(1986)** Inhibitors of Purine Nucleoside Phosphorylase - Effects of 9-Deazapurine Ribonucleosides and Synthesis of 5'-Deoxy-5'-Iodo-9-Deazainosine. *Cancer Research 46*, 1774-1778.

[193] Gogia, S., Balaram, H., and Puranik, M. **(2011)** Hypoxanthine Guanine Phosphoribosyltransferase Distorts the Purine Ring of Nucleotide Substrates and Perturbs the pK(a) of Bound Xanthosine Monophosphate. *Biochemistry 50*, 4184-4193.

[194] Shanmugasundaram, M., and Puranik, M. **(2009)** Computational prediction of vibrational spectra of normal and modified DNA nucleobases. *Journal of Raman Spectroscopy 40*, 1726-1748.

[195] Podolyan, Y., Rubin, Y. V., and Leszczynski, J. **(2001)** An ab initio post-Hartree-Fock study of vibrational infrared spectra of 5-azacytosine and cytosine. *International Journal of Quantum Chemistry 83*, 203-212.

[196] Shishkin, O. V., Gorb, L., and Leszczynski, J. **(2000)** Conformational flexibility of pyrimidine ring in adenine and related compounds. *Chemical Physics Letters 330*, 603-611.

[197] Sauve, A. A., Cahill, S. M., Zech, S. G., Basso, L. A., Lewandowicz, A., Santos, D. S., Grubmeyer, C., Evans, G. B., Furneaux, R. H., Tyler, P. C., McDermott, A., Girvin, M. E., and Schramm, V. L. **(2003)** Ionic states of substrates and transition state analogues at the catalytic sites of N-ribosyltransferases. *Biochemistry 42*, 5694-5705.

[198] Chai, J.-D., and Head-Gordon, M. **(2008)** Long-range corrected hybrid density functionals with damped atom-atom dispersion corrections. *Physical Chemistry Chemical Physics 10*, 6615-6620.

[199] Dennington, R. K., T.; Millam, J. **(2009)** GaussView, Version 5. Semichem Inc., Shawnee Mission, KS.

[200] Hernandez, B., Orozco, M., and Luque, F. J. **(1996)** Tautomerism of xanthine and alloxanthine: A model for substrate recognition by xanthine oxidase. *Journal of Computer-Aided Molecular Design 10*, 535-544.

[201] Deng, H., Callender, R., and Dale, G. E. **(2000)** A vibrational structure of 7,8-dihydrobiopterin bound to dihydroneopterin aldolase. *Journal of Biological Chemistry 275*, 30139-30143.

[202] Latajka, Z., and Scheiner, S. **(1990)** Correlation between Interaction Energy and Shift of the Carbonyl Stretching Frequency. *Chemical Physics Letters 174*, 179-184.

[203] Deng, H., Burgner, J., and Callender, R. **(1992)** Raman-Spectroscopic Studies of the Effects of Substrate Binding on Coenzymes Bound to Lactate-Dehydrogenase. *Journal of the American Chemical Society 114*, 7997-8003.

[204] Mroginski, M. A., Murgida, D. H., and Hildebrandt, P. **(2007)** The chromophore structural changes during the photocycle of phytochrome: A combined resonance raman and quantum chemical approach. *Accounts of Chemical Research 40*, 258-266.

[205] Majoube, M., Millie, P., Chinsky, L., Turpin, P. Y., and Vergoten, G. **(1995)** Resonance Raman-Spectra for Purine. *Journal of Molecular Structure 355*, 147-158.

[206] Iancu, C. V., Borza, T., Fromm, H. J., and Honzatko, R. B. **(2002)** IMP, GTP, and 6-Phosphoryl-IMP complexes of recombinant mouse muscle adenylosuccinate synthetase. *Journal of Biological Chemistry 277*, 26779-26787.

[207] Jordheim, L. P., Durantel, D., Zoulim, F., and Dumontet, C. **(2010)** Advances in the development of nucleoside and nucleotide analogues for cancer and viral diseases. *Nature Reviews Drug Discovery 12*, 447-464.

[208] Galmarini, C. M., Mackey, J. R., and Dumontet, C. **(2002)** Nucleoside analogues and nucleobases in cancer treatment. *Lancet Oncology 3*, 415-424.

[209] Iancu, C. V., Borza, T., Choe, J. Y., Fromm, H. J., and Honzatko, R. B. **(2001)** Recombinant mouse muscle adenylosuccinate synthetase - Overexpression, kinetics, and crystal structure. *Journal of Biological Chemistry 276*, 42146-42152.

[210] Poland, B. W., Bruns, C., Fromm, H. J., and Honzatko, R. B. **(1997)** Entrapment of 6-thiophosphoryl-IMP in the active site of crystalline adenylosuccinate synthetase from Escherichia coli. *Journal of Biological Chemistry 272*, 15200-15205.

[211] Soans, C., and Fromm, H. J. **(1991)** Studies of Ligand-Binding to Escherichia-Coli Adenylosuccinate Synthetase. *Archives of Biochemistry and Biophysics 291*, 107-112.

[212] Walters, E. W., Lee, S. F., Niderman, T., Bernasconi, P., Subramanian, M. V., and Siehl, D. L. **(1997)** Adenylosuccinate synthetase from maize - Purification, properties, and mechanism of inhibition by 5'-phosphohydantocidin. *Plant Physiology 114*, 549-555.

[213] Deng, H., Burgner, J., and Callender, R. **(1991)** Raman-Spectroscopic Studies of Nad Coenzymes Bound to Malate-Dehydrogenases by Difference Techniques. *Biochemistry 30*, 8804-8811.

[214] FonnePfister, R., Chemla, P., Ward, E., Girardet, M., Kreuz, K. E., Honzatko, R. B., Fromm, H. J., Schar, H. P., Grutter, M. G., and CowanJacob, S. W. **(1996)** The mode of action and the structure of a herbicide in complex with its target: Binding of activated hydantocidin to the feedback regulation site of adenylosuccinate synthetase. *Proceedings of the National Academy of Sciences of the United States of America 93*, 9431-9436.

[215] Deng, H., Zheng, J., Burgner, J., and Callender, R. **(1989)** Molecular-Properties of Pyruvate Bound to Lactate-Dehydrogenase - a Raman-Spectroscopic Study. *Proceedings of the National Academy of Sciences of the United States of America 86*, 4484-4488.

[216] Nishimura, Y., Tsuboi, M., Sato, T., and Aoki, K. **(1986)** Conformation-Sensitive Raman Lines of Mononucleotides and Their Use in a Structure-Analysis of Polynucleotides - Guanine and Cytosine Nucleotides. *Journal of Molecular Structure 146*, 123-153.

[217] Markham, G. D., and Reed, G. H. **(1977)** Adenylosuccinate Synthetase from Azotobacter-Vinelandii - Purification, Properties and Steady-State Kinetics. *Archives of Biochemistry and Biophysics 184*, 24-35.

[218] el Kouni, M. H. **(2003)** Potential chemotherapeutic targets in the purine metabolism of parasites. *Pharmacology & Therapeutics 99*, 283-309.

[219] Sherman, I. W. **(1979)** Biochemistry of Plasmodium (Malarial Parasites). *Microbiological Reviews 43*, 453-495.

List of Publications

1. **Vishakha Karnawat**, Namrata Jayanth and Mrinalini Puranik **(2012)**, Substrate Recognition in Multi-substrate Nucleic-acid binding Enzyme (A Review). *Current Science*, 102, 298-313.
2. **Vishakha Karnawat**, Spriha Gogia, Hemalatha Balaram and Mrinalini Puranik **(2015)**, Differential Distortion of Purine Substrates by Human and *Plasmodium Falciparum* HGPRT to Catalyze Formation of Mononucleotides, *ChemPhysChem*, 16, 2172-2181.
3. **Vishakha Karnawat** and Mrinalini Puranik **(2015)**, Solution state structures of purine base analogues 9-deazaguanine and 9-deazahypoxanthine, *Journal of Biomolecular Structure and Dynamics,* DOI: 10.1080/07391102.2015.1042916.
4. **Vishakha Karnawat** and Mrinalini Puranik **(2015)**, Solution Structure of Ligands involved in Purine Salvage Pathway, Spectrochemica Acta Part A: Molecular and Biomolecular Spectroscopy, 151, 679-686.
5. **Vishakha Karnawat**, Sonali Mehrotra, Hemalatha Balaram and Mrinalini Puranik **(2015)**, Recognition, Distortion and Allosteric Control of Purine Ligands by Adenylosuccinate Synthetase, *Manuscript in communication.*
6. **Vishakha Karnawat**, Hemalatha Balaram and Mrinalini Puranik **(2015)**, *Plasmodium falciparum* Adenylosuccinate Synthetase involves Ground-state Distortion of Ligands, *Manuscript in preparation.*